

1714

INSTITUTE

for

FLUID DYNAMICS

and

APPLIED MATHEMATICS

Technical Note BN-737

June 1972

OBSERVATIONS OF INTERCHANGE BETWEEN ACCELERATION
AND THERMALIZATION PROCESSES IN AURORAL ELECTRONS

by

Morris B. Pongratz

(NASA-CR-127522) OBSERVATIONS OF
INTERCHANGE BETWEEN ACCELERATION AND
THERMALIZATION PROCESSES IN AURORAL
ELECTRONS Ph.D. Thesis M.B. Pongratz

(Maryland Univ.) Jun. 1972 275 p CSCL 03B G3/13

N72-27346

Unclas
15841

UNIVERSITY OF MARYLAND
College Park

APPROVAL SHEET

Title of Thesis: Observations of Interchange Between Acceleration
and Thermalization Processes in Auroral Electrons

Name of Candidate: Morris B. Pongratz
Doctor of Philosophy, 1972

Thesis and Abstract Approved: David L. Matthews
David L. Matthews
Research Associate Professor
Institute for Fluid Dynamics
and Applied Mathematics

Date Approved: April 10, 1972

Details of illustrations in
this document may be better
studied on microfiche ✓

VITA

Name: Morris Bernard Pongratz.

Permanent address: 9919 Good Luck Road, Seabrook, Maryland, 20801.

Degree and date to be conferred: Ph.D., June 1972.

Date of birth: April 10, 1942.

Place of birth: O'Neill, Nebraska.

Secondary education: Saint Mary's Academy, O'Neill, Nebraska, 1960.

Collegiate institutions attended	Dates	Degree	Date of Degree
Creighton University	1960-1964	B.S.	1964
University of Maryland	1964-1972	Ph.D.	1972

Major: Space Physics

Minors: General Physics and Plasma Physics.

Positions held:

Laboratory Assistant, Creighton University, 1963-1964.

Graduate Teaching Assistant, University of Maryland, 1964-1966.

Graduate Research Assistant, University of Maryland, 1966-1972.

ABSTRACT

Title of Thesis: Observations of Interchange Between Acceleration
and Thermalization Processes in Auroral Electrons

Morris B. Pongratz, Doctor of Philosophy, 1972

Thesis directed by: Research Associate Professor David L. Matthews

The results of high time resolution measurements of energetic electrons in an auroral break-up are presented. Electrons with energies from 500 eV to over 100 keV and pitch angles from 0° to 150° were detected with two detectors onboard sounding rocket 18:63 UE. Complete energy spectra were taken every 0.1 seconds.

The procedure for cleaning and activating the BeCu dynodes of a small, rugged, high-gain electron multiplier is described. A theoretical study of the energy-angular response of a spherical plate electrostatic analyzer is compared to experimental results. An energy-spectrum unfolding technique which does not require the assumption of a histogram-type energy spectrum is presented. A method of determining sounding rocket orientation from the output of a single magnetometer is described.

A burst of enhanced electron precipitation was particularly interesting. The electron pitch angle distribution became anisotropic during the burst. At very high energies ($E > 80$ keV) the flux was peaked at a pitch angle corresponding to the boundary of the loss cone. The auroral electron differential energy spectrum had a characteristic peak near 10 keV. The electron energy spectrum in the energy range 0.5-20 keV is fitted with two functions. A power law ($\sim E^{-n}$) dependence

is used at low energies, and a function with the energy dependence of a Maxwellian electron gas with density, n_e , and temperature, T_e , moving relative to the observer with a velocity corresponding to an electron kinetic energy, E_o , is used to fit the peaked portion of the energy spectrum. Typical values are $E_o \sim 10$ keV, $T_e \sim 400$ eV, $n_e \sim 0.5 \times 10^{-3} \text{ cm}^{-3} - \text{sr}^{-1}$. The drifting Maxwellian accounts for nearly half of the electron energy flux into the auroral ionosphere.

Of special interest are occasions where E_o decreases as T_e and n_e increase which are called thermalization and cases where E_o increases as T_e and n_e decrease which corresponds to particle energization. The thermalization process is suggestive of wave-particle stabilization of a bump-in-tail velocity distribution. During each of these processes the temperature and density vary in a manner corresponding to adiabatic compression ($T_e \sim n_e^{\gamma - 1}$) with $\gamma \sim 5/3$. The value of E_o was not correlated with the total downward electron flux (electrons $\text{cm}^{-2} - \text{sec}^{-1}$) above 500 eV.

Three ratios R_{E_o} , R_{T_e} and R_{n_e} are computed from the ratios of E_o , T_e and n_e for electrons with pitch angles between 60° and 93° to the corresponding parameters describing electrons with pitch angles less than 45° . The temperature and density ratios are always ≥ 1 indicating preferential heating of the $60^\circ - 90^\circ$ pitch angle electrons as well as the anisotropic pitch angle distribution. The large deviations from unity of R_{n_e} and R_{T_e} are suggestive of local causes rather than sources in the magnetic equatorial plane. Although the values of E_o , T_e and n_e are consistent with acceleration by a parallel electric field of auroral electrons measured by satellite at higher altitudes [Frank and Ackerson, 1971] the deviations from unity of R_{E_o} (generally

to values < 1) indicate that such a mechanism is not solely responsible for the auroral electrons.

OBSERVATIONS OF INTERCHANGE BETWEEN ACCELERATION
AND THERMALIZATION PROCESSES IN AURORAL ELECTRONS

by
Morris Bernard Pongratz

Dissertation submitted to the Faculty of the Graduate School
of the University of Maryland in partial fulfillment
of the requirements for the degree of
Doctor of Philosophy
1972

ACKNOWLEDGMENTS

I would like to thank Dr. Matthews for his advice, guidance and leadership during the course of my research. I would also like to thank Mr. J. Kempton for preparing the detector drawings and Mr. E. Grossenbacher and his staff for their craftsmanship in making the detectors. I am especially grateful to Mr. J. Sisson for making the electron multiplier dynodes. I wish to thank K. Christoph and S. McPhillips for the design and construction of the electronics.

I wish to thank the personnel of the Churchill Research Range and Dr. F. Creutzberg for their assistance at the launch site. I would like to acknowledge the assistance and cooperation of the Sounding Rocket Branch of the Goddard Space Flight Center and Mr. H. Albright in particular. I would like to thank Mr. B. Powelless and the Information Processing Branch of the Goddard Space Flight Center for their data reduction assistance.

I also appreciate many helpful discussions with Dr. K. Papadopoulos. I would like to thank Mrs. C. Stephan and Mrs. M. Walsh for typing this thesis.

I am especially grateful to my wife, Cheryl, and my parents for their help and understanding.

I also wish to acknowledge the support of this research under NASA grants NSR 21-002-077 and NSG-~~398~~ NG2.21.002.008

TABLE OF CONTENTS

Chapter	Page
ACKNOWLEDGMENTS	ii
I. INTRODUCTION	1
A. Essential Capabilities of an Experiment to Measure Auroral Electrons	3
B. Summary of Results	10
II. DESCRIPTION OF DETECTORS	13
A. Primary Electron Spectrometer (PESPEC)	15
1. Physical Description	15
2. Primary Electron Spectrometer (PESPEC) Electronics	17
3. Electron Multipliers	21
4. PESPEC Geometric Factor	28
5. Unfolding the Energy Spectrum	56
B. Scintillator-Photomultiplier Detector (P.H.A.).	67
1. Physical Description	67
2. P.H.A. Electronics	70
3. Determination of the Energy Spectrum from P.H.A. Data	72
III. VEHICLE POSITION AND ATTITUDE	89
A. Vehicle Position	90
B. Payload Attitude	98
C. Pitch Angle Determination	118
IV. DATA REDUCTION TECHNIQUES	121
A. "Spray" Digitizing of FM-FM-PCM Signal	122
B. Intensity Contour Displays	126

Chapter	Page
C. Averaging Techniques	129
D. Interpretation of Overranges on PHA	138
V. GENERAL OBSERVATIONS-18:63 UE	144
A. Results from other Experiments of Parameters Related to the Aurora Observed with 18:63 UE.	146
B. Total Energy of Electrons Detected by Electron Spectrometer from 0604:20-0608:20 UT	155
C. Energy-Time Contours from the Spectrometer Data	160
D. Temporal Features of the Pitch Angle Distributions from Pulse Height Analyzer (P.H.A.) Data	170
VI. DETAILED EXAMINATION OF BURST [0604:30-0605:00 UT]	176
A. Parameterizing the Auroral Electron Differential Energy Spectrum	178
B. Observations of Interchange between Acceleration and Thermalization Processes during the Burst	185
C. Pitch Angle Distributions during the Burst	204
D. Discussion	232
APPENDIX 1. PROCEDURE FOR ACTIVATING BERYLLIUM-COPPER DYNODES FOR ELECTRON MULTIPLIER	252
APPENDIX 2. DETERMINATION OF $\Delta\alpha_{ij}$ - THE RANGE OF ALLOWED ENTRANCE ANGLES IN i_j THE PLANE OF THE TRAJECTORY	254
REFERENCES	261

CHAPTER I

INTRODUCTION

The aurora has long been the subject of man's curiosity. These visible radiations originating in the upper atmosphere with their dancing, flaming movements and diverse, variegated forms attract scientific inquiry. The proper explanation of some auroral features provides a rigorous challenge to many theories of magnetospheric physics. The study of aurora requires a multi-disciplinary approach involving, among others, spectroscopy, aeronomy, geomagnetism, solar physics and plasma physics. In addition an *in situ* experimental study requires considerable engineering skill.

Birkeland [1908, 1913], Störmer [1955] and Alfvén [1939] in the first half of the century were among the first to attempt to determine the cause of aurora. Vegard [1948] discovered the hydrogen Balmer lines in auroral spectra. He noted that H β was shifted to shorter wavelengths and correctly interpreted this phenomenon. Fast protons were striking the upper atmosphere, undergoing neutralizing collisions without losing much velocity and therefore the characteristic H β decay line was Doppler shifted.

Intense international cooperative efforts began with the organization of an International Geophysical Year (IGY, July 1, 1957 to December 31, 1958). The consequent availability of high latitude launch sites for sounding rockets allowed the first direct measurement of the energetic particles producing the aurora. McIlwain [1960] found that energetic electrons precipitating into the upper atmosphere were the dominant cause of the most dramatic features of the aurora.

O'Brien [1962] and Davis et al [1960] have shown that most of the energy precipitated, especially in discrete forms and short term enhancements, is provided by electrons ; the proton contribution is more diffuse, less time dependent and generally does not deposit as much energy [Eather, 1967]. Sufficient energy for the auroral substorm [Akasofu, 1964] which includes visible aurora, ionospheric currents, magnetic disturbances, ring currents, etc. appears to be available. It requires the conversion of less than one percent of the energy flux of the solar wind incident upon the magnetosphere [Akasofu and Chapman, 1967]. The goal of our research was to determine the nature and source of the auroral particles. We felt that we could better accomplish this goal by making very detailed measurements of the auroral electrons rather than less complete surveys of particles of both charge species.

A. Essential Capabilities of an Experiment to Measure Auroral Electrons

The principal measurements needed to characterize auroral electrons are the spatial and temporal variations of the electron flux, the energy spectrum and the pitch-angle distribution (electrons follow helical paths about the earth's magnetic field and the pitch angle is the angle between the electron velocity and the magnetic field). Corroborative measurements of magnetic and electric fields, plasma waves, ionospheric absorption and some characteristic emissions in the auroral spectrum are also helpful. Coordinated measurements between sounding rockets and satellites would provide additional magnetospheric and interplanetary parameters, but such coordination is difficult because of limited launch windows, meteorological considerations and the uncertain temporal and spatial features of the aurora.

We want to avoid completely describing the morphology of the auroral substorm, but some general considerations of spatial and temporal features are necessary in order to understand the limitations and capabilities of an experiment to measure auroral electrons. Vertical luminosity profiles show that most of the light in an aurora comes from the altitude range between 90 km and 120 km. The luminosity profile is a function of the energy of the precipitating particles. Higher energy particles penetrate deeper into the atmosphere before being stopped by collisions. Because of the steep gradient in atmospheric density they cause most of the light emission near the end of their path. Aurorae are also very structured in horizontal extent. Auroral arcs are several kilometers in width and may be hundreds of kilometers long. Typically such quiet arcs and homogeneous forms are seen in the early evening.

Near midnight the forms become striated, develop loops and merge with similar forms which then brighten and produce an enthralling chaos of luminosity called the 'break-up'. Horizontal auroral motions having speeds up to 2.5 km/sec have been observed [Davis, 1968].

Periodic fluctuations of electron intensity have also been observed with time scales ranging from 0.1 second to 15 seconds [Barcus, et al , 1971; Evans, 1967]. High-time-resolution measurements have proven to be valuable in determining the time lag of the peak of the cross-correlation between time series of varied energies. This lag can be interpreted as a velocity dispersion of particles accelerated at a common place and time some distance from the point of observation [Evans, 1967; Johnstone, et al, 1971].

Balloon-borne detectors which measured bremsstrahlung x-rays from electrons with energies above 25 KeV were first used to measure auroral electrons [Winckler, 1958]. They give no information about pitch-angle distribution or height profiles and determining the electron energy spectrum from the x-ray spectrum is difficult. The balloon technique is still popular because of the relative cost, and simplicity in construction and launch and because this technique is excellent for studying temporal variations [Barcus, et al, 1971].

The use of satellites to detect auroral electrons is complicated by the high satellite velocity (~ 8 km/sec) relative to the aurora. This makes it very difficult to separate temporal and spatial variations. Recently the ISIS-I [Heikkila, et al, 1970] and INJUN-5 [Frank and Ackerson, 1971] satellites using very high data rates have provided excellent information about auroral particles.

Sounding rockets suffer from a limited flight time ~ 500 sec, but they do allow the experimenter to directly measure the electrons. The sounding rocket has much less horizontal velocity than a satellite. Near apogee the sounding rocket spends much time at nearly the same altitude. Therefore when coupled with ground-based measurements it may be possible to separate spatial and temporal variations. Using high data rates one can obtain numerous measurements during the flight. With sounding rockets one can determine height profiles, energy spectra, pitch-angle distributions and data on short term temporal variations.

High data rates imply small sampling times and in order to accumulate a statistically significant number of counts during each sampling interval we needed electron detectors with rather large geometric factors. The consequent large exit apertures and need to be able to sustain maximum count rates of several megahertz induced us to choose discrete-dynode electron multipliers rather than the more conventional Channeltrons for detecting electrons.

The auroral electron energy spectrum may vary in intensity at a given energy by several orders of magnitude and there have been nearly as many shapes to the spectrum as there have been experimenters. Hones et al [1971] has reviewed the various auroral electron energy spectra measured by sounding rockets. Many of the spectra have one or more peaks in the 1-10 KeV energy range. In general the maximum of the spectrum is at the lowest detectable energy (when it is less than 1 KeV). Several experimenters [Matthews and Clark, 1968; Choy, et al, 1971; Ogilvie, 1968] have found that the low-energy (< 1 KeV) portion of the spectrum rises very steeply suggesting possible local acceleration.

Because of the variability of the auroral electron energy spectrum an energy budget for an aurora cannot be calculated unless one has complete coverage of the electron energy spectrum.

This requirement convinced us of the necessity of using spectrometers to cover the important energy interval from 10eV to 30KeV. Because energy-loss type detectors were not suitable for these low energies we chose electrostatic deflection for electron energy determination. By using curved deflection plates it was possible to obtain differential energy determination. Energy resolution adequate to see peaks in the spectrum determined the plate spacing. We used two electrostatic spectrometers: A primary electron spectrometer to cover the energy interval from 500eV to 30KeV (primary electrons are those incident upon the atmosphere as opposed to secondary electrons which are the products of ionizing collisions in the atmosphere) and a secondary electron spectrometer to cover the energy interval from 10eV to 750eV.

Aluminum coated scintillators mounted on photomultiplier tubes were used to detect electrons with energies greater than 20 KeV. Differential energy determination was obtained by five channel pulse height analysis.

The thermal and super-thermal ($E < 10$ eV) electrons were measured by retarding potential analyzers. These detectors are similar to Langmuir probes, but the current collector is biased positively to avoid collecting positive current due to ions. They are also capable of determin-

ing the vehicle potential, electron density and thermal electron temperature.

McDiarmid and Budzinski [1969] and McDiarmid et al [1967] have made excellent measurements of the pitch-angle distribution of the higher energy electrons ($E > 20$ KeV). They found that the pitch-angle distribution of the precipitated electrons (pitch angles less than 90°) was generally isotropic. Anisotropic distributions were generally peaked toward 90° pitch angle rather than being field-aligned. This anisotropic distribution was more unstable - not persisting for very long and becoming more isotropic during enhancements of the electron intensity. Courtier, et al [1971] have recently reported similar observations and have interpreted them in terms of pitch-angle diffusion [Kennel and Petschek, 1966] from a reservoir of trapped electrons into the loss cone (the loss cone describes the range of pitch angles which escape from a magnetic mirror geometry such as the dipole-like field of the earth).

Pitch-angle distributions which tend to be field-aligned have also been observed with sounding rockets [Cloutier, et al, 1970; Choy, et al, 1971] and satellites [Hoffman and Evans, 1968; Hultquist, et al, 1971]. Differences in the pitch-angle distributions of electrons and ions can contribute to Birkeland (field-aligned) currents [Park and Cloutier, 1971] and even to electric fields parallel to the magnetic field via Alfvén's mechanism [Alfvén and Fälthammer, 1963].

Theories of particle precipitation also predict various pitch-angle distributions. They range from Chamberlain's model [Chamberlain, 1969] which predicts both particle acceleration and precipitation to Kennel and Petschek's [1966] theory of pitch-angle diffusion which

precipitates particles from a reservoir without energization of the particles. In the pitch-angle diffusion theory a small diffusion coefficient will result in anisotropic pitch-angle distributions peaked towards 90° . A larger diffusion coefficient will precipitate more particles and the auroral electron pitch-angle distribution will be isotropic over the downward hemisphere. The upward-going electrons should also be monitored because there have been observations [McDiarmid, et al, 1961] in which the fluxes of these electrons were not consistent with atmospheric scattering and mirroring in the geomagnetic field.

Adequate pitch-angle information therefore requires measurements of electrons: precipitating nearly parallel to the magnetic field (pitch angles less than 45°), mirroring in the magnetic field (pitch angles near 90°) and coming up the field (pitch angles greater than 90°). In general complete coverage of these pitch angles is more important than high angular resolution; however Albert and Lindstrom [1970] with very high angular resolution ($\sim 1/2^\circ$) saw statistically significant fluctuations on a scale of 1° - 2° in the electron pitch-angle distributions.

From a satellite with the spin axis oriented perpendicular to the magnetic field a single detector mounted to look radially from the spin axis could provide adequate pitch-angle coverage sampling at pitch angles from 0° to 180° twice per roll. However a sounding rocket launched from an auroral launch site typically has an angle of only 10° - 20° between the rocket angular momentum vector and the earth's magnetic field. If it is not despin or has a nominal despin the coning angle (angle of precession about angular momentum vector) will typically be less than 20° . Consequently a single radially looking detector will only

measure a pitch angle interval from $\sim 60^\circ$ to $\sim 120^\circ$. Therefore adequate pitch-angle coverage requires multiple detectors.

We chose spherical plate electrostatic energy analysis through a central angle of 90° for our primary electron spectrometer. A central angle of 90° , rather than 180° , gave better pitch-angle resolution without sacrificing adequate energy resolution. The geometry of the spherical plate analyzer is especially conducive to multiple entrance and exit apertures allowing one to acquire measurements at several pitch angles with a single set of deflection plates and deflection voltages. Because we expected less pitch-angle structure and wanted better energy resolution we chose a spherical plate analyzer with a central angle of 180° for our secondary electron spectrometer.

We had to use multiple detectors to obtain good pitch-angle coverage of the higher energy ($E > 20$ KeV) electrons. We were fortunate with vehicle 18:63, which had only one detector, in that a very large coning angle allowed it to sample a very large range of pitch angles.

B. Summary of Results

We have launched three Nike-Tomahawk sounding rockets into aurorae from Fort Churchill, Manitoba. Most of the data which have been analyzed were obtained by the first vehicle, 18:63 UE, which was launched near local midnight, March 21, 1968 into a break-up aurora. As revealed by ground based photometer and by data on high energy electrons ($E \sim 90$ KeV) the time profile was characterized by a decay from an initial peak and an enhancement or burst in light and electron intensity when the rocket was approaching apogee. Throughout most of the flight the pitch-angle distribution of the electrons was isotropic. The significant exception occurred during the burst of increased precipitation when the pitch-angle distribution became anisotropic.

Because, at first glance, a pitch-angle distribution which becomes more anisotropic as the precipitation increases is contrary to current theories of pitch-angle diffusion [Courtier, et al, 1971] we chose this burst for further more detailed analysis. We have found that the pitch-angle distribution of the highest energy electrons ($E \sim 90$ keV) tends to peak near 70° which is near the local boundary of the loss cone for trapped particles.

With supporting evidence from the ground-based photometer we believe that the burst occurred in the time domain rather than being due to a form moving across the trajectory.

The auroral electron differential energy spectrum had a characteristic peak near 10 keV. We fitted the electron energy spectrum in the energy range 0.5-20 keV with two functions. A power law dependence was used at low energies. A function with the energy

dependence of a Maxwellian electron gas with density, n_e , and temperature, T_e , moving relative to the payload with a velocity corresponding to an electron kinetic energy, E_o , was used to fit the peaked portion of the spectrum. Variations of E_o by 50% and n_e and T_e by a factor of ten were observed during the burst. Cases where E_o decreases as T_e and n_e increase have been designated thermalization. Particle energization corresponds to the situation where E_o increases as T_e and n_e decrease. The relationship between T_e and n_e was consistent with an adiabatic compression of the electron gas. The anisotropic pitch-angle distribution resulted from preferential heating of electrons with pitch angles greater than 60° . The variation of the E_o parameter is similar to the "inverted V's" of Frank and Ackerson [1971].

We needed all the capabilities of the detectors to observe this phenomenon. Without measuring the entire energy spectrum one would have been unable to detect the smooth change from thermalization to particle energization. The high time resolution was needed to insure significant counts per collection interval and the intervals were small enough to allow many complete energy spectra to be measured per roll. The resulting good pitch angle information measured the development of the anisotropy during the burst.

In the next chapter we present a more complete and detailed description of the electron detectors and their associated electronics. In the third chapter we describe the methods used to determine the vehicle position and attitude and the detector pitch angles. In the fourth chapter we describe the techniques and methods used in reducing

the data from the telemetry signal tape to the final values of electron flux. We will also define several averages which will be used to describe the electron flux. In the fifth chapter we present the general features of the data obtained through the flight. These general features will serve as a reference with which the burst data presented in chapter six can be compared. In this final chapter we discuss possible theoretical implications to be drawn from the data. Several appendices have been added to preserve continuity in the main text.

CHAPTER II

DESCRIPTION OF DETECTORS

We have constructed and launched into aurora three Nike-Tomahawk sounding rocket payloads - 18:63 UE, 18:64 UE and 18:65 UE. Consideration of the type of sounding rocket dictates to some degree the types of measurements that can be obtained. The essential characteristics to consider are the apogee height and attitude control. A Nike-Tomahawk with a 200 pound payload will reach an altitude of about 260 km. Many experiments would suffer from atmospheric friction or high voltage breakdown if they were switched on too low in the atmosphere therefore the flight duration for altitudes above 70 km determine the practical data acquisition time. For a Nike-Tomahawk this time is about 400 seconds. The Nike-Tomahawk is spin stabilized and has no attitude control system, therefore the only change in attitude of a rigidly mounted detector results from the spinning and precession of the entire vehicle about the angular momentum vector. When necessary the spin rate can be decreased by despin mechanisms after exiting from the atmosphere.

The Sounding Rocket Branch at the Goddard Space Flight Center (NASA) provided multiplexers and transmitters, turn on signals and magnetometers for our sounding rockets. The telemetry system was a two transmitter FM-FM system. The two main carrier frequencies were in the 216 to 260 MHz range, and the subcarrier channels were at standard IRIG (Inter-Range Instrumentation Group) frequencies ranging from 165 kHz to 2.3 kHz. Each carrier signal was sent to two antennas mounted 180° apart flush with

rocket skin. The four antennae were separated from each other by 90° in the plane perpendicular to the payload spin axis.

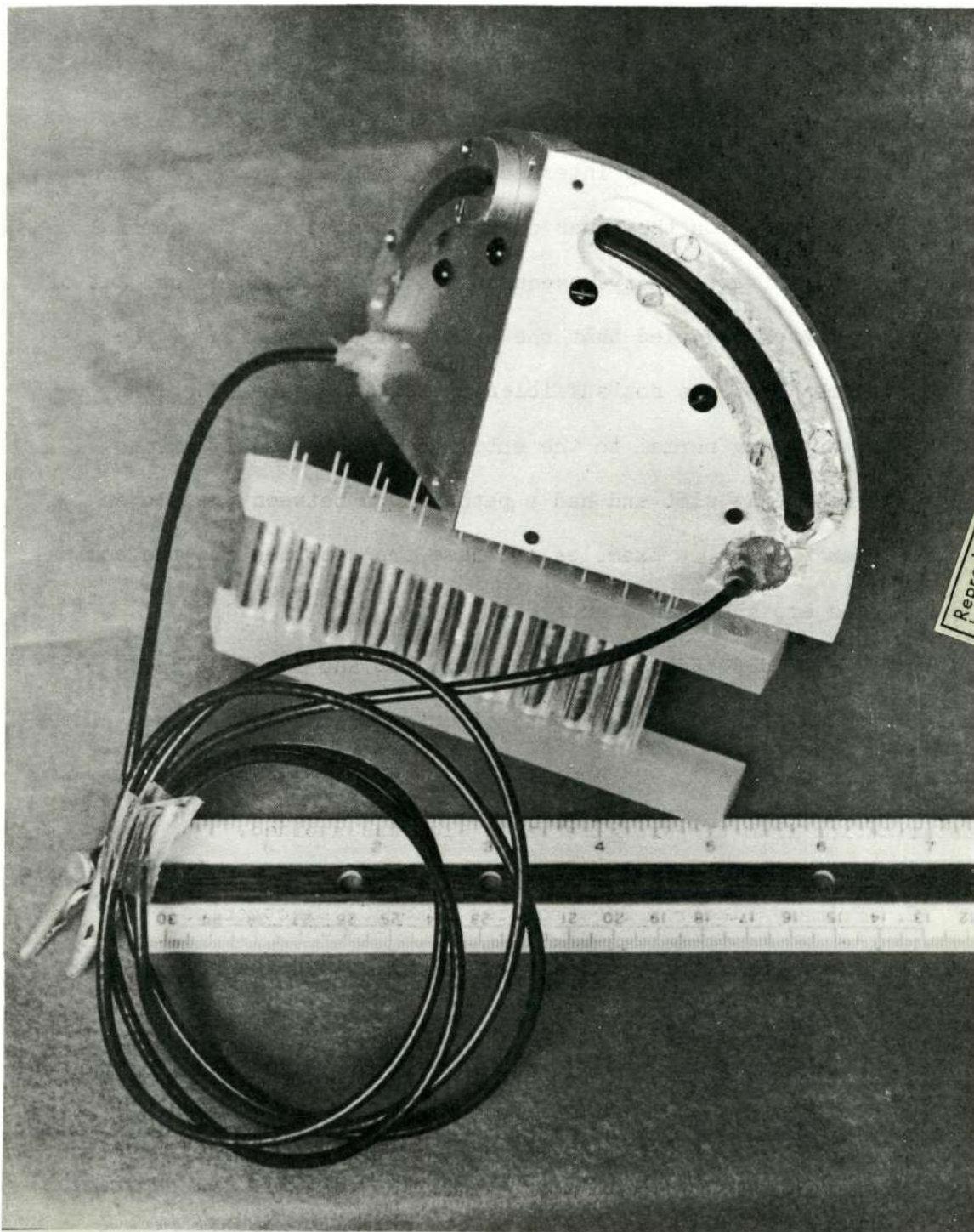
Invited experimenters on the payloads measured optical auroral emissions, plasma density and temperature, plasma waves and electric fields. The University of Maryland experiments were similar in purpose and type on all three payloads. Because the data for this thesis were obtained from our first vehicle we will concentrate on describing the 18:63 UE detectors in this chapter. The University of Maryland electron detection experiments on 18:63 UE were: (i) a Retarding Potential Analyzer (R.P.A.) to measure properties of thermal and superthermal electrons ($E < 10$ eV), (ii) a Secondary Electron Spectrometer (SESPEC) which measured differential electron energy spectra in the energy range $1 \text{ eV} < E < 750 \text{ eV}$, (iii) a Primary Electron Spectrometer (PESPEC) which measured differential electron energy spectra in the energy range $0.5 \text{ KeV} < E < 40 \text{ KeV}$, and (iv) a scintillator-photomultiplier tube with pulse height analysis (referred to as the P.H.A.) to measure electrons with energies greater than 20 KeV. The retarding Potential Analyzer (R.P.A.) will be described elsewhere [Matthews, 1972a]. The Secondary Electron Spectrometer (SESPEC) failed and will not be described further.

A. Primary Electron Spectrometer (PESPEC)

1. Physical Description

The PESPEC detector used spherical plate electrostatic deflection through a central angle of 90° for energy analysis and 20-stage electron multipliers for electron detection. The two concentric deflection plates were held in place by KeL-F structures and were separated by 0.250 in. The inner plate radius, R_i , was 2.50 in. The plates were spherical triangles with vertex angles of 90° , 90° and 120° (a central vertex angle of 180° rather than 120° would describe a quadrispherical analyzer) (see figure 2.1). A positive potential on the inner plate and a negative voltage on the outer plate deflected electrons to orbit between the plates. If the electron velocity was in the proper range it would pass between the plates striking neither the inner plate nor the outer plate. The entrance apertures were the two 2.9 in. slots on either side of the central vertex angle. These slots were covered by a fine, high transmission tungsten mesh grid which was at ground (vehicle) potential. The exit apertures were 0.5 in. x 0.25 in. slots in the KeL-F at right angles (on the spherical triangle) opposite the entrance slots. The electron multipliers were mounted adjacent to the exit apertures. The PESPEC was connected to a sliding rail and was held inside the payload during the initial part of the flight by an ejectable door. After despin at $t + 50$ sec the door was ejected, and the PESPEC was deployed.

Nominal electron trajectories from each slot required electrons to enter essentially perpendicular to the entrance slots. For a



Reproduced from
best available copy.

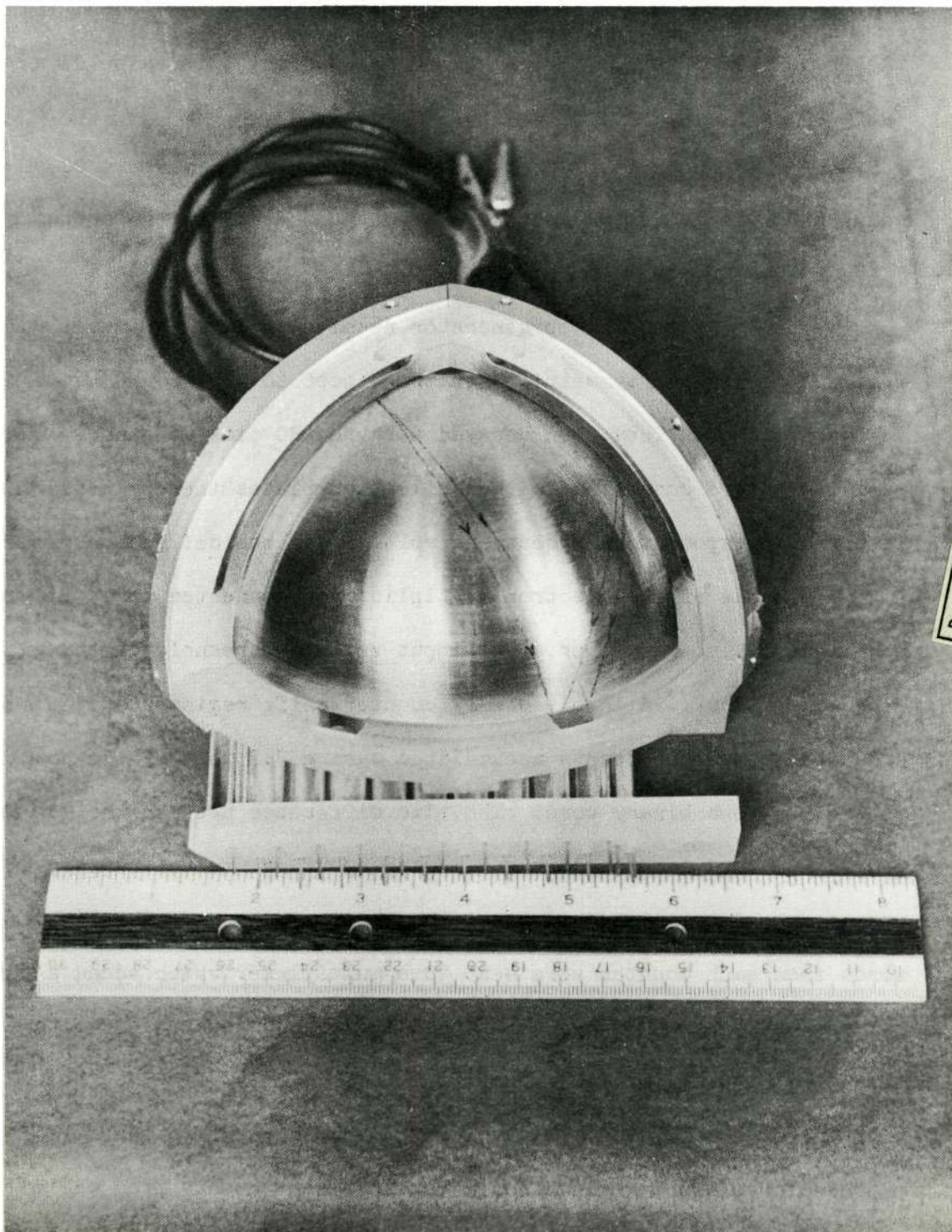
Figure 2.1. View of entrance to analyzer plates and electron multiplier.

nominal trajectory the upper slot was oriented to detect electrons at an angle of 10° from the payload axis of symmetry, 0° being the upward direction. The lower slot was oriented to look 70° from the spin axis. The minimum arc length traveled in a nominal trajectory was $\pi/2 R_1$. The paths of the nominal electrons from each entrance slot to the designed exit slot actually intersected between the plates. During pre-launch calibration there was only time for testing the nominal trajectories. After launch subsequent testing of an identical set of deflection plates revealed that the exit slot collimation of the 0.25 in. thick KeL-F was not sufficient to exclude some electrons which, not entering normal to the entrance slot, actually exited at the nearest exit slot and had a path length between the plates of less than $\pi/2 R_1$. Examples of these trajectories and the nominal trajectories are shown in figure 2.2.

The PESPEC detector on vehicles 18:64 UE and 18:65 UE had a 90° central vertex angle and three sets of entrance and exit slots. These three slots looked 45° , 90° and 135° from the payload spin axis. Contamination from the wrong entrance slot was avoided.

2. Primary Electron Spectrometer (PESPEC) Electronics

The electronics section for the PESPEC provided the high voltage for the electron multiplier, the positive and negative voltage sweeps for the deflection plates and amplified and counted the anode pulses from the electron multipliers. The sweep generator and counting section were given timing commands from a digital programmer which provided the basic repetition or cycle and counting or word intervals from multiples of the basic digital bit rate or "clock"



Reproduced from
best available copy.

Figure 2.2. View of analyzer plates showing typical allowed trajectories.

frequency. See figure 2.3 for a block diagram of the PESPEC electronics section. The cycle or "frame" interval was 0.1088 sec. A PESPEC energy spectrum was measured each frame. This was done by subdividing the frame into 32 equal time segments or counting intervals (data "words") each 3.4 msec in length.

The electron multiplier high voltage power supply was a DC-DC converter. Input voltage was +28 V. It was capable of an output of 7 KV at 100 μ A.

When the voltage sweep generator received a frame interval pulse from the programmer symmetrical (with respect to ground) RC networks were charged up. They then decayed with the RC time constant. The capacitors were connected to the deflection plates thereby producing essentially exponentially decaying voltages on the deflection plates.

The anode of the electron multiplier was connected to a wide-band, non-linear pulse amplifier. The input voltage threshold of the amplifier was ~ 700 μ V. A 16-bit binary counter-shift register system encoded the number of counts accumulated during 3.2 msec of the counting interval into a binary word. The time difference between the 3.4 msec programmer word length and the 3.2 msec count accumulation interval was used to dump, clear and reset the count registers. The 16-bit words from each counter were sent to a multiplexer which added a parity bit to insure an odd number of "ones" and a word separation voltage level one bit long called a "hole".

Three data words following the frame pulse sent to the deflection plate voltage sweep generator did not represent counts from the pulse amplifier during the voltage recharge interval, but they consisted of three words of an identical bit pattern which was used for identifying

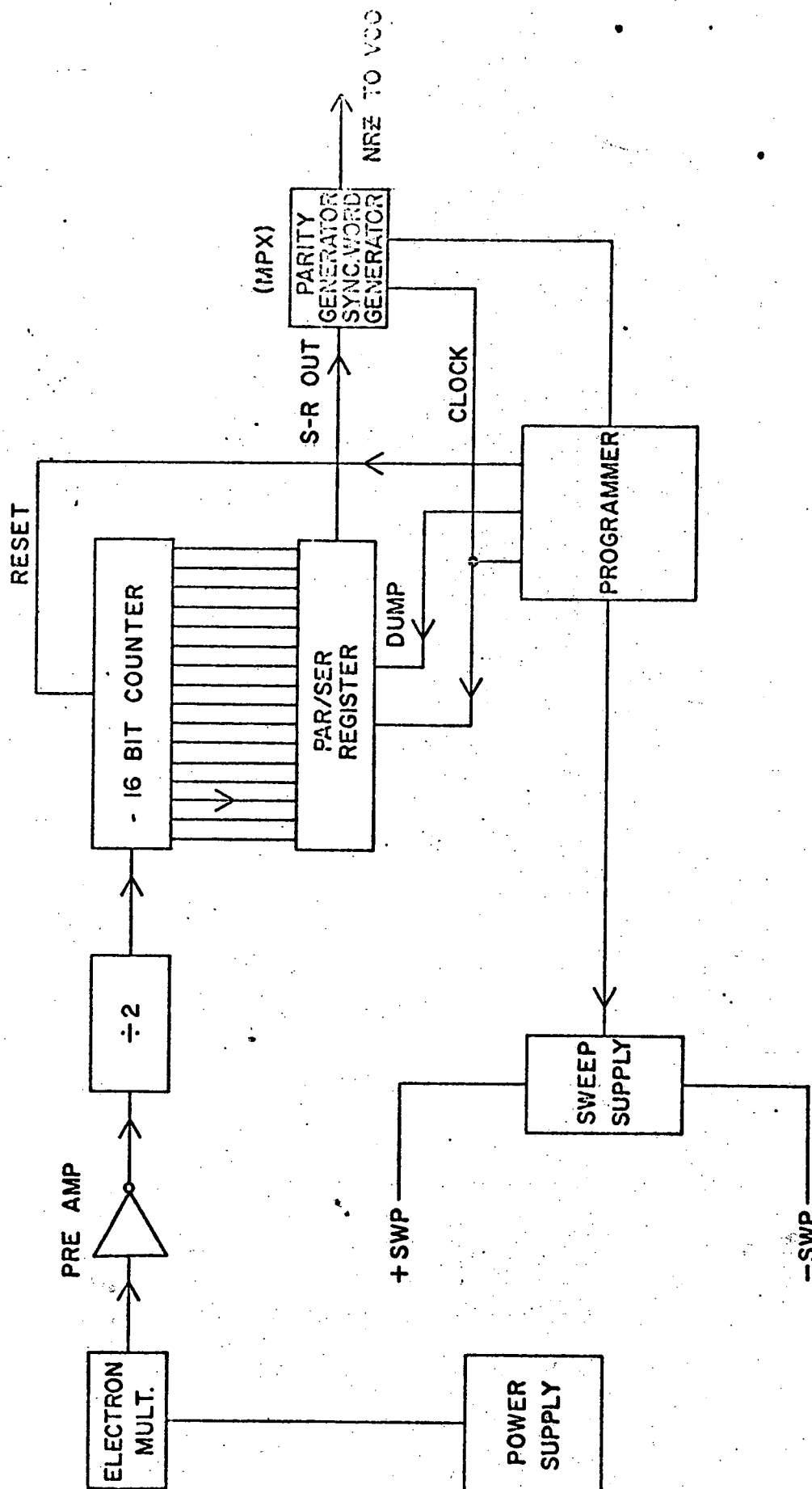


Figure 2.3. PESPEC electronics block diagram.

the beginning of a new frame and a new energy spectrum. The 34 bit serial data word consisting of three voltage levels was sent to the VCO of the PESPEC FM subcarrier in the transmitter. Figure 2.4 shows the temporal relationship between the voltage sweeps and the serial data string.

3. Electron Multipliers

Electron multipliers were used to detect the electrons which had suitable energy to pass through the deflection plates. The electron gain, G , (number of electrons at anode per incident electron at first dynode) is given by

$$G = \gamma^n$$

where γ is the secondary emission coefficient and n is the number of stages of the multiplier. Because the anode is at a high positive voltage the pulse is capacitor coupled to the input of the pulse amplifier.

The electron multipliers used on 18:63 UE had 20 dynodes in the Allen [Allen, J.S., 1947] configuration with KeL-F supports. The dynode height was 1.0 in. which was reduced from the 1.75 in. of Allen's because of size limitations. The multiplier dimensions were approximately 5 in. x 2 in. x 1 in. A voltage divider network of 20 13M Ω resistors was appropriately tapped to provide an increasing potential on each dynode. We chose aluminum dynodes for 18:63 UE because the aluminum secondary emission coefficient [Bingham, R.A., 1966] is apparently unaffected by exposure to air.

With the physical modifications to the PESPEC detectors in 18:64 UE and 18:65 UE we found that the 20-stage aluminum multiplier was

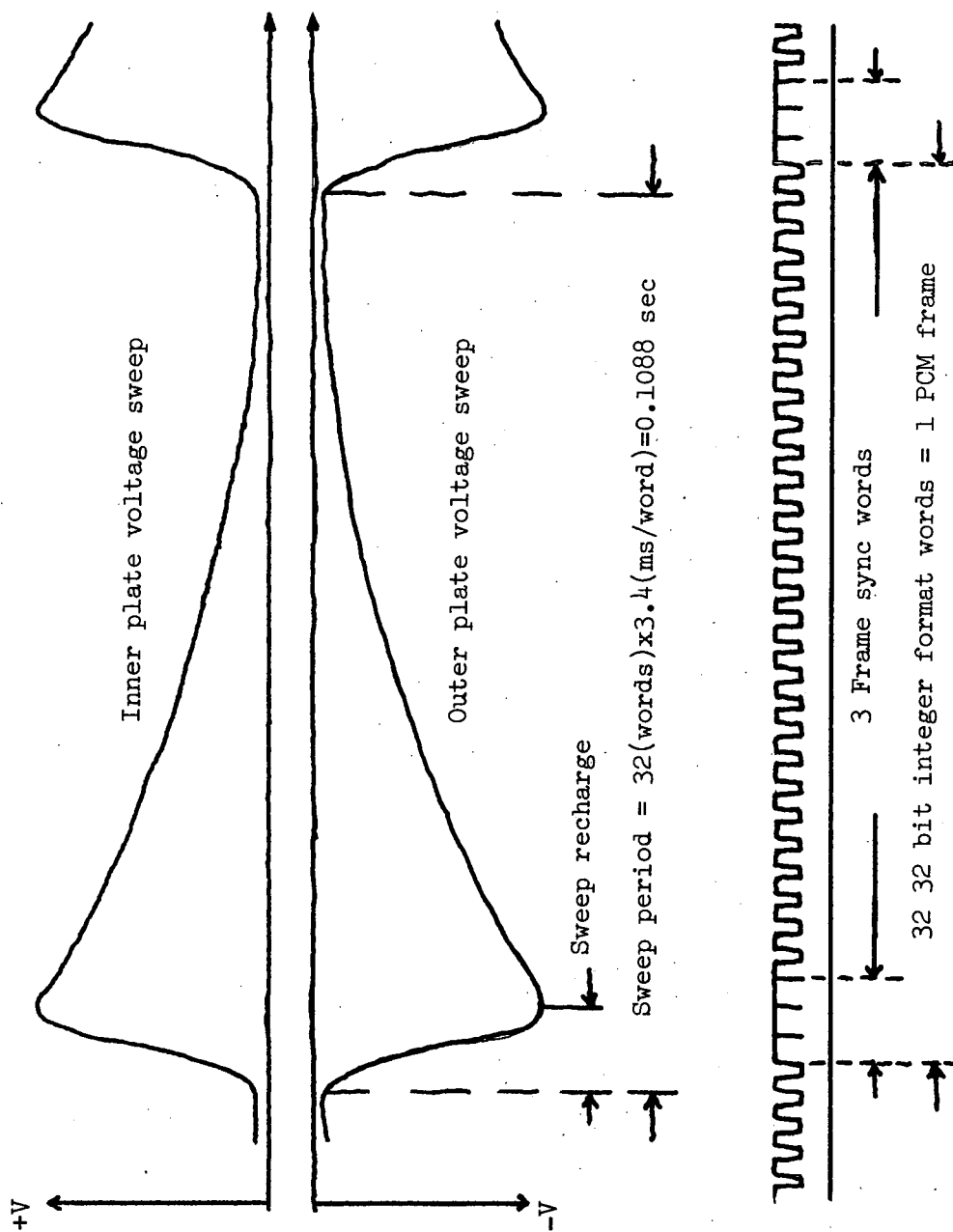


Figure 2.4. The voltage sweeps and the serial data string.

too large. We initially tried 14 stage activated beryllium-copper dynodes of the same shape and configuration as before except that the dynodes were only 0.5 in. in height. (The activation procedure which produces Be O on the surface of the dynode to enhance the secondary emission coefficient is described in appendix I.) A computer simulation demonstrated that losses to the KeL-F sides because of the short dynode height may have caused substantial gain reduction. We then redesigned our dynode to put a top and bottom on each dynode to prevent losses to the sides. We also made the dynodes at a smaller scale than the Allen size, and we made them 0.60 in. high. This had the effect of improving the height to separation distance ratio which is critical in preventing losses. We were able to make a 17-stage activated Be-Cu electron multiplier with a gain of 10^7 which was only 3 in. x 1.5 in. x 1.0 in. These multipliers showed no degradation in gain after being exposed to air for several months.

The size of the voltage pulse from the electron multiplier is given by

$$V = q/C = G e/C = \gamma^n e/C \quad (2.1)$$

where q is the amount of charge collected at the anode, e is the electronic charge and C is the capacitance from anode to ground. To be counted the voltage of the pulse, V , must exceed the amplifier threshold. In practice one wants the amplifier as close to the multiplier as possible to minimize the capacitance, C . On 18:64 UE and 18:65 UE we installed an emitter-follower circuit inside the box containing the electron multiplier to minimize these capacitive losses.

For a time τ , called the dead time, after the non-linear pulse

amplifier detects a pulse above its threshold voltage it cannot respond to another pulse. Therefore whether or not an electron of energy E will be counted depends upon $\eta(E)$, the efficiency at which the multiplier produces pulses above the amplifier threshold, and the rate at which these pulses are coupled into the amplifier. Using Poisson statistics it can be shown that the rate at which electrons are counted, r , is related to the rate at which they enter the multiplier, R , by

$$r[\text{counts/sec}] = R[\text{electrons/sec}] \eta(E)[\text{pulses/electron}] \times e^{-R\eta(E)\tau} \quad (2.2)$$

We were able to measure τ with an electron gun providing 1 KeV electrons by measuring the beam current, R , with a Faraday cup and then directing the beam into the electron multiplier and computing r from the number of counts in the data word. If one then varies R and records r for k cases using equation (2.2) it is possible to make a least-squares determination of τ as a function of $\eta(E)$,

$$\tau = \frac{\sum_{i=1}^k R_i \left[\ln \left(\frac{\eta(E) R_i}{r_i} \right) \right]}{\eta(E) \sum_{i=1}^k R_i^2} \quad (2.3)$$

The correct value of $\eta(E)$ at 1 KeV is determined by varying $\eta(E)$ in equation (2.2) until the quantity

$$S \equiv \sum_{i=1}^k (r_i - R_i \eta(E) e^{-R_i \eta(E) \tau})^2 \quad (2.4)$$

reaches a minimum. The latter technique is called a single-parameter direct-search least-squares fit. The value of τ from equation (2.3)

must be used in equation (2.4). τ was found to be

$$\tau = (88 \pm 5) \times 10^{-9} \text{ sec}$$

Figure 2.5 is a plot of r vs R .

Because η is a function of energy it was necessary to use data from a fixed energy to determine τ . Once τ is known one can use values of r and R at other energies and by varying $\eta(E)$ attempt to satisfy the equality of equation (2.2). The values of η which come closest to satisfying equation (2.2) for various values of energy are shown in figure 2.6. The values of $\eta(E)$ were then fitted to a function of the form

$$\eta(E) = C_1 e^{-E/E_1} + C_2 e^{-E/E_2} . \quad (2.5)$$

This also involved a direct search least squares fit wherein for given values of E_1 and E_2 one analytically computes the correct values of C_1 and C_2 . Then one computes the quantity

$$S(E_1, E_2) \equiv \sum_{i=1}^k [\eta_i - C_1 e^{-E_i/E_1} - C_2 e^{-E_i/E_2}]^2 \quad (2.6)$$

One varies E_1 and E_2 to find a minimum for $S(E_1, E_2)$. Table 2.1 gives the values of C_1 , C_2 , E_1 and E_2 for the 18:63 UE PESPEC.

TABLE 2.1

$$C_1 = 0.271$$

$$C_2 = 0.088$$

$$E_1 = 10.2 \text{ KeV}$$

$$E_2 = 0.570 \text{ KeV}$$

Equation (2.5) with the correct values of the parameters is also

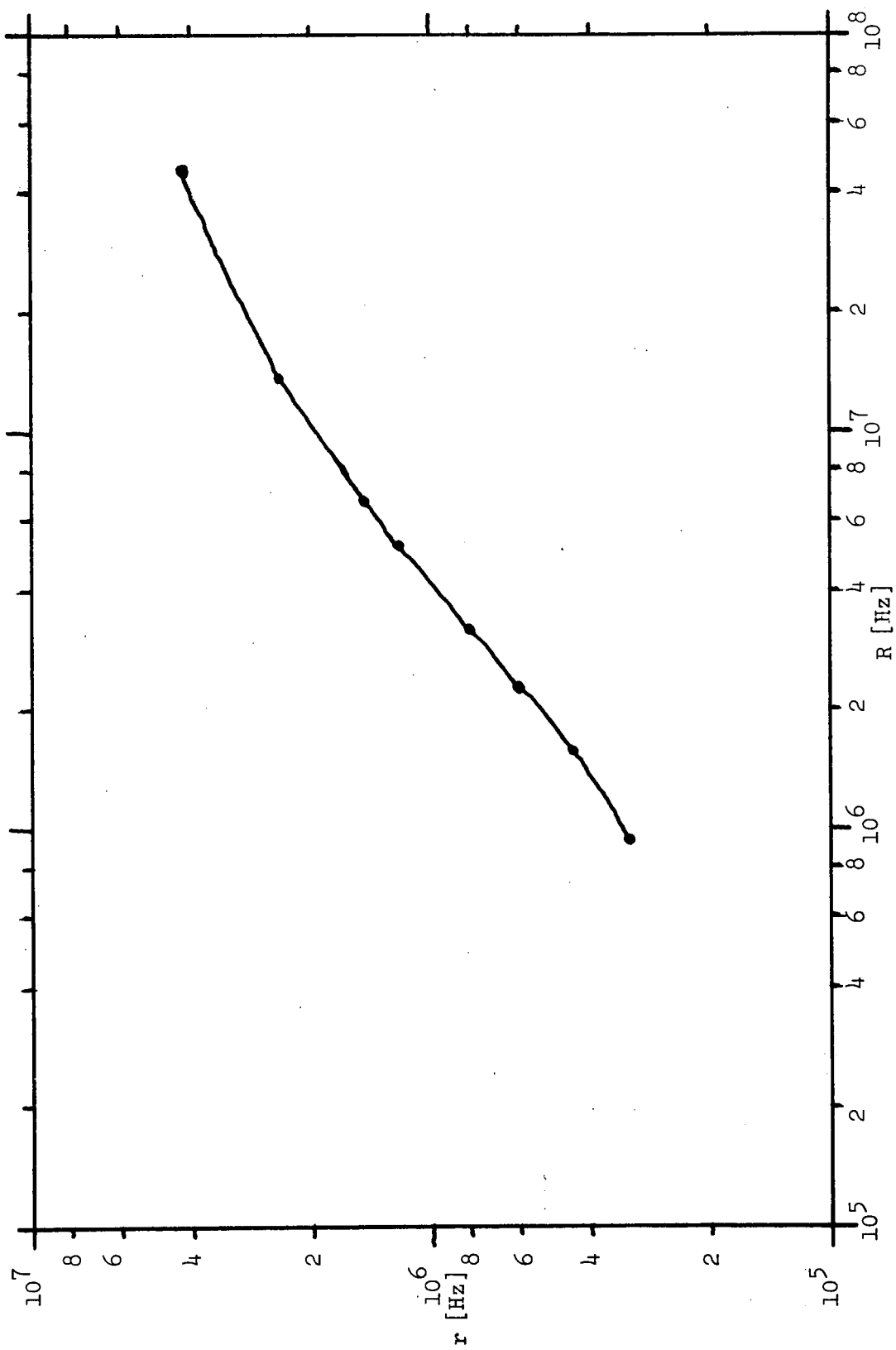


Figure 2.5. Output count rate versus input count rate.

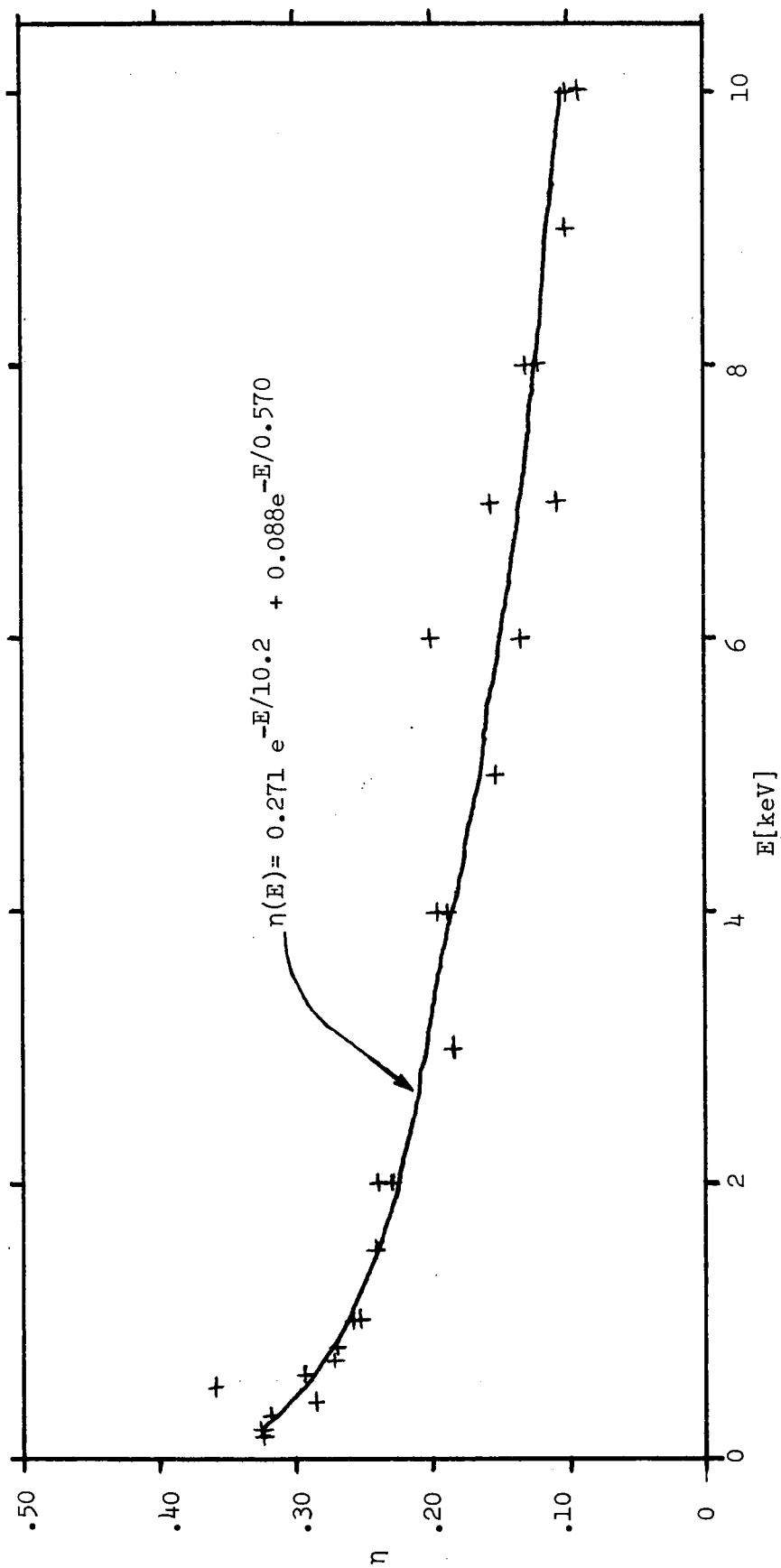


Figure 2.6. Multiplier efficiency versus energy.

shown in figure 2.6. The value of $\eta(E)$ for $E > 10$ KeV was not measured, but because of the weak energy dependence beyond 2 KeV and for better agreement with the lowest energy P.H.A. channel it was assumed to be 0.10.

For values of $R\eta\tau$ less than 0.15 (this corresponds to an observed count rate of ~ 1.5 MHz or ~ 5000 counts/data word) a correction for dead time losses good to $\sim 2\%$ can be obtained by approximating equation (2.2) by

$$r = R\eta e^{-r\tau} \quad (2.7)$$

therefore the true count rate R is given by

$$R = \frac{r}{\eta} e^{r\tau} \equiv r/\eta^* \quad (2.8)$$

where $\eta^* \equiv \eta e^{-r\tau}$ is the effective efficiency.

4. PESPEC Geometric Factor

The analyzer geometric factor, $GF(E, V(t))$, detector efficiency, $\eta(E)$, and dead time, τ , must be known in order to convert the number of counts per word, N , into the differential flux, $\frac{dj}{dE}$ [electrons -cm^{-2} -sec^{-1} -sr^{-1} -KeV^{-1}]. N and $\frac{dj}{dE}$ are related by

$$N = \int_0^{\tau_\omega} dt \int \eta^*(E) GF(E, V(t)) \frac{dj}{dE}(E) dE \quad (2.9)$$

where $\tau_\omega = 3.2$ msec, the sampling time, and $\frac{dj}{dE}$ is isotropic over the angular response of the detector. The geometric factor is essentially a response function. For an electrostatic analyzer the angular acceptance is a function of the incoming electron energy and the voltages

on the deflection plates, and therefore, the geometric factor is not a constant. Many authors, most notably Theodoridis and Paolini [1967, 1969] have calculated the geometric factor for various electrostatic analyzers.

While we have adopted the coordinate system used by Theodoridis and Paolini we have chosen to determine the geometric factor by a method which does not require some of their simplifying assumptions. Allowed trajectories between the deflection plates actually follow elliptical not circular paths. The angle α , defined in the plane of the trajectory, is the angle of incidence of the electron with respect to the normal to the entrance slot. The angle β is measured in a plane which is normal to the plane of the entrance slot and tangent to the deflection plates at the point of entrance to the plates. The polar coordinates (r_o, γ) describe the entry point in the entrance slot. The polar coordinates (r, ϕ) describe the position of the electron in the plates. (See figure 2.7 for definition of α, ϕ, r). (See figure 2.8 for definition of β , and $\Delta\beta$). $\Delta\alpha$ is the range of the angle α for trajectories which remain between the inner and outer plates. $\Delta\beta$ is the range of the angle β for which the plane of the trajectory is such that the electron can pass through the exit slot. For a given energy E , $\Delta\alpha$ is a function of r_o and possibly γ if the central angle ϕ_o depends upon γ . With no exit aperture collimation $\Delta\beta$ would be independent of (r_o, γ) , but for the 18:63 UE PESPEC the exit aperture collimation did not allow any trajectories entering at certain regions along the slot to exit. However it was possible for electrons entering at either slot to exit at either exit aperture. Therefore for each exit aperture one must compute a total geometric

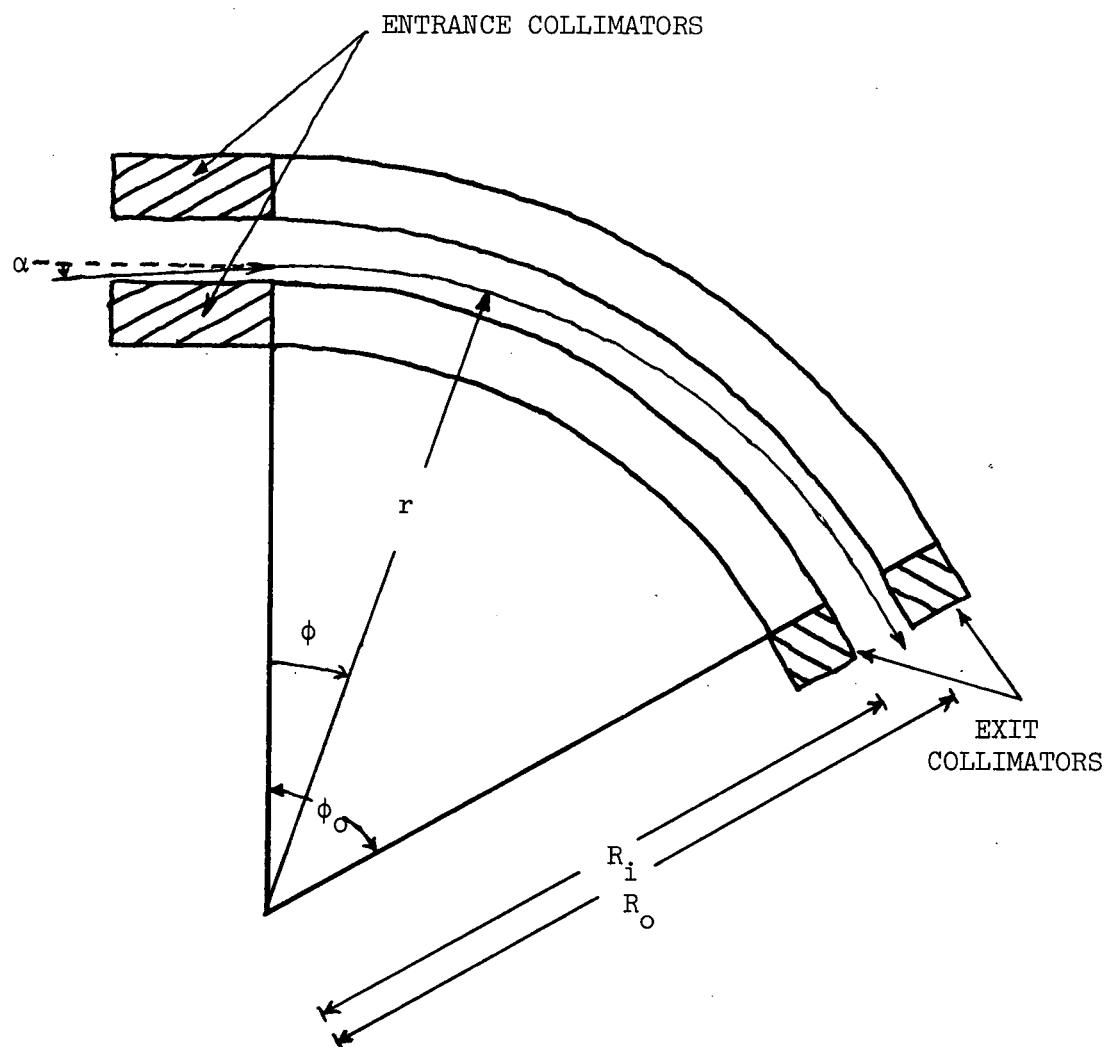


Figure 2.7. Electron trajectory between plates.

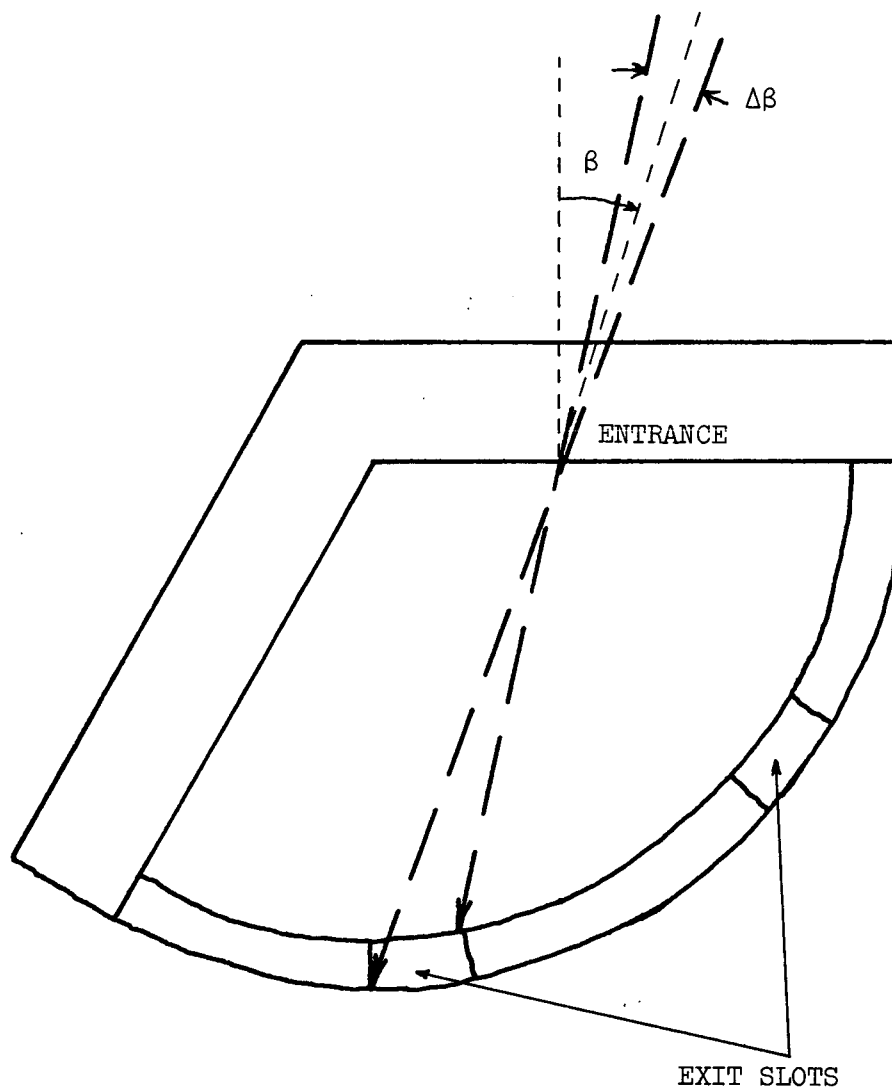


Figure 2.8. Top view of plates showing electron trajectory.

factor which is composed of the geometric factor for nearly normal incidence electrons at one slot, called the nominal geometric factor, NGF, and the response to electrons from the other entrance slot. Because of a failure in the amplifier and counter for the apertures which nominally looked 10° from the rocket spin axis we obtained good data only from the exit aperture which was to detect electrons entering at 70° to the spin axis. For this exit aperture the abnormal entrance slot was the upper slot, and therefore the response to trajectories from the upper slot to its nearest aperture was called the upper geometric factor (UGF). (See figure 2.2 for examples of these trajectories and $\Delta\beta$.) For the UGF the central angle of energy analysis was less than 90° , and the energy and angular resolution were much poorer than for the NGF. However the values of the upper geometric factor and the nominal geometric factor can be determined by essentially the same method, the only difference being that the central angle, ϕ_0 , varies with position (r_0, γ) in the upper slot.

Because the values of $\Delta\alpha$ and $\Delta\beta$ vary with position (r_0, γ) within the entrance slot we subdivide the entrance aperture into many smaller apertures each with some small area ΔA over which $\Delta\alpha$ and $\Delta\beta$ are assumed constant. For each entrance slot the geometric factor is the sum of the geometric factors of each of these small subdivisions. If the exit aperture were also so large that $\Delta\alpha$ or $\Delta\beta$ from a given entrance subdivision would not be constant over the area of the exit aperture one would also have to subdivide the exit aperture. Fortunately most counting mode particle detectors have small entrance apertures which require the analyzer exit aperture to be small also. For the 18:63 UE PESPEC because the central angle for a given entrance subdivision did

not vary within the exit aperture we did not have to subdivide the exit aperture. Figure 2.9 shows the pattern for subdividing each entrance slot. The angle, γ_j , and the distance, r_{oi} , are the polar angle and radial position respectively of the small area ΔA_{ij} .

For each ΔA_{ij} one can determine $\Delta\alpha_{ij}$ and $\Delta\beta_{ij}$. Then the solid angle, Ω_{ij} , subtended by the subdivision ΔA_{ij} can be determined [see Theodoridis and Paolini, 1969] from

$$\Omega_{ij} = 2\Delta\beta_{ij} \sin(1/2\Delta\alpha_{ij}) \quad (2.10)$$

ΔA_{ij} can be determined from the radial, Δr , and angular, $\Delta\gamma$, spacing between subdivisions and the radial distance, r_{oi}

$$\Delta A_{ij} = (\Delta r)(\Delta\gamma)r_{oi} \quad (2.11)$$

For the upper slot where the center of the $\Delta\beta_{ij}$ range is not normal to the ΔA_{ij} one must use the area projected by the ΔA_{ij} normal to the center value of β . The values of $\Delta\alpha_{ij}$ will depend upon the incident electron energy, E , and plate voltage, V , and therefore the geometric factor for each entrance slot can be written

$$GF(E,V) = \sum_{i=1}^{i_{\max}} \sum_{j=1}^{j_{\max}} (\Delta A_{ij})(\Omega_{ij}). \quad (2.12)$$

For fixed physical dimensions of the electrostatic analyzer the value of $\Delta\alpha_{ij}$ depends upon the inner and outer plate voltages, V_i and V_o , the kinetic energy of the electron as it enters the plates, T_∞ , the entrance radius, r_o , and central angle, ϕ_o , subtended by the plates between entrance and exit points and often the most overlooked factor, the limits on $\Delta\alpha_{ij}$ imposed by collimation. The entrance collimation

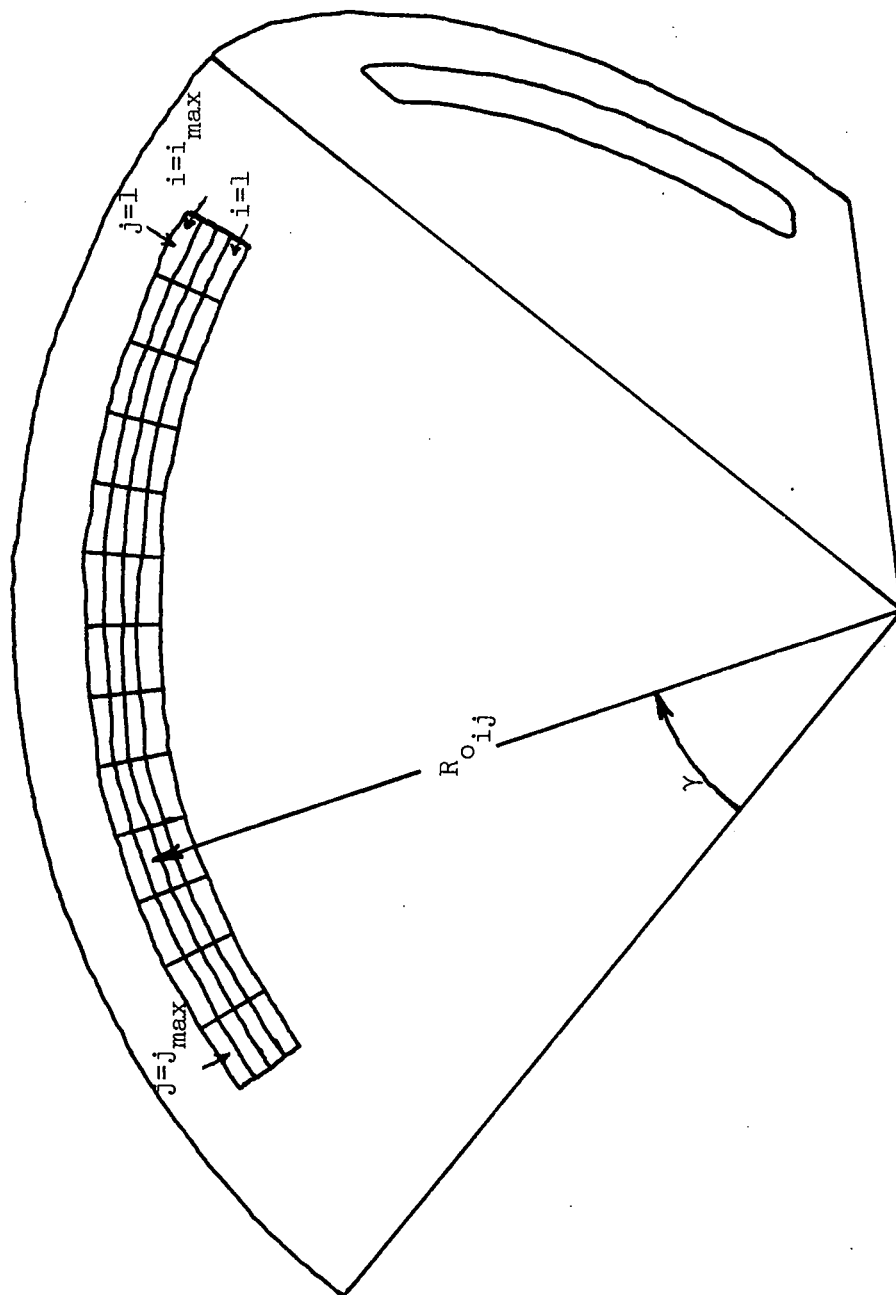


Figure 2.9. Entrance slot subdivisions.

defines a maximum value of α , α_{\max} , and a minimum value, α_{\min} , necessary for the electrons to be able to even reach the region between the deflection plates. From purely geometrical considerations one can compute α_{\max} and α_{\min} for each ΔA_{ij} . Figure 2.10 defines the angles and sides of the spherical triangles needed to determine the $\Delta\alpha_{ij}$ parameters for the upper slot. The inner triangle extends on the base to the nearest point of the exit aperture. The outer triangle includes the exit aperture in its base. The subscripts "I" and "O" denote the inside and outside spherical triangles respectively. a_I , a_O , b_I and b_O are determined from the entrance point (r_{O_i}, γ_j) . Angles C_I and C_O are both 90° . For a spherical triangle (see figure 2.10 for equations 2.13 - 2.18)

$$\cos c = \cos b \cos a + \sin b \sin a \cos C \quad (2.13)$$

Therefore

$$\cos c_I = \cos b_I \cos a_I \quad (2.14)$$

determines c_I and equation (2.13) also gives c_O . c_I is equal to the central angle ϕ_O needed to determine $\Delta\alpha_{ij}$. B_I and B_O are needed to determine $\Delta\beta_{ij}$. Napier's first rule for a right spherical triangle is

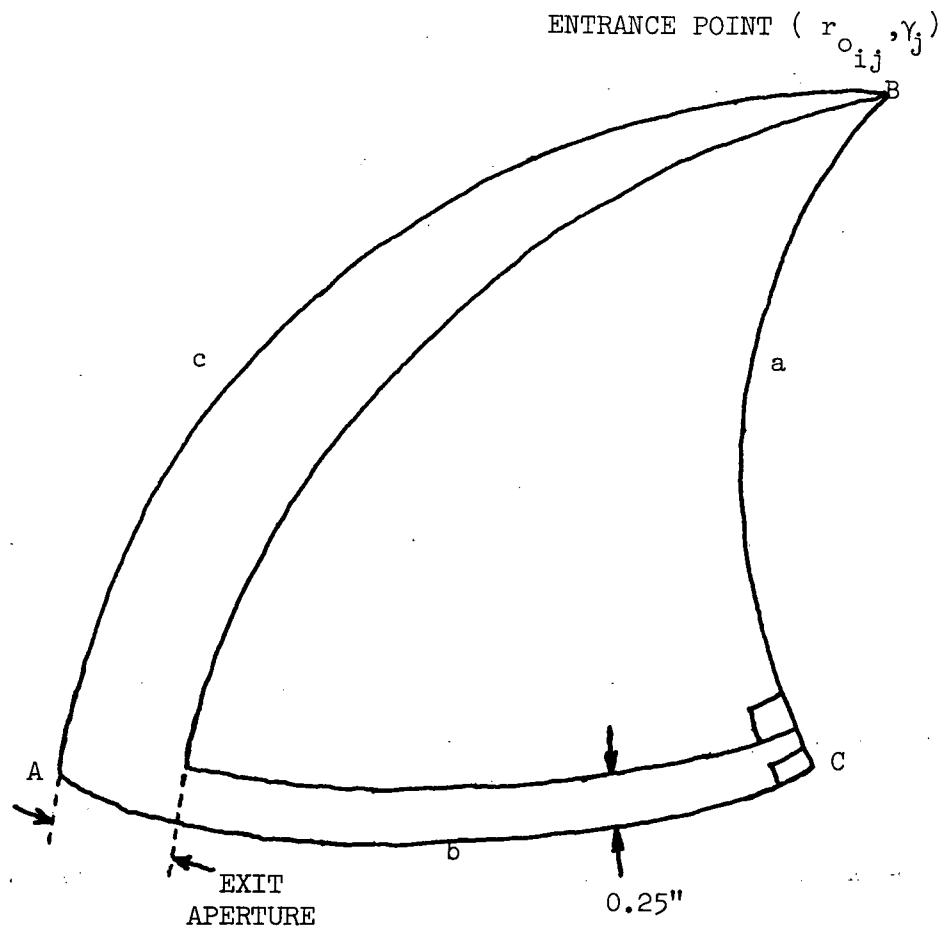
$$\sin a = \tan b \tan (C_O - B). \quad (2.15)$$

therefore

$$\tan (\pi/2 - B_I) = \sin a_I / \tan b_I \quad (2.16)$$

and

$$\tan (\pi/2 - B_O) = \sin a_O / \tan b_O \quad (2.17)$$



$$b_I = 30^\circ$$

$$a_I = \gamma_j$$

$$b_o = b_I + 0.500/r_{oij}$$

$$a_o = \gamma_j + 0.250/r_{oij}$$

Figure 2.10. Spherical triangle used to determine $\Delta\alpha$ and $\Delta\beta$ for upper slot.

give B_I and B_O .

$\Delta\beta_{ij}$ is given by

$$\Delta\beta_{ij} = B_O - B_I \quad (2.18)$$

It is possible for $B_I > B_O$ (if γ_j is small) in which case $\Delta\beta_{ij}$ is zero.

If $\bar{\beta}_{ij}$ is the center value of allowable β 's for a given $\Delta\beta_{ij}$, and the entrance collimator length is δ , one can determine $\alpha_{\max ij}$ and $\alpha_{\min ij}$. Let R_O and R_I be the outer and inner plate radii then

$$\alpha_{\max ij} = \tan^{-1}[(\sqrt{(R_O)^2 - (\delta/\tan \bar{\beta}_{ij})^2} - r_{O_i})/\delta] \quad (2.19)$$

and

$$\alpha_{\min ij} = \tan^{-1}[(\sqrt{(R_I)^2 - (\delta/\tan \bar{\beta}_{ij})^2} - r_{O_i})/\delta]. \quad (2.20)$$

We have now demonstrated how to compute all the parameters needed to determine $\Delta\alpha_{ij}$ as a function of energy and plate voltages. Appendix II describes our method for determining $\Delta\alpha_{ij}$ when given ϕ_O , r_{O_i} , the physical dimensions of the plates, the plate voltages, the effective exit collimation length and the electron kinetic energy, T_∞ . (Before it enters the plates the electron is free and $T_\infty = E$.)

Figure 2.11 shows the geometric factor from each slot and the total geometric factor as a function of E/V where V is the plate voltage for symmetrical positive and negative voltages on the plates. The actual plate voltages on the 18:63 UE PESPEC deviated somewhat from symmetry due to differences in the capacitance of the inner and outer plates themselves, but the computer simulations described in Appendix II demonstrated that for the small departures from symmetry

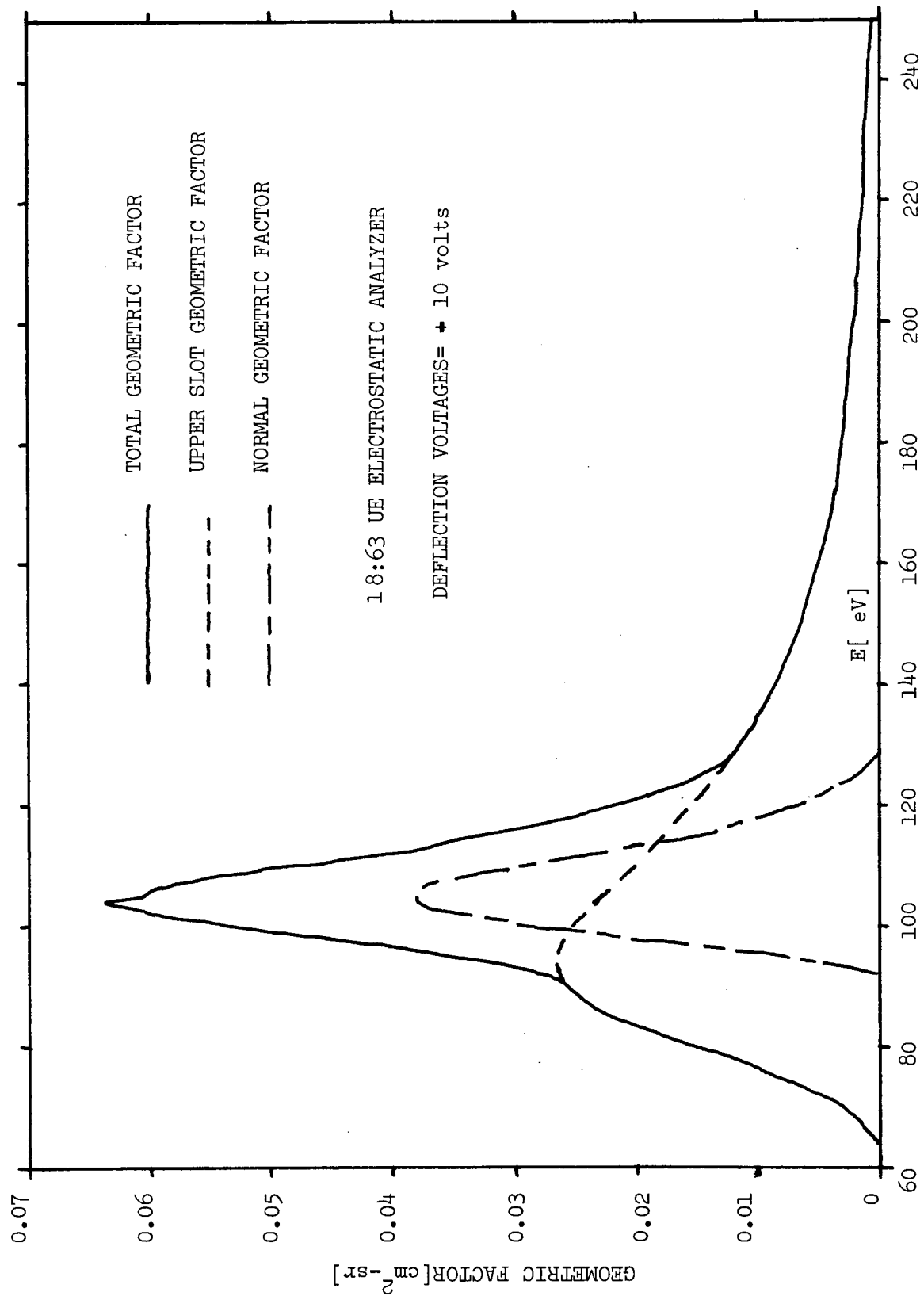


Figure 2.11. Geometric factor versus energy.

on 18:63 UE the effects were negligible.

Laboratory calibration of the $\Delta\alpha_{ij}$ and $\Delta\beta_{ij}$ was also performed. An electron gun which could be varied in α and β independently was directed at various points (r_{oi}, γ_j) along each entrance slot. Electrons transmitted through the plates were collected by a Faraday cup, and the current was measured by an electrometer. Another moveable Faraday cup could be positioned to measure the electron gun beam current before it entered the plates. At each position (r_{oi}, γ_j) along the slots one could measure the current transmitted while varying α , β or the deflection plate voltage V while holding the other two parameters fixed. Examples of these types of profiles are shown in figures 2.12, 2.13, 2.14. Figure 2.12 shows a plot of current versus α' where α' is a linear function of α . Figure 2.13 shows a plot of electrometer current versus β' where β' is a linear function of β . Figure 2.14 is a plot of electrometer current versus deflection plate voltage V . These measurements were made at a beam energy of 5 KeV. This energy was chosen because it was high enough to permit the use of phosphorescent screens to determine (r_{oi}, γ_j) and insure that the beam diameter was less than 0.080 in. The deflection plate voltage, V , was varied rather than electron energy, E , and therefore it was easier to maintain a constant beam current. Uncertainties in r_{oi} were ~ 0.05 in. Uncertainty in γ_j was $\sim 1^\circ$.

The values of α' , β' and V at the half-maximum values of the beam current were used to determine $\Delta\alpha_{ij}$, $\Delta\beta_{ij}$ and the energy resolution. The $1/4$ and $3/4$ values of the beam current determined the uncertainties. α' and β' measured the rotations of the two mechanical feedthrus which varied α and β . The rate of change of α and β with α' and β'

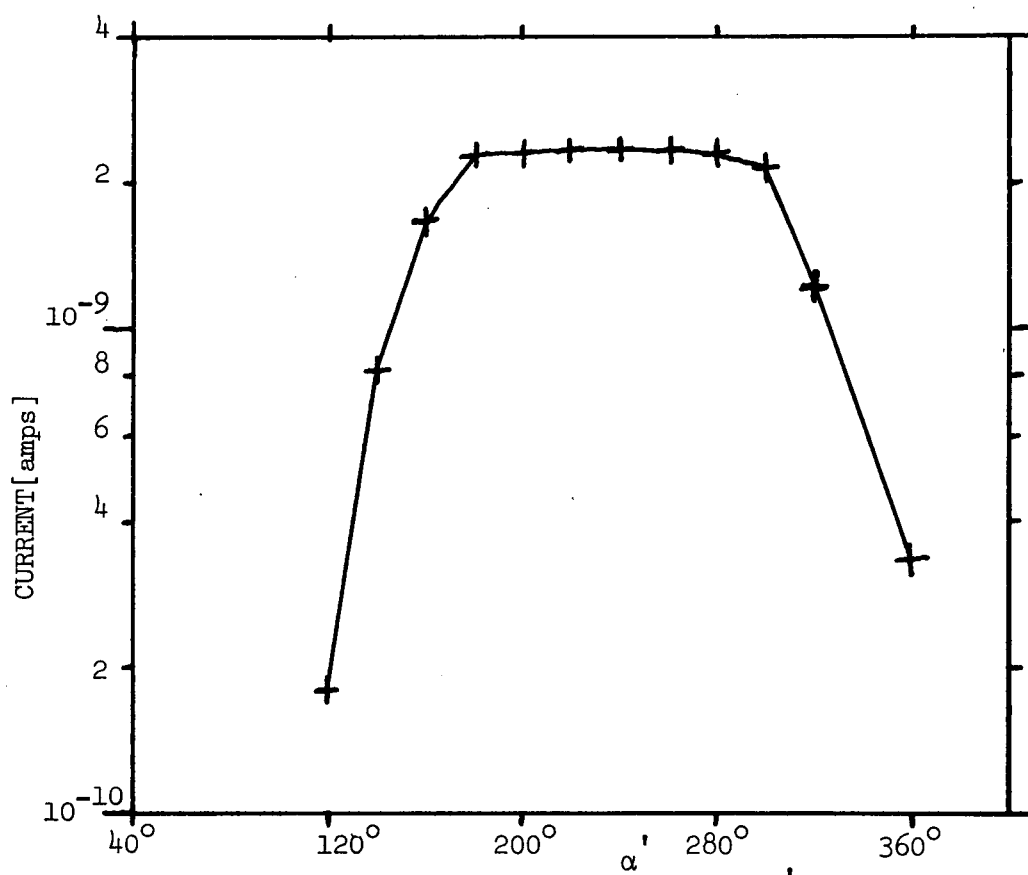


Figure 2.12. Current transmitted versus α' .

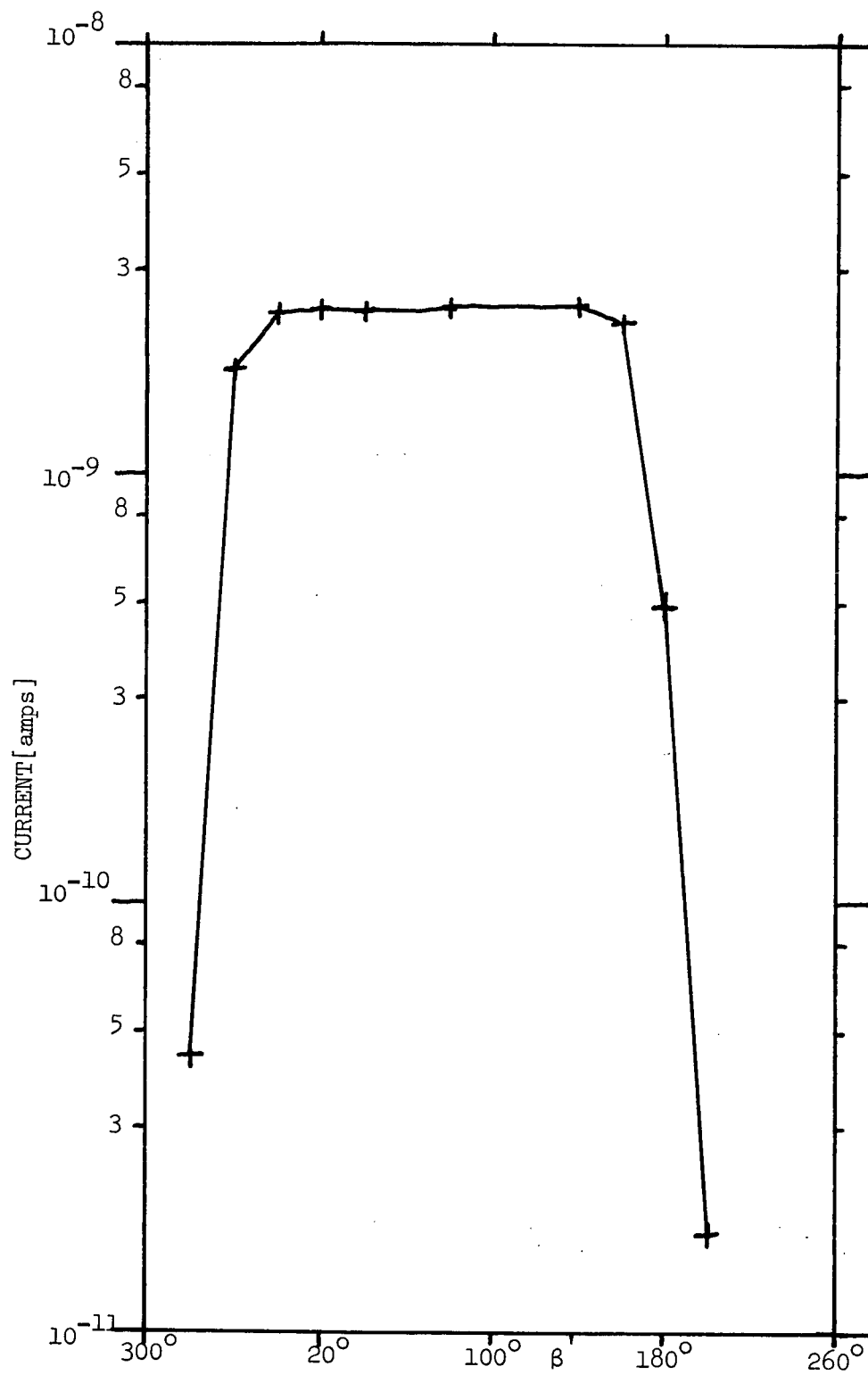


Figure 2.13. Current transmitted versus β' .

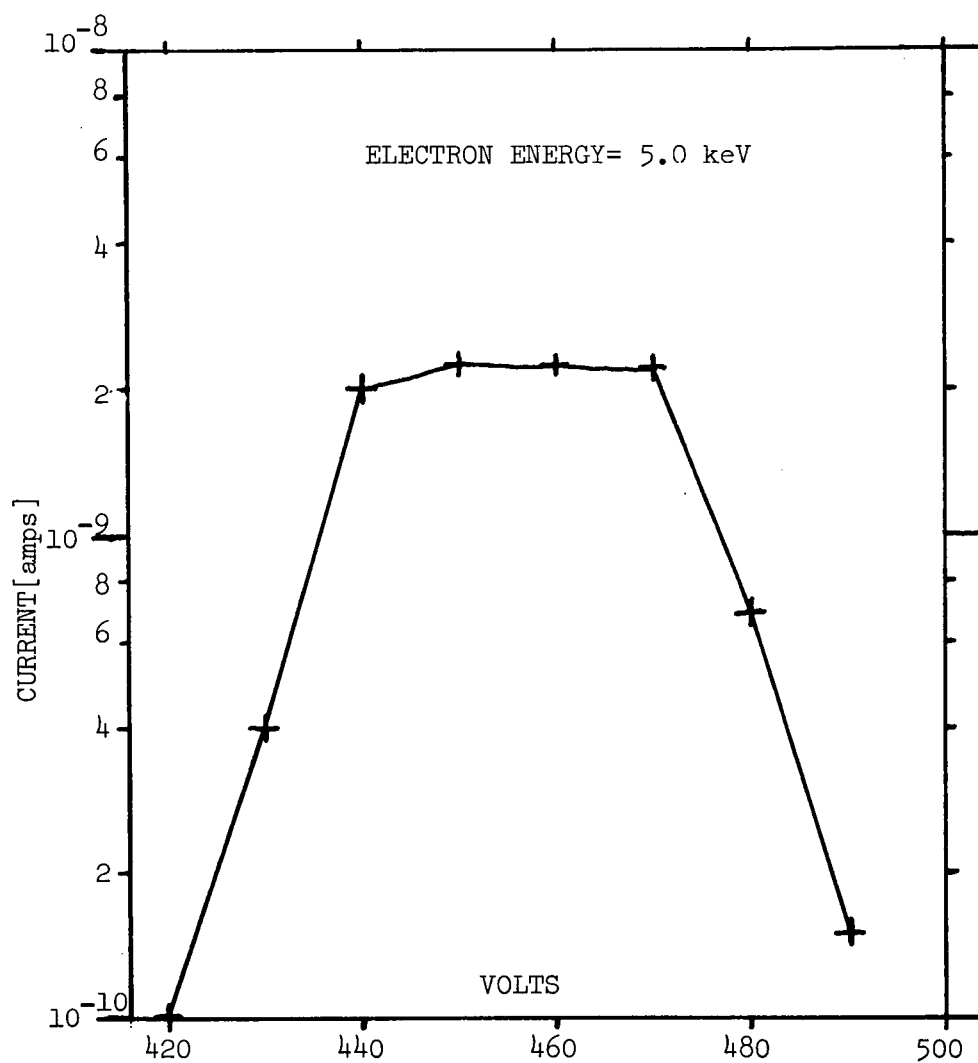


Figure 2.14. Current transmitted versus deflection plate voltage.

respectively was calibrated to a few percent. Absolute determinations of α and β were difficult because they required a very accurate positioning and measurement of orientation of a very irregularly shaped detector in very cramped quarters in the vacuum chamber. Comparison with the theoretical determinations of $\Delta\alpha_{ij}$ required an absolute value of α . Following the practice of Theodoridis and Paolini [1969] we chose the reference between α and α' which allowed the best fit between the theoretical and experimental limiting values of α and V . The maximum we had to shift the reference from the rather uncertain experimental reference was 3.3° .

Figure 2.15 is a plot of the experimental and theoretical limiting orbits in $(\alpha - V)$ space for the nominal slot. The experimental values of r_{oi} and γ_j are:

$$r_{oi} = 2.625 \text{ in.} \qquad \gamma_j = 72^\circ.$$

The shift in absolute α was -3.0° . The theoretical limiting values in $(\alpha - V)$ space are for $r_{oi} = 2.662$ in. This was the closest theoretical r_{oi} to the experimental value which was computed. For these experimental values of (r_{oi}, γ_j) the value of $\Delta\beta_{ij}$ was

$$\Delta\beta_{ij} = 11.3^\circ \pm 1.1^\circ.$$

The theoretical values of $\Delta\beta_{ij}$ for various γ_j for the nominal entrance slot are shown in figure 2.16. For $\gamma_j = 72^\circ$ the theoretical value is 9.9° .

Figure 2.17 depicts the limiting values in $(\alpha - V)$ space for the nominal slot with $r_{oi} = 2.625$ in. and $\gamma_j = 45^\circ$. The shift in absolute α was -2.4° . The theoretical limits are again for $r_{oi} = 2.662$ in.

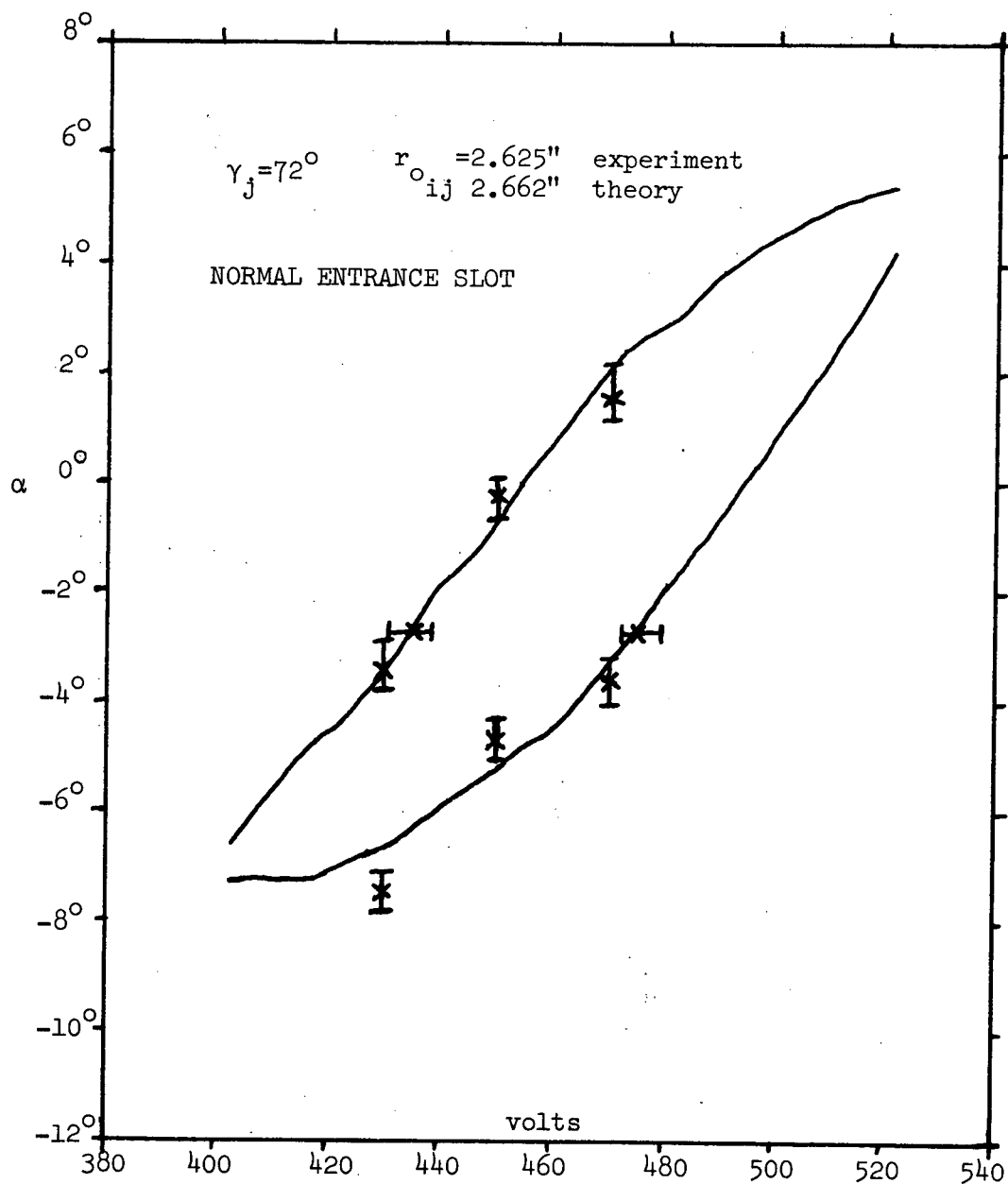


Figure 2.15. Allowed orbits in deflection voltage- α space.

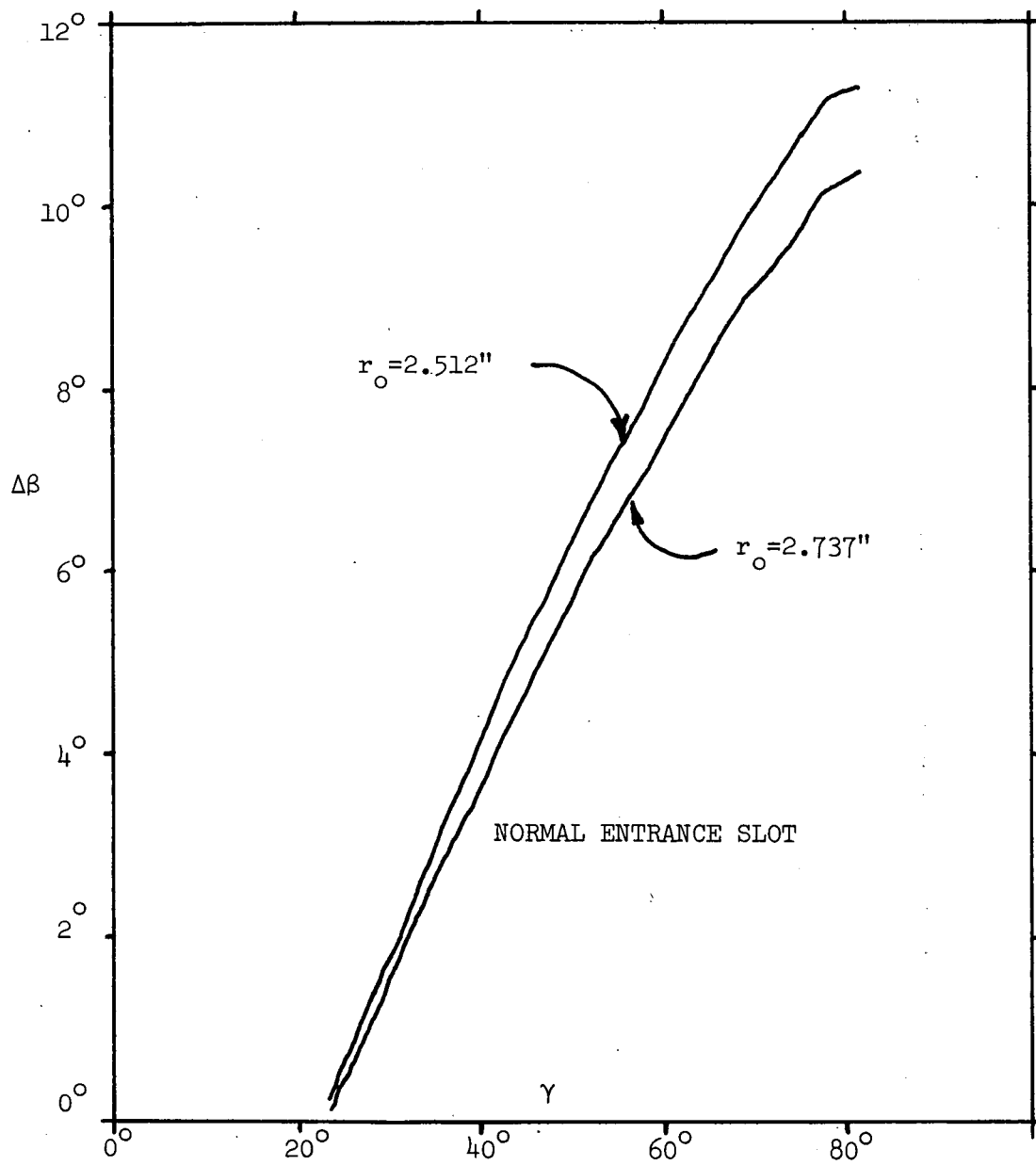
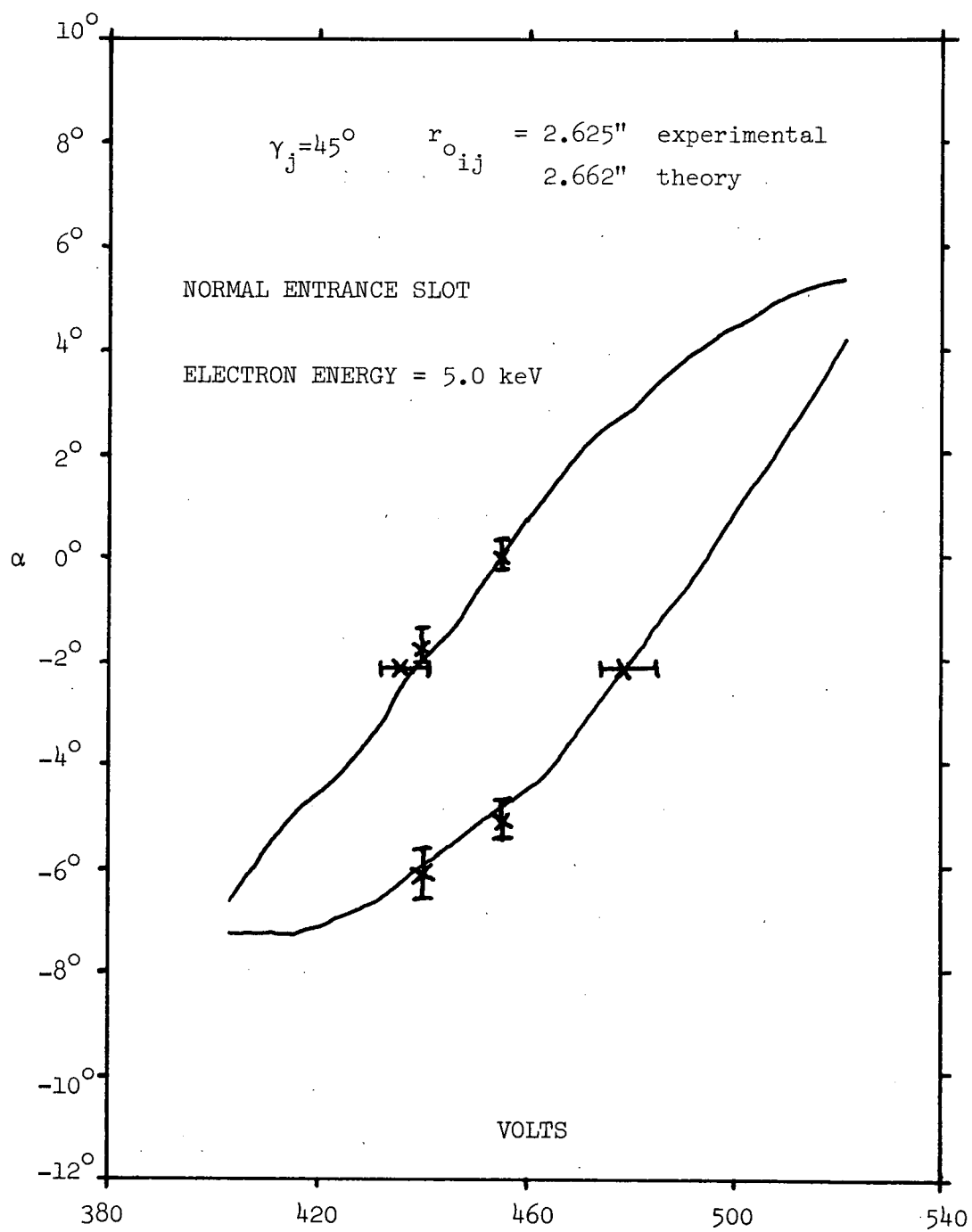


Figure 2.16. $\Delta\beta$ versus γ along slot.



The value of $\Delta\beta_{ij}$ was

$$\Delta\beta_{ij} = 7.2^\circ \pm 2.7^\circ$$

compared to the theoretical value of 5.2° .

The limiting values of α and deflection voltage, V , for various values of (r_{oi}, γ_j) for the upper slot are shown in figures 2.18-2.21. Also shown are the theoretical limiting values for the entrance position closest to the experimental (r_{oi}, γ_j) . In general there is very good agreement between the computed curves and the experimental limiting values.

Figure 2.22 shows the minimum and maximum angle β for $\gamma_j = 45^\circ$ for the upper slot measured by fixing α' and V and varying β' . The theoretical value for $\Delta\beta_{ij}$ is 9.1° . From figure 2.22 the average $\Delta\beta_{ij}$ is 10.7° , but this is consistent with the theory within the experimental error. The theoretical value for B_I is 39.4° , and the experimental value was $39.4^\circ \pm 2^\circ$ confirming that absolute determination of β was easier than α .

Because measurement of $\Delta\beta$ with fixed α' and V gave large uncertainties in determining β'_{\max} for the upper slot with $\gamma_j = 20^\circ$ we measured $\Delta\alpha'$ at various angles β' with fixed V . This combination of methods gave the results of figure 2.23. Within the limits of uncertainty these values are consistent with the theoretical values of $\Delta\beta_{ij} = 4.3^\circ$.

The angular resolution as well as the energy resolution (see figure 2.11) of the 18:63 UE PESPEC was impaired by the electrons which were able to enter the upper slot and exit at the wrong exit aperture. The angular response of the nominal entrance slot was

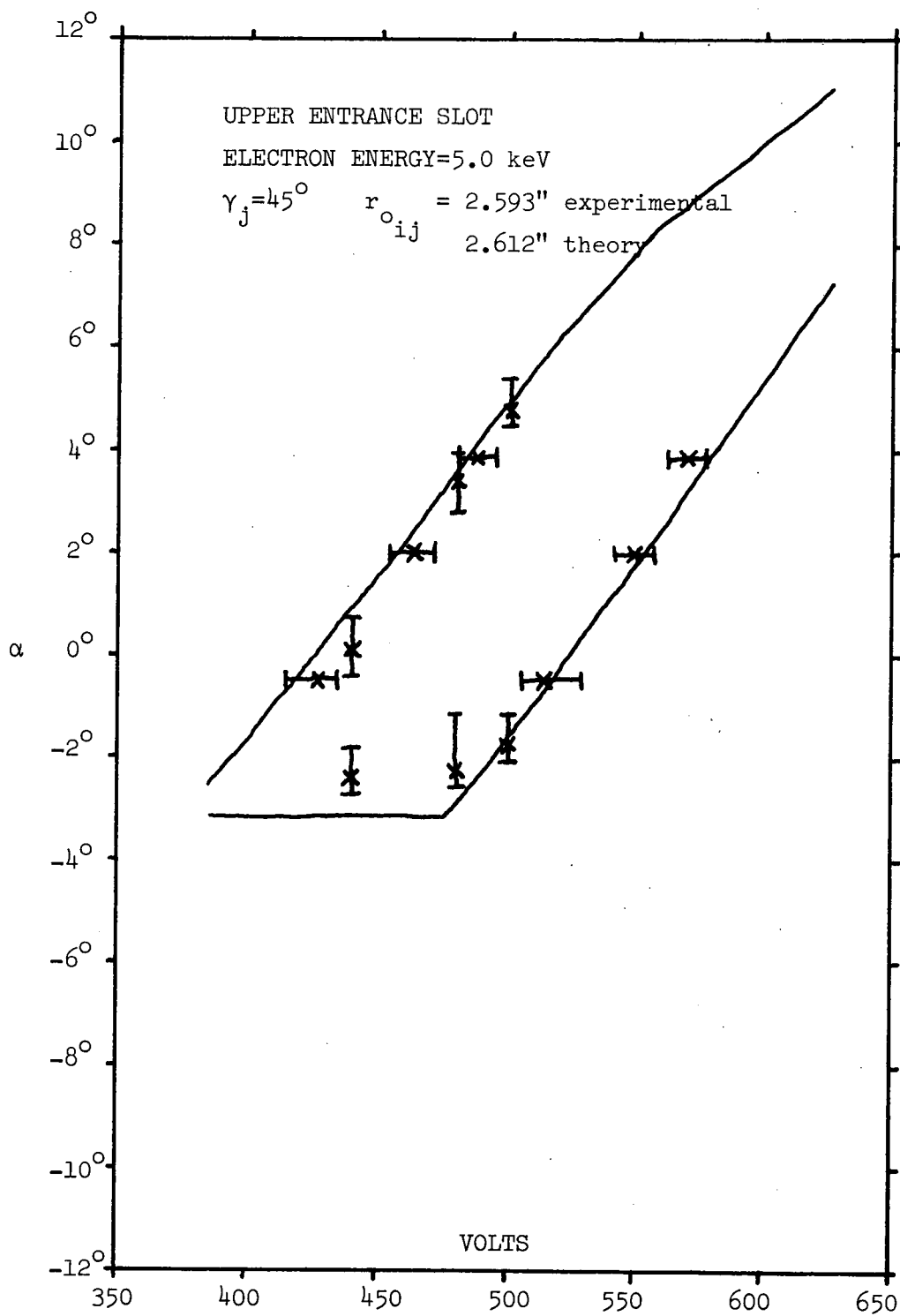


Figure 2.18. Allowed orbits in deflection voltage- α space.

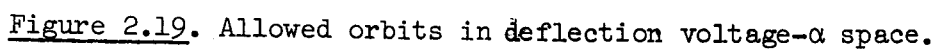


Figure 2.19. Allowed orbits in deflection voltage- α space.

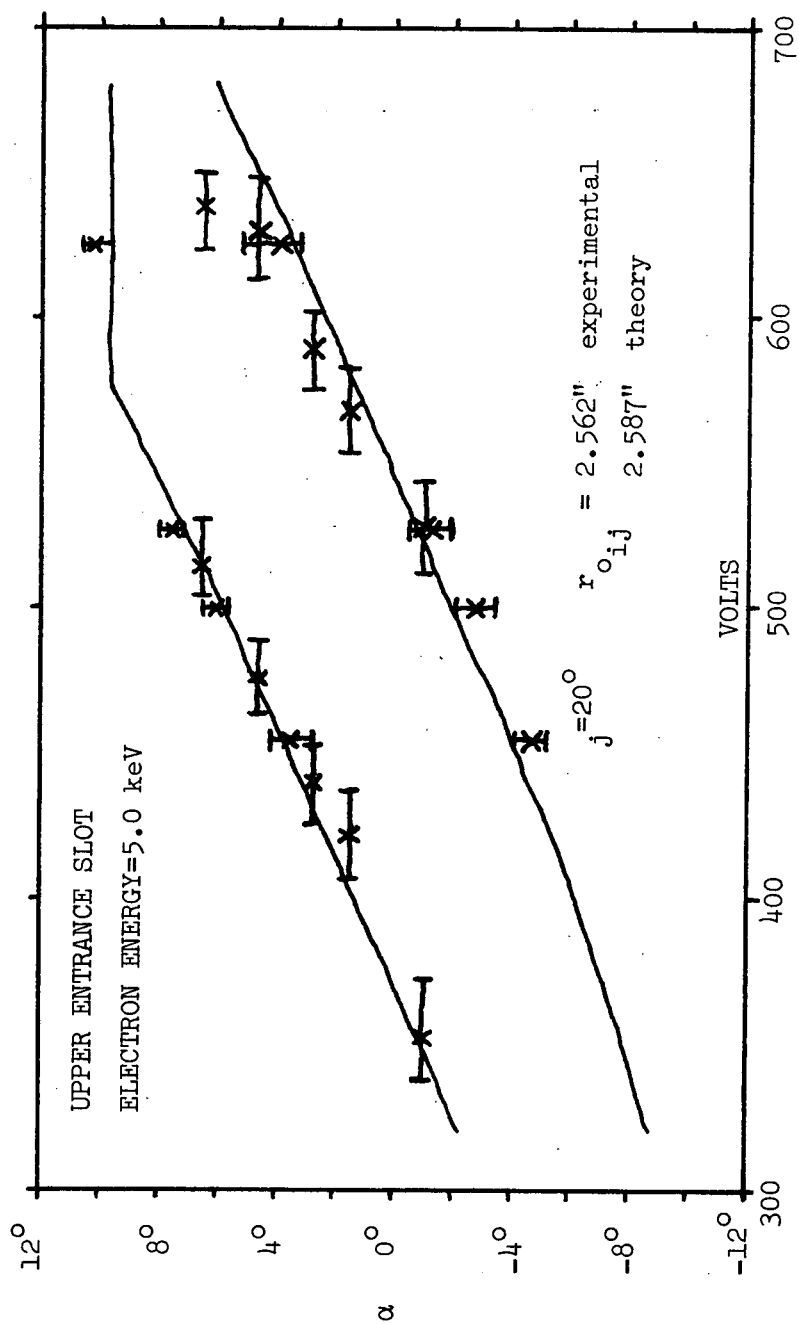


Figure 2.20. Allowed orbits in deflection voltage- α space.

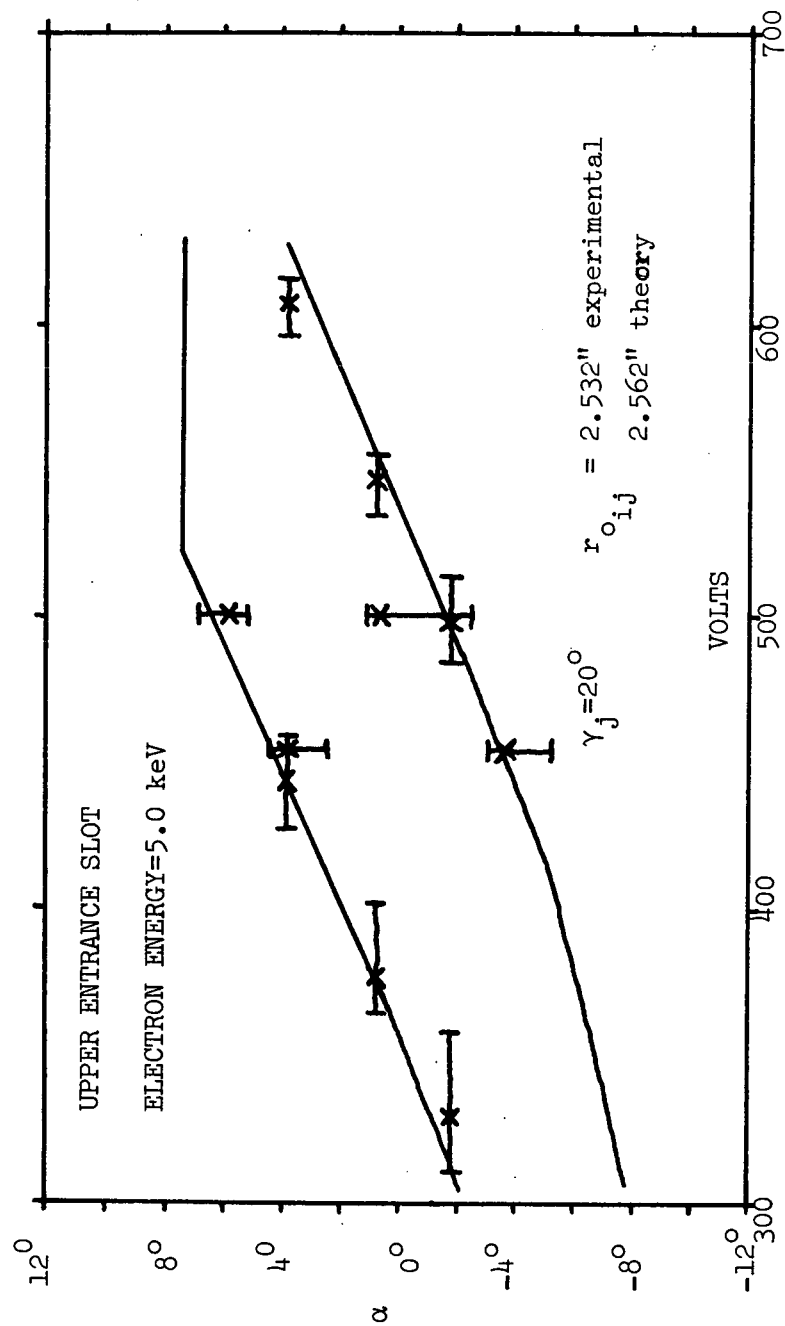


Figure 2.21. Allowed orbits in deflection voltage- α space.

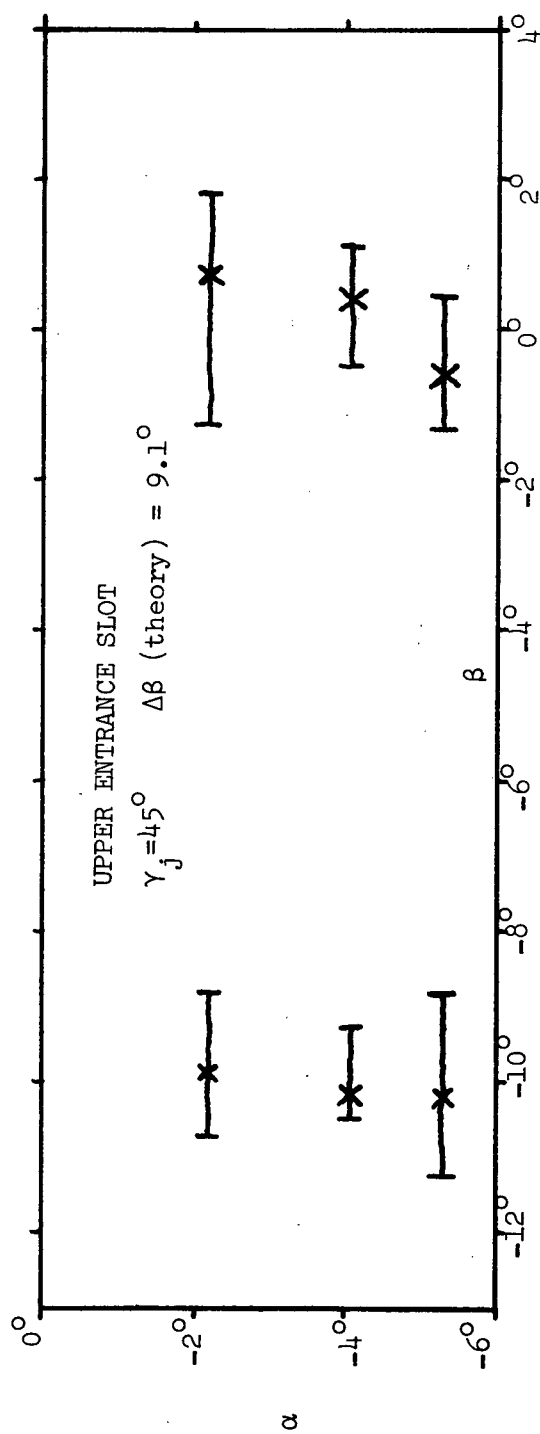


Figure 2.22. $\Delta\beta$ measurement for $\gamma_j = 45^\circ$.

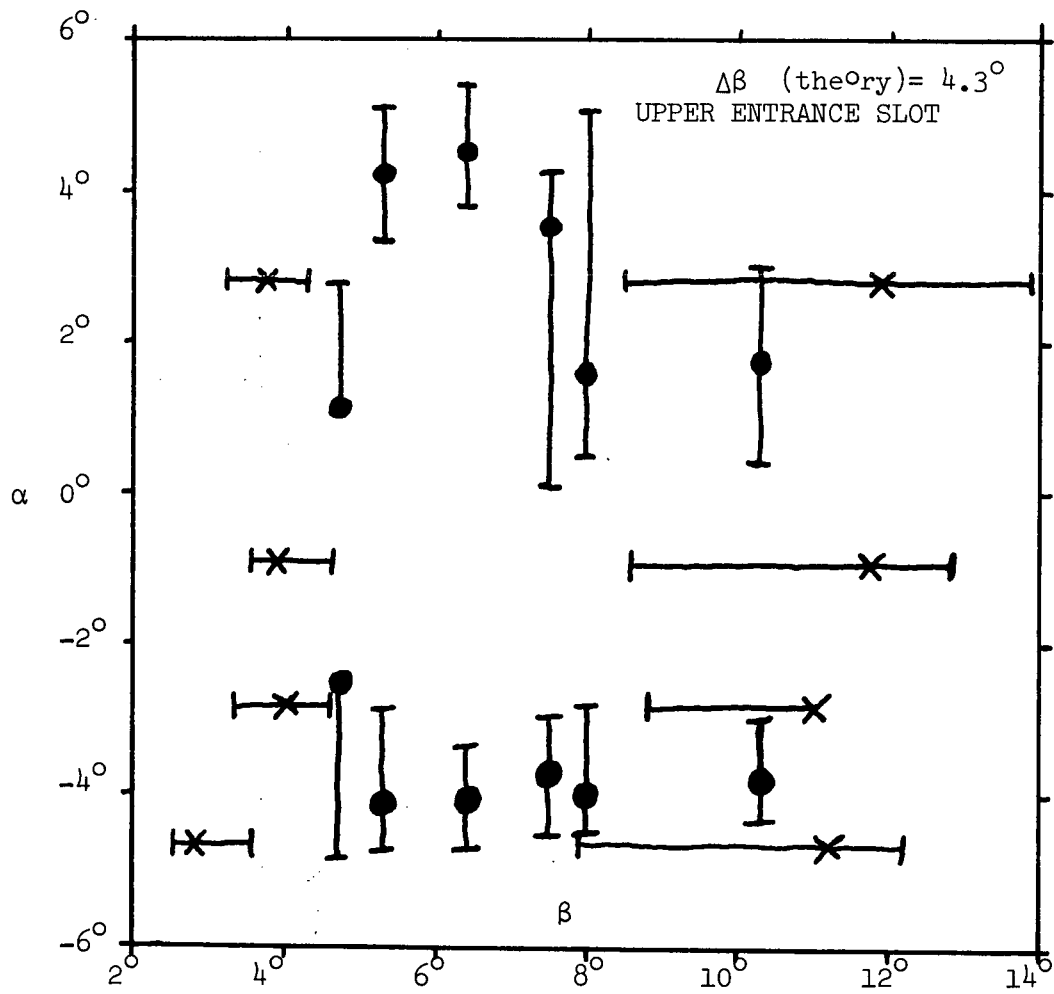


Figure 2.23. $\Delta\beta$ measurement for $\gamma_j = 20^\circ$.

$\sim 6^\circ \times 6^\circ$ (see figures 2.15 and 2.16). The acceptance direction in a plane perpendicular to the spin axis was 123.5° from a payload reference direction. This can be considered the azimuth of the look of the slot. The elevation of look can be determined to be 20° from the fact that it looked 70° away from the spin axis. One needs to know the azimuth and elevation of the look of the upper slot as a function of γ . Let $\delta(\gamma)$ be the increase in azimuth of the upper slot look over the nominal slot azimuth as a function of γ . Using the fact that the upper slot normal is 10° from the spin axis it can be shown that

$$\tan \delta(\gamma) = \tan(\gamma) / \cos(10^\circ) \quad (2.21)$$

The elevation of the look of the upper detector $\epsilon(\gamma)$, can be computed from γ and $\beta(\gamma)$ by

$$\sin \epsilon(\gamma) = \sin \beta(\gamma) \cos(10^\circ) - \cos \beta(\gamma) \sin(10^\circ) \sin \gamma. \quad (2.22)$$

The upper slot was then considered to be five separate detectors with γ_j values $\gamma_j = 19.5^\circ, 28.5^\circ, 37.5^\circ, 46.5^\circ, 55.5^\circ$. The geometric factor of each of these five detectors was then computed as a function of E/V . The results are shown in figure 2.24. Weights which consisted of the product of the maximum value of the geometric factor times the full width at half-maximum were then calculated for each of the five detectors. The values of the azimuth, $A(\gamma_j)$, and elevation, $\epsilon(\gamma_j)$, were then weighted with the corresponding weight and an effective azimuth and elevation for the upper slot were computed. Table 2.2 lists the values of azimuth and elevation for each slot and the approximate angular resolution.

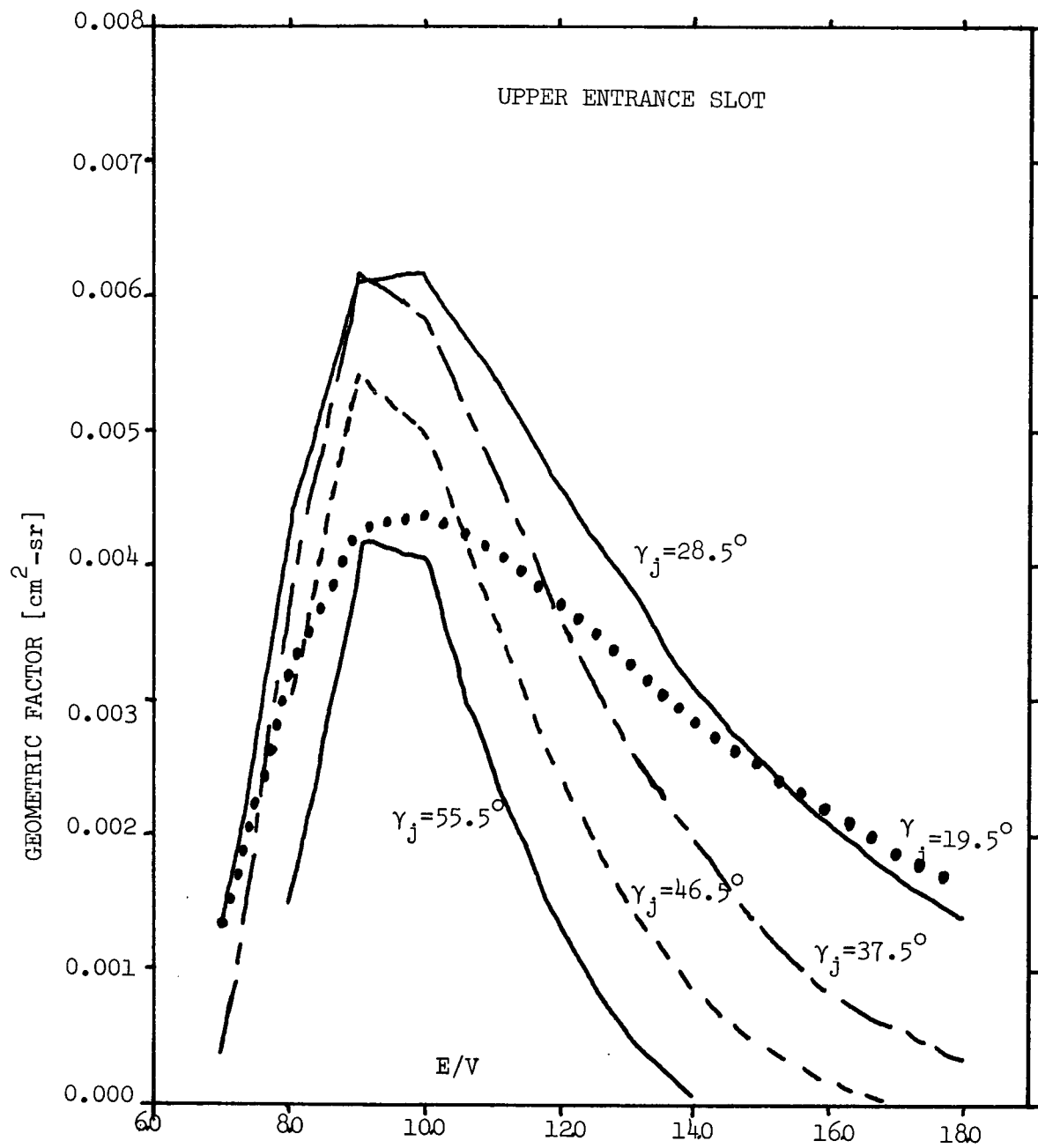


Figure 2.24. Upper slot geometric factor for various γ 's.

TABLE 2.2

<u>Slot</u>	<u>Azimuth</u>	<u>Elevation</u>	<u>Angular Resolution</u>
Nominal Slot	123.5°	20°	~6° x 6°
Upper Slot	180.8°	42.4°	~7° x 35°

It should be noted that the large angular response of the upper slot will tend to obscure variations in the pitch angle distribution.

5. Unfolding the Energy Spectrum

One must solve the integral equation (2.9) in order to determine the differential spectrum $\frac{dj}{dE}(E)$. In this section we describe our algorithm for converting the counts per word into the differential electron flux. We define

$N_i \equiv$ the number of counts in word i

$\tau_w \equiv$ sample time = 0.0032 sec

$\eta_i^* \equiv$ effective efficiency averaged over energy of word i

$\tau_i \equiv$ exponential decay parameter of sweep voltage for word i

$V_{0i} \equiv$ average of absolute values of plate voltage at start of collection of counts for word i .

$G(E/V) \equiv$ geometric factor from both slots combined.

$\frac{dj}{dE}(E) \equiv$ Electron differential energy spectrum with units
[electrons - sec⁻¹ - cm⁻² - sr⁻¹ - KeV⁻¹].

We can write equation (2.9) as

$$N_i = \eta_i^* \int_0^{\tau_w} dt \int G(E/V(t)) \frac{dj}{dE}(E) dE. \quad (2.23)$$

We assume that $\frac{dj}{dE}(E)$ can be written as a polynomial in E ,

$$\frac{dj}{dE} = \sum_{j=1}^{j_{\max}} C_j E^j - 1 \quad (2.24)$$

Define I_j by

$$I_j \equiv \int G(E/V(t)) E^j - 1 dE. \quad (2.25)$$

Equation (2.23) can now be written as

$$N_i = \eta^*_i \int_0^{\tau_\omega} dt \sum_{j=1}^{j_{\max}} C_j I_j \quad (2.26)$$

By numerically integrating I_j we found that we could write

$$I_j = F_j V^j(t) \quad (2.27)$$

where the values of the constants F_j for $j = 1, \dots, 5$ are given in table 3.

TABLE 3

j	F_j
1	0.223
2	0.266×10^1
3	0.360×10^2
4	0.584×10^3
5	0.119×10^5

We interchange the order of integration and summation in equation (2.26) to obtain

$$N_i = \eta^*_i \sum_{j=1}^{j_{\max}} C_j F_j \int_0^{\tau_\omega} V(t)^j dt \quad (2.28)$$

The deflection plate voltage can be represented by an exponential decay from the value V_{o_i}

$$V(t) = V_{o_i} e^{-t/\tau_i} \quad (2.29)$$

When the integral is computed equation (2.28) has the form

$$N_i = \eta_i^* \tau_i \sum_{j=1}^{j_{\max}} C_j F_j \left[\frac{1 - e^{-j \tau_\omega / \tau_i}}{j} \right] V_{o_i}^j \quad (2.30)$$

We can define,

$$H_{ij} \equiv \frac{F_j}{j} [1 - e^{-j \tau_\omega / \tau_i}] \quad (2.31)$$

Equation (2.30) can now be written as

$$N_i = \eta_i^* \tau_i \sum_{j=1}^{j_{\max}} C_j H_{ij} V_{o_i}^j \quad (2.32)$$

We define a count rate, R_i ,

$$R_i \equiv \frac{N_i}{\eta_i^* \tau_i V_{o_i}} \quad (2.33)$$

and by factoring out V_{o_i} from equation (2.32) we obtain

$$R_i = \sum_{j=1}^{j_{\max}} C_j H_{ij} V_{o_i}^{j-1} \quad (2.34)$$

Equation (2.34) is a system of simultaneous equations which can be solved for the values of C_j allowing one to determine $\frac{dj}{dE}(E)$.

Exact solutions to the system of equations (2.34) for higher order polynomials ($j_{\max} > 3$) may display erratic behavior between the

fitted points. Closer examination of equation (2.34) reveals that if we define

$$B_{ij} \equiv C_j H_{ij} \approx B'_j \quad (2.35)$$

we can express R_i as a polynomial and compute B'_j by a least squares fit. The approximation in equation (2.35) would be exact if the voltage sweep could be fitted by a single decay time (see equation (2.31)). Table 2.4 lists the values of V_{o_i} , τ_i , η_i and H_{ij} for $j_{\max} = 5$. The values for V_{o_i} and τ_i were determined from a prelaunch calibration of the deflection plate voltages.

i	V_{o_i} [kV]	τ_i [sec]	η_i	H_{i1}	H_{i2}	H_{i3}	H_{i4}	H_{i5}
1	3.933	.0164	.100	.0395	.430	5.31	79.1	1480.
2	3.197	.0166	.100	.0392	.426	5.28	78.6	1470.
3	2.604	.0171	.100	.0381	.415	5.16	76.9	1450.
4	2.135	.0195	.100	.0338	.372	4.67	70.3	1330.
5	1.793	.0212	.100	.0313	.347	4.37	66.2	1260.
6	1.527	.0214	.100	.0310	.344	4.34	65.7	1250.
7	1.303	.0212	.100	.0312	.346	4.37	66.1	1260.
8	1.110	.0215	.100	.0308	.342	4.32	65.5	1250.
9	.948	.0217	.108	.0306	.340	4.30	65.2	1240.
10	.810	.0221	.124	.0301	.335	4.23	64.3	1230.
11	.694	.0220	.138	.0302	.336	4.24	64.4	1230.
12	.595	.0225	.152	.0296	.330	4.17	63.4	1210.
13	.511	.0226	.165	.0294	.328	4.15	63.1	1210.
14	.440	.0227	.177	.0294	.327	4.14	63.0	1200.
15	.379	.0226	.188	.0295	.329	4.16	63.2	1210.
16	.326	.0229	.198	.0290	.324	4.10	62.4	1200.
17	.281	.0232	.207	.0287	.321	4.06	61.9	1190.
18	.243	.0236	.215	.0282	.315	4.01	61.0	1170.
19	.210	.0240	.223	.0278	.311	3.96	60.3	1160.
20	.182	.0240	.230	.0278	.311	3.95	60.3	1160.
21	.158	.0244	.238	.0274	.307	3.91	59.7	1150.
22	.138	.0249	.245	.0269	.302	3.84	58.8	1130.
23	.120	.0252	.252	.0266	.299	3.81	58.2	1120.
24	.105	.0257	.258	.0261	.293	3.74	57.3	1100.
25	.092	.0262	.265	.0256	.288	3.68	56.4	1090.
26	.081	.0268	.272	.0251	.282	3.61	55.4	1070.
27	.071	.0303	.277	.0224	.253	3.26	50.3	977.
28	.064	.0279	.283	.0242	.273	3.50	53.8	1040.
29	.056	.0347	.288	.0196	.224	2.90	45.0	879.

The maximum error in the coefficients for the assumption for a 9 point least squares fit is ~3%. We therefore perform a least squares fit to

$$R_i = \sum_{j=1}^{j_{\max}} B_j' V_{o_i}^{j-1} \quad (2.36)$$

The values of C_j are given by

$$C_j = B_j' / H_{ij} \quad (2.37)$$

Of course these coefficients are valid only for some energy range near the energy of the central word of the least squares fit. For a flat spectrum, the average energy detected during word i , \bar{E}_i , can be computed by first numerically computing equation (2.25) for $j = 1$

$$I_1 = \int G(E/V(t)) dE = F_1 V(t) \quad (2.38)$$

Then \bar{E}_i is given by

$$0.5 F_1 V(t) \equiv \int_0^{\bar{E}_i} G(E/V(t)) dE \quad (2.39)$$

Equation (2.39) can be numerically solved for \bar{E}_i

$$\bar{E}_i = 10.6 \bar{V} \quad (2.40)$$

where \bar{V} is the average value of $V(t)$ during the time τ_w . \bar{V} can be evaluated, and we obtain

$$\bar{E}_i = \frac{10.6 V_{o_i} \tau_i}{\tau_w} [1 - e^{-\tau_w/\tau_i}] \quad (2.41)$$

Table 5 lists the value of \bar{E}_i for each of the 29 words per frame.

TABLE 2.5

<u>i</u>	<u>\bar{E}_i [keV]</u>
1	37.8
2	30.8
3	25.1
4	20.8
5	17.6
6	15.0
7	12.8
8	10.9
9	9.33
10	7.99
11	6.84
12	5.87
13	5.05
14	4.34
15	3.74
16	3.22
17	2.78
18	2.40
19	2.08
20	1.80
21	1.57
22	1.36
23	1.19
24	1.04
25	.916
26	.806
27	.715
28	.636
29	.569

Before proceeding further we evaluate our results for $j_{\max} = 1$ in the limit where $\tau_{\omega}/\tau_i \ll 1$ which would correspond to constant deflection plate voltages and a histogram type electron differential energy spectrum (a histogram type spectrum is constant over the energy interval of the detector response for a given word but need not have that value at other energies)

$$[1 - e^{-\tau_{\omega}/\tau_i}] \rightarrow 1 - (1 - \tau_{\omega}(\tau_i)) = \tau_{\omega}/\tau_i \quad (2.42)$$

Therefore

$$\bar{E}_i \rightarrow 10.6 V_{o_i}$$

$$H_{il} \rightarrow F_l \tau_w / \tau_i$$

$$\frac{N_i}{\eta_i^* \tau_i V_{oi}} \rightarrow C_l F_l \tau_w / \tau_i$$

and

$$C_l \rightarrow \frac{N_i}{\eta_i^* \tau_w F_l V_{oi}}$$

as one would expect.

For a square box geometric factor with energy resolution $\Delta E/E = 2r$ and a first order energy dependence for $\frac{dj}{dE}$ it can be shown that the average energy of the detected particles is

$$(\bar{E}/\bar{E}_0) = 1 + \left(\frac{C_2}{2}\right) \left(\frac{\bar{E}_0}{\frac{dj}{dE}(\bar{E}_0)}\right) r^2 + O(r^4) \quad (2.43)$$

where \bar{E}_0 is the average energy when C_2 , the slope of the energy spectrum, is zero. We numerically solved for the correct value of r^2 in equation (2.43) for $\frac{dj}{dE}(\bar{E}_0)$ from $10^6 - 10^8$, \bar{E}_0 from 1 KeV to 10 KeV and C_2 from -10^8 to $+10^8$. The results are shown in figure 2.25. The value of r^2 depends upon the sign of the slope which is reasonable considering our skewed geometric factor. For a positive slope we find

$$r_+^2 = 0.12$$

and for a negative slope we obtain

$$r_-^2 = 0.07.$$

The values of the geometric factor for data words 6 - 11 when the plate voltage is at the average value for the word are plotted versus energy in figure 2.26. Considerable overlap is evident. To aid in

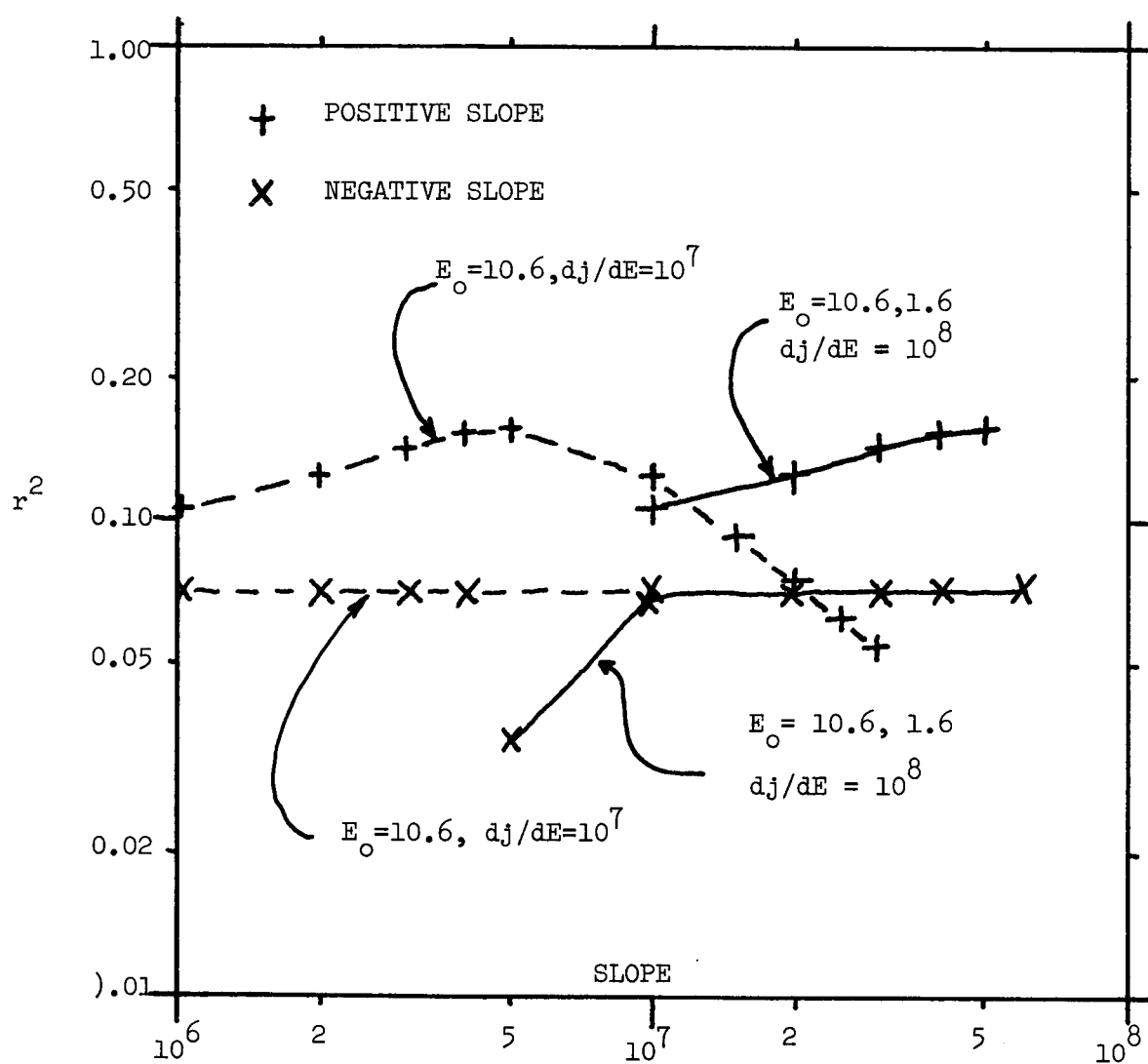


Figure 2.25. Slope dependent energy correction factor.

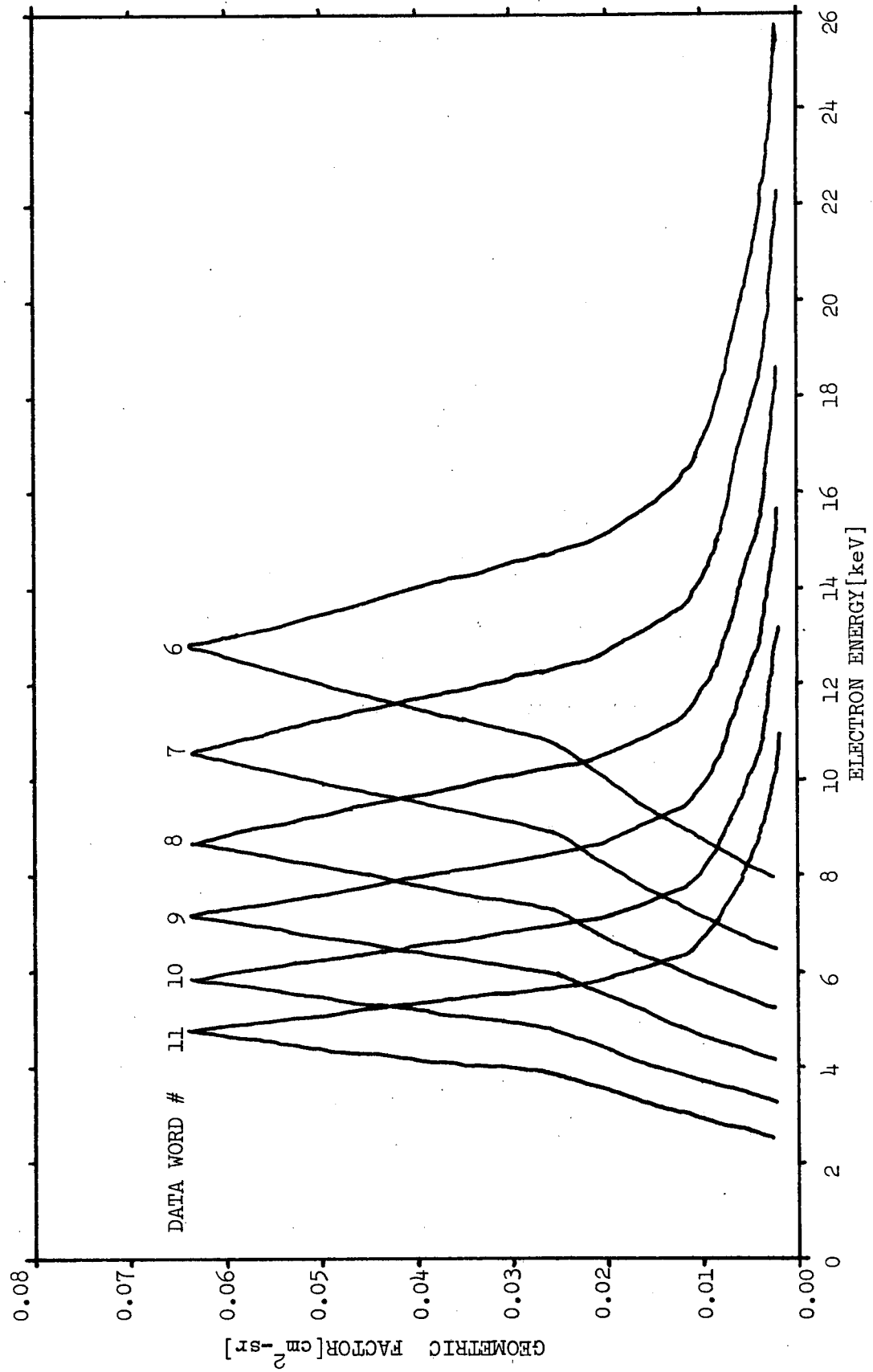


Figure 2.26. Geometric factor when sweep voltage is at average value during word.

deciding how many values of N_i to use in the least squares fit we have computed (for a flat energy spectrum) the fraction of the counts detected during word i_o which have energies within the upper and lower energies of the range of words about i_o (the ranges are determined by $E_{i_{\max}} = 10.6 V_{o_i}$; $E_{i_{\min}} = 10.6 V_{o_i + 1}$). For example, if we fit about $i_o = 9$ the nominal upper and lower limits of energy seen by word 9 are $10.6 V_{o_9}$ and $10.6 V_{o_{10}}$; however, the fraction of the electrons detected during word 9 which have energies in this range is only 0.384. Therefore using only one word to compute the flux for energies in the range of that word would be questionable because for a flat spectrum most of the electrons detected would have energies outside the range attributed to the word. Table 2.6 lists the number of words used and the fraction within the energy limits.

TABLE 2.6

<u>No. of Words Used</u>	<u>Words</u>	<u>Fraction of counts actually in energy range</u>
1	i_o	0.384
3	$(i_o - 1), i_o, (i_o + 1)$	0.719
5	$(i_o - 2), \dots, (i_o + 2)$	0.874
7	$(i_o - 3), \dots, (i_o + 3)$	0.930
9	$(i_o - 4), \dots, (i_o + 4)$	0.961

We now have an algorithm for unfolding the energy spectrum from the counts, N_i . If for example we choose to fit the counts from 5 words for up to second order energy dependence in $\frac{dj}{dE}(E)$ we begin with word 3 and fit equation (2.36) for $i = 1$ to $i = 5$ with $j_{\max} = 3$. The values of C_j are determined from

$$C_j = B_j' / H_{3j} \quad (2.44)$$

Using these C_j and $E = \bar{E}_3$ from equation (2.41) we compute $\frac{dj}{dE}(\bar{E}_3)$ from equation (2.24). The slope at $E = \bar{E}_3$ can also be computed from the C_j . These values are then inserted into an equation of the form of (2.43), and the corrected average energy of the electrons counted during word 3 is computed. Inserting this corrected average energy into equation (2.24) gives the value of the differential flux seen at the corrected average energy for word 3. This process is repeated for word 4 except that now the fit begins with counts from word 2 rather than word 1. This procedure would be repeated through word 27. The extreme words must be evaluated for only a 2 point fit and $j_{\max} = 2$.

B. Scintillator - Photomultiplier Detector (P.H.A.)

1. Physical Description

An aluminum-coated Pilot-B scintillator mounted on a RCA type 70102M ten-stage photomultiplier tube was used to detect electrons with energies greater than 20 KeV. Five channel pulse height analysis provided differential energy determination. Because of the pulse height analysis this detector is referred to as the P.H.A. Figure 2.27 shows the entrance collimator, the scintillator and the photomultiplier tube inside the brass tube holding them. The photomultiplier tube is a ruggedized version of RCA type 7767. The brass tube was inserted into a hole in the mounting holding the PESPEC. The azimuth and elevation of the look of the brass tube were $183^{\circ}25'$ and $16^{\circ}50'$ respectively. The PHA was also deployed at $t + 50$ when the door holding in the PESPEC and PHA mounting was blown off. The high voltage for the tube was switched on at $t + 66$. Because the center of the look of the collimator was 25° off axis a rotation of the tube could change the elevation of the detector look by $\pm 25^{\circ}$. Actually these up and down extremes will not be considered. When rotated to the upper extreme the tube would not clear the door opening, and for rotation to the lower extreme the field of view was blocked by the PESPEC. This will be further discussed in Chapter III.

The scintillator was coated with a 2662\AA ($70.7\mu\text{g}/\text{cm}^2$) thickness of aluminum to keep out light and low energy protons. The cone half-angle of the collimator was 11° . For this detector the geometric factor is a constant, $0.127\text{ cm}^2 - \text{sr}$. The angular response is shown in figure 2.28.

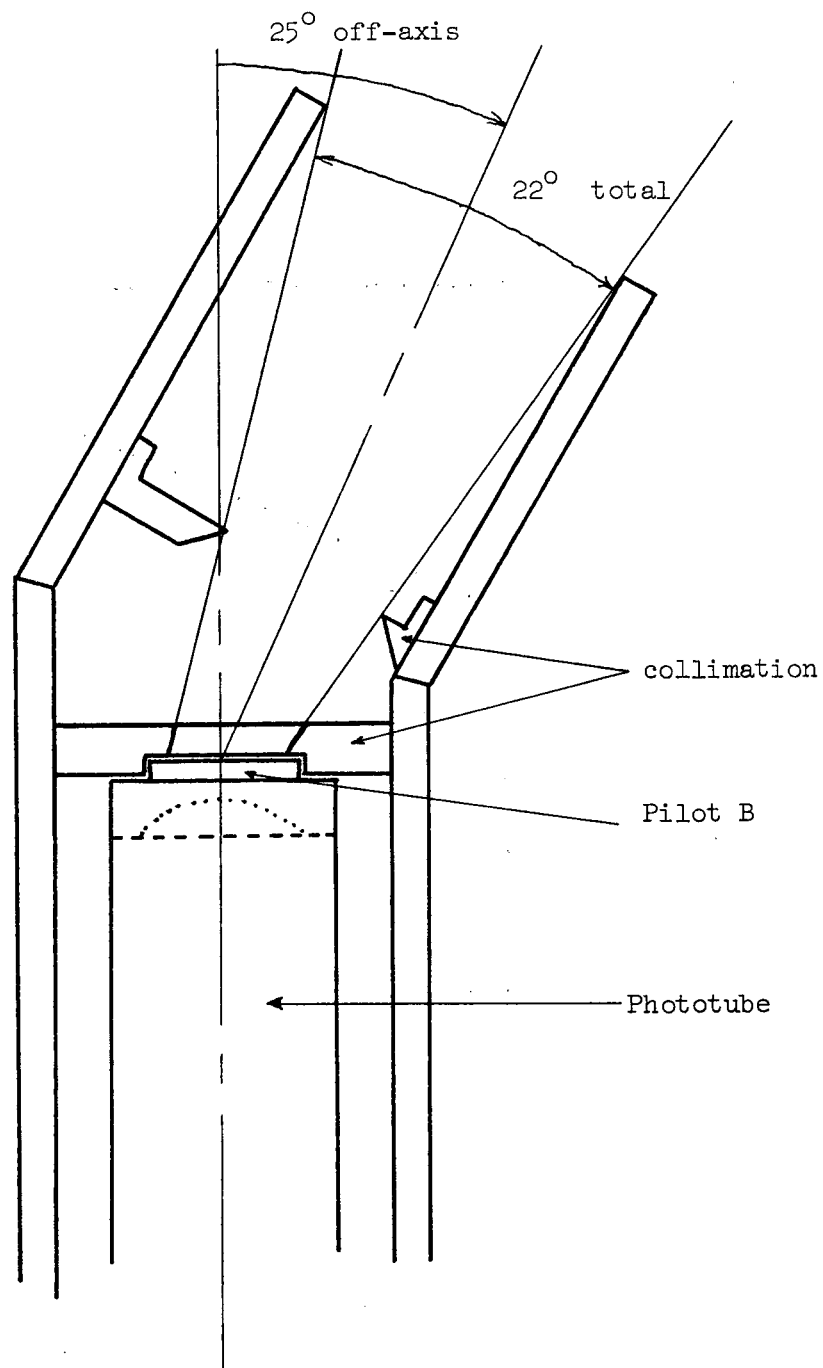


Figure 2.27. P.H.A. detector.

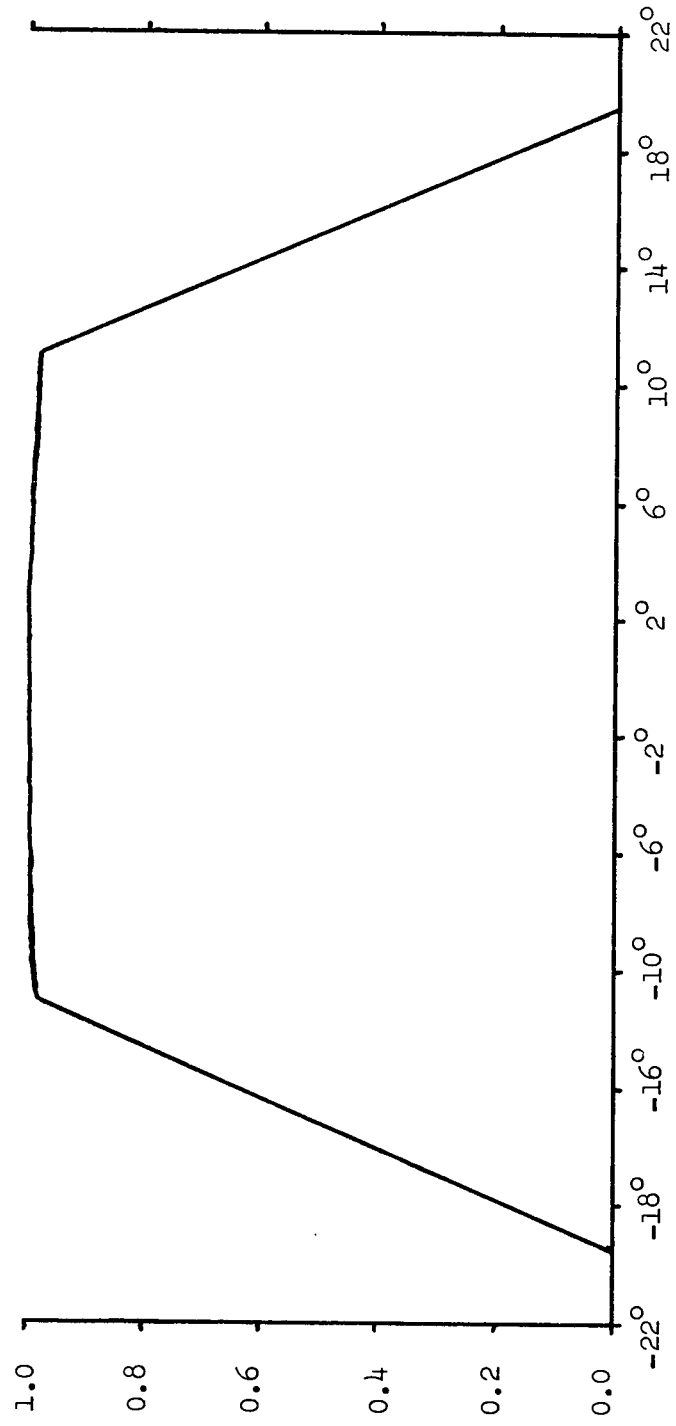


Figure 2.28. P.H.A. angular response.

2. P.H.A. Electronics

A DC-DC converter capable of producing 1500V @ 50 μ A was used to provide a negative high voltage to the phototube. A resistor divider network of 10 6.8M Ω resistors and one 13 M Ω resistor provided the proper voltage to each dynode. The negative high voltage was applied to the photocathode, and the potential difference between it and the first dynode was twice the potential difference between the other adjacent dynodes. The anode of the photomultiplier tube was connected directly to the input stage of a linear pre-amplifier (see figure 2.29). The frequency response and linearity of this pre-amplifier have been measured. It remains linear and can distinguish between pulses for an input pulse rate greater than 10 MHz. This corresponds to a dead time of ~100 nanoseconds. The output of the preamp went to the 5 channel pulse height analyzer. The threshold voltages on the 18:63 UE P.H.A. are given in Table 2.7.

TABLE 2.7

<u>Channel</u>	<u>Threshold Voltage</u>
A	0.21V
B	0.54V
C	0.99V
D	1.76V
E	2.90V

To obtain differential energy determination the discriminator memory circuit allowed only the counter for which the pulse was greater than the threshold but less than the threshold of the next channel to

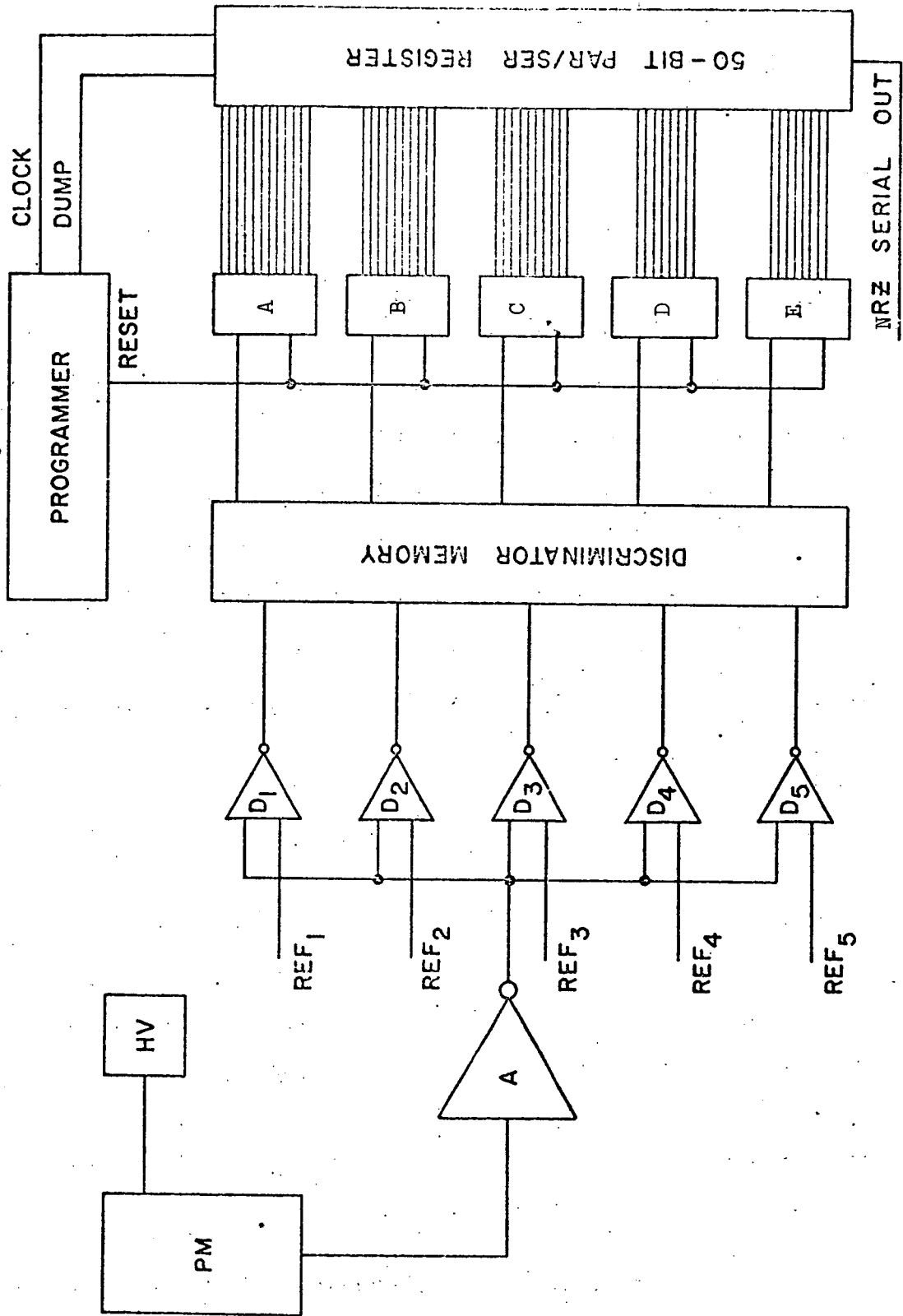


Figure 2.29. P.H.A. electronics block diagram.

be incremented. The channel A counter was a 12 bit counter. Channels B and C had 10 bit counters, and channels D and E had 8 bit counters. The P.H.A. programmer had a clock or bit rate of 2 KHz. There were 50 bits including a parity bit and a "hole" bit per data frame. The "hole" bit provided frame synchronization. Therefore a complete frame or P.H.A. energy spectrum was obtained every 25 msec. Like the PESPEC the three voltage level output from the P.H.A. electronics was connected to the VCO of the proper FM subcarrier in the telemetry section.

3. Determination of the Energy Spectrum from P.H.A. Data

An electron striking the aluminum coating on the scintillator loses some energy in passing through the aluminum. If the electron penetrates the aluminum it then begins to lose energy in the Pilot-B scintillator. Some of the energy lost is converted into photons and some of these photons leave the scintillator and strike the photo-cathode of the photomultiplier. Therefore if the electron loses all its energy and stops in the scintillator the number of photons striking the photo-cathode is proportional to the energy of the electron after penetrating the aluminum. Depending upon the quantum efficiency and the spectral response of the photocathode a fraction of the photons striking the photocathode emit electrons which begin the cascade leading to a voltage pulse at the anode. The size of the pulse can be related to the energy of the incident electron.

This process is quite complex and noisy, and, in practice, one usually avoids treating it in detail by making calibrations of the response of the detector-amplifier-counting system to electrons of known energy. One can adjust the high voltage on the multiplier to

vary the tube gain to insure that electrons of a given energy are counted in the desired channel. The output pulse distribution, $O(V, E)$, from the photomultiplier at a given energy is very broad. This output pulse distribution was measured with a 1000 channel pulse height analyzer for electrons from the Van de Graff accelerator at the N.A.S.A. Goddard Space Flight Center (G.S.F.C.) for various electron energies and photomultiplier tube voltages. For the 18:63 UE P.H.A. we were unable to use the flight pre-amplifier and 5 channel pulse height analyzer during calibration at G.S.F.C. We therefore needed to use the G.S.F.C. 1000 channel analyzer channel numbers, n , as a parameter from which we compute the relationship between pulse height, V , and energy, E . The output pulse distribution was also determined when the electron source was β particles from Nickel-63, and the tube voltage, V_T , was 1200V.

For the monoenergetic incident electrons the output pulse distribution was approximately a Gaussian where the channel number of the peak, n_o , and the width of the peak were related to the incident electron energy, E , and the tube voltage, V_T . We let $O(n)$ be the value of the output pulse distribution for channel n , then we found

$$O(n) = \frac{O_o}{\sigma} e^{-(n - n_o)^2 / 2\sigma^2} \quad (2.45)$$

where

$$n_o = n_o(E, V_T) = a + b(V_T)E \quad (2.46)$$

and

$$\sigma = \sigma(n_o) = a' + b'n_o \quad (2.47)$$

and O_o is a normalizing constant. The value of b in equation (2.46) is a function of the tube voltage and is proportional to the tube gain. a in equation (2.46) is nonzero (the initial channels of the 1000 channel analyzer weren't used and a finite energy particle may produce no pulse if it can not penetrate the aluminum). Figure 2.30 shows the channel number of the peak, n_o , versus the incident electron energy for $V_T = 1200V$. This figure determines $a = 7.0$ and $b = 0.784$ [channels/kilovolt] @ $V_T = 1200V$. The variation of n_o with V_T for $E = 120$ KeV is shown in figure 2.31. Also shown is the current gain for the RCA type 7767 phototube [see R.C.A., Phototubes and Photocells, 1963] versus V_T . Note that as expected the average size of the output pulse is directly proportional to the tube gain.

The relationship between the 1000 channel pulse height analyzer channel number, n , and the 18:63 UE P.H.A. threshold voltages was determined from the pulse distribution of the Ni^{63} source. A pre-launch calibration of the P.H.A. with the Ni^{63} source gave ~45 counts in channel A, ~16 counts in channel B and no counts in channel C @ $V_T = 1300V$. Figure 2.32 is a graph of the pulse distribution from the Ni^{63} source with the 1000 channel analyzer. Using a relationship of the form

$$n = C_1 + C_2(V_T)V \quad (2.48)$$

where V is the size of the input pulse to the 18:63 UE P.H.A. 5 channel analyzer, we were able to compute the proper threshold values of n for each of the five channels. Then we numerically integrated the areas under the curve in figure 2.32 between the various threshold values of n . These areas are proportional to the counts in the

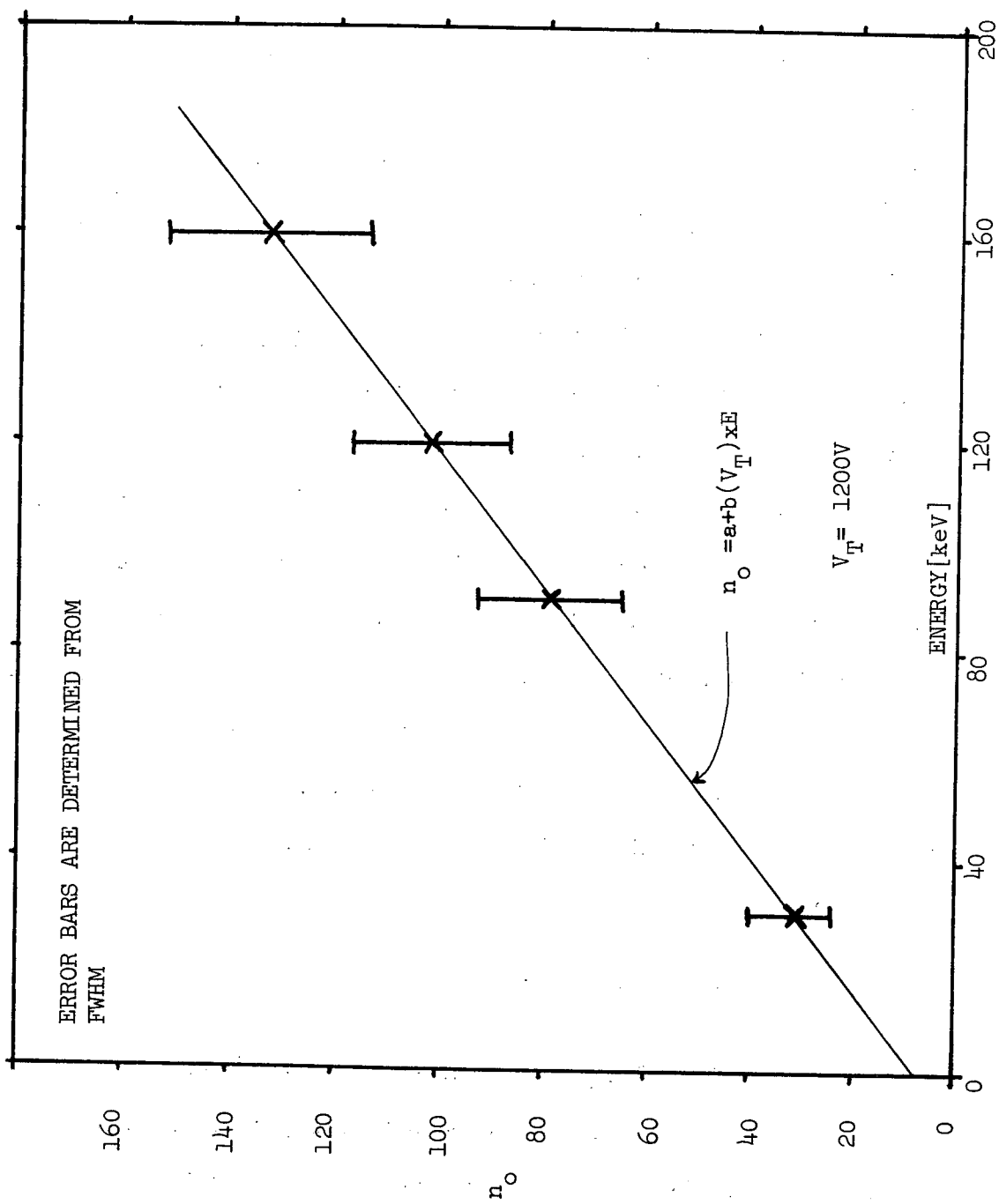


Figure 2.30. Channel number of peak versus incident electron energy.

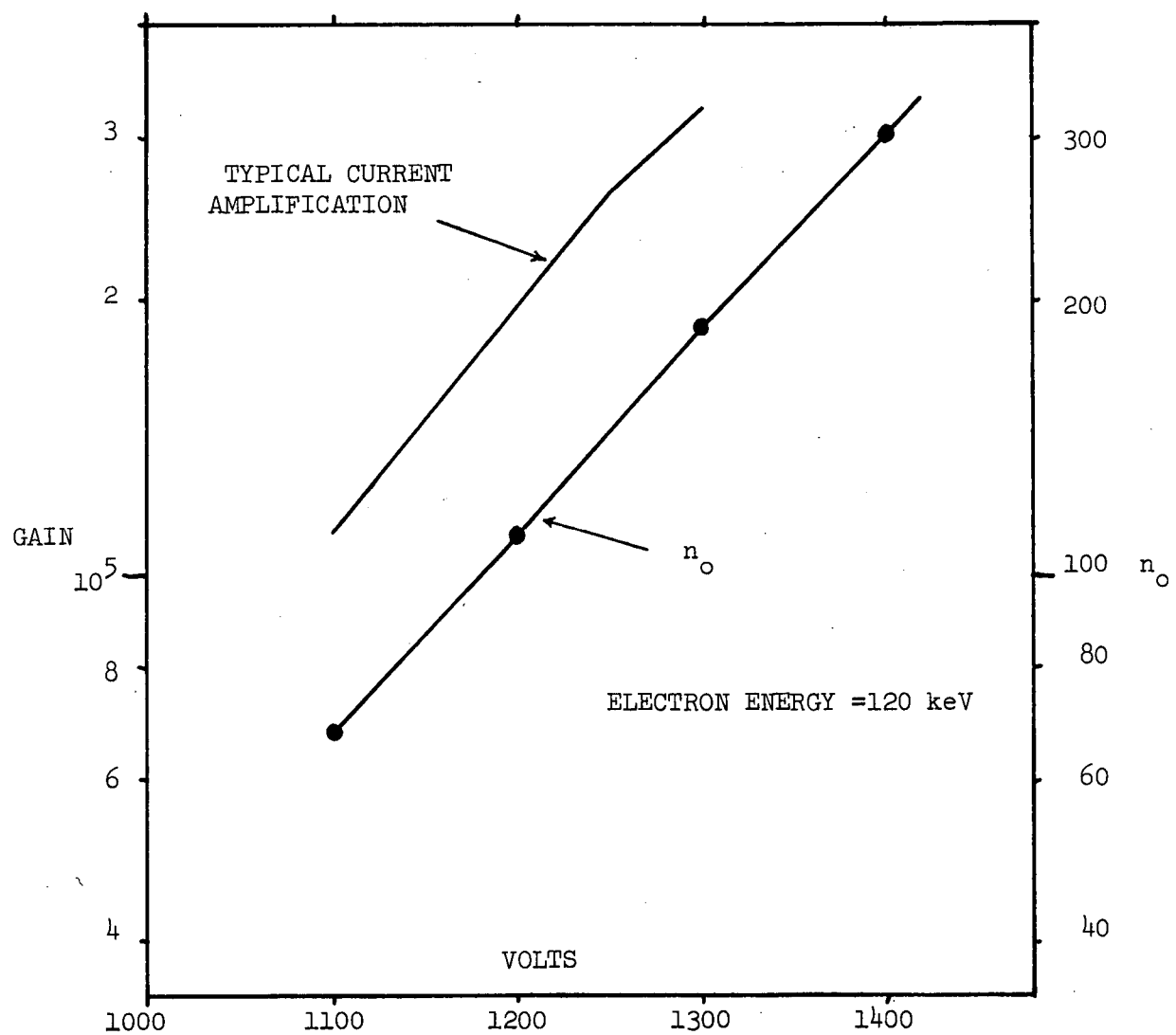


Figure 2.31. Channel number of peak versus tube high voltage.

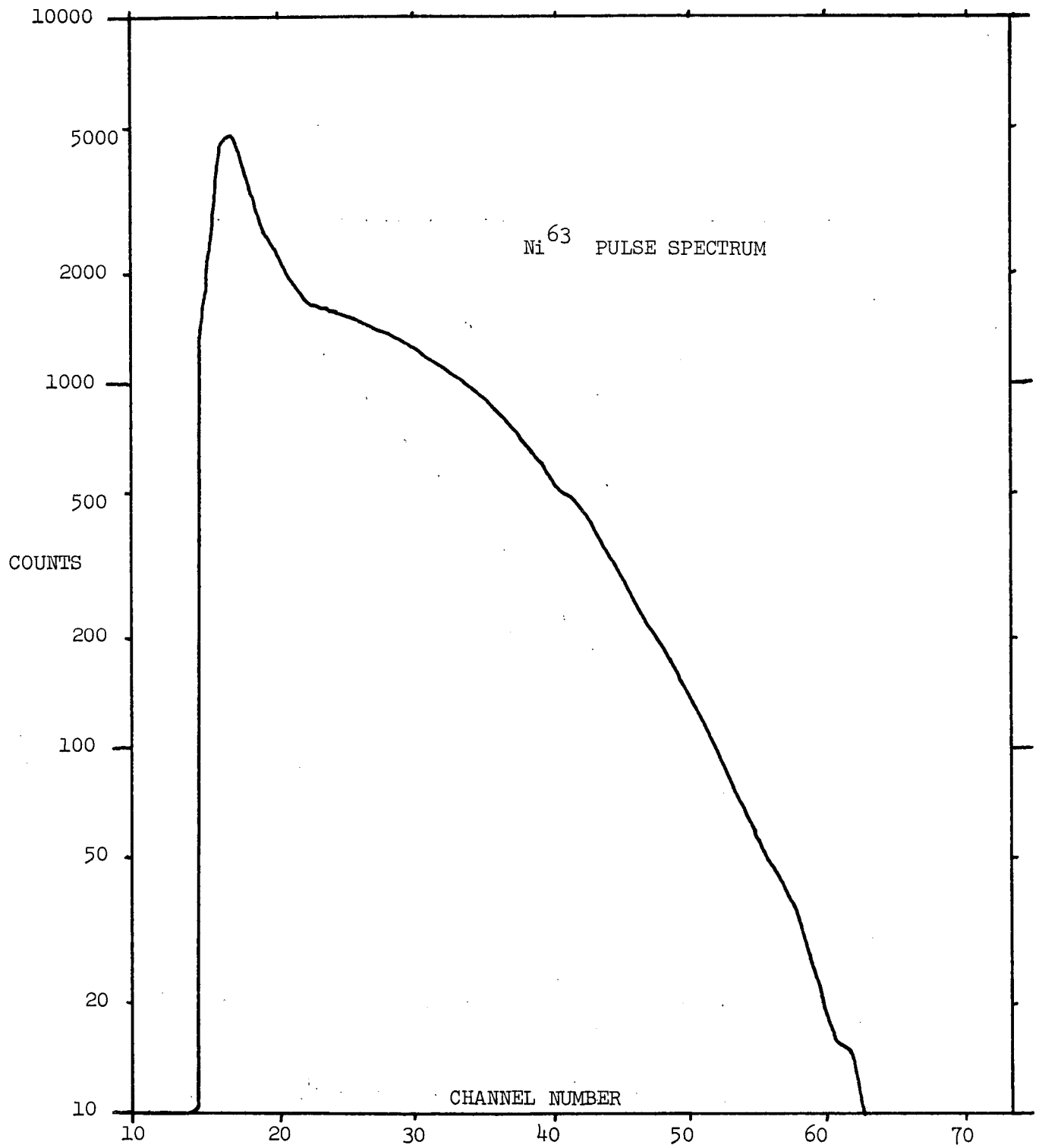


Figure 2.32. Ni⁶³ pulse distribution.

five P.H.A. channels. By requiring that the ratio of the channel A area to the channel B area be $\sim 45/16$, and that the area corresponding to channel C be much, much less than the area corresponding to channel B we were thus able to determine C_1 and C_2 .

$$C_1 = 11.09 \pm 4$$

$$C_2 = (46.2 \pm 1) \text{ channels/volt @ } V_T = 1300V.$$

Again C_1 is non-zero because approximately the first ten channels of the analyzer were not used. Measurements of the tube voltage monitor indicated that the nominal flight value of V_T was 1250V not the 1300V of the prelaunch calibration or the value used in obtaining the pulse distribution in figure 2.32. However we can use the information in figure 2.31 to determine the variation of $C_2(V_T)$ and $b(V_T)$ with tube voltage. With electron energy equal to 120 KeV the pulse distribution for $V_T = 1200V$ peaked at $n_o(120, 1200) = 112$. With the tube voltage at $V_T = 1300V$ the same energy had its distribution peak at $n_o(120, 1300) = 188$. Therefore a Ni^{63} pulse distribution measured at $V_T = 1300V$ would have been shifted to the higher channels. We can compute $C_2(1300)$ by

$$C_2(1300) = C_2(1200) \times 188/112 = 77.4 \text{ channels/volt}$$

The initial channel C_1 is unaffected by the value of the tube voltage.

In like manner the channel numbers of the peak of the distributions in figure 2.30 must be adjusted to give the inflight relationship between the channel number, n , and incident electron energy, E . For $V_T = 1250V$ the curve on figure 2.31 shows that the pulse distribution would peak at about $n_o(120, 1250) = 143$. We can now compute the

value of $b(1250)$

$$\begin{aligned} b(1250) &= b(1200) \times n_o(120, 1250)/n_o(120, 1200) \\ &= 0.784 \times 143/112 = 1.001 \end{aligned} \quad (2.49)$$

Then we compute the relationship between the incident electron energy, E , and the value of the voltage, V_o , at the peak of the output pulse distribution from the P.H.A. pre-amplifier, using equations (2.48) and (2.46),

$$E = 4.09 + 77.4 V_o \quad @ V_T = 1250V \quad (2.50)$$

The width of the pulse distribution equation (2.47) can be computed in terms of the voltage of the peak, V_o . Figure 2.33 shows various values of $\sigma(V_o)$ versus V_o . A fit to the points gives

$$\sigma(V_o) = 0.0721 + 0.0909 V_o (\pm 0.011) \quad (2.51)$$

We can now determine the parameters for the Gaussian voltage pulse distribution

$$O(V, E) = \frac{O_o(V_o/\sigma)}{\sigma} e^{-\frac{(V - V_o)^2}{2\sigma^2}} \quad (2.52)$$

from equations (2.50) and (2.51). The normalizing constant $O_o(V_o/\sigma)$ is determined by the requirement that the integral from $V = 0$ to $V = \infty$ of equation (2.52) be unity whereas the usual normalizing constant (which would imply negative values of V) would have $V = -\infty$ to $V = +\infty$ as the limits of integration.

The pulse distributions from the calibrations which were used to determine equation (2.52) refer to electrons which produced pulses.

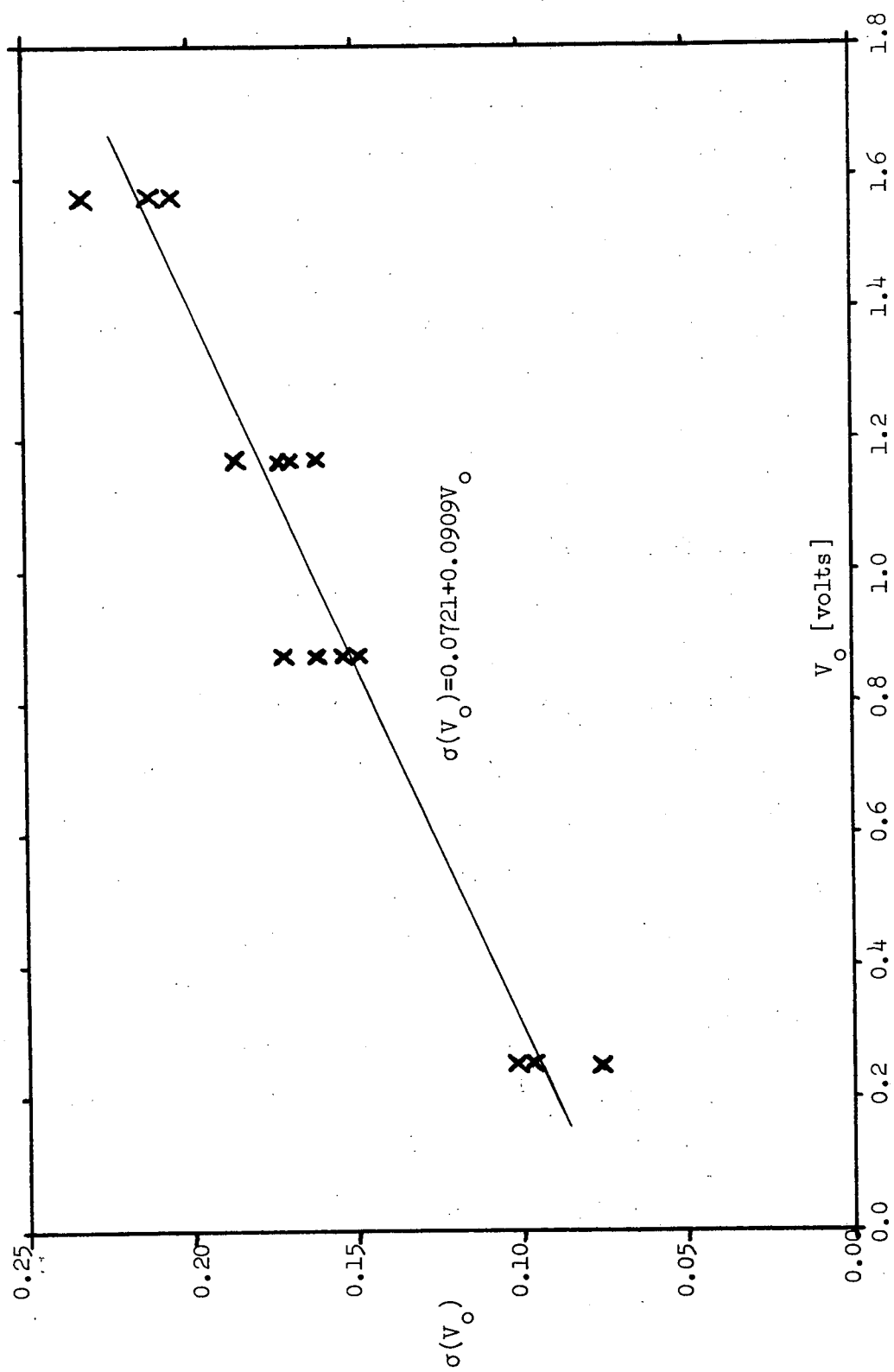


Figure 2.33. Width of pulse distribution versus voltage of peak.

For high enough electron energies the efficiency of the P.H.A. is unity, but the efficiency with which low energy electrons produce pulse distributions of the form of equation (2.52) is very important in considering the number of counts in channel A. We define the P.H.A. efficiency, $\eta(E)$, to be the probability that electrons with incident energy, E , will produce a pulse distribution of the form of equation (2.52). There are three factors governing $\eta(E)$: (i) if the energy is too low ($E \lesssim 4$ KeV) the electrons will be unable to penetrate the aluminum coating of the scintillator (this is the transmission efficiency, $\eta_T(E)$), (ii) the relative light output of the Pilot-B deviates from equation (2.50) becoming less for low energy electrons Reagan, J.B., et al, [1967], and (iii) the pulse distribution becomes more characteristic of a "noise" distribution Sherman, I.S., et al, [1964] rather than a Gaussian distribution when the average energy of the transmitted electrons, E_a , is less than 20 KeV. We define $\epsilon(E_a)$ to be the efficiency with which the Pilot-B produces pulses of the form of equation (2.52). Kanter, [1961] and Kanter and Sternglass, [1962] have made excellent empirical determinations of $\eta_T(E)$ and E_a for various thickness of aluminum. Reagan, et al, [1967] presents measurements of $\epsilon(E_a)$, but they were making current-mode, not pulse-mode, measurements of the output of the photomultiplier therefore their values should be regarded as an upper limit of $\epsilon(E_a)$ for a pulse-mode operation.

Direct measurements of $\eta(E)$ for the 18:63 UE P.H.A. were not made. We did measure the low energy ($E < 20$ KeV) efficiency of the P.H.A.'s for 18:64 UE and 18:65 UE. The aluminum coatings on these detectors were nearly twice as thick, $135\mu\text{g}/\text{cm}^2$. This lowered the transmission

efficiency, $\eta_T(E)$ as well as the average energy of the transmitted electrons, E_a .

Figure 2.34 shows the results of the measurements of efficiency. The data points are the ratio of pulses counted in all channels at a beam energy E to a Faraday cup measurement of the beam input. The threshold voltage for channel A was non-zero, therefore the solid curve is the value the ratio would have for $\eta(E) = 1.0$. From Kanter and Sternglass, [1962] we can determine the critical energy, E_c , corresponding to the practical range of electrons in the aluminum coatings for the 18:63 UE P.H.A. and for the 18:64 UE and 18:65 UE P.H.A.'s,

$$E_c(18:63 \text{ UE}) = 4.3 \text{ KeV}$$

$$E_c(18:64 \text{ UE and } 18:65 \text{ UE}) = 6.4 \text{ KeV.}$$

We use Kanter, [1961] to determine the transmission efficiency $\eta_T(E)$, and Kanter and Sternglass, [1962] to determine the average energy, $E_a(E)$, for these values of E_c (see figure 2.35). Using figure 2.35 for E_a and η_T and figure 2.34 for the 18:64 UE and 18:65 UE $\eta(E)$ we can compute $\epsilon(E_a)$. The values of $\epsilon(E_a)$ are shown in figure 2.36. Then using figure 2.35 to determine $\eta_T(E)$ and $E_a(E)$ for $E_c = 4.3 \text{ KeV}$ and figure 2.36 for $\epsilon(E_a)$ we can determine $\eta(E)$ for the 18:63 UE P.H.A. The large scatter and uncertainty of $\epsilon(E_a)$ in figure 2.36 limit the accuracy of $\eta(E)$. We chose to express $\eta(E)$ by

$$\eta(E) = \eta_0 10^{\frac{E}{E_0}} \quad (2.53)$$

$$(10.0 < E < 18.0).$$

where $\eta_0 = 10^{-4.2}$ and $E_0 = 4.2$.

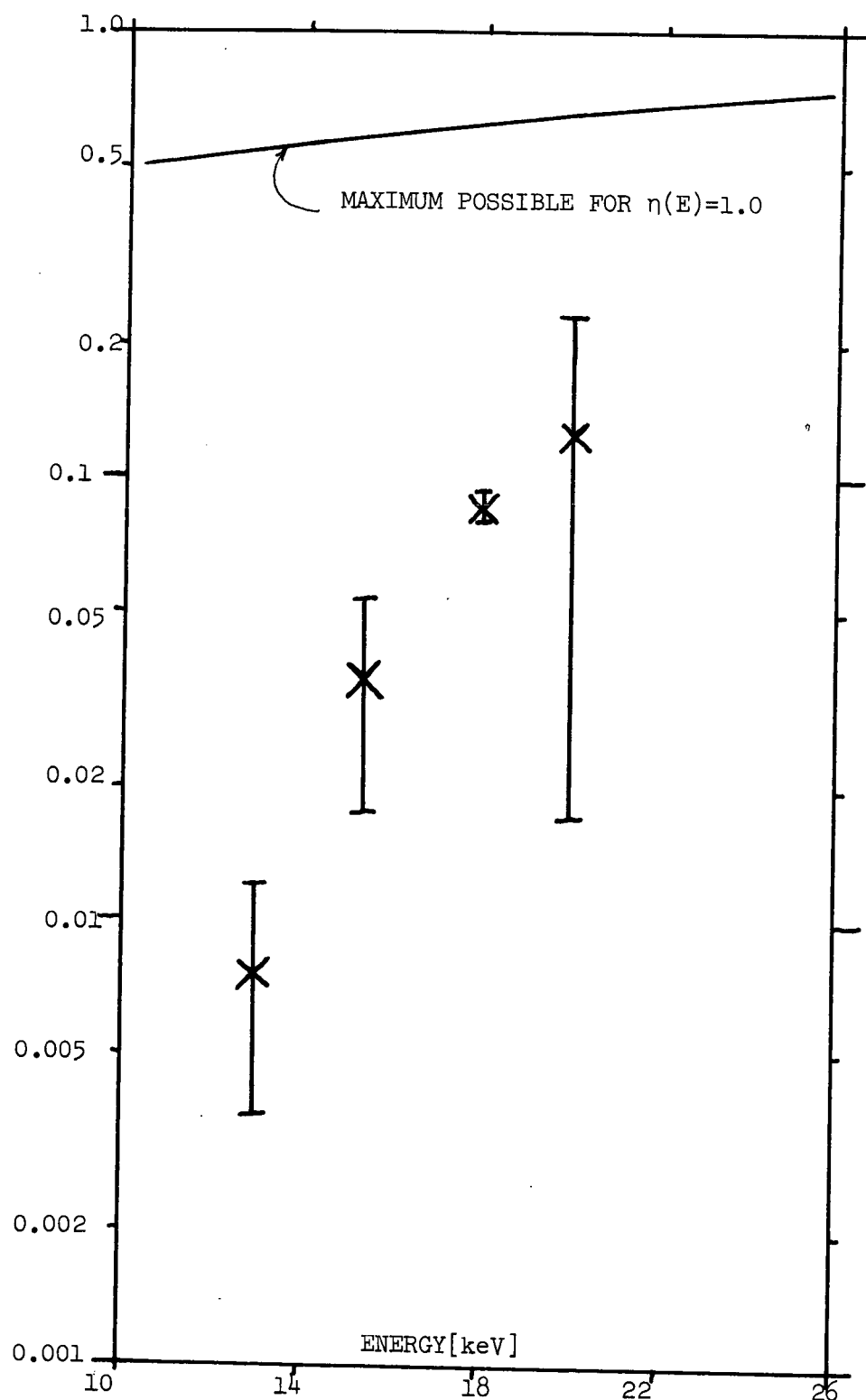


Figure 2.34. Ratio of pulses counted to input versus E.

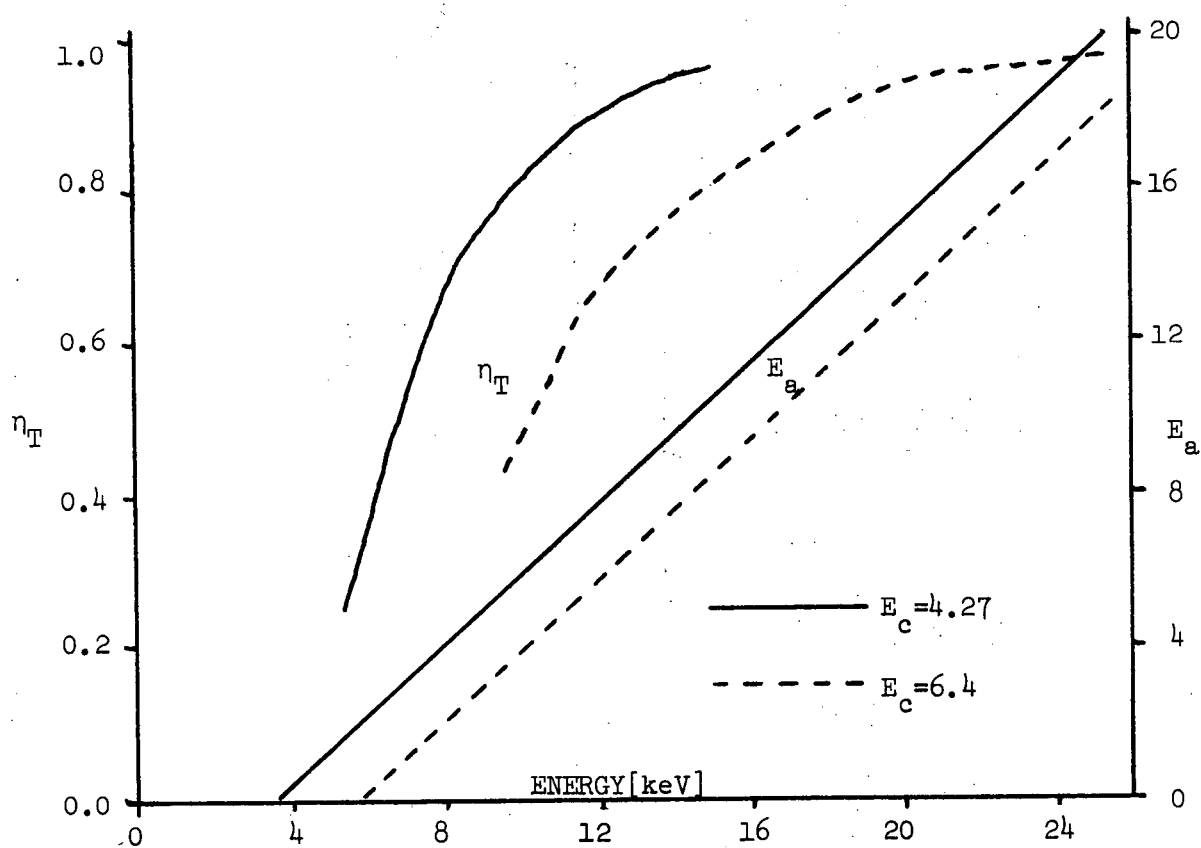


Figure 2.35. Transmission efficiency, $\eta_T(E)$, and average transmitted energy, E_a , versus incident energy.

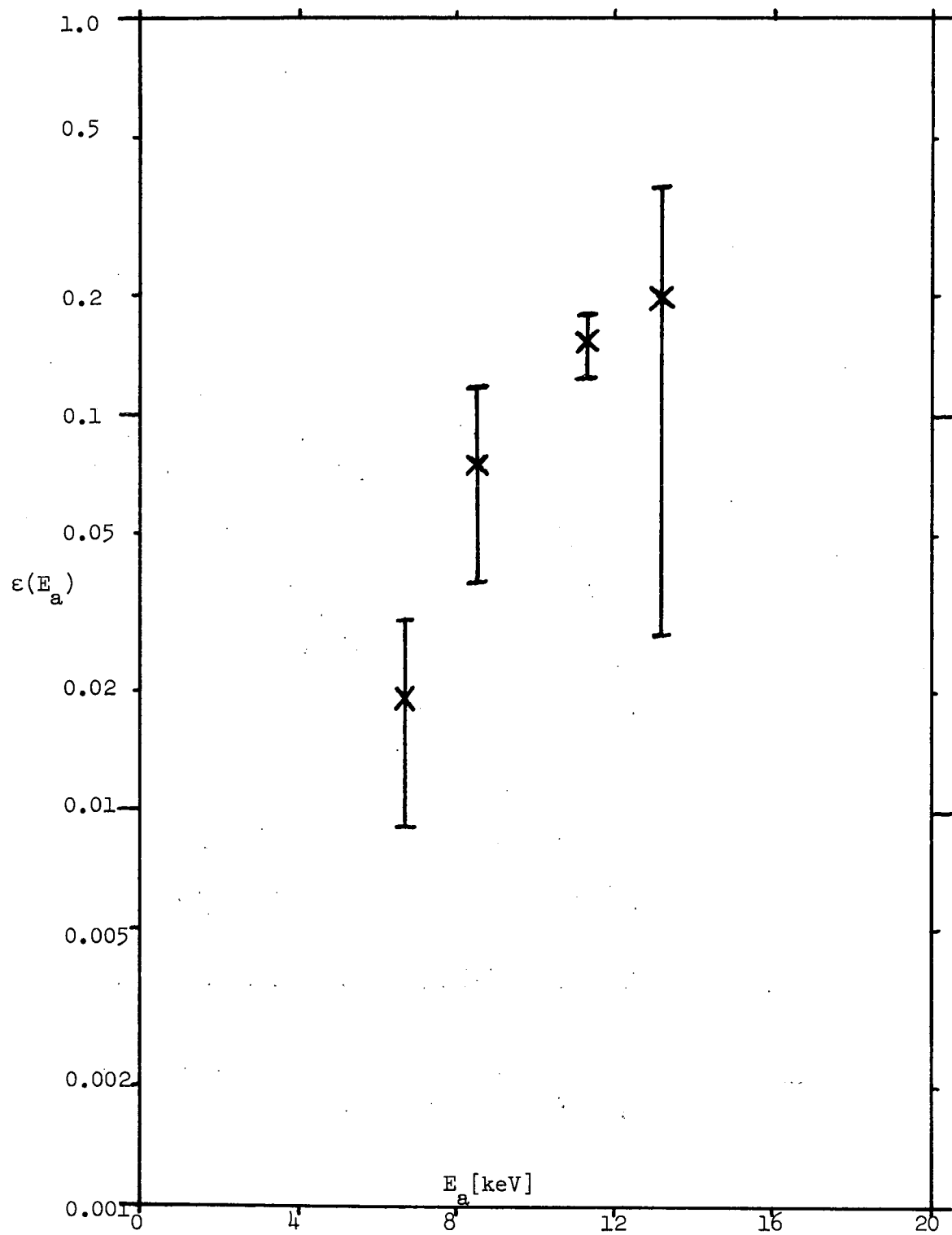


Figure 2.36. Pilot B pulse efficiency versus energy.

Because of the uncertainty in determining $\eta(E)$ it is difficult to compare the data from channel A of the 18:63 UE P.H.A. with the higher energy PESPEC channels.

Using equation (2.53) for $\eta(E)$ and equation (2.52) which describes the output pulse distribution for monoenergetic input one can compute the output pulse distribution for a differential flux, $\frac{dj}{dE}(E)$,

$$O(V) = \int_0^\infty \eta(E) \frac{O_0}{\sigma} e^{-\frac{(V - V_0(E))^2}{2\sigma^2}} \frac{dj}{dE}(E) dE \quad (2.54)$$

The number of counts in a given channel (for example channel B) is given by

$$N_B = \tau_\omega \times GF \times \int_{V=0.54V}^{V=0.99V} O(V) dV \quad (2.55)$$

where τ_ω the sample time was 24.7 ms and GF is the geometric factor.

The flux $\frac{dj}{dE}(E)$ was assumed to have the form

$$\frac{dj}{dE}(E) = J_0 E^{-N} \quad (2.56)$$

Equations of the form of (2.55) were numerically integrated for various values of N. In general the ratio of counts between two channels determines the value of N in that energy range, and numerically computed tables allowed one to determine N from any ratio and then it was easy to determine J_0 , and the electron flux in a given energy range.

We can unfold the pitch angle distribution of the electrons detected by the P.H.A. to second order in the pitch angle. For a square

box angular response $R(\alpha', \alpha_0)$ centered about α_0 , of width 2ω , and a pitch angle distribution given by

$$I(\alpha') = A_N \alpha'^N \quad (2.57)$$

the number of counts, $O_N(\alpha_0)$, is given by

$$O_N(\alpha_0) = \int_{0^\circ}^{180^\circ} R(\alpha', \alpha_0) I(\alpha') d\alpha' \quad (2.58)$$

For $N = 0, 1, 2$ we have

$$\begin{aligned} O_0(\alpha_0) &= A_0 \\ O_1(\alpha_0) &= A_1 d_0 \\ O_2(\alpha_0) &= A_2 \alpha_0^2 + A_2 \omega^2/3 \end{aligned} \quad (2.59)$$

We have numerically evaluated equation (2.58) for $N = 0, 1, 2$ with $R(\alpha', \alpha_0)$ being the actual P.H.A. response. We find that we can satisfy equations (2.59) provided: (i) $\alpha_0 > 16^\circ$ and (ii) $\omega^2/3 = 83.49 \equiv \delta$.

When the pitch angle distribution can be written

$$I(\alpha') = A_0 + A_1 \alpha' + A_2 \alpha'^2 \quad (2.60)$$

the number of counts detected when looking at pitch angle, α_i , will be given by

$$O(\alpha_i) = (A_1 + A_3 \delta) + A_2 \alpha_i + A_3 \alpha_i^2 \quad (2.61)$$

using equations (2.59) and (2.60).

A series of measurements $O_i(\alpha_i)$ can then be least squares fitted by a polynomial of the form

$$O_i(\alpha_i) = B_1 + B_2\alpha_i + B_3\alpha_i^2 \quad (2.62)$$

Using these B_j and equation (2.61) the pitch angle distribution near α_o (which would be the center of the α_i) can be computed

$$I(\alpha_o) = (B_1 - B_3\delta) + B_2\alpha_o + B_3\alpha_o^2 \quad (2.63)$$

Using equally spaced α_o for example one can unfold the complete pitch angle distribution for $\alpha > 16^\circ$ (this restriction comes from the fact that the pitch angle distribution must be symmetric about $\alpha = 0^\circ$ whereas equation (2.60) is not).

CHAPTER III

VEHICLE POSITION AND ATTITUDE

In order to determine pitch angle information about energetic electrons and for analysis of data from other experiments on board it is necessary to be able to describe the position and attitude of the payload. The payloads are launched with a Nike booster which falls away when spent and a Tomahawk second stage which burns out before atmospheric exit and remains attached to the payload. To achieve stability the vehicles are spun at about 7 rps during burning. After burn-out they are despun to about 1 rps to facilitate collection of angular information in the data. Radar plots furnished by the Churchill Research Range were used to determine vehicle position. On-board magnetometers which measured the component of the earth's magnetic field parallel to their orientation were used to determine payload attitude with respect to the magnetic field. The Churchill Research Range is at an invariant latitude of 69° with a magnetic L shell value of $L = 7.6$.

A. Vehicle Position

The effects of coriolis and centripetal accelerations upon sounding rockets launched from Churchill show up most dramatically in reducing the eastward distance traveled by several kilometers (the earth rotates under the payload). The North-South location of the impact point is virtually unaffected. In practice one is most concerned with the effect upon the altitude where the effect of centripetal acceleration is less than 0.1%. However, since most vehicles are launched eastward the coriolis acceleration is in the opposite sense to the centripetal acceleration and can be of nearly the same magnitude so one can safely ignore these effects. Because the exact impact point is generally not needed and because radar data frequently is not good enough to justify further precision we will adopt a coordinate system assuming a flat, nonrotating earth with positive z representing altitude and positive x representing eastward direction. Normally a flat earth assumption would have g , the acceleration of gravity, independent of z . However over the range of z for the sounding rocket this represents an appreciable error so we will use an expansion of the potential energy, V , for the inverse square gravitational force,

$$V = - \frac{GM_e m}{r} = - \frac{GM_e m}{R_e + z} \quad (3.1)$$

where G is the gravitational constant, M_e is the mass of the earth, m is the mass of the payload, r is radial distance from center of the earth and R_e is the radius of the earth at Churchill.

Expanding (3.1) in z/R_e gives

$$\begin{aligned}
 V &= \frac{-GM_e m}{R_e} (1+z/R_e)^{-1} \\
 &= \frac{-GM_e m}{R_e} [1 - z/R_e + (z/R_e)^2 - (z/R_e)^3 + \dots] \\
 &= \frac{-GM_e m}{R_e} + \frac{GM_e m}{R_e^2} z - \frac{GM_e m}{R_e^3} z^2
 \end{aligned} \tag{3.2}$$

neglecting the cubic and higher terms.

The payload kinetic energy can be written,

$$T = 1/2 m (\dot{x}^2 + \dot{y}^2 + \dot{z}^2) \quad . \tag{3.3}$$

Hence the Lagrangian is,

$$L = T - V = 1/2 m (\dot{x}^2 + \dot{y}^2 + \dot{z}^2) + \frac{GM_e m}{R_e} - \frac{GM_e m}{R_e^2} z + \frac{GM_e m}{R_e^3} z^2 \quad . \tag{3.4}$$

Since x and y do not appear in L the corresponding velocities are constant above the atmosphere. The differential equation in z is

$$\ddot{z} = -\frac{GM_e}{R_e^2} + 2 \frac{GM_e}{R_e^2} \frac{z}{R_e} = -g_0 + 2 g_0 \frac{z}{R_e} \tag{3.5}$$

where g_0 is the acceleration of gravity on surface of earth,

$$g_0 \equiv \frac{GM_e}{R_e^2} \quad . \tag{3.6}$$

The general solution to (3.5) is

$$z = B_1 e^{\alpha t} + B_2 e^{-\alpha t} + B_3 \tag{3.7}$$

where α and B_3 are given by,

$$\alpha = (2g_0/R_e)^{1/2} \quad B_3 = R_e/2 \quad (3.8)$$

Using (3.6) and the value of g measured at Churchill of $g = 981.761 \text{ cm/sec}^2$ one can solve for the value of R_e to use. These values are in Table 3.1.

Table 3.1

$$R_E = 6377.0 \text{ km}$$

$$B_3 = 3188.5 \text{ km}$$

$$\alpha^2 = 0.307907 \times 10^{-5} \text{ sec}^{-2}$$

$$\alpha = 0.175473 \times 10^{-2} \text{ sec}^{-1}$$

The problem remaining is to use the measured z_i and t_i from the radar plot to least squares fit for the initial conditions B_1 and B_2 . This analysis was quite satisfactory for 18:63 and 18:64, but for 18:65 we obtained a better fit to the points using slightly different values for R_E and fitting for B_3 also.

Apogee time, t_A , and height, z_A , can be found by differentiating (3.7)

$$t_A = \frac{1}{2} \ln (B_2/B_1)^{1/2} \quad (3.9)$$

$$z_A = -2 (B_1 B_2)^{1/2} + B_3 \quad (3.10)$$

The values for liftoff time, t_A , z_A and the four coefficients in (3.7) for t and t_A measured from liftoff are given in Table 3.2.

Table 3.2

Vehicle	Liftoff	t_A	z_A [km]	B_1 [km]	B_2 [km]	B_3 [km]	α [sec ⁻¹]
18:63	21 Mar '68 0601:32.7	241.09	241.76	-965.129	-2249.25	3188.5	0.17547×10^{-2}
18:64	14 Jan '70 0405:30.0	250.24	259.74	-943.961	-2271.7	3188.5	0.17547×10^{-2}
18:65	17 Jan '70 0303:20.0	248.16	252.48	-779.05	-1989.9	2742.7	0.18894×10^{-2}

One can use (3.7) to determine v_z by differentiation. Figures 3.1 - 3.3 are plots of the altitude and v_z versus Universal Time in minutes. The x and y components of velocity are given in Table 3.3.

Table 3.3

Vehicle	v_x (East) [km/sec]	v_y (North) [km/sec]	v_{xy} [km/sec]
18:63	0.051	- 0.101	0.113
18:64	0.203	- 0.005	0.206
18:65	0.276	0.168	0.322

It is interesting to compare the altitude at which the payloads were inverted by the atmospheric drag on the fins and the altitude at which the electronics began experiencing sustained high voltage breakdowns in Table 3.4.

Table 3.4

Vehicle	Turnover altitude [km]	Breakdown altitude [km]
18:63	72	83
18:64	65	81
18:65	73	81

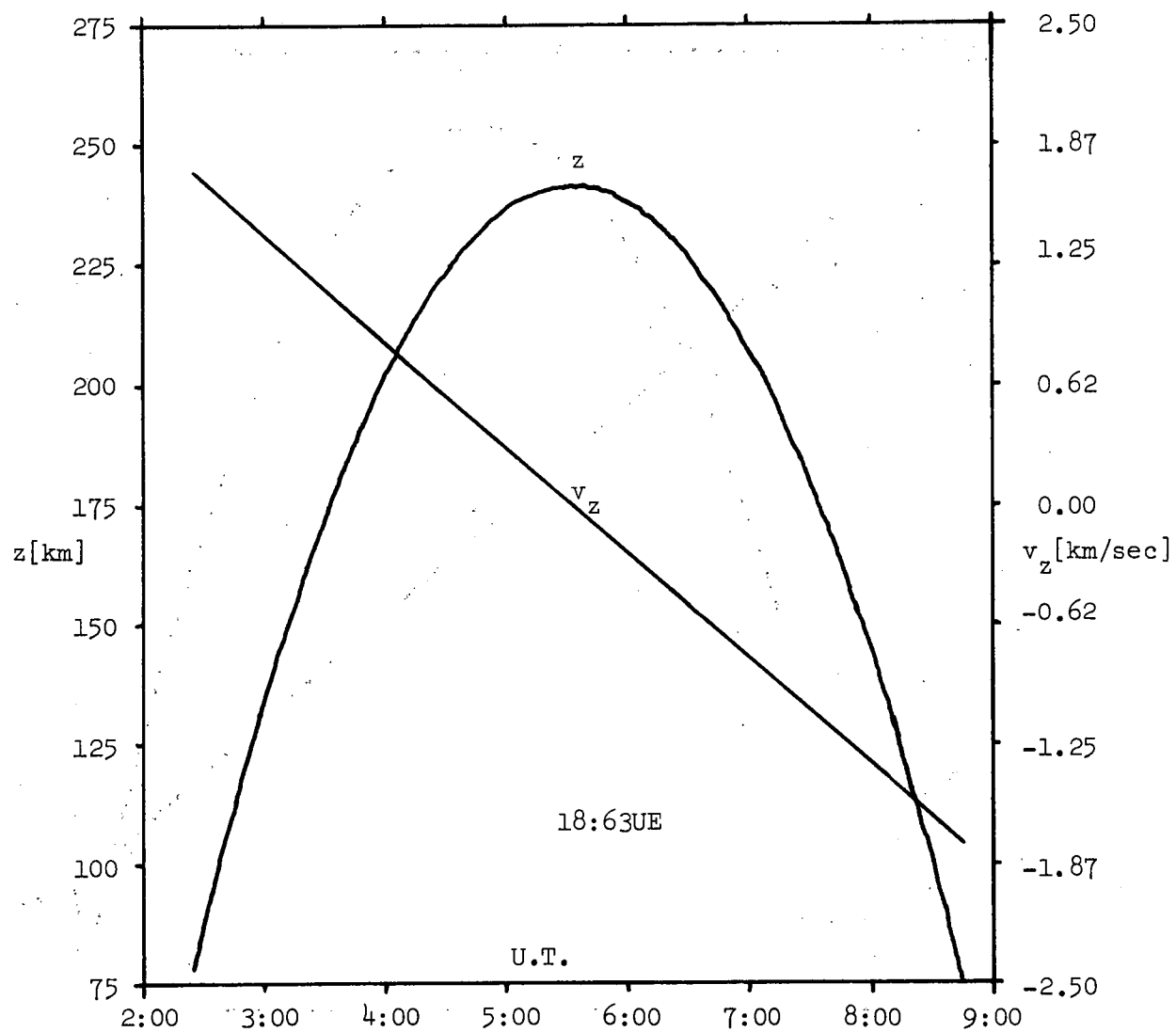


Figure 3.1. Altitude and velocity versus Universal Time.

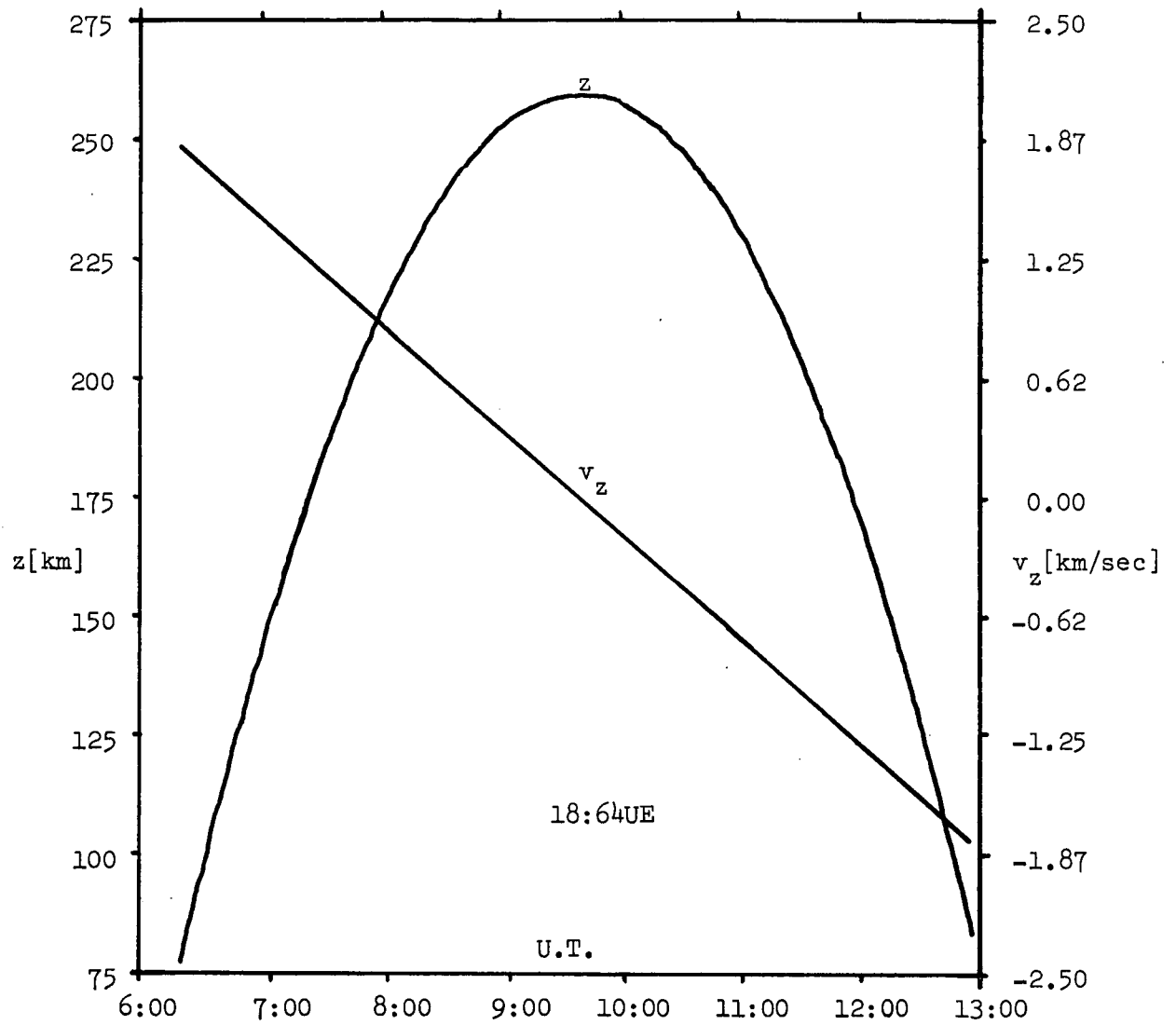


Figure 3.2. Altitude and velocity versus Universal Time.

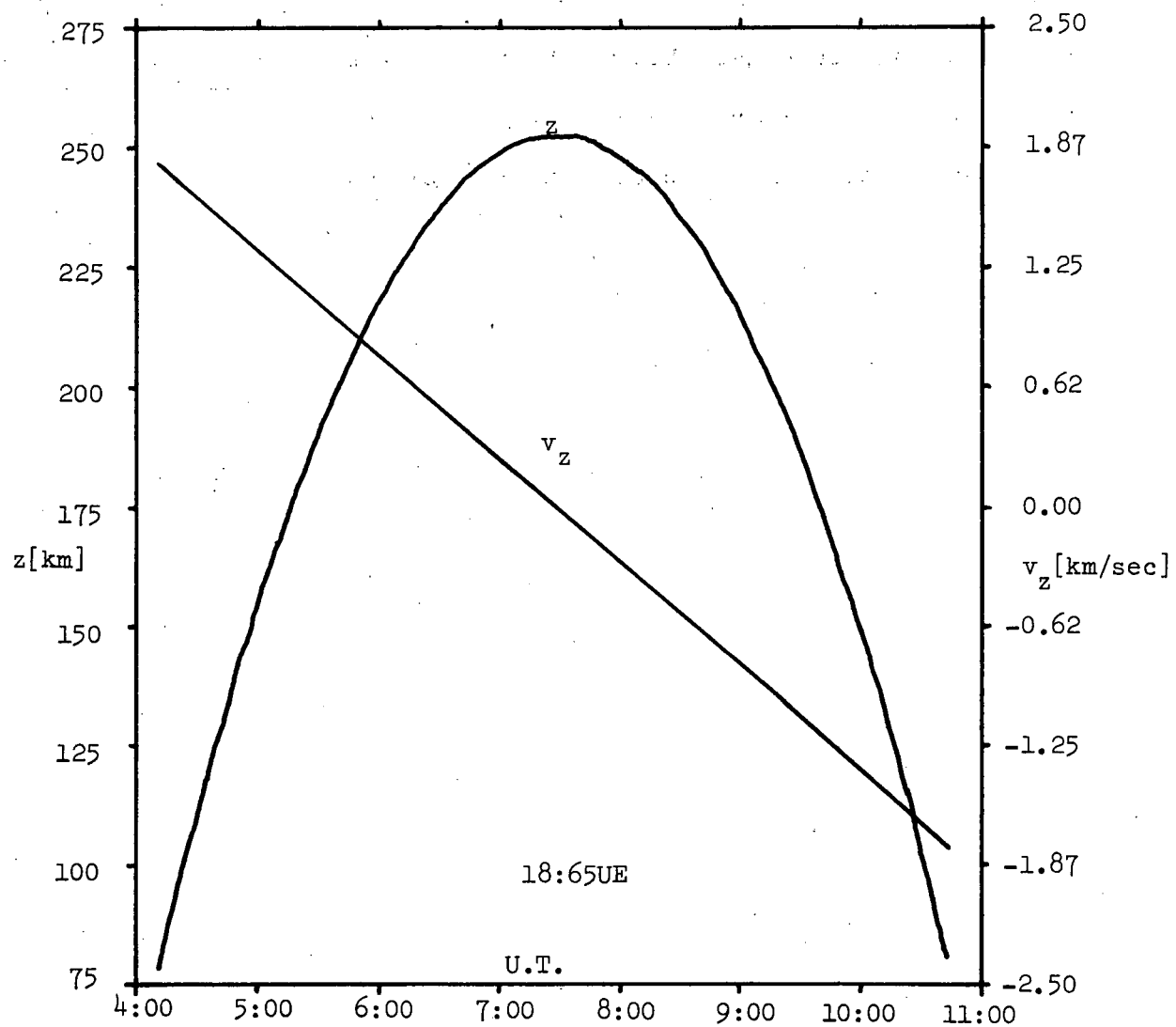


Figure 3.3. Altitude and velocity versus Universal Time.

Because the radar did not track the payloads throughout the flights there may be several kilometer uncertainties in z below about 120 km on the downward leg of the flight. The uncertainty on the upward leg is on the order of 100 meters. It is possible to obtain an exact analytical solution to this problem for t as a function of z , but it would be very difficult to use least squares technique to obtain the initial conditions.

B. Payload Attitude

After despin the payload is sufficiently above the atmosphere to enable one to neglect torques due to atmospheric friction. In the absence of net torques \vec{L} , the total angular momentum vector, is constant in an inertial frame. We will then choose the direction of \vec{L} to be the +z' direction of the space axes for our description of payload attitude. This space set of axes is not the system used to describe position of the payload. More aspect information than supplied by the magnetometers is necessary to relate the two systems.

Barring the unfortunate and rare case where \vec{L} and \vec{B} would be parallel or antiparallel we will use the direction of \vec{B} to provide the other direction necessary for the space axes. Assuming that over the altitude and temporal range of interest \vec{B} is nearly constant in direction we define the x' direction by specifying that \vec{B} lie in the x' - z' plane and that $B_{x'}$, the component of \vec{B} parallel to x', be negative. In a simplified case where \vec{L} is in the local vertical direction and the magnetic declination is zero this coordinate system would have the x' axis pointing south (equatorward from Churchill) and the y' axis pointing eastward because the magnetic field is in the northward direction. Figure 3.4 represents this simplified case. In this coordinate system we can describe the magnetic field as

$$\vec{B} = B_0(t) \hat{b} = B_{x'}(t) \hat{i}' + B_{z'}(t) \hat{k}' = B_0(t) [\sin \beta \hat{i}' + \cos \beta \hat{k}'] \quad (3.11)$$

where the magnitude of \vec{B} , $B_0(t)$, does have the altitude dependence, through t, and β is the angle between \vec{B} and \hat{k}' , the unit vector along \vec{L} .

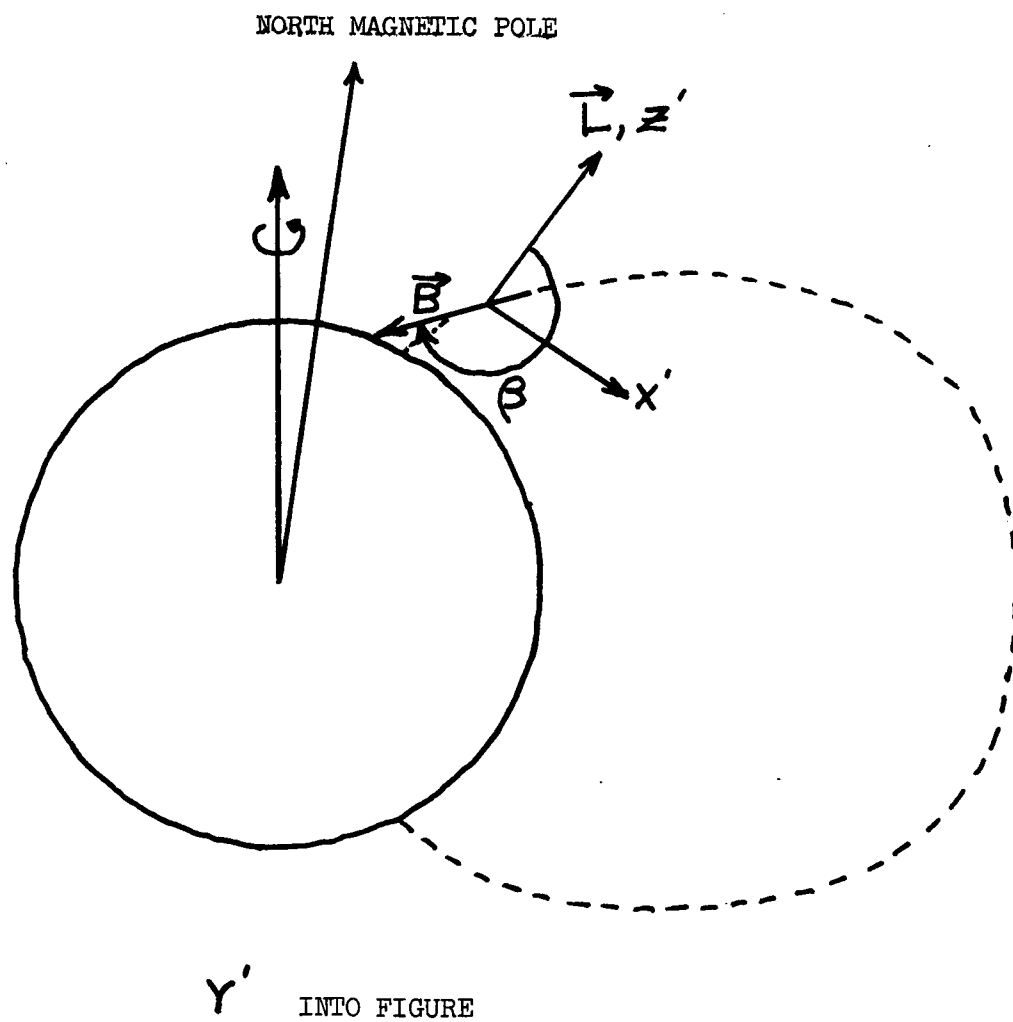


Figure 3.4. Typical orientation of space fixed axes.

By definition of $\hat{i}' \cos \beta < 0$ and for a typical \vec{L} direction $\sin \beta < 0$ so β would lie in the third quadrant.

The body coordinate system, $x'' y'' z''$, is used to describe position and orientation within the payload. We choose the z'' axis to be a principal axis and assume that it coincides with the symmetry axis which describes the axial dimension of the payload parallel to the geometric center line and in the direction of the nose of the payload. The x'' and y'' axes are also principal axes and are assumed along the directions specified by the magnetometers as in Figure 3.5. The origins of the two systems coincide at the center of gravity of the payload.

We define the following Euler Angles: (i) θ , the coning half-angle (the angle between the vehicle spin axis, z'' , and the angular momentum direction, z'), (ii) ϕ , the precession angle, and (iii) ψ , the vehicle spin angle (see figure 3.6).

For time independent moments of inertia and for a rigid body rotating about its center of gravity with body-fixed axes coinciding with the principal axes it can be shown [Goldstein, H., 1950] that the Euler angles can be described by

$$\begin{aligned}\theta &= \theta_0 \\ \phi &= \omega_p t + \phi_0 \\ \psi &= \omega_s t + \psi_0\end{aligned}\tag{3.12}$$

We are now prepared to describe the way the magnetic field, \vec{B} , which is fixed in the space frame will be seen by the magnetometers on board the payload - the body frame.

The magnetometers measure the component of magnetic field parallel

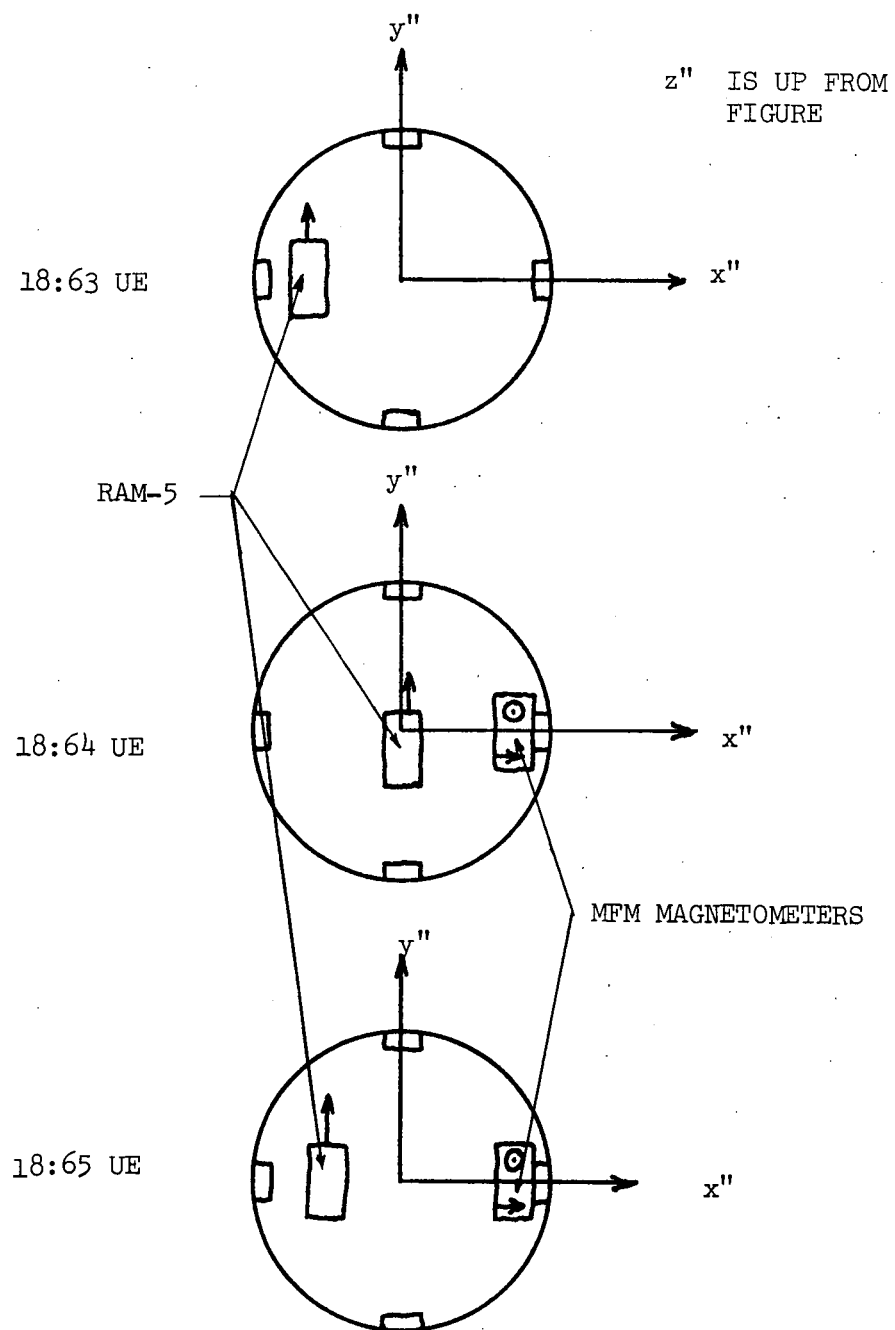


Figure 3.5. Magnetometer positions and body axes.

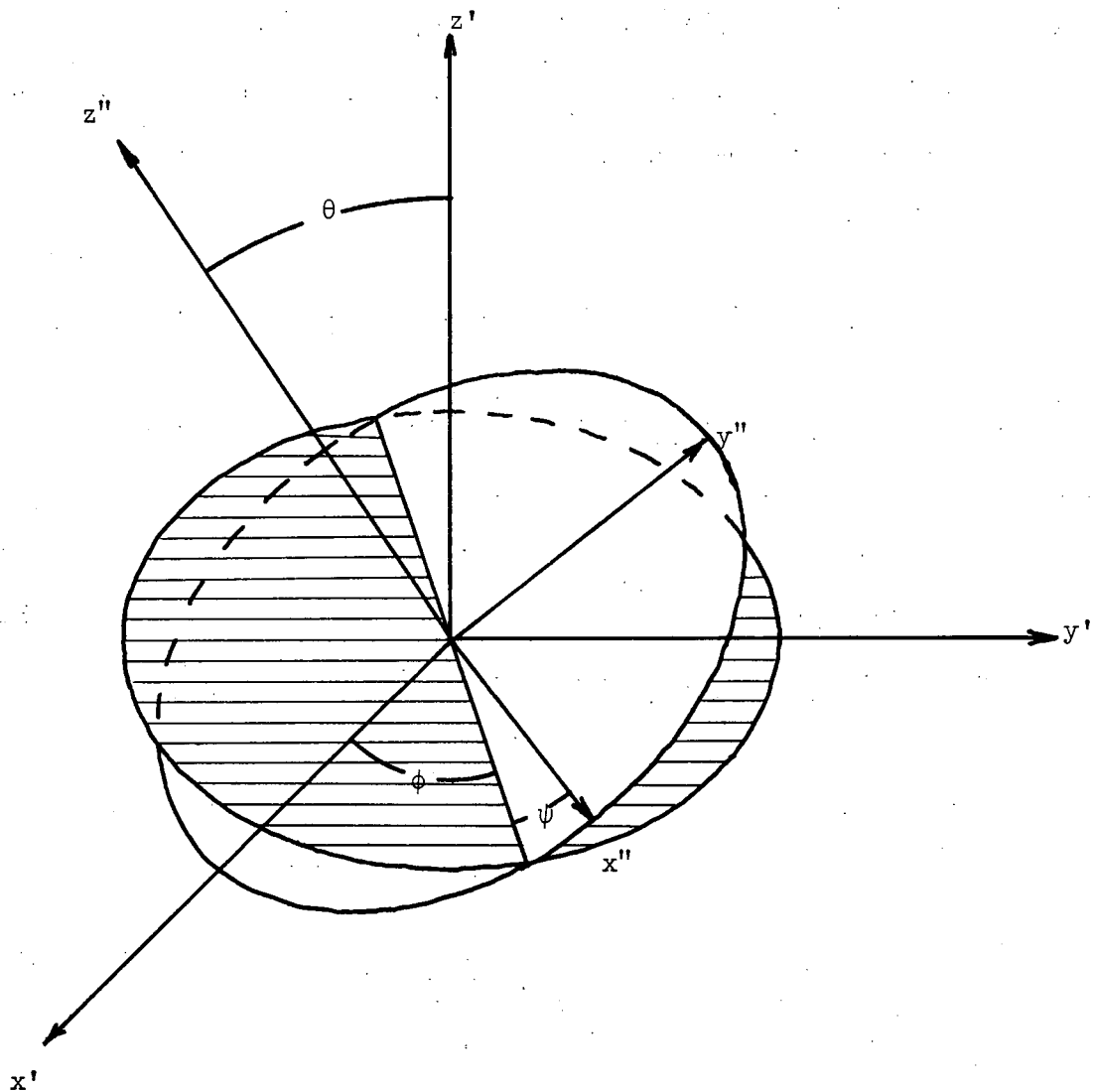


Figure 3.6. Euler angles and the two sets of axes.

to their orientation. They output a bias voltage, CB , of about 2.5 V plus a voltage linearly dependent upon the magnitude of the component of \vec{B} parallel to their orientation. The linear coefficient, CA , is about 4.0V/Gauss. Let \hat{n}_i'' be a unit vector in body frame in the direction measured by the i magnetometer, then the output voltage, V_i , has the form

$$V_i = CA_i \vec{B} \cdot \hat{n}_i'' + CB_i \quad (3.13)$$

Therefore if \vec{B} is antiparallel to \hat{n}_i'' the output is less than CB_i and vice-versa. The analysis used here will assume the form of (3.13) for V_i and neglect non-linear terms.

From (3.13), if \vec{B} and \hat{n}_i'' were measured in the same frame, the output voltage would be a constant term modulated by a cosine term, but alas all is not so simple! We need to know the components of \vec{B} in the body frame to be able to compute the dot product required in (3.13). This transformation, using (3.11), is given by

$$\vec{B}'' = \overleftrightarrow{A} \cdot \vec{B} = B_o(t) \overleftrightarrow{A} \begin{pmatrix} \sin \beta \\ 0 \\ \cos \beta \end{pmatrix} \quad (3.14)$$

where \overleftrightarrow{A} is

$$\overleftrightarrow{A} = \begin{pmatrix} \frac{\cos \psi \cos \phi - \cos \theta \sin \phi \sin \psi}{\sin \psi \sin \theta} & \frac{\cos \psi \sin \phi + \cos \theta \cos \phi \sin \psi}{\cos \psi \sin \theta} & \frac{-\sin \psi \cos \phi - \cos \theta \sin \phi \cos \psi}{\cos \theta} \\ \frac{-\sin \psi \cos \phi - \cos \theta \sin \phi \cos \psi}{\sin \theta \sin \phi} & \frac{-\sin \psi \sin \phi + \cos \theta \cos \phi \cos \psi}{- \sin \theta \cos \phi} & \frac{\sin \psi \sin \theta}{\cos \theta} \end{pmatrix} \quad (3.15)$$

Equation (3.14) then becomes

$$\vec{B}'' = \vec{A} \cdot \vec{B} = B_{x''} \hat{i}'' + B_{y''} \hat{j}'' + B_{z''} \hat{k}'' \quad (3.16)$$

where

$$\begin{aligned} B_{x''} &= B_0(t) [\sin \beta (\cos \psi \cos \phi - \cos \theta \sin \phi \sin \psi) + \cos \beta \sin \psi \sin \theta] \\ B_{y''} &= B_0(t) [\sin \beta (-\sin \psi \cos \phi - \cos \theta \sin \phi \cos \psi) + \cos \beta \cos \psi \sin \theta] \\ B_{z''} &= B_0(t) [\sin \beta \sin \theta \sin \phi + \cos \beta \cos \theta] . \end{aligned} \quad (3.17)$$

Now one can compute the dot products for the three possible magnetometers measuring the x'' , y'' , z'' components of the field. For the x'' component, $\hat{n}_{i''}$ in (3.13), is \hat{i}'' and

$$\begin{aligned} \vec{B}'' \cdot \hat{n}_{x''} &= B_0(t) [\sin \beta \cos \psi \cos \phi - \sin \beta \cos \theta \sin \phi \sin \psi + \\ &\quad + \cos \beta \sin \psi \sin \theta] . \end{aligned} \quad (3.18)$$

For the y'' component, $\hat{n}_{i''}$ is \hat{j}'' and

$$\begin{aligned} \vec{B}'' \cdot \hat{n}_{y''} &= B_0(t) [-\sin \beta \sin \psi \cos \phi - \sin \beta \cos \theta \sin \phi \cos \psi + \\ &\quad + \cos \beta \cos \psi \sin \theta] . \end{aligned} \quad (3.19)$$

For the z'' component $\hat{n}_{i''}$ is \hat{k}'' and

$$\vec{B}'' \cdot \hat{n}_{z''} = B_0(t) [\sin \beta \sin \theta \sin \phi + \cos \beta \cos \theta] . \quad (3.20)$$

To simplify these equations we define

$$\begin{aligned}
 a &= \sin \beta \sin \theta \\
 b &= \cos \beta \cos \theta \\
 c &= \sin \beta \cos \theta \\
 d &= \cos \beta \sin \theta \\
 e &= d - c \sin \phi \\
 f &= \sin \beta \cos \phi .
 \end{aligned}
 \tag{3.21}$$

We shall restrict ourselves to the case where \vec{L} is upward rather than downward over Churchill. This is the condition before despin and it is improbable that despinning could invert the payload angular momentum vector. For 18:64 and 18:65 the z'' axis magnetometers indicate that \vec{L} remained nearly vertical. This assumption puts β in the third quadrant and makes the first four quantities defined in (3.21) negative.

The resulting equations are

$$\vec{B}'' \cdot \hat{n}_{x''} = B_0(t) [e \sin \psi + f \cos \psi] \tag{3.22}$$

$$\vec{B}'' \cdot \hat{n}_{y''} = B_0(t) [e \cos \psi - f \sin \psi] \tag{3.23}$$

$$\vec{B}'' \cdot \hat{n}_{z''} = B_0(t) [a \sin \phi + b] . \tag{3.24}$$

We choose t in equation (3.12) to be zero at a time when the payload (and z'' axis) is most antiparallel to \vec{B} (when z'' is nearest $-\vec{B}$). This means that equation (3.24) is at a minimum value indicating ($a < 0$) that $\sin \phi$ is unity, hence

$$\begin{aligned}
\phi(t = 0) &\equiv \phi_0 = \pi/2 \\
e_0 &\equiv e(t = 0) = d - c \\
f_0 &\equiv f(t = 0) = 0 .
\end{aligned}
\tag{3.25}$$

Because ϕ varies much slower than ψ one can also require that $t = 0$ be chosen at a time where $V_{y''}$, the voltage from y'' - axis magnetometer (the RAM-5) is less than $CB_{y''}$ - the bias value. This means that (3.23) is at a minimum value at $t = 0$. Recalling that $f_0 = 0$ determines ψ_0 to be 0 or π depending upon the sign of e_0 . Because c and d are typically both negative we can define a positive quantity, g ,

$$g \equiv c/d = \tan \beta / \tan \theta . \tag{3.26}$$

If $g > 1$, then $e_0 > 0$ and $\psi_0 = \pi$ and if $g < 1$, $e_0 < 0$ and $\psi_0 = 0$. Since β is in the third quadrant (3.26) implies that if $\beta - \pi > \theta$, $\psi_0 = \pi$ whereas if $\beta - \pi < \theta$, $\psi_0 = 0$. When $\beta - \pi > \theta$ the payload precession cone does not include \vec{B} and when $\beta - \pi < \theta$ the precession cone does include \vec{B} . Hence, if the payload precesses around \vec{B} , $\psi_0 = 0$ and if the payload does not precess around \vec{B} , $\psi_0 = \pi$. Figures 3.7 and 3.8 show the two cases.

We will now outline the procedure for determining the two constant angles θ and β . We have measured the times and voltages at local maxima and minima on the y'' - axis magnetometer and x'' - axis magnetometer for 18:64 and 18:65 respectively. 18:63 had only the y'' - axis magnetometer. For 18:64 and 18:65 we made detailed, simultaneous measurements from all three magnetometers during the several second

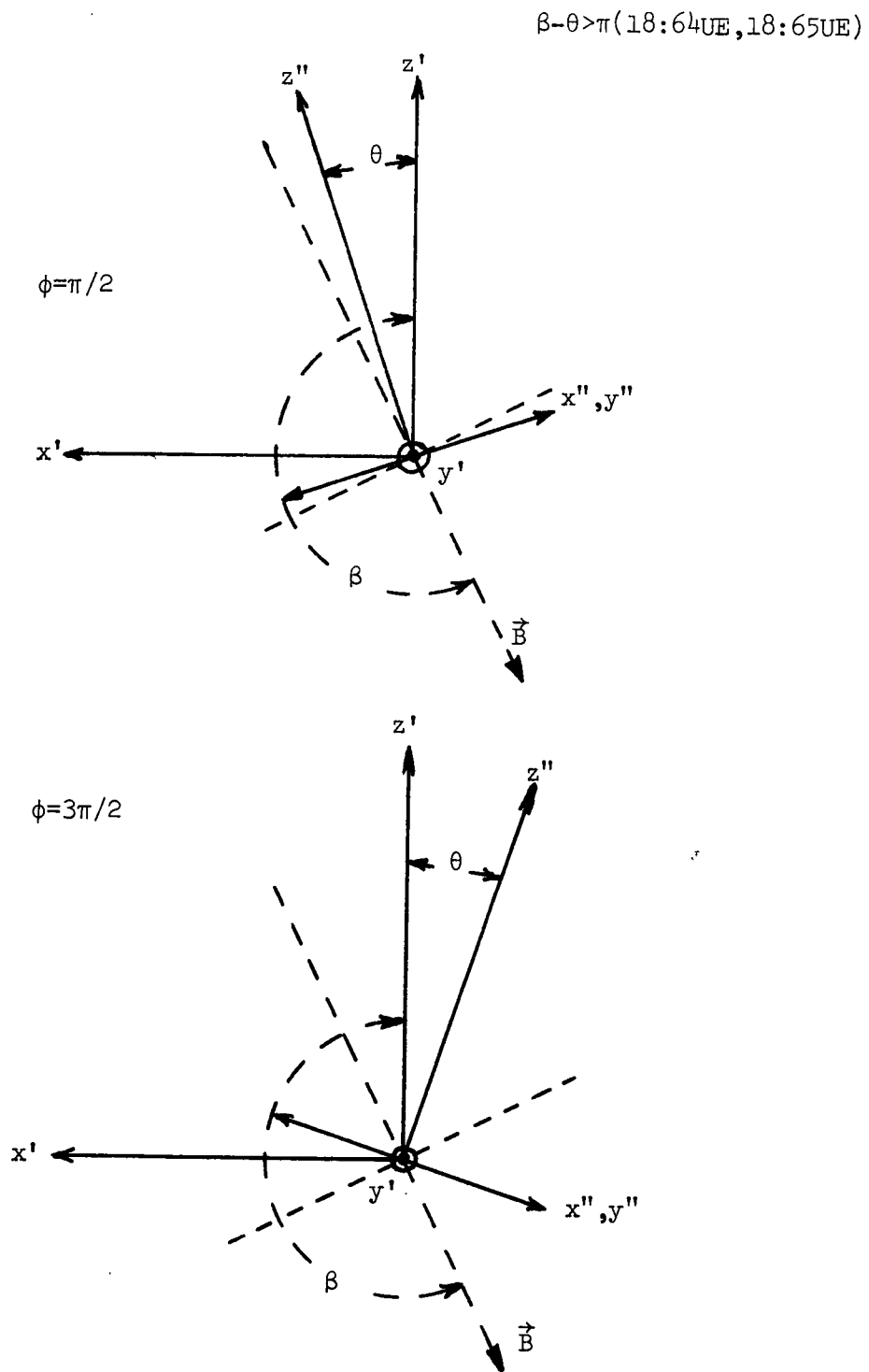


Figure 3.7. Relative positions when coning angle does not contain \vec{B} .

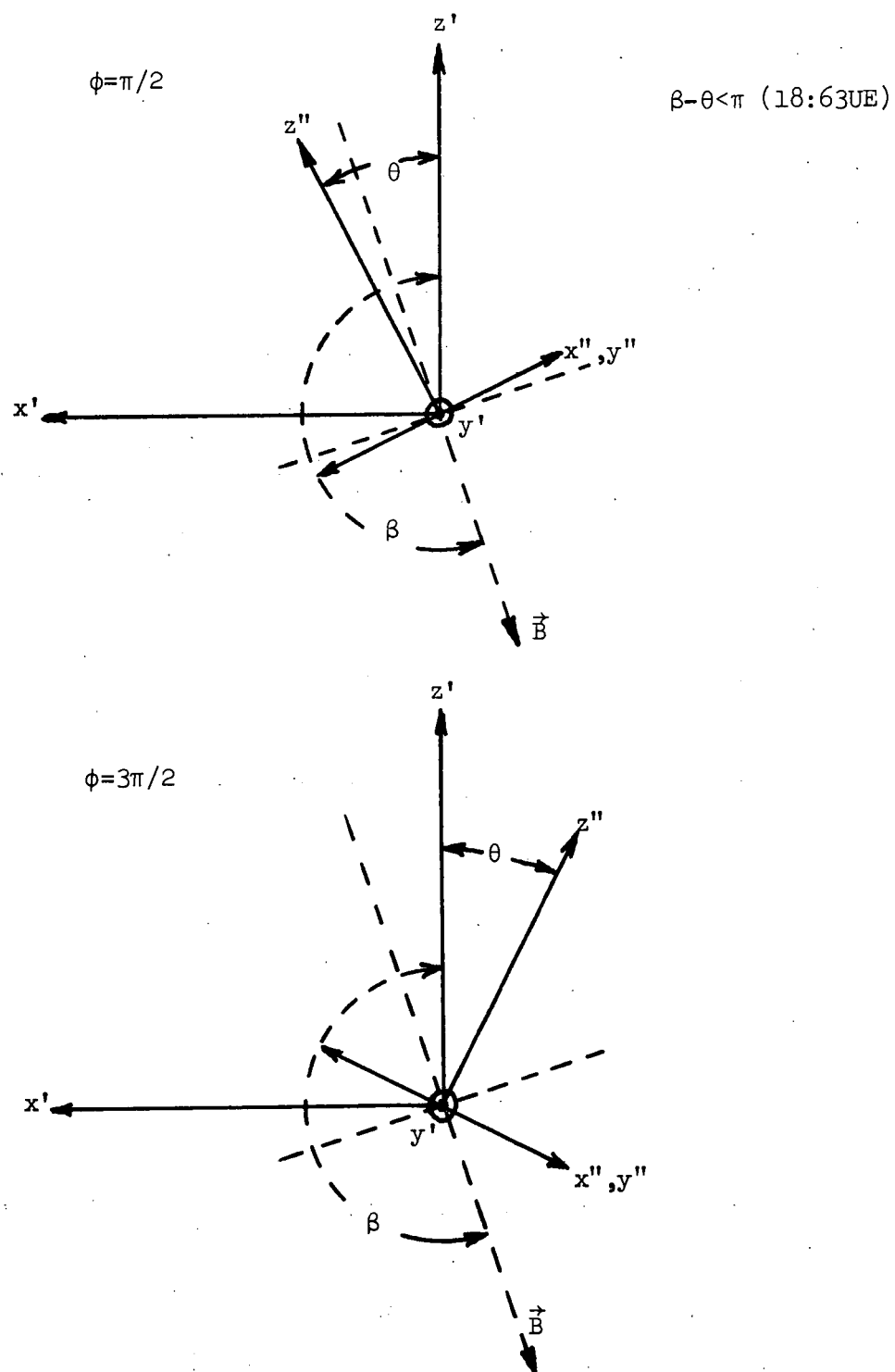


Figure 3.8. Relative positions when coning angle does contain \vec{B} .

time interval where the payloads turned over and all three magnetometers sampled a full range of values. Taking advantage of the fact that the magnitude of the field was nearly constant over this short time interval we were able to make self-consistent checks on the calibrated values of the CA's and CB's.

We also picked several times encompassing the complete altitude range where we simultaneously measured the voltage output from all three magnetometers. Using the calibrations we converted these voltages into values for the magnetic field components parallel to the three axes. We then summed the components to obtain the field magnitudes.

$$B_o(t) = [B_{x''}^2(t) + B_{y''}^2(t) + B_{z''}^2(t)]^{1/2}, \quad (3.27)$$

over a range of altitudes. We found that we could model the altitude dependence as

$$B_o(t) = B_o(z(t)) = \frac{B_\infty}{(R_E + z(t))^3} \quad (3.28)$$

as would be expected for a dipole field model.

The next step is to look at the components of \vec{B} which are parallel and perpendicular to the payload spin axis, z'' . Let α be the instantaneous angle between the z'' axis and \vec{B} , then we define

$$\begin{aligned} B_\perp &\equiv |\vec{B}| \sin \alpha \\ B_\parallel &\equiv |\vec{B}| \cos \alpha \\ |\vec{B}| &\equiv (B_\perp^2 + B_\parallel^2)^{1/2} = B_o(t) . \end{aligned} \quad (3.29)$$

Since we measure x'' or y'' magnetometer voltages only at their local maxima or minima the corresponding y'' or x'' magnetometers are perpendicular to B_{\perp} and measure no field at these times. Hence, by measuring the voltages at local maxima and minima we know that they correspond to the instantaneous value of B_{\perp} . The import of this is that in general the dot product in (3.13) for the x'' magnetometer is

$$\vec{B} \cdot \hat{n}_{x''} = B_{x''}$$

which is only some part of B_{\perp} , but at the special times we measured $V_{x''}$ we have

$$\vec{B} \cdot \hat{n}_{x''} = B_{x''} = B_{\perp} = B_o(t) \sin \alpha.$$

To generalize let m refer to the indices x'' or y'' when y'' or x'' respectively are perpendicular to the field, then (3.13) becomes

$$V_m = CA_m B_o(t) \sin \alpha + CB_m. \quad (3.30)$$

Equation (3.30) has only $\sin \alpha$ unknown. It can be solved for $\sin \alpha$ and then for $\cos \alpha$,

$$\cos \alpha = \pm \left[1 - \frac{(V_m - CB_m)^2}{(CA_m B_o(t))^2} \right]^{1/2}. \quad (3.31)$$

We will choose the negative sign in (3.31) when we can tell from the envelope of the values of V_m that the z'' axis is still above the magnetic horizon. This will be discussed in further detail later.

Of course, $\cos \alpha$ is very easy to compute from the output of the z'' - axis magnetometer,

$$V_{z''} = CA_{z''} B_o(t) \cos \alpha + CB_{z''}$$

$$\cos \alpha = \frac{V_{z''} - CB_{z''}}{CA_{z''} B_o(t)} \quad (3.32)$$

here there is no ambiguity about the sign of $\cos \alpha$.

Comparison of (3.13), (3.24) and (3.32) shows that

$$\cos \alpha = b + a \sin \phi. \quad (3.33)$$

By inspection of the envelope curve for a node or by finding minima in B_{\perp} one can determine the Universal Time, t_o , where the z'' axis is closest to $-\vec{B}$ and the voltage is a local minimum. The time to the next similar node gives τ_p , the precession period. One can then write ϕ

$$\phi = \left(\frac{2\pi}{\tau_p} \right) t + \phi_o \quad (3.34)$$

where $t = t^* - t_o$ and $\phi_o = \pi/2$ and t^* is Universal Time.

Armed with an expression for ϕ one can perform a least squares fit to equation (3.33) to determine the constants a and b . Using the first two equations of (3.23) we found two pairs of β and θ ($a < 0$, $b < 0$). One pair, β_1 and θ_1 , corresponds to a precession cone not including \vec{B} and the other pair, β_2 and θ_2 , does correspond to z'' - axis precession around \vec{B} .

Vehicle 18:63 had only a y'' - axis magnetometer which was shifted upwards in $CB_{y''}$ and consequently for much of the flight local maxima of $V_{y''}$ were greater than the telemetry voltage limit. We also suffered some telemetry dropouts which unfortunately coincided in time

with the local maxima and minima of $V_{y''}$ further hampering data reduction. To fill the gaps where $V_{y''}$ could not be measured at local minima or maxima we decided to use the values of local maxima or minima of $V_{y''}$ which were reconstructed from the slope of $V_{y''}$ evaluated at $CB_{y''}$. We had about 90 directly measured values and about 50 indirectly measured values of $V_{y''}$ with some overlapping to check the accuracy of the slope reconstruction method.

Using (3.13) and (3.25) we have

$$V_{y''} = CA_{y''} B_0(t) [e \cos \psi - f \sin \psi] + CB_{y''} . \quad (3.35)$$

The expression in brackets can be written

$$[e \cos \psi - f \sin \psi] = h \sin (\psi_0 - \psi) \quad (3.36)$$

where $h^2 = e^2 + f^2$ and $\tan \psi_0 = e/f$. Taking advantage of the fact that $B_0(t)$, e and f are nearly constant over a few spin periods one can compute the derivative of (3.35),

$$\begin{aligned} \frac{\partial V_{y''}}{\partial t} &= CA_{y''} B_0(t) h \cos (\psi_0 - \psi) (-\dot{\psi}) \\ &= -CA_{y''} B_0(t) h \dot{\psi} \cos (\psi_0 - \psi) . \end{aligned} \quad (3.37)$$

But we measured the slope where $V_{y''} = CB_{y''}$ which meant that $\psi_0 - \psi = n\pi$ and consequently $\cos (\psi_0 - \psi) = \pm 1$. This means that we can solve (3.37) for h in terms of known quantities ($\dot{\psi}$ is the spin frequency which for 18:63 could be directly measured by a few percent),

$$h = \mp \left(\frac{\partial V_{y''}}{\partial t} \right)_{V_{y''} = CB_{y''}} / CA_{y''} B_0(t) \dot{\psi} . \quad (3.38)$$

But at a time $\pm \tau_s/4$ from where $V_{y''} = CB_{y''}$ the angle ψ will change to where $\sin(\psi_0 - \psi) = \pm 1$ and we can substitute the value of h from (3.38) into (3.35) - (3.36) to get

$$V_{y''} = \mp \left(\frac{\partial V_{y''}}{\partial t} \right)_{V_{y''} = CB_{y''}} / \dot{\psi} + CB_{y''} \quad (3.39)$$

Therefore by measuring the slope and spin rate we were able to reconstruct values to give the correct envelope voltages to use in determining θ and β . This method was checked in several overlap regions by measuring both the slope and local maxima and minima and the results agreed to within 4%.

Normally the envelope of local maxima-minima voltages will exhibit nodes with the frequency of the precession of z'' about \vec{L} . These nodes correspond to times where the z'' - axis is nearest to $-\vec{B}$. For 18:63 secondary nodes between precession period nodes indicated that the z'' - axis had dropped below the magnetic horizon giving the envelope primary nodes when $\phi = \pi/2 + 2n\pi$ and secondary nodes when $\phi = 3\pi/2 + 2n\pi$ (see figure 3.9). This was very fortunate giving a built-in calibration of the product $CA_m B_o(t)$ in equation (3.31) at the times when the payload was perpendicular to \vec{B} . Equation (3.33) had $/a/>/b/$ and we varied the amount of time spent below the magnetic horizon to give the best fit to the measured envelope. Figure 3.10 indicates that the fit was very good except when α was near 90° when the telemetry problem was most severe.

By measuring times of adjacent magnetometer maxima and minima one can determine the spin frequency, ω_s , to only about $\pm 4\%$ because (3.35) for example is not a pure sine wave and the time between adjacent

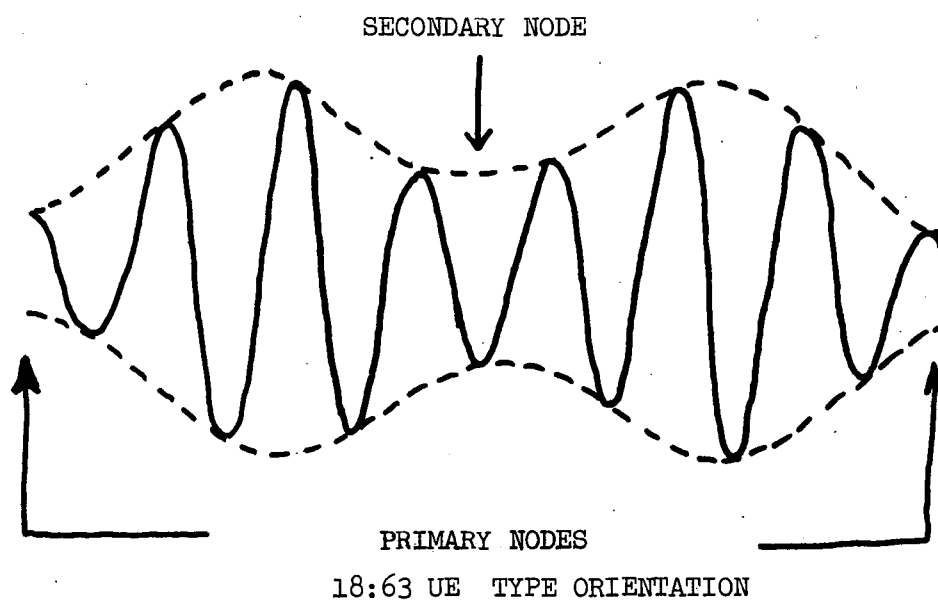
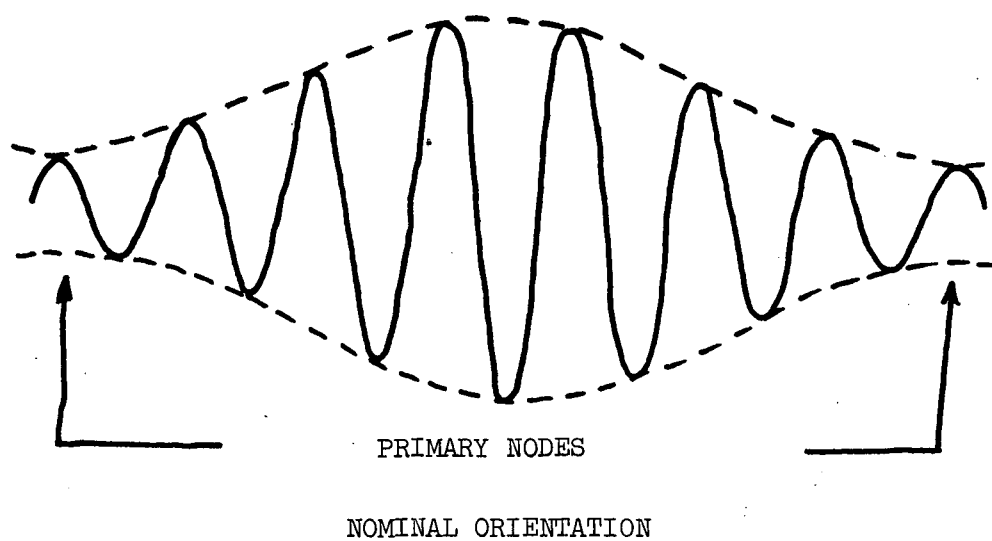


Figure 3.9. Nodes in magnetometer output voltage.

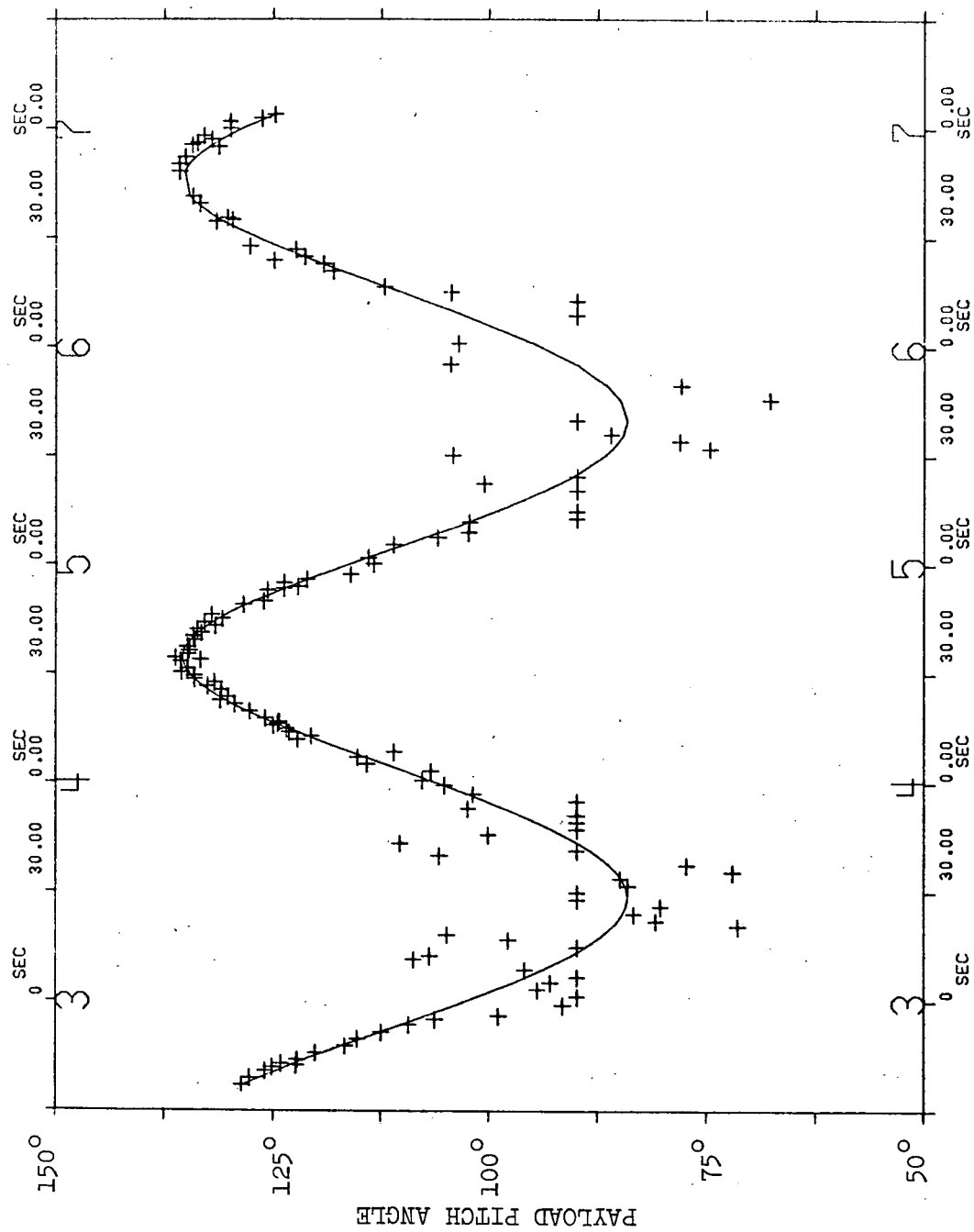


Figure 3.10. Measured and fitted payload pitch angle.

maxima reflects variations in parameters other than ψ alone. To improve this measurement we counted the number of oscillations, n_o , in an approximate precession period (to the nearest complete cycle). We then accurately (± 5 ms) measured the time elapse, Δt , during the n_o oscillations. The hypothesis was then made that ω_s had one of the three values given by

$$\begin{aligned}\omega_{s-} &= \frac{2\pi(n_o-1)}{\Delta t} \\ \omega_{s_o} &= \frac{2\pi n_o}{\Delta t} \\ \omega_{s+} &= \frac{2\pi(n_o+1)}{\Delta t}\end{aligned}\tag{3.40}$$

A computer program was written to make the final determination of the correct set of (θ, β) and ω_s . The procedure involved a double loop which tested the six possible combinations of the ω_s 's and (β, θ) 's in equation (3.22) or (3.23) to predict the times and voltages of the maxima and minima. For each of the three possible ω_s 's both (θ_1, β_1) and (θ_2, β_2) were tested. The procedure was very sensitive in that the five incorrect possibilities had obvious phase shifts from the observed maxima-minima during precession whereas the one correct combination predicted the maxima-minima times to within the measurement error. The results matched the pair (β_1, θ_1) with $\omega_s = \omega_{s+}$ and the pair (β_2, θ_2) had $\omega_s = \omega_{s_o}$.

In order to specify the attitude of the payload with respect to \vec{B} one needs to determine θ , the coning half-angle, β , the angle between \vec{L} and \vec{B} , ϕ , the Euler precession angle and ψ , the Euler spin angle. ϕ is found from the primary nodes in the envelope curves.

The time between them gives τ_p , the precession period. ϕ is found using (3.34). θ and β are found by fitting equations (3.33) for a and b and then simultaneously solving the first two equations of (3.21) for pairs of (θ, β) . The choice of which pair of (θ, β) and which ω_s to use is then determined by testing the possible cases to minimize the phase and amplitude errors between results from equations (3.22) or (3.23) and the measured values.

Tables 3.5 and 3.6 give the frequency-period results and the angular results respectively.

Table 3.5

Vehicle	$T\phi$ (first node)	TP (Precession period)	TS (spin period)
18:63	0604:34.38	131.5 sec	1.93976sec
18:64	0409:38.516	185.751	1.05540
18:65	0306:26.245	199.104	1.06209

Table 3.6

Vehicle	ϕ_0	ψ_0	θ	β	average angle between $\mathbf{z''}$ and $-\vec{B}$	θ, β uncertainty
18:63	$\pi/2$	0	70.2°	205.6°	72°	$\pm 6^\circ$
18:64	$\pi/2$	π	20.50°	203.4°	31°	$\pm 1^\circ$
18:65	$\pi/2$	π	9.023°	193.6°	16°	$\pm 2^\circ$

C. Pitch Angle Determination

When one has determined β and the Euler angles θ , ϕ , and ψ it is possible to determine the pitch angle, α , of a detector at a given time. We define a unit vector \hat{m} in the direction of look of the detector. If Az is the azimuth (measured counterclockwise from x'') of the vector \hat{m} in the $x'' - y''$ plane and EL is the elevation of \hat{m} above this plane (see figure 3.5) we can write \hat{m} as

$$\hat{m} = (\cos EL \cos Az, \cos EL \sin Az, \sin EL). \quad (3.41)$$

This detector accepts particles going in the $\hat{n} = -\hat{m}$ direction. Therefore \hat{n} is given by

$$\begin{aligned} \hat{n} &= (-\cos EL \cos Az, -\cos EL \sin Az, -\sin EL) \\ &\equiv (n_{x''}, n_{y''}, n_{z''}) \end{aligned} \quad (3.42)$$

Equation (3.42) defines $n_{x''}, n_{y''}, n_{z''}$.

We need to determine \vec{B} in the vehicle $x''y''z''$ frame. From equation (3.11) we can determine \vec{B} in the $x'y'z'$ frame. Equations (3.17) provide the components of \vec{B} along the \hat{i}'', \hat{j}'' and \hat{k}'' directions, $B_{x''}, B_{y''}$ and $B_{z''}$ respectively. The dot product of \vec{B} in the $x''y''z''$ frame with \hat{n} gives

$$\begin{aligned} \vec{B} \cdot \hat{n} &= B_o(t) \cos \alpha \\ &= n_{x''} B_{x''} + n_{y''} B_{y''} + n_{z''} B_{z''}, \end{aligned} \quad (3.43)$$

and we can solve (3.43) for the pitch angle α

$$\alpha = \cos^{-1} \left(\frac{n_{x''} B_{x''} + n_{y''} B_{y''} + n_{z''} B_{z''}}{B_o(t)} \right). \quad (3.44)$$

The quantity $B_o(t)$ is common to the values of $B_{x''}$, $B_{y''}$ and $B_{z''}$, and actually α is only a function of Az, EL, β , θ , ϕ and ψ .

As was stated in Chapter II the exact rotation of the brass tube holding the PHA on 18:63 UE was not measured prior to launch. When it was inserted and rotated so that the plane of figure 2.27 was vertical with the off-axis bend pointing up the look azimuth was $183^\circ 25'$ and the look elevation was $41^\circ 50'$. It was rotated towards a smaller azimuth from this value in order to clear the ejectable door. We had to use minima in the particle data to establish the actual value of the 18:63 UE PHA azimuth. We defined a parameter μ which was a measure of the rotation of the brass tube. We then computed the times of minima of counts in channels A and B over various values of the precession angle ϕ . Because for any reasonable values of μ these minima times corresponded to pitch angles greater than 90° (i.e. the detector was essentially looking at upcoming electrons at the time of minima) and because the distributions about the minima were quite symmetric we assumed that the minima times corresponded to the local maxima of the pitch angle. The value of μ which best gave the maximum pitch angle at these times of minima in the counts corresponds to a tube rotation of 60° from the maximum vertical look described above. The effect of the 60° rotation upon the values of the azimuth and elevation of the detector look came from the 25° off axis acceptance shown in figure 2.27. The effect upon the elevation was very small giving an actual value of the elevation angle for the 18:63 UE PHA of 37.8° . The azimuth corresponding to the 60° rotation was 167.9° which agrees with the known direction the tube was rotated. The actual range of the pitch angles measured was virtually the same as for the vertical

case, but the times at which the pitch angle local maxima were measured was shifted by $\sim 4\%$ of the spin period.

CHAPTER IV

DATA REDUCTION TECHNIQUES

We received over 5 million bits of data from the flight of 18:63 UE. In this chapter we will describe how we converted the video recording of the transmitter signal into digital, computer compatible magnetic tape. This tape was analyzed to obtain the actual number of counts in each data word. We then describe a simple computer print-out display technique which allowed one to treat the 5 million bits of data in a finite amount of space and time. The actual values of electron flux, energy spectra, etc. were computed from various methods of averaging the data. We will discuss these averages, their uncertainties and their motivation. The 18:63 UE PHA occasionally measured fluxes so high that the 10 and 12 bit counters were overranged. We will describe our technique for determining the actual number of counts detected.

A. "Spray" Digitizing of FM-FM-PCM Signal

When the signal from the proper track of the video tape recording of the telemetry signal is fed to a discriminator tuned to the frequency of the subcarrier for the PESPEC or PHA the output signal from the discriminator matches the signal sent to the VCO of the subcarrier in the pay load. Digital (Pulse Code Modulation or PCM) data normally has only two voltage levels one referring to a bit being "one" and another referring to a bit being "zero". Assuming that there are sufficient transitions between the two levels it is possible to build equipment which can electronically recreate the original programmer "clock" or basic bit pattern. When some part of the bit string is repeated to provide synchronization each "frame" of the detector electronics output signal can be recreated. This provides an absolute reference for the serial bit pattern, and it can then be converted serial to parallel to give the actual number of counts in each data word. The basic electronic equipment which performs the above task is called a bitsynchronizer. Unfortunately our bit pattern had three voltage levels, and available bitsynchronizers were unable to interpret our data.

We developed a technique to use the computer as a "digital bitsynchronizer". First we had our data "spray" digitized. By "spray" digitizing we mean a periodic but non-synchronous analog to digital conversion of the voltage levels of our serial bit pattern. If one could recreate the original programmer "clock" signal one could synchronously sample the voltage levels, and one would only need sample at the "clock" frequency to be able to determine whether the bits were "ones" or "zeroes". To provide the equivalent information with the

"spray" digitizing technique one must sample at a frequency ≥ 4 times the "clock" frequency. Figure 4.1 shows the two types of A-D sampling. The digital values of the sampled voltage were recorded on computer compatible digital magnetic tape. The timing track of the video tape was also monitored, and the first two words on each block of the computer tape contained the Universal Time (with millisecond accuracy) of the first voltage sample in the block.

A FORTRAN program was written to function as a "digital bit-synchronizer" and convert the voltage samples into the counts per word. The key element of this program was a pattern recognition section. If one could digitally describe some pattern expected in the data this section would search for it and determine at which sample the pattern started.

If it could not find the pattern in the allotted number of samples it determined at which sample to begin searching when more samples were available. Vehicle 18:63 UE had a very serious telemetry dropout problem, and therefore we had to design the pattern recognition section to allow some noise values of the data. For the 18:63 UE PESPEC and PHA data we had the pattern recognition section search for the word separation bits or "holes".

When it found one "hole" we used a rough estimate of the ratio of the sampling frequency to the "clock" frequency to compute which samples should contain the next "hole". When it was found one knew that there were 33 (for PESPEC) or 49 (for PHA) bits between them and then one had a reference for the determination of the voltage level of each bit in the word. When the "hole" could not be found we had to increase the number of samples over which the search was made

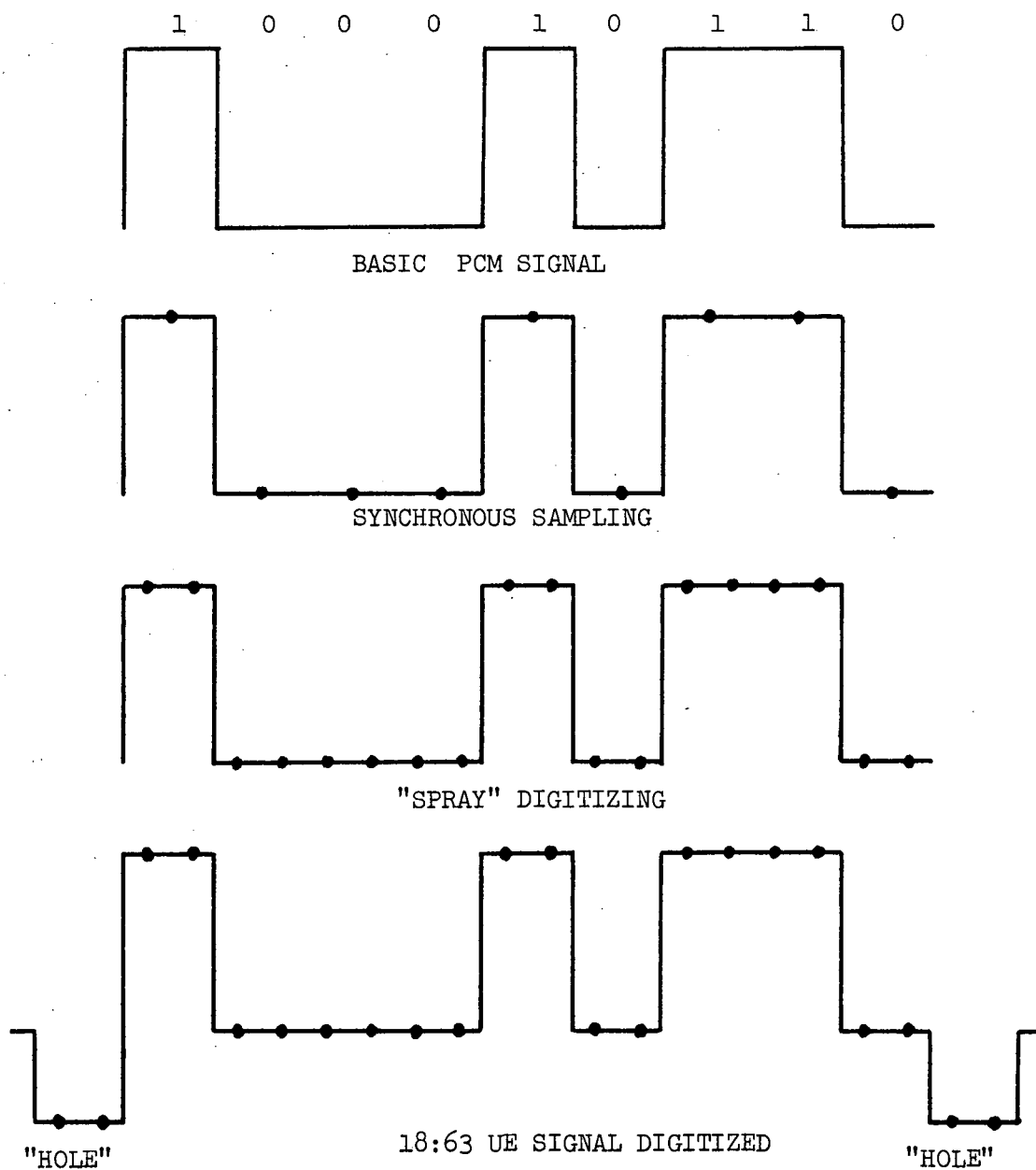


Figure 4.1. A-D sampling of PCM signal.

taking care not to waste time by searching repeatedly over the same samples. When the number of samples was roughly equivalent to the word length and no "hole" was found we assigned a "bad" code to that word and went to the next word.

The 18:63 UE P.H.A. had "frames" equivalent to data words, and therefore we needed no frame pattern search. The bits corresponding to the various channels A, B, C, etc. were located, and the number of counts in each channel were decoded. We were also able to interpolate from the Universal time of the start of each block of the "spray" digitized data tape to determine the Universal Time at which the counts were measured. For the 18:63 UE PESPEC it was necessary to locate the "frame" synchronization words in order to associate the number of counts with the correct portion of the voltage sweep. The interpolated Universal Time was determined only for the beginning of data word number one of each frame.

It was also possible to make a parity check, and when bad parity was discovered we assigned a negative value to the number of counts as a warning. The word or frame (sweep) number, the time and the number of counts in each channel or word were recorded on tape by the computer.

B. Intensity Contour Displays

Confronted with the problem of trying to analyze 5 million bits of information one searches for graphical display techniques. Plotting the number of counts versus time at a rate of 1 second per inch would produce a plot 40 feet long for each of the 29 separate energy channels on the PESPEC. By plotting data from several different energy channels simultaneously one could more easily observe the temporal behavior and correlations between different energies. One must be careful in doing this however because frequently the individual time series plots intersect, and it is sometimes difficult to follow several channels of data at once. Certainly a plot of all 29 separate energy channels simultaneously would be unintelligible.

Basically the data from the 18:63 UE PESPEC had a three dimensional nature. We let $N_i(t_j)$ be the number of counts in data word i at frame beginning time, t_j . The average energy of the electrons counted in data word i can be determined from equation (2.43).

$$(\overline{E}/\overline{E}_{o_i}) = 1 + \left(\frac{C_2}{2}\right) \left(\frac{\overline{E}_{o_i}}{\frac{dj}{dE}(E_{o_i})}\right) r^2 + O(r^4) \quad (2.43)$$

Therefore the three dimensions are the number of counts $N_i(t_j)$, the energy of word i , E_i , and the time t_j . Some caution must be used because successive words at different energies are not measured at the same time with the PESPEC. The result is that the actual time $N_{29}(t_j)$ was measured is closer to the time, $t_j + 1$, which marks the beginning of the count interval for $N_1(t_j + 1)$. (The voltage sweep recharges from its lowest value to its highest value faster than it decays from the peak value to the lowest value.) This minor complication

does not occur in the 18;63 UE P.H.A. data where counts in all energy channels are accumulated simultaneously, and therefore the energy axis is truly orthogonal to the time axis.

For the purpose of allowing one to analyze large amounts of data in an energy-time space one can treat the $N_i(t_j)$ as if all the counts in the j^{th} frame were measured at time t_j . Having resolved this small ambiguity we had to choose a three dimensional display technique. Because it was simple and readily accessible we chose to use the computer printer to display our data. When it was possible to describe the data by

$$Z = f(x,y) \quad (4.1)$$

we were able to graphically display the data. We assigned the various print columns on the printer page to be our y axis. By using integer arithmetic one can convert the y value in equation (4.1) to an integer value, I_y , which designates which column corresponds to the value y . There are over 100 columns on the printer page, and therefore one has ~1% resolution in the y dimension. Similarly the x value in equation (4.1) can be converted to an integer, I_x , which controls the line spacing on the printer page. The intensity of the shading of the print character printed at column I_y , line I_x , can be determined from the value of the dependent variable Z in equation (4.1). By using overprinting we had 25 levels of shading available. This would correspond to ~4% resolution in displaying the dependent variable. By limiting the number of levels of shading one can heighten the contrast.

As an example, to display the counting data using this technique

we adopt the following form of equation (4.1)

$$N_i(t_j) = f(t_j, E_i). \quad (4.2)$$

One could also let the y dimension correspond to pitch angle. Within the accuracy described above this technique is also a very inexpensive and simple technique for producing contour maps. The various contours are drawn between discontinuities in intensity of the print characters. Various techniques similar to ours have been used to display spectrometer data. Frank and Ackerson [1971] used a color code to display the value of Z in equation (4.1). DeForest and McIlwain [1971] and Heikkila, et al [1970] have used levels of gray shading to achieve the same purpose somewhat less spectacularly. However both of these methods do require special equipment.

C. Averaging Techniques

We chose to compute values of energy flux, electron differential number flux, energy spectra, etc. from averaged values of the 18:63 UE PESPEC counting data for three reasons: (i) the lack of sufficient collimation on the exit aperture, which allowed electrons from the wrong slot to be counted, virtually prohibited the assignment of a unique pitch angle to a given measurement (the detector had two acceptance angles and in general they were not the same), (ii) the telemetry dropout problem made it necessary to have an internally consistent method of noise rejection (an average and standard deviation were computed, and if the standard deviation was abnormally large, and if we could find an obvious noise point the average was recalculated omitting the noise point), and (iii) averaging reduced the vast volume of data to a tractable level. Typical value of the number of counts $N_i(t_j)$ was $\sim 10^3$. One would then anticipate (for a Poisson distribution) the uncertainty to be $\sim \pm 30$. A bonus from the averaging was that we could calculate the standard deviations. Because the number of counts was pitch angle dependent and the averages were over various pitch angles the standard deviations were somewhat larger than the Poisson prediction. However in general any fluctuations greater than 5% are real and not statistical.

To be able to describe the various averages we first define:

$PN(t) \equiv$ pitch angle seen by the nominal detector slot at time t .

$PU(t) \equiv$ pitch angle seen by the upper detector slot at time t .

$\alpha(t) \equiv$ pitch angle of the payload spin axis at time t .

$PA(t) \equiv 1/2(PN(t) + PU(t))$, average pitch angle seen by PESPEC at time t .

$DP(t) \equiv PN(t) - PU(t)$, difference between pitch angle seen by nominal slot and pitch angle seen by upper slot at time t .

$t_o \equiv 0604:18.910$ U.T. 21 March, 1968, reference time for computing number of rolls of payload.

$t_{ij} \equiv t_j + (i - 1)0.0034$, actual time of measurement of sample N_i during frame j (t_j is time for start of frame j).

Using t_o we were able to compute a "roll number", n , for some time t_{ij} from

$$n = \frac{(t_{ij} - t_o)}{\tau_s} + 0.5 \quad (4.3)$$

where τ_s is the spin period given in Chapter III. The following averages were computed over a roll period where equation (4.3) was used to determine the "roll number". The subscript i refers to the channel number which ranges from 1 to 29 for the 18:63 UE PESPEC.

$D_i(n) \equiv$ "Dumped" electrons, average value of counts $N_i(t_{ij})$ at roll, n , subject to constraints that $DP(t_{ij}) < 40^\circ$ and $PA(t_{ij}) \leq 45^\circ$.

$M_i(n) \equiv$ "Mirroring" electrons, average value of counts $N_i(t_{ij})$ at roll, n , subject to constraints that $DP(t_{ij}) < 40^\circ$ and $60^\circ < PA(t_{ij}) < 93^\circ$.

$P_i(n) \equiv$ "Precipitating" or "downcoming" electrons, average value of counts $N_i(t_{ij})$ at roll, n , subject to constraints that $PN(t_{ij}) \leq 90^\circ$ and $PJ(t_{ij}) \leq 90^\circ$.

(If $DP(t_{ij})$ were zero this average would include both the dumped and mirroring electrons.)

$U_i(n) \equiv$ "Upgoing" electrons, average value of counts, $N_i(t_{ij})$,

at roll, n , subject to constraints that $PN(t_{ij}) > 90^\circ$
and $PU(t_{ij}) > 90^\circ$.

We also computed the average time at which the averages were measured. For example, $t_D(n, i)$ would be the average value of the t_{ij} used in computing $D_i(n)$. Using equation (4.3) we computed the center time, $t_c(n)$, of each roll

$$t_c(n) = t_o + n * \tau_s . \quad (4.4)$$

In the following definition the superscript "1" will indicate the interpolated value of the average at time $t_c(n)$. These interpolations were performed to normalize the ratios because the various averages were not determined at identical times.

$$A_i(n) \equiv \frac{M_i^1(n)}{D_i^1(n)} , \text{ anisotropy parameter - for an isotropic pitch angle distribution } A_i(n) = 1.$$

$$R_i(n) \equiv \frac{P_i^1(n)}{U_i^1(n)} , \text{ backscatter ratio.}$$

Using figures 4.2 and 4.3 we can better grasp the meanings and limitations of these averages and ratios. The time intervals are 2.5 sec which is slightly more than one roll. The figures are for two different values of $\alpha(t)$ and indicate that the interpretation of the averages may be weakly dependent upon $\alpha(t)$. At the top of each figure we see the values of $PN(t)$ and $PU(t)$. The curves intersect twice per roll where $DP(t)$ is zero. We should also notice that $DP(t)$ is not symmetrical. For these values of α $DP(t)$ is larger when $PA(t)$ goes from maximum to minimum than when $PA(t)$ goes from minimum to maximum. The middle section of each figure shows the values of $PN(t)$ and $PU(t)$

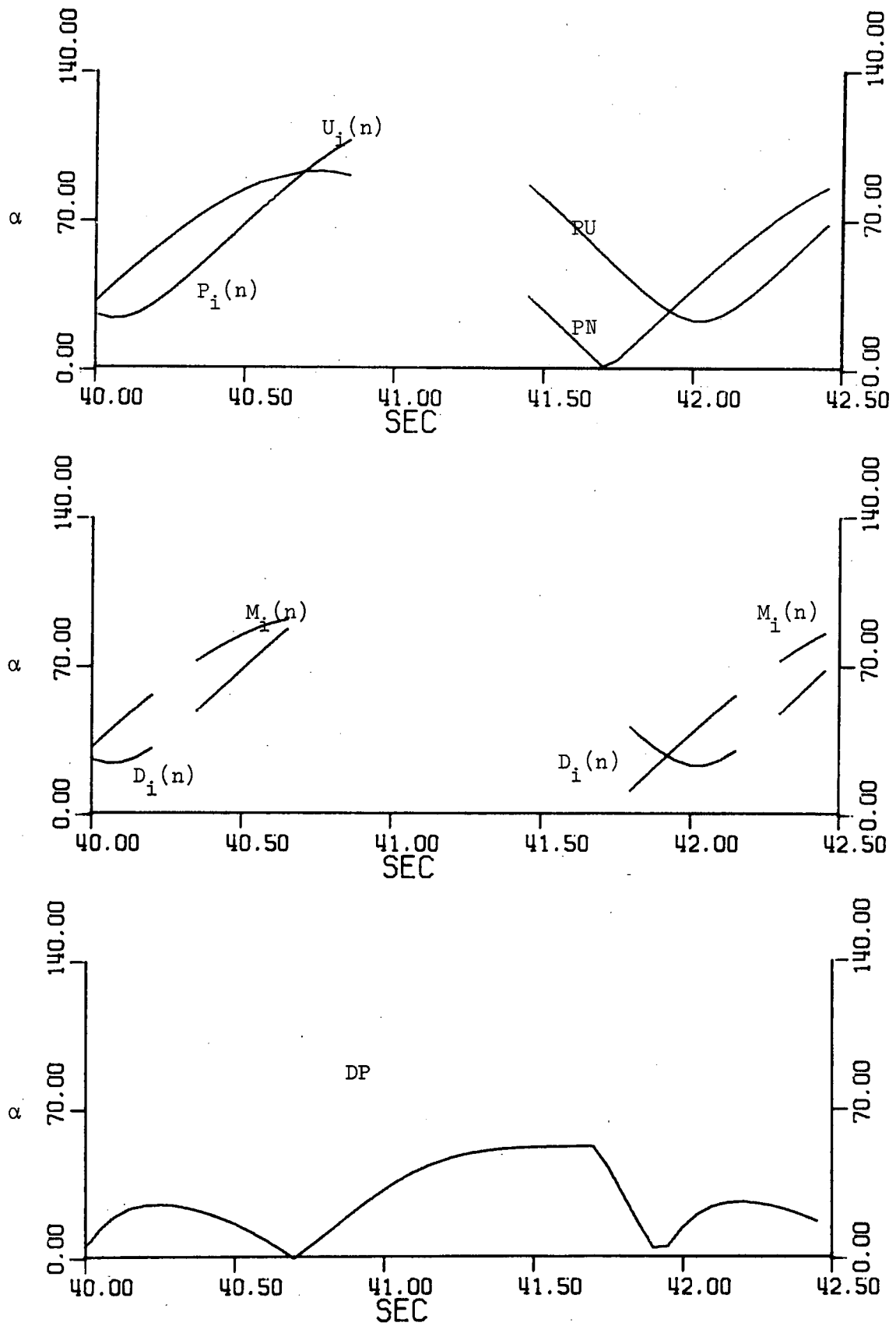


Figure 4.2. Pitch angle intervals used in computing averages.

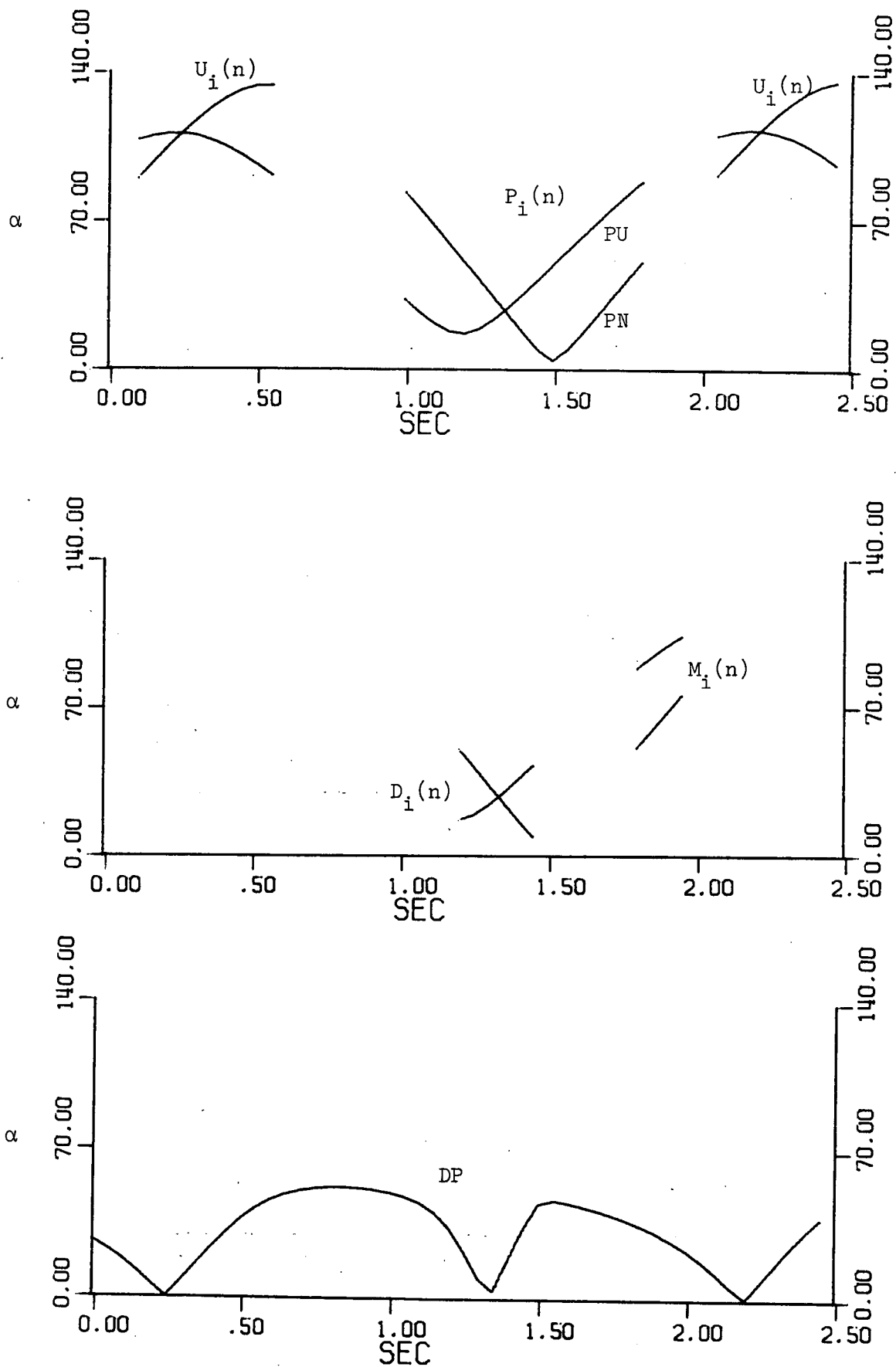


Figure 4.3. Pitch angle intervals used in computing averages.

over which the averages $M_i(n)$ and $D_i(n)$ are calculated. We want to emphasize that the range of pitch angles averaged over to determine $P_i(n)$ is essentially from 0° to 90° , and this range is virtually independent of α . The average value of the pitch angles averaged over in determining $P_i(n)$ as a function of α are shown in figure 4.4. The entire range from 0° to 90° is nearly randomly sampled. This is not the case for the averages $U_i(n)$. For the smaller values of $\alpha(t)$ the range of pitch angles over which $U_i(n)$ is computed is quite small ($\sim 20^\circ$), and the average $U_i(n)$ is determined mostly from pitch angles near 90° . As $\alpha(t)$ increases the range of pitch angles increases, but the upper limit of the range never reaches 180° . See figure 4.4 for the average pitch angle used in determining $U_i(n)$. As a matter of fact pitch angle distributions generally fall off very steeply beyond $\sim 110^\circ$ pitch angle, and therefore even if the level of electron flux were to remain constant the value of $U_i(n)$ would vary with α . Because of this the backscatter ratio, $R_i(n)$, has its most significance in the i or energy dependence at fixed n .

To avoid this problem in computing the anisotropy parameter, $A(i, n)$, we limited the separation between the acceptance directions of the slots $DP(i, n)$ to less than 40° . This facilitates the analysis of the data because we exclude for example the case where $PA(t)$ is 70° because $PN(t)$ is 20° and $PU(t)$ is 120° . We do have some degree of equality between the acceptance directions of the slots. This restriction prohibited the calculation of $M(i, n)$ and $D(i, n)$ for some values of $\alpha(t)$ because no measurements satisfying the constraints were made. There are gaps in the values of $M(i, n)$ near $\alpha(t) = 80^\circ$ and in the values of $D(i, n)$ near $\alpha(t) = 95^\circ$. For $DP(t) < 40^\circ$ one

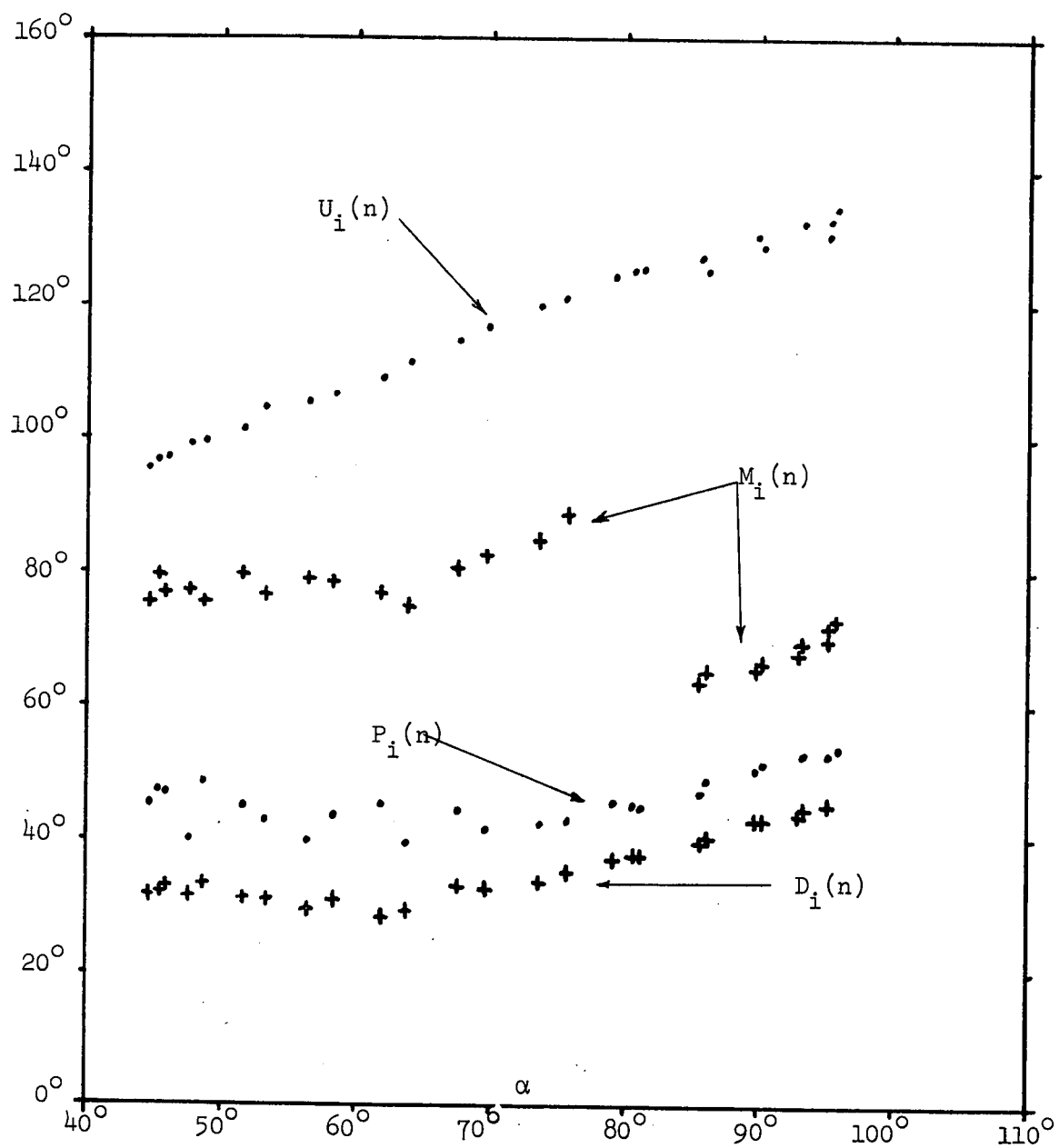


Figure 4.4. Average value of pitch angles averaged over versus α .

can define the anisotropy parameter, $A(i, n)$ for about 75% of the flight. Making the $DP(t)$ constraint more restrictive would have given a more precise interpretation to the anisotropy parameter, but reducing the range to $DP(t) < 30^\circ$ would have allowed us to compute $A(i, n)$ for less than 50% of the flight.

Using figure 4.4 we see that the average value of the pitch angle used in computing $M(i, n)$ is roughly constant. Near $\alpha(t) = 80^\circ$ the average value shifts from being near the upper limit, 93° , to a value near the lower limit, 60° , but in practice the effect of this is nullified because there is a gap in the values of $M(i, n)$ near $\alpha(t) = 80^\circ$. Also one would not expect to see the large variations in the pitch angle distribution between 65° and 85° that one would expect to see between 100° and 130° which can complicate the interpretation of $U(i, n)$. We also emphasize that for $\alpha(t) \lesssim 65^\circ$ there is equal weighting for all pitch angles in the correct interval.

The average value of the pitch angle used in computing $D(i, n)$ has no significant dependence upon $\alpha(t)$ for $\alpha(t) < 75^\circ$. For the larger values of $\alpha(t)$ the pitch angles averaged over tend toward the upper limit of 45° until finally at the maximum value of $\alpha(t)$ one cannot define $D(i, n)$.

We therefore state that the average $P(i, n)$ is unaffected by the value of $\alpha(t)$ and reflects only temporal or spatial changes in the precipitated electron flux. For $\alpha(t) < 70^\circ$ (50% of the flight) the averages $M(i, n)$ and $D(i, n)$ reflect only temporal or spatial changes in the "mirroring" or "dumped" electron flux respectively. For $\alpha(t) > 70^\circ$ one must use caution in interpreting the long term ($\Delta n > 10$) roll variations of $M(i, n)$ and $D(i, n)$. For any value of $\alpha(t)$ the

energy dependence of the anisotropy parameter has significance.

D. Interpretation of Overranges on PHA

On the 18:63 UE PHA when the number of electrons counted during a sample time exceeded the number the counter was capable of storing the counter overranged. For example the channel A counter was a 12 bit counter which meant that it could count $2^{12}-1 = 4095$ counts. This would mean that every bit had the "one" value. Another count detected before the end of the counting interval would reset all the bits to their "zero" value. Subsequent counts detected before the end of the counting interval are then counted normally until the count reaches 4095 when the counter would overrange again and the cycle would repeat itself.

Several times during the flight of 18:63 UE the PHA appeared to be overranging. It is impossible to be absolutely certain a counter is overranging, but there is a characteristic signature which with supporting evidence one can assume to be an overranging. An overrange is generally seen as a sudden drop in the number of counts from a value near the upper limit of the counter to a substantially lower number. For this to be an overrange it should eventually be accompanied by the underranging wherein the number of counts suddenly jumps to a value near the counter limit. One may in fact see more than one overranging before the counter begins to underrange. The identification of an overrange condition is somewhat subjective - generally one expects the data to be continuous and have a continuous slope.

Supporting evidence such as the count profile from a counter which is not overranging is helpful. If the true count rate is increasing or decreasing slowly enough relative to the dynamic range of the counter one will be able to see the number of counts approach the

upper limit slowly and then fall sharply and then build up slowly again. In interpreting the overranges on 18:63 UE PHA we also knew the basic spin period of the payload, and since the count rate was spin modulated we expected the true count rate to be periodic at the payload spin period. We found that except for the most intense precipitation the counters were not overranged when measuring at the maximum pitch angles. Therefore in any given roll period we needed to find an underranging to match each assumed overranging.

Figure 4.5 is a plot of the number of counts in channel A versus time near 0604:55. We believe that the very sharp drops and jumps represent overranges and underranges respectively. We have developed a graphical technique to facilitate determining the true count profile. We begin with actual number of counts, $N_0(t)$, and compute the possible overranged values

$$N_k(t) = N_0(t) + k*4096 \quad (4.5)$$

for k , which is the degree of overranging, from $k = 1, \dots, 5$.

Using different symbols for each value of k we plot all the $N_k(t)$ ($k = 0, 5$)(see figure 4.6). Knowing that the $N_0(t)$ value is correct at the beginning and end of the plot it is rather simple to trace out the correct time profile by eye which a very good instrument for preserving the continuity of value and slope through the overranges.

Figure 4.7 is a plot of the accepted values.

We feel that we have correctly determined all the overranges on the 18:63 UE PHA channel A data. Because it had a smaller dynamic range (only a 10 bit counter) we feel that we cannot correctly determine some of the overranges on channel B. Channel C overranged only

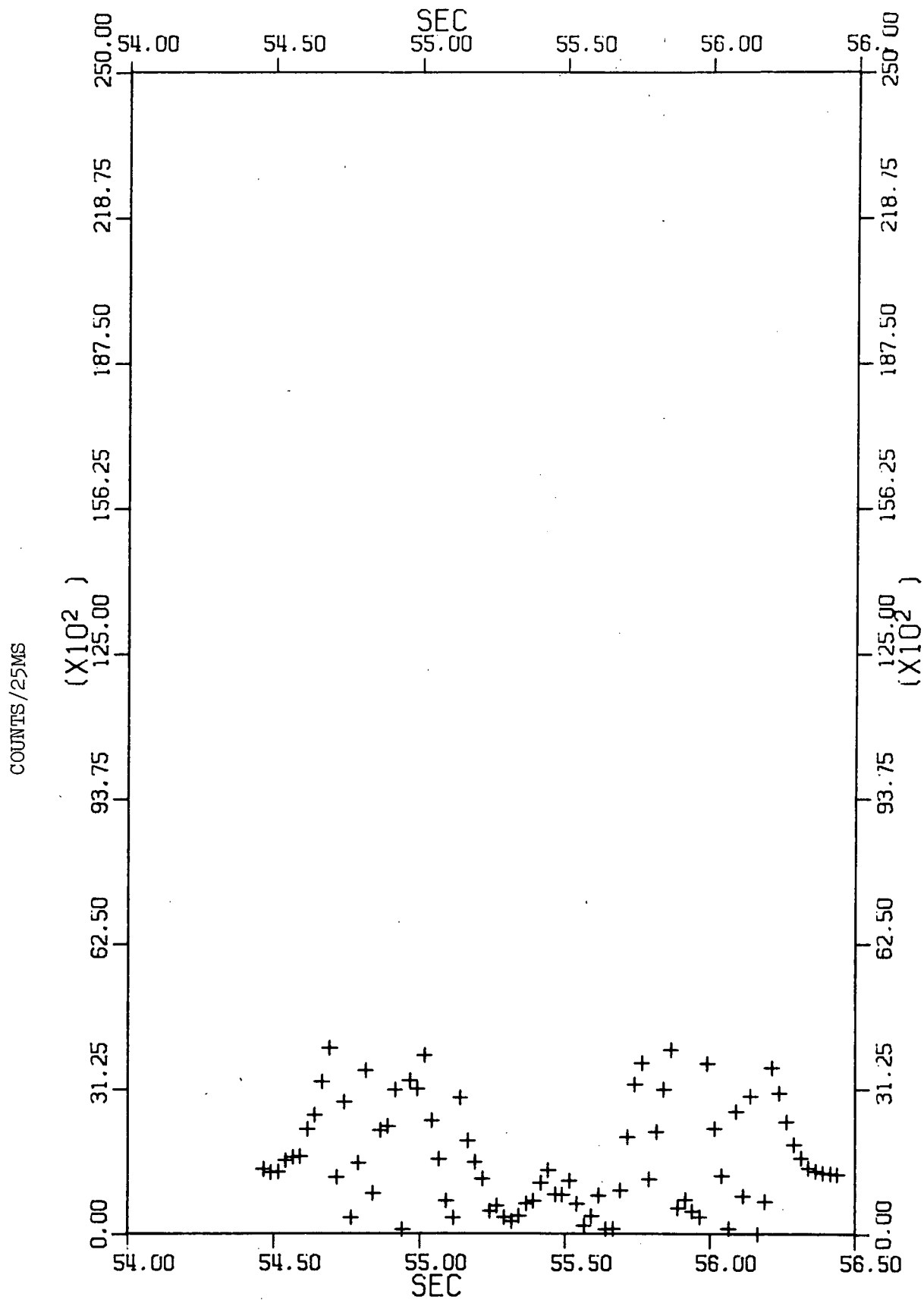


Figure 4.5. Counts in channel A before overrange correction.

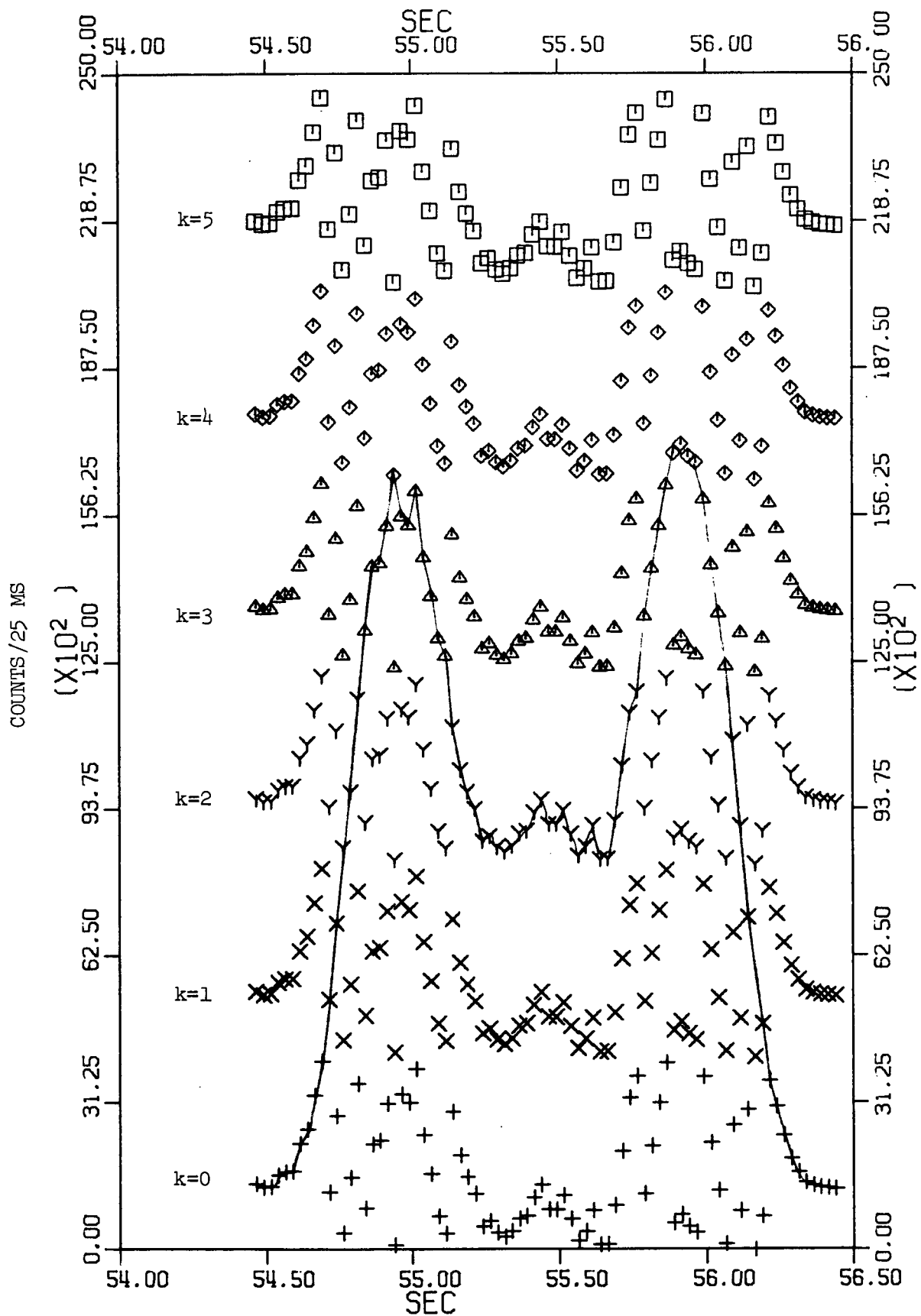


Figure 4.6. Various overrange possibilities and line which preserves continuity and smoothness.

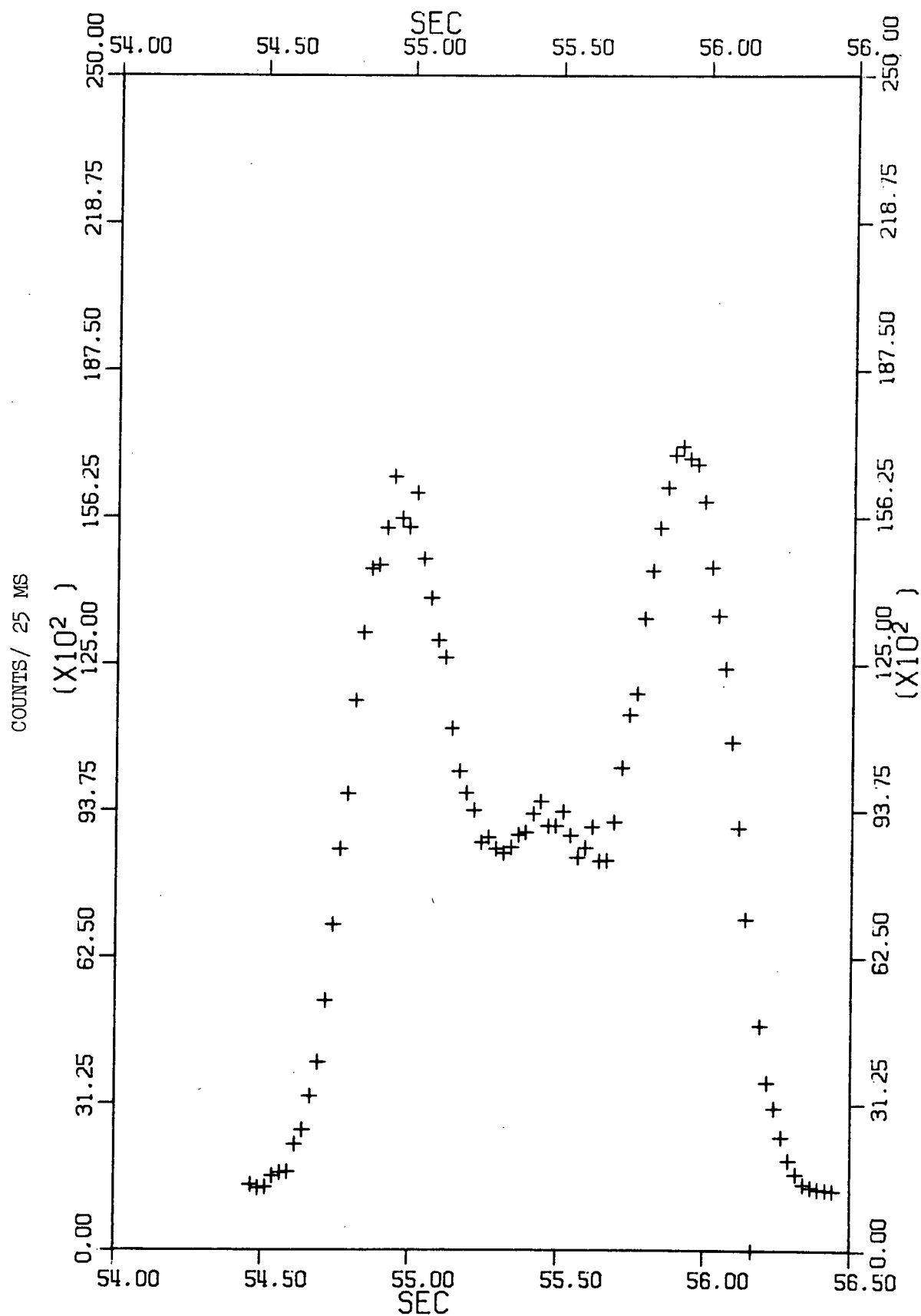


Figure 4.7. Accepted values corrected for overranging.

about 5 times out of more than 30,000 measurements, and they were rather trivial to identify.

CHAPTER V

GENERAL OBSERVATIONS - 18:63 UE

In this chapter we will describe the gross spatial and temporal features associated with the flight of vehicle 18:63 UE. We will begin by presenting some solar wind parameters because the solar wind is probably the most removed of the direct influences upon auroral processes. We then present data from ground-based magnetometers during a period preceding and following the 18:63 UE flight. Next we describe the measurements of the launch site zenith riometer. (The riometer measures the opacity of the ionosphere to cosmic radio noise @ 30 MHz - the absorption of the cosmic noise being due to enhanced levels of ionization below about 95 km). Photometer measurements of the levels of emission at 5577 Å (the auroral green line due to atomic oxygen OI) [made by Dr. F. Creutzberg] will help to establish the relationships between the auroral light and the precipitating energetic particles measured with the sounding rocket. And finally the measurement of parameters in the vicinity of the payload (other than the energetic electrons themselves) the data from the Retarding Potential Analyzer will be presented.

The amount of energy carried by the electrons measured by the PESPEC in units of $\text{ergs} - \text{cm}^{-2} - \text{sec}^{-1} - \text{sr}^{-1}$ will be the first energetic particle data presented. This information allows one to observe the large scale temporal features of the energetic particle precipitation during the flight.

In order to show the changes of shape of the energy spectrum we will use contour plots as described in Chapter 4 which show the flux as a function of time and energy. To better acquaint one with the

temporal features at each energy we will also present time series plots of the flux measured at selected energy channels.

We have used the 18:63 UE P.H.A. data to present the pitch angle distribution characteristics throughout the flight. Complete flight graphs of the flux at pitch angles of 40° and 70° allow one to observe departures from pitch angle isotropy.

As previously reported [McDiarmid, et al, 1967] auroral electron pitch angle distributions are generally isotropic. In particular when the flux increases the pitch angle distribution tends toward isotropy if anisotropy initially prevails at the lower levels of flux. These observations are consistent with current theories of pitch angle diffusion. In this chapter we hope to provide a reference frame from which we can examine in detail an enhancement of the level of electron precipitation which occurred near apogee and which was characterized by the development of an anisotropy in the pitch angle distribution.

A. Results from other Experiments of Parameters Related to the
Aurora Observed with 18:63 UE.

The solar wind is probably the basic energy source for disturbances in the magnetosphere. Recently it has been shown [Foster, et al, 1971] that the occurrence of auroral substorms is related to the direction of the north-south component of the solar wind magnetic field. In particular when the solar wind has a southward component at the sub-solar point (this component is then directed opposite to direction of the geomagnetic field) Dungey [1961] has suggested that the coupling between the solar wind and the magnetosphere may be stronger. Measurements of solar wind velocity, v_{sw} , density, n_{sw} , and magnetic field for the month of March, 1968 are available [STP Notes, 1971]. The solar wind velocity, density and magnetic field data are hourly average values from Explorer 33 and Explorer 35. From 1000 UT to 1400 UT on March 20, 1968 the θ component (north-south) of the solar wind magnetic field was directed southward ($\theta \sim -40^\circ$). However for the next 16 hours until the flight of 18:63 UE θ was positive or only briefly and slightly negative. The direction of the field in the solar ecliptic plane was consistently near the value corresponding to the outward direction at the spiral or "garden hose" angle. The field strength nearly constant at about 5 γ . The solar wind density was very constant near 2 cm^{-3} . The solar wind velocity was decreasing from a value of $\sim 650 \text{ km/sec}$ @ 1200 UT, March 20, 1968 to $\sim 550 \text{ km/sec}$ @ 0600 UT, March 21, 1968.

The parameter, K_p , is used as a measure of planetary magnetic activity. The larger the value of K_p the more magnetic activity on a global scale during the corresponding three-hour time interval. The

values of K_p for the three three-hour intervals preceeding launch were 4, 3⁻ and 2 [Lincoln, 1968]. This indicates that planetary magnetic activity went from a moderate level to a relatively quiet level before launch.

Next we examine local magnetic activity. We have examined the x, y and z deviations of earth's magnetic field (x is north, y is east and z is downward) from their baseline values for magnetic records [R. Langel, private communication] from the Canadian observatories at Fort Churchill, Baker Lake and Great Whale River. Table 5.1 lists the geomagnetic latitude and longitude of these magnetic observatories.

TABLE 5.1

<u>Observatory</u>	<u>Geomagnetic Latitude</u>	<u>Geomagnetic Longitude</u>
Fort Churchill	68.8°N	322.5°E
Baker Lake	73.9°N	314.8°E
Great Whale River	66.8°N	347.2°E

A comparison between the Fort Churchill and Baker Lake data shows variations due to geomagnetic latitude at nearly the same local time. On the other hand a comparison between the Fort Churchill data and the Great Whale River data shows effects due to local time (longitudinal) separation at nearly the same latitude.

Figure 5.1 shows the x, y, and z magnetic deviations at Fort Churchill from 0300 UT to 1100 UT March 21, 1968. From 0000 UT to 0400 UT none of the components vary by more than 20 γ . This corresponds to a local time interval from 6 p.m. to 10 p.m. The Great Whale River and Baker Lake magnetometers were also very quiet during this time interval. At ~ 0500 UT the Fort Churchill observatory recorded

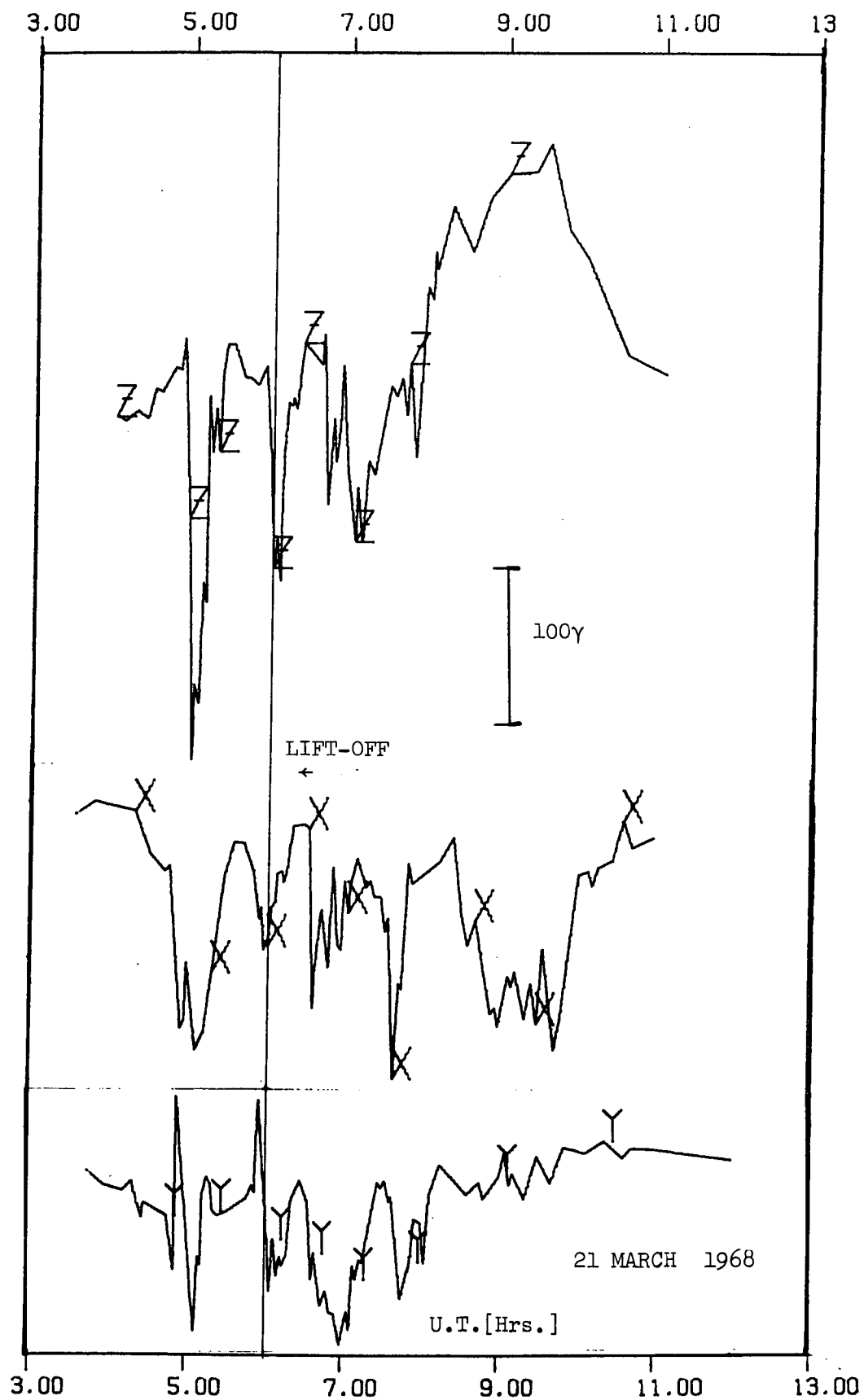


Figure 5.1. Ground-based magnetometer measurements.

a 200 γ negative bay (a negative deviation from the normal value) in z and x. At Baker Lake this disturbance caused a small positive bay in z and a negative bay in x. This is the disturbance pattern a westward flowing current in the ionosphere located at a geomagnetic latitude between Fort Churchill and Baker Lake would cause. Because this disturbance appeared earlier (~ 0430 UT) at Great Whale River one can deduce that it was moving westwards towards the evening sector from local midnite. This could be identified as the westward travelling surge of Akasofu's auroral substorm theory [Akasofu, 1964].

Figure 5.1 shows that near local midnight at Fort Churchill (0600 UT) there was another ~ 150 γ negative bay. This disturbance coincided with the breakup display into which 18:63 UE was launched. Because the disturbances at Baker Lake and Great Whale River are very small at this time the phenomena at Churchill may have been somewhat localized. All three observatories detected more activity at ~ 0700 UT with no significant time variation, and the Baker Lake-Fort Churchill profiles were similar to the 0500 UT disturbance. The only remaining significant feature of the ground based magnetometer data is the slow development of the ~ 200 γ z component positive bay and $\sim 150\gamma$ x component negative bay between 0800 UT and 1000 UT. This could have been caused by a compression of the nightside geomagnetic field.

We further reduce our time and space reference frame in considering data from the launch site zenith riometer. The westward surge reaching Churchill at ~ 0500 UT had a peak absorption of cosmic noise of about 1.5-2 db at 0457 UT. The breakup display into which we launched 18:63 UE at 0601:32 UT reached a maximum level of absorption of ~ 1 db at ~ 0602 UT. Again we emphasize that the riometer is

essentially sensitive to electrons with energies greater than ~ 40 keV.

The most important ground-based instrument with which we hope to correlate our results is Dr. F. Creutzberg's 5577 \AA° photometer. This radiation comes from the ^1S to ^1D forbidden (lifetime = 0.74 sec) neutral atomic oxygen, OI, transition. The excitation energy required to reach the ^1S state is only 4.17 eV, and therefore the intensity of 5577 \AA° is very sensitive to the low energy electron flux. Light intensity in auroras is measured in units of Kilorayleighs which represents 10^9 photons $\cdot \text{cm}^{-2} \cdot \text{sec}^{-1}$ (column) where the "column" indicates that this is the number of photons coming from a column of 1 cm^2 cross-sectional area.

Figure 5.2 shows the intensity of 5577 \AA° as a function of time. These data were measured ~ 15 km from the launch site. The azimuth and elevation of the photometer were changed during the flight to follow the planned rocket trajectory. Because the actual launch elevation angle was steeper than that used to calculate the correct look angles for the photometer the photometer only briefly was directed at the point in the atmosphere at 105 km (assumed height of most of the light emission) which was on the same magnetic field line as the sounding rocket. Figure 5.3 indicates on a horizontal plane at 105 km the areas at which the photometer was looking. They are the elliptical areas and correspond to the 2° photometer field of view. Also shown on figure 5.3 is the intersection with the 105 km plane of the magnetic field line at the position of the sounding rocket. This intersection was computed for various angles of inclination and declination for the earth's magnetic field, and the results were rather insensitive to the particular values chosen. One can observe that only

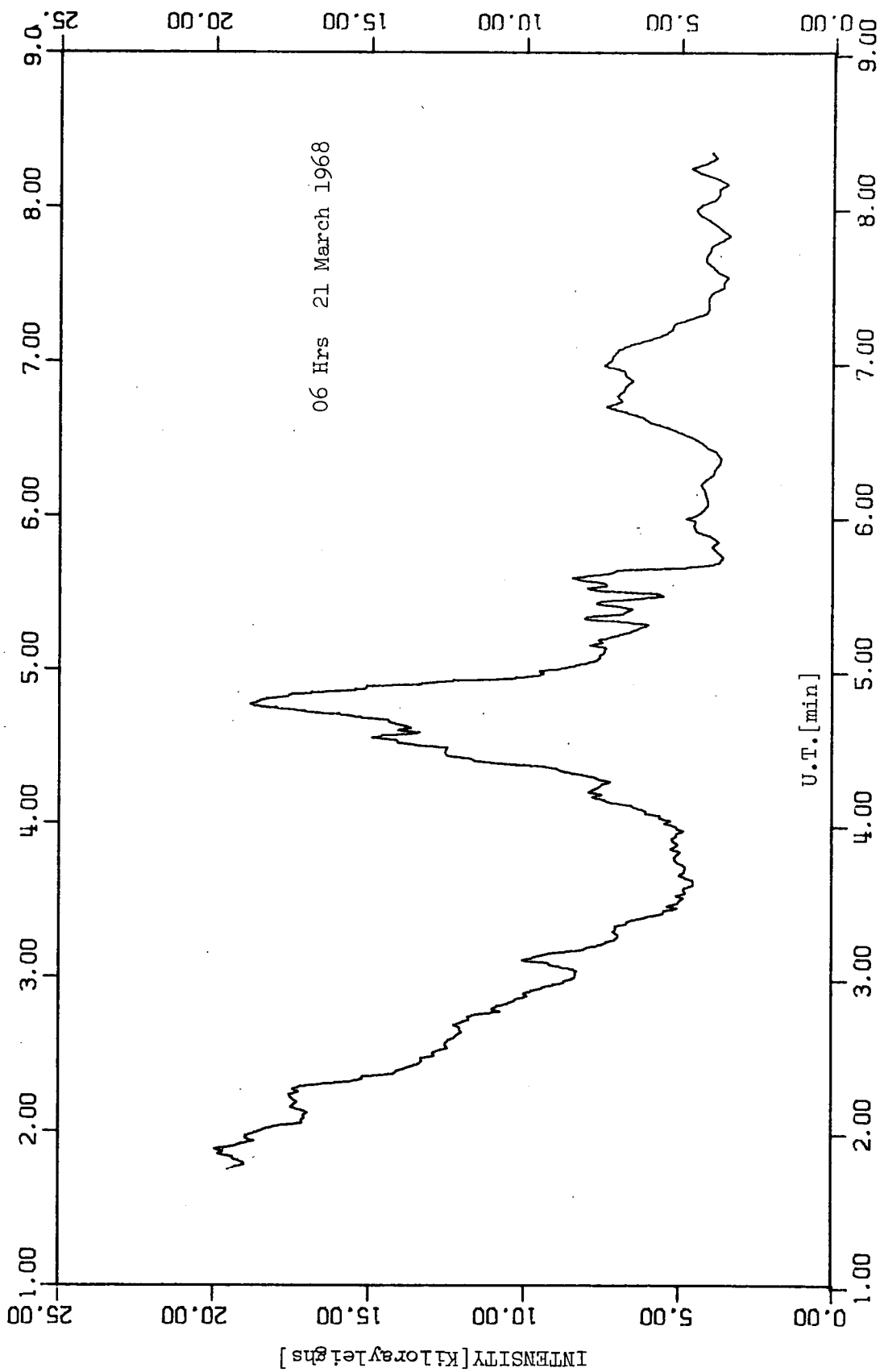


Figure 5.2. Intensity of 5577 Å versus time.

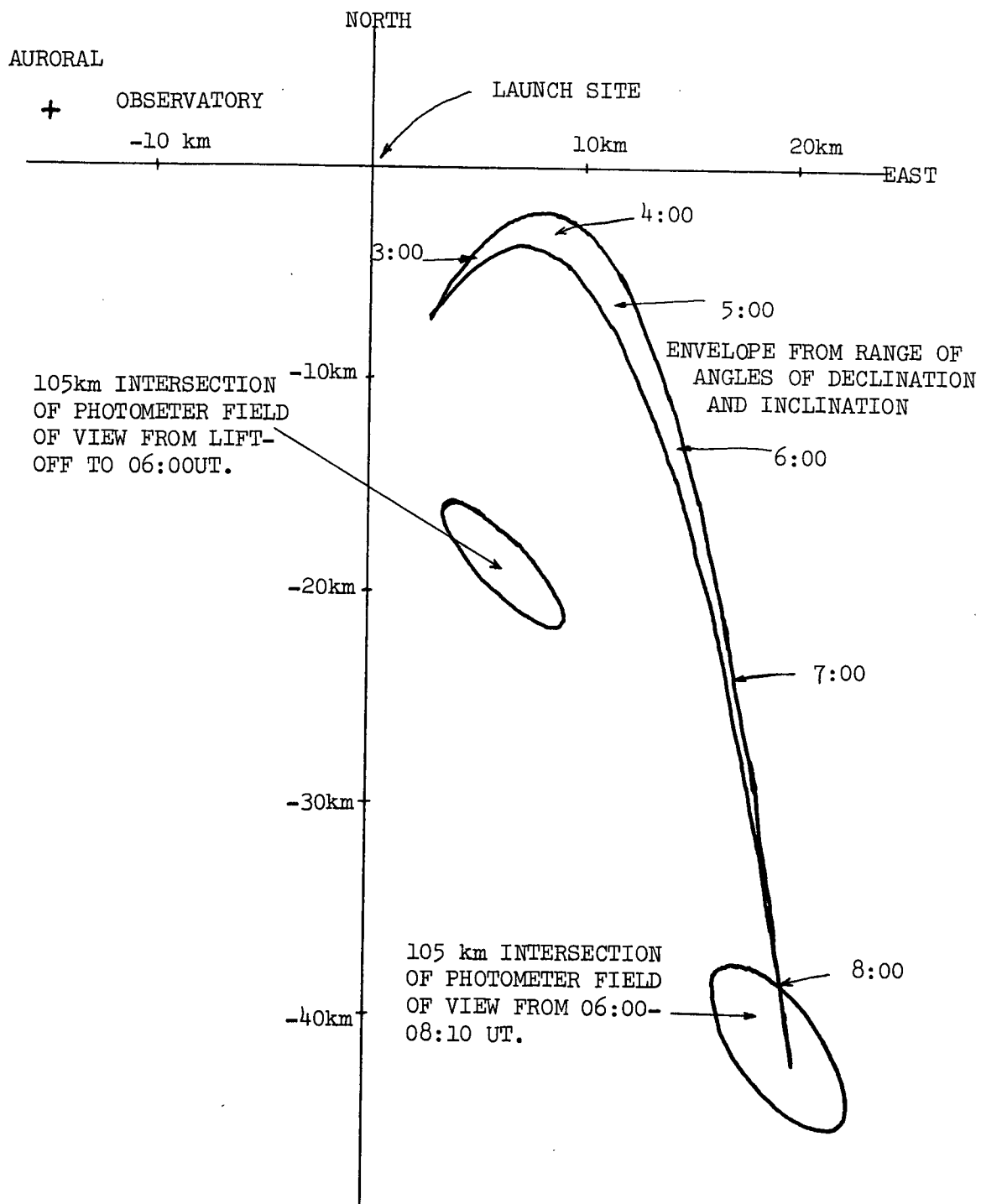


Figure 5.3. Comparision at 105 km between intersection of field line passing through rocket and field of view of ground-based photometer.

for $08:00 < t < 08:10$ was the photometer oriented in the proper direction.

Figure 5.2 shows that with some small fluctuations the intensity decreased from ~ 20 KR @ 0602:00 UT to ~ 5 KR @ 0603:45 UT. Between 0604:00 UT and 0605:00 UT there was a fourfold increase in the emission at 5577 \AA . This burst will be discussed in detail later. From 0605:00 UT to $\sim 0605:40$ UT the intensity decreases with some 2-3 KR fluctuations. From then until the end of the flight the intensity remains low at ~ 4 KR except for an enhancement to ~ 7 KR centered about 0606:50 UT.

Figure 5.4 (courtesy of D. L. Matthews) shows the values of thermal electron temperature and density as measured by the Retarding Potential Analyzer on 18:63 UE. The electron temperature ranges from $\sim 700^\circ\text{K}$ @ 105 km to a peak value of $\sim 2300^\circ\text{K}$ at a time coinciding with the burst of light between 0604:00 UT and 0605:00 UT. The electron density decreases from an initial E region peak of $\sim 10^6 \text{ cm}^{-3}$ to $\sim 10^5 \text{ cm}^{-3}$ for most of the remaining time of the flight. It should be emphasized that the peak in electron temperature is probably not an altitude effect because it occurs before apogee (apogee is at 0605:34 UT) and is not observed on the downleg. In the time interval from 0604:30 - 0605:00 UT the payload moves only 13 km in altitude from 223 km to 236 km (the scale height at this altitude is ~ 45 km). In the same time it moves only ~ 3 km horizontally (a satellite would move ~ 240 km in this time interval). Therefore horizontally relative to satellite motion and vertically relative to the ambient atmosphere the payload was nearly stationary during this time interval.

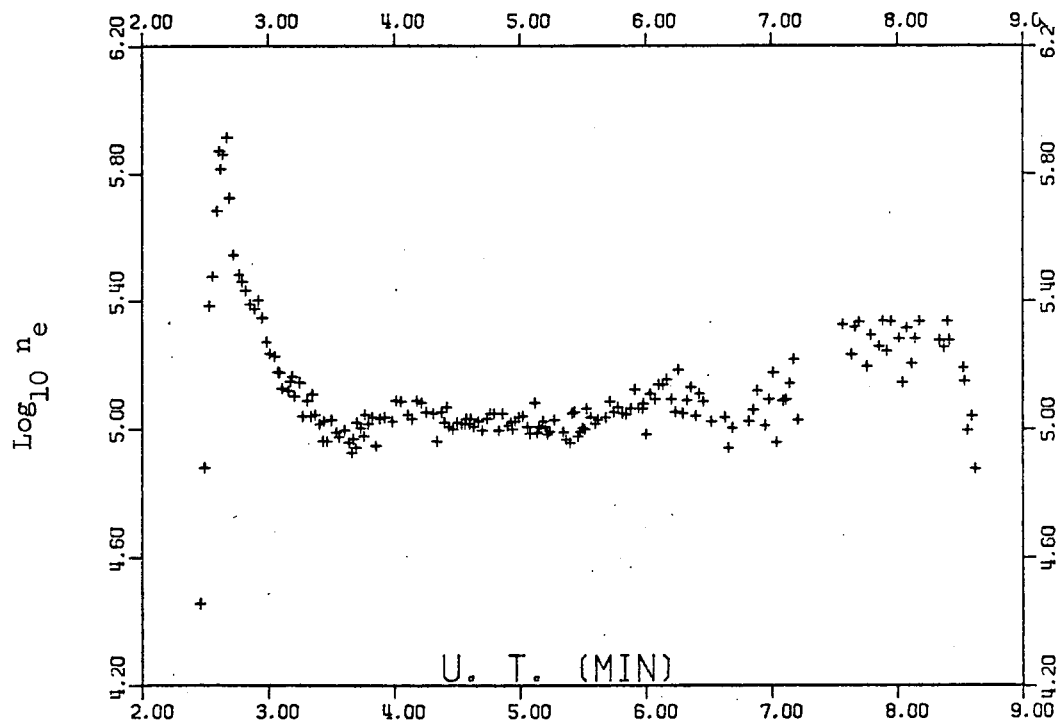
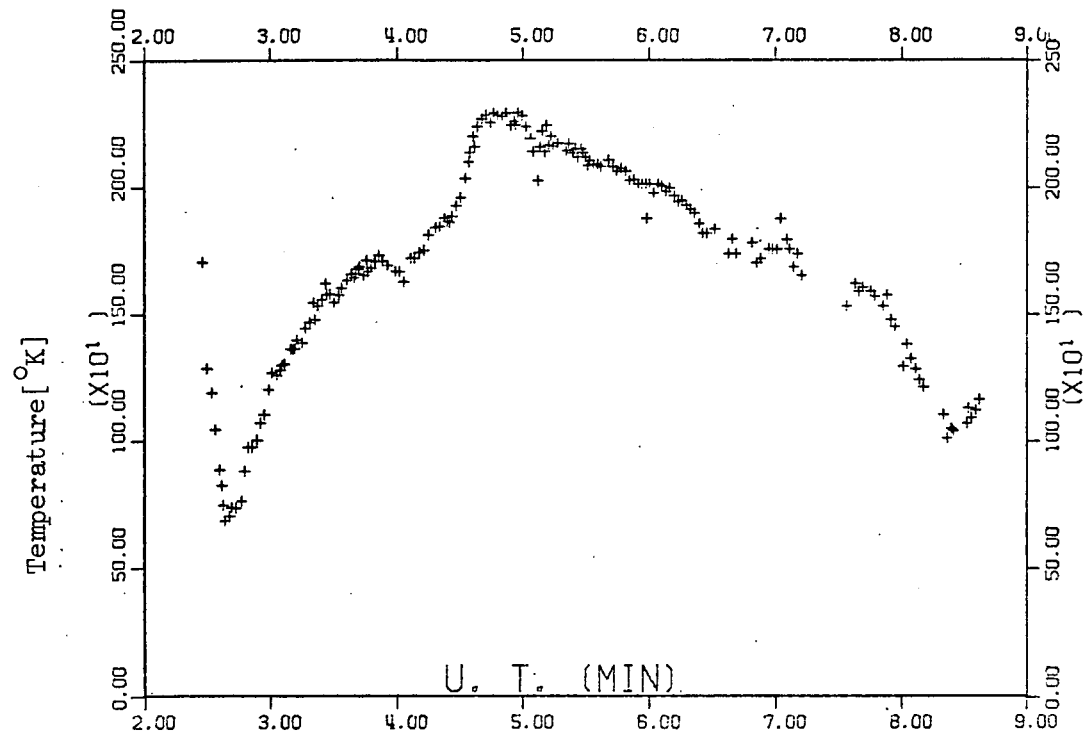


Figure 5.4. R.P.A. measurements of thermal electron density and Temperature.

B. Total Energy of Electrons Detected by Electron Spectrometer
from 0604:20 - 0608:20 UT.

After computing the differential flux one can calculate the total energy of the electrons over some energy range (E_1 , E_2) from

$$E_{TOT} = \int_{E_1}^{E_2} \frac{dj}{dE}(E) E dE \quad . \quad (5.1)$$

We computed the total energy deposited as a function of time by the dumped (D), mirroring (M) and precipitating (P) electrons (see Chapter 4 for the definition of these categories) from the PESPEC data. The energy limits in equation (5.1) were $E_1 \sim 500$ eV and $E_2 \sim 30$ keV. This interval contained an overwhelming fraction ($> 99\%$) of the energy deposited from 500 eV to 150 keV. The energy spectra were unfolded from the averaged counts as described in Chapter 2. We used a 5 point quadratic ($j_{max} = 3$) fit. Some degree of fitting was needed to stabilize the unfolding process, and the quadratic order was used because it gave the best results when tested by unfolding the counts (N_i) that a monoenergetic spectrum would have produced.

The data from the PESPEC was contaminated until 0604:18 UT by interference counts from the SESPEC which failed. At that time the interference abruptly ceased. Therefore all the data to be presented from the PESPEC comes from times after 0604:20 UT. At that time the vehicle was on the upleg at 216 km.

Figure 5.5 shows the energy deposited by the precipitating, mirroring and dumped electrons from 0604:20 - 0608:20 UT. The dominate feature is the peak between 4:30 - 5:00 UT. This feature corres-

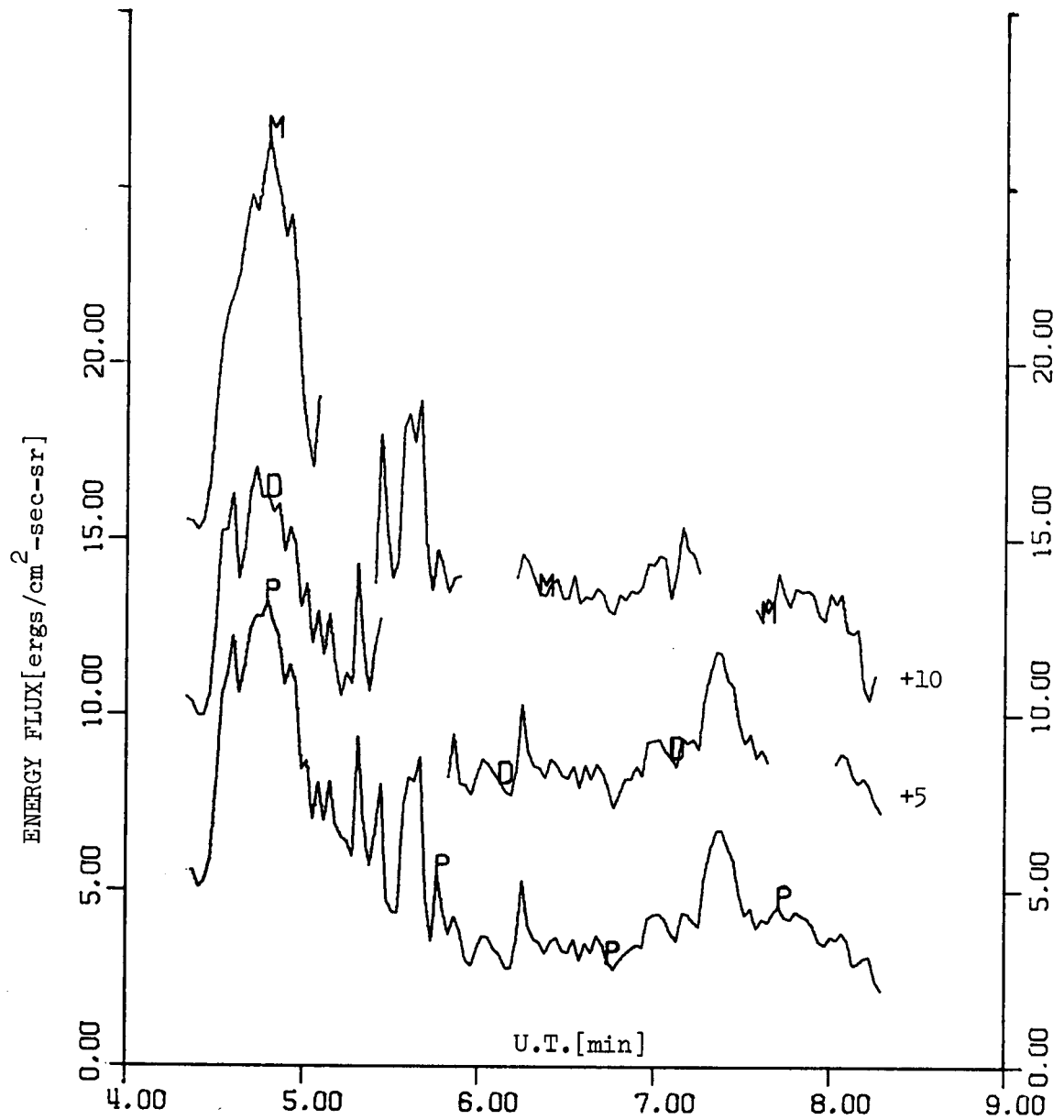


Figure 5.5. Energy flux versus time for P,D,and M averages.
 (Note each successive origin displaced by 5)

ponds to the burst of $5577 \overset{\circ}{\text{\AA}}$ and peak in the electron temperature. After this burst, from 5:00 - 5:50 UT the amount of energy deposited fluctuates in a manner similar to emission of $5577 \overset{\circ}{\text{\AA}}$ in the same time period. From 5:50 to re-entry the amount of energy carried by the precipitating electrons was rather constant with the dominant exception being the small burst centered at 7:25 UT. The burst in $5577 \overset{\circ}{\text{\AA}}$ (see figure 5.2) in this time interval occurred ~ 35 sec earlier. This indicates that the enhancement was probably caused by a form moving from the region observed by the photometer to the field line of the sounding rocket. The maximum velocity needed for the form would be ~ 300 m/sec which is well below the maximum observed velocities of forms. Unfortunately the records from the all-sky camera which might have clarified the situation were lost after we had made some preliminary notes from them. We have attempted to determine whether the burst in the time interval 4:30 - 5:00 UT was spatial or temporal in nature. From the all-sky camera data it was noted that until 5:40 UT the motions (if any) of all forms had been towards an azimuth of 235° . From figure 5.3 we can determine that during this time the region observed by the photometer was ~ 14 km from the intersection of the field line at the sounding rocket with the 105 km horizontal plane. Therefore if a form were moving at 2000 m/sec towards 235° azimuth it should be observed by the photometer ~ 7 sec after being detected onboard the rocket. Figure 5.6 shows both the energy deposited by the precipitating electrons and the photometer measurements of $5577 \overset{\circ}{\text{\AA}}$ as a function of time for the burst time interval. The near coincidence of the profiles (certainly the photometer

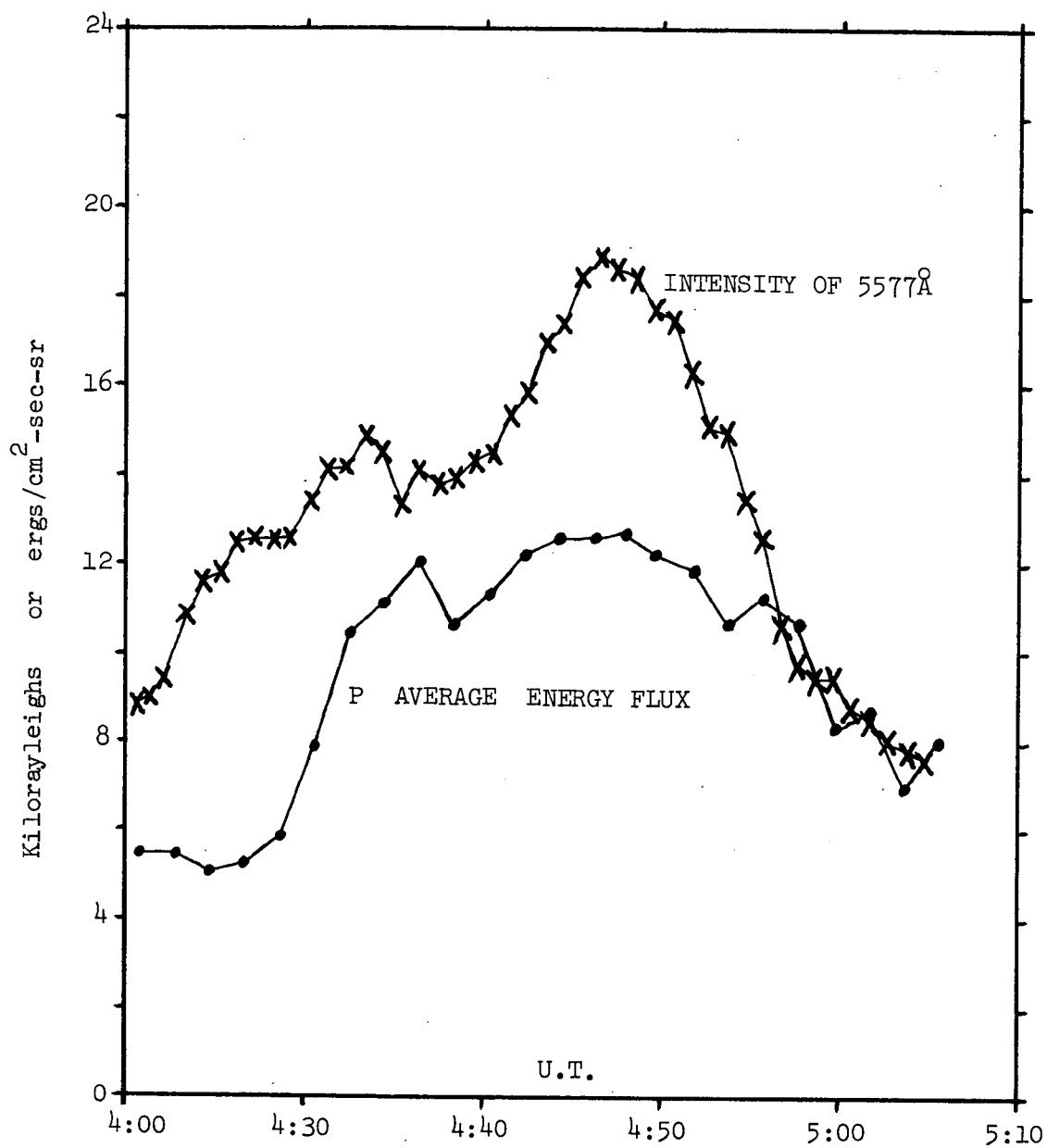


Figure 5.6. Energy deposited by precipitating electrons and emission of 5577Å during burst.

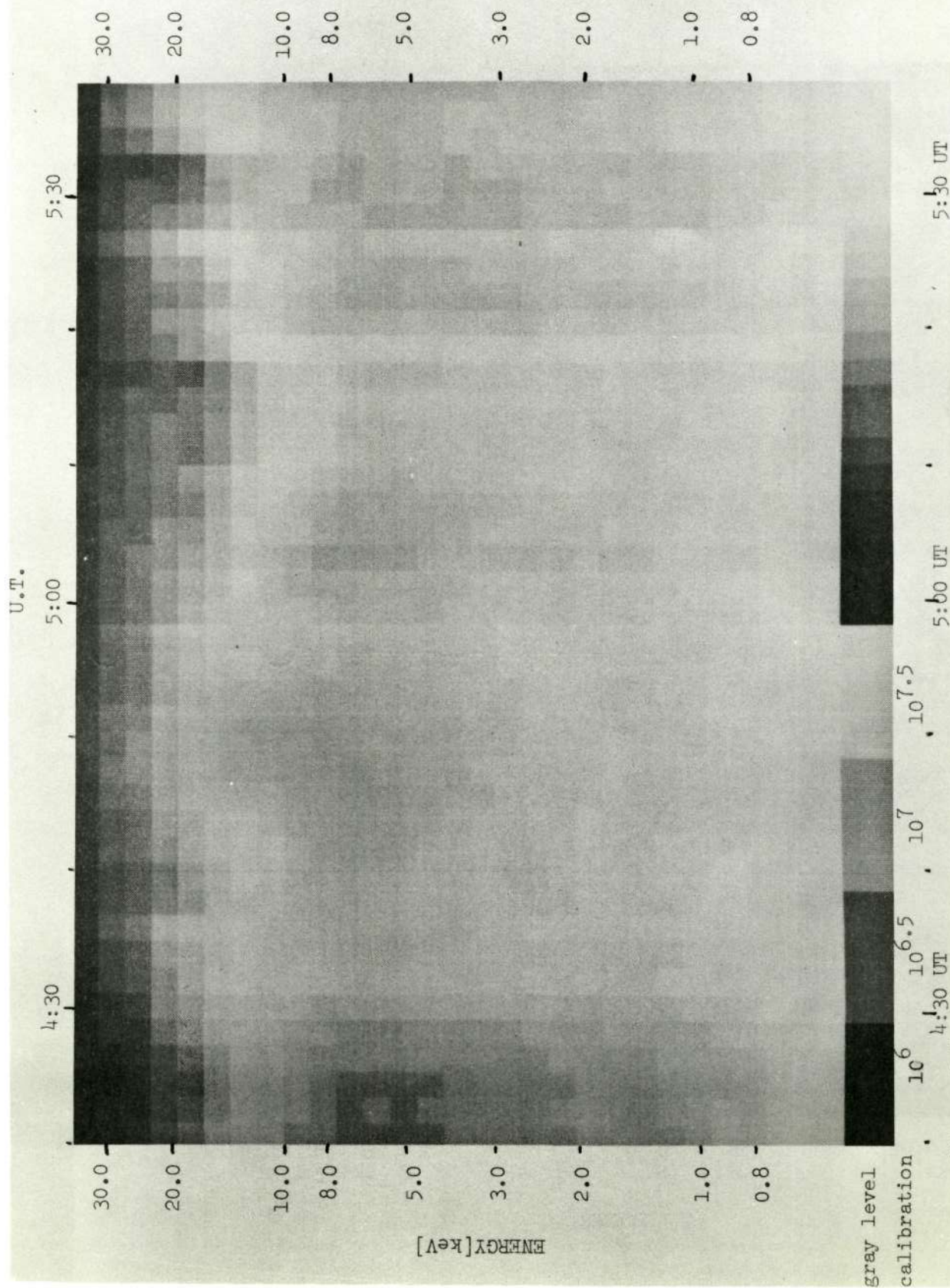
measurement does not lag 7 seconds behind the PESPEC measurement) suggests that the burst was a temporal not a spatial phenomenon. In the literature the term burst generally signifies a short term temporal enhancement of some quantity, and we believe that the time duration should be specified to avoid having the semantics confuse the physics. For example at $\sim 5:19$ UT there were bursts in the precipitated energy deposited and in the 5577 \AA° intensity, yet the physics unlying this short duration burst may be entirely different from that causing the ~ 30 sec burst previously mentioned. This distinction will be further discussed later.

Figure 5.5 also shows the energy deposited by the dumped (D) electrons and the mirroring (M) electrons. It also allows us to observe one of the shortcomings of these averages - the data gaps when the conditions on the pitch angle described in Chapter 4 could not be satisfied. The mirroring and dumped electron energy flux profiles are similar to the precipitated electron profile, but they are distinct in two ways. The first and most obvious is that for the burst between 4:30 and 5:00 the mirroring electrons carry much more energy. Secondly the precursor peak is much more pronounced in the dumped electrons.

C. Energy-Time Contours from the Spectrometer Data

In the previous section we used the graphs of the energy deposited versus time to establish a temporal reference frame. Such a single independent variable presentation does not convey the energy spectrum information. In this section we use contours of constant flux in an energy-time reference frame to illustrate the variation of the energy spectrum with time. We will use the same technique to display contours of constant levels of the anisotropy parameter, $A(E, t)$, defined in Chapter 4.

Figures 5.7, 5.8 and 5.9 show contours of constant values of flux computed from the averages of precipitated (P) electrons. The most obvious persistent feature of these figures is the dramatic decrease in the differential energy flux above ~ 15 keV. Secondly the differential energy spectrum consistently has a local peak near 10 keV. We also note that the energy spectrum is increasing as the energy approaches the PESPEC low energy limit. Temporal variations were generally quantitative in nature in that they preserved these three features of the shape of the spectrum. The peak values of the flux at each energy were observed during the burst between 4:30 and 5:00 UT. Smaller bursts occurred at 5:19, 5:37, 6:15 and 7:20. Frequently these enhancements were accompanied by a shift in the energy of the local peak near 10 keV. An example of this can be seen in figure 5.8. At 6:11 UT the local peak is at an energy of ~ 6.5 keV. About 4 seconds later the peak has shifted to an energy of ~ 10.5 keV. Another type of variation of the energy spectrum with time can be seen in figure 5.7 by noting that the width of the peaked portion of the spectrum at 4:23 UT is much less than at 4:36 UT.



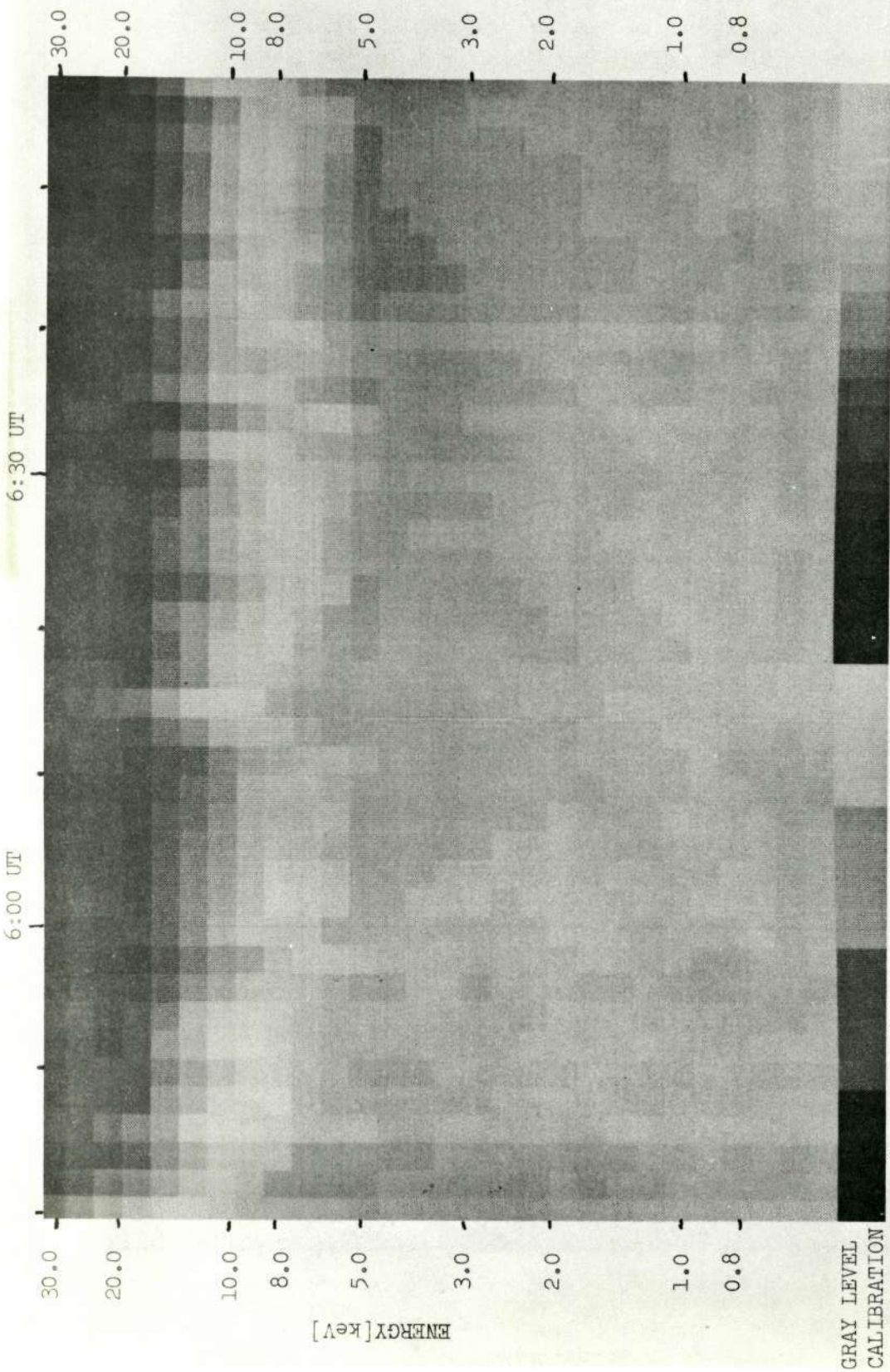


Figure 5.8. 16 gray level energy-time spectrogram of differential electron flux (P average)

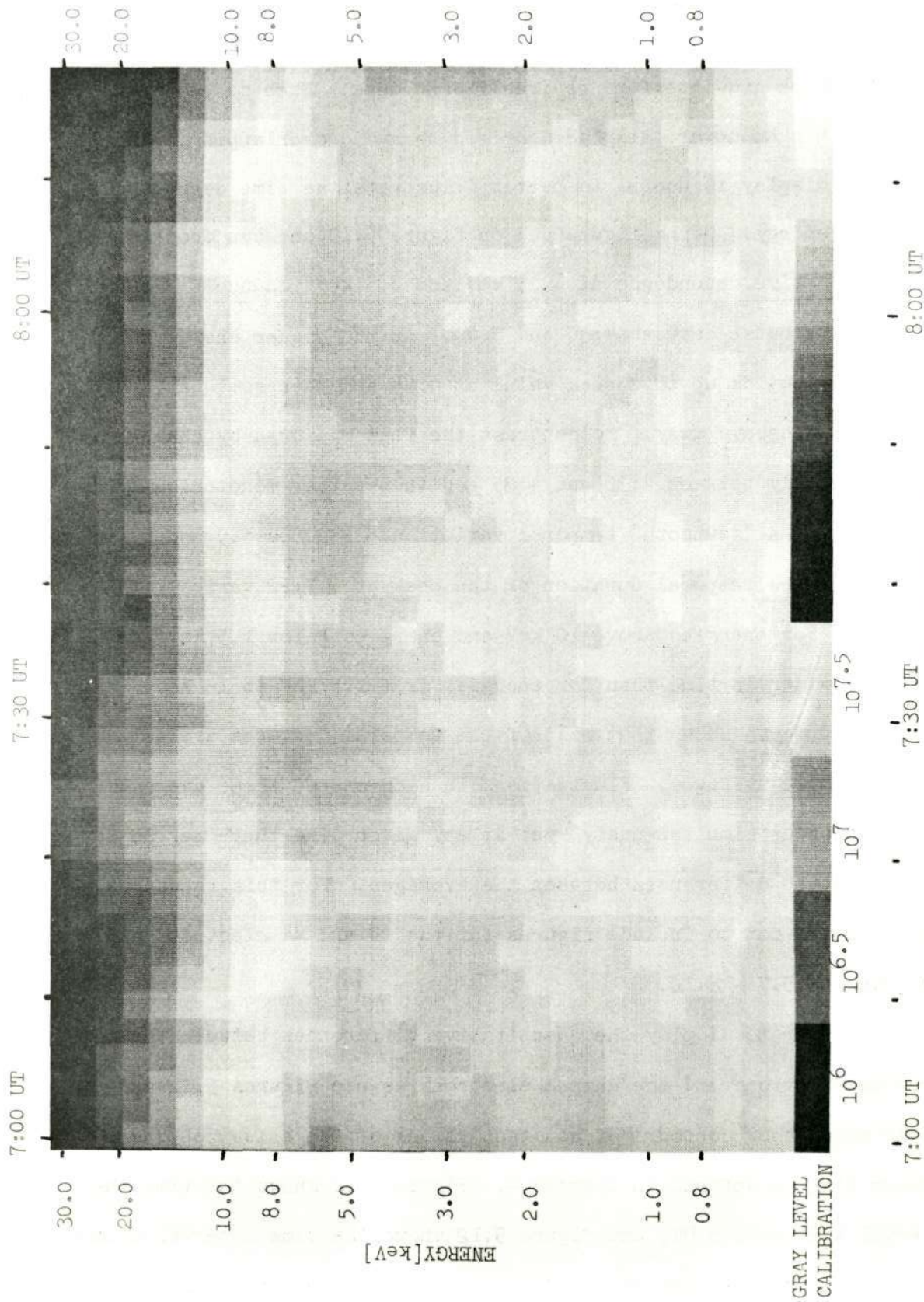


Figure 5.9. 16 gray level energy-time spectrogram of differential electron flux (P average)

Reproduced from
best available copy.

Figure 5.10 shows the time series profiles of the precipitated flux from selected energy channels for the complete portion of the flight which had interference free PESPEC data. Each succeeding channel has an upward displaced origin to avoid overlapping. This type of display is useful to better illustrate the time dependence at each energy. Using figure 5.7 or figure 5.10 one can observe the different time dependence at ~ 25 keV and ~ 5 keV (channels 3 and 13) during the burst between 4:30 and 5:00. At the higher energy the flux gradually builds up to a peak value at 4:48 and then somewhat symmetrically decays away. By contrast the flux measured by channel 13 rises steeply between 4:30 and 4:35 and then rather monotonically decays giving a "sawtooth" temporal variation. Figures 5.9 and 5.10 show that the temporal duration of the peak at $\sim 7:22$ varies with energy. For energies above 10 keV and energies below 1.5 keV the peak is wider in time than for energies from 1.5 keV to 10 keV.

Figure 5.5 shows that most of the temporal features are common to all three averages. Fluctuations in each of the three averages tend to occur simultaneously, yet at any given time there may be large quantitative differences between the averages. For this reason we have chosen not to include figures for the D and M electrons similar to figures 5.7 - 5.10.

However to display the quantitative differences between the mirroring electrons and the dumped electrons we use figures 5.11 and 5.12 which show contours of constant values of the anisotropy parameter $A(E, t)$ defined in Chapter 4. Figure 5.11 shows the time interval 4:20 - 5:15 UT, and figure 5.12 shows the time interval 6:10 - 7:20 UT. The contours are drawn for $A(E, t)$ values of 0.55, 0.85,

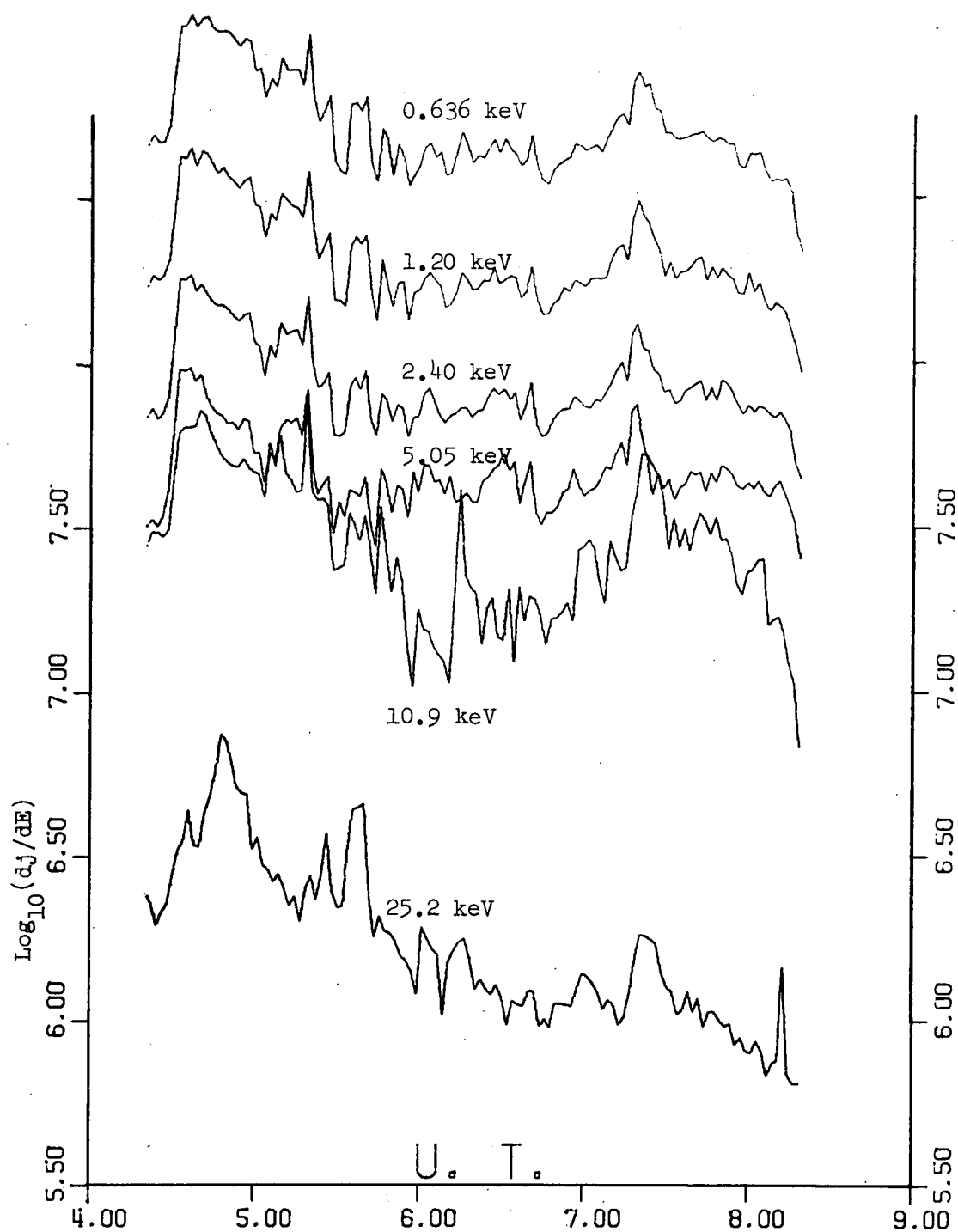


Figure 5.10. Time series' of P electron differential flux
 (Note each succeeding curve has origin displaced
 by 0.25 - dj/dE increased by $10^{0.25}$)

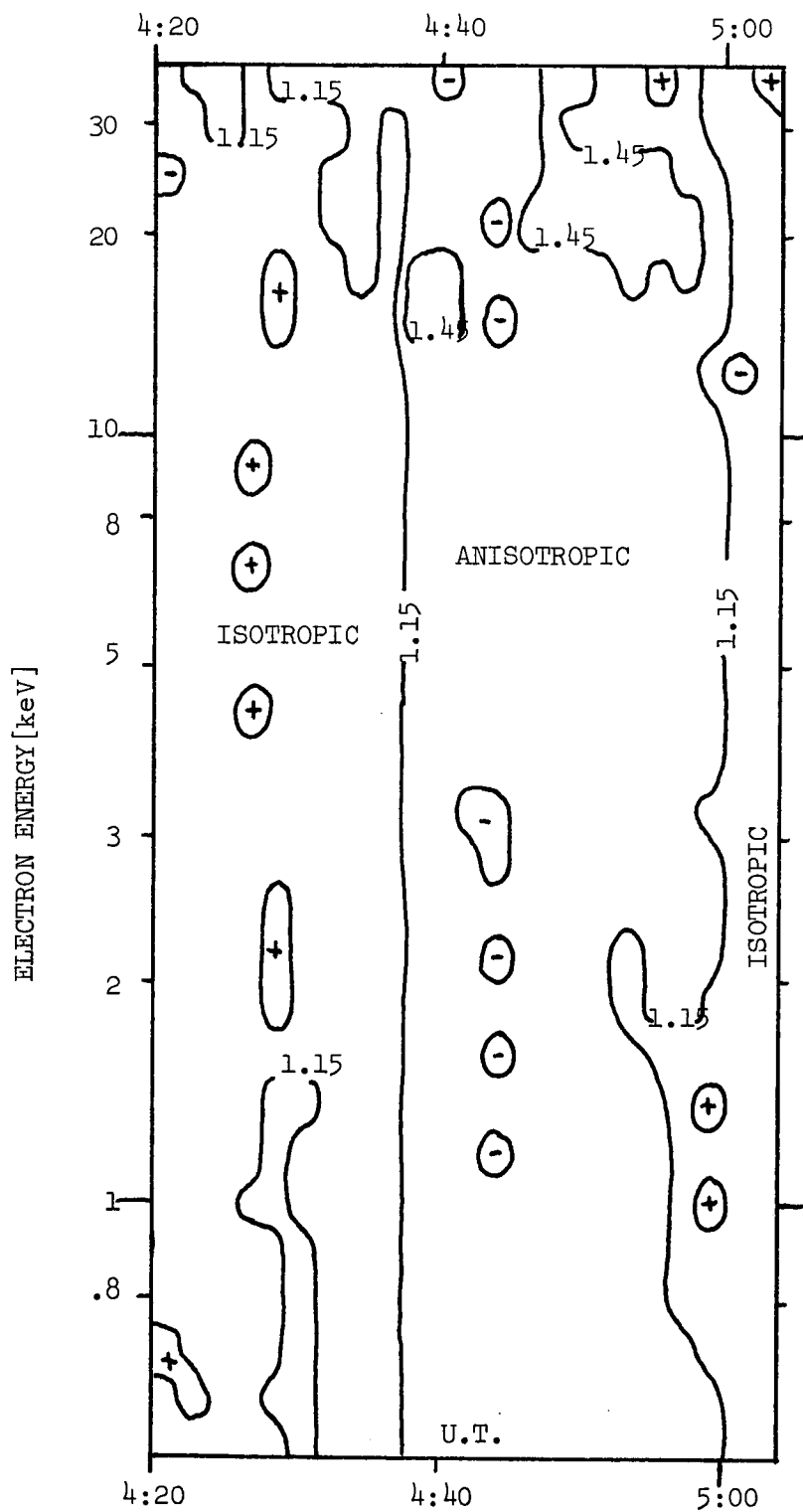


Figure 5.11. Contours of constant values of anisotropy parameter $A(E,t)$ (+ or - indicate small local deviations)

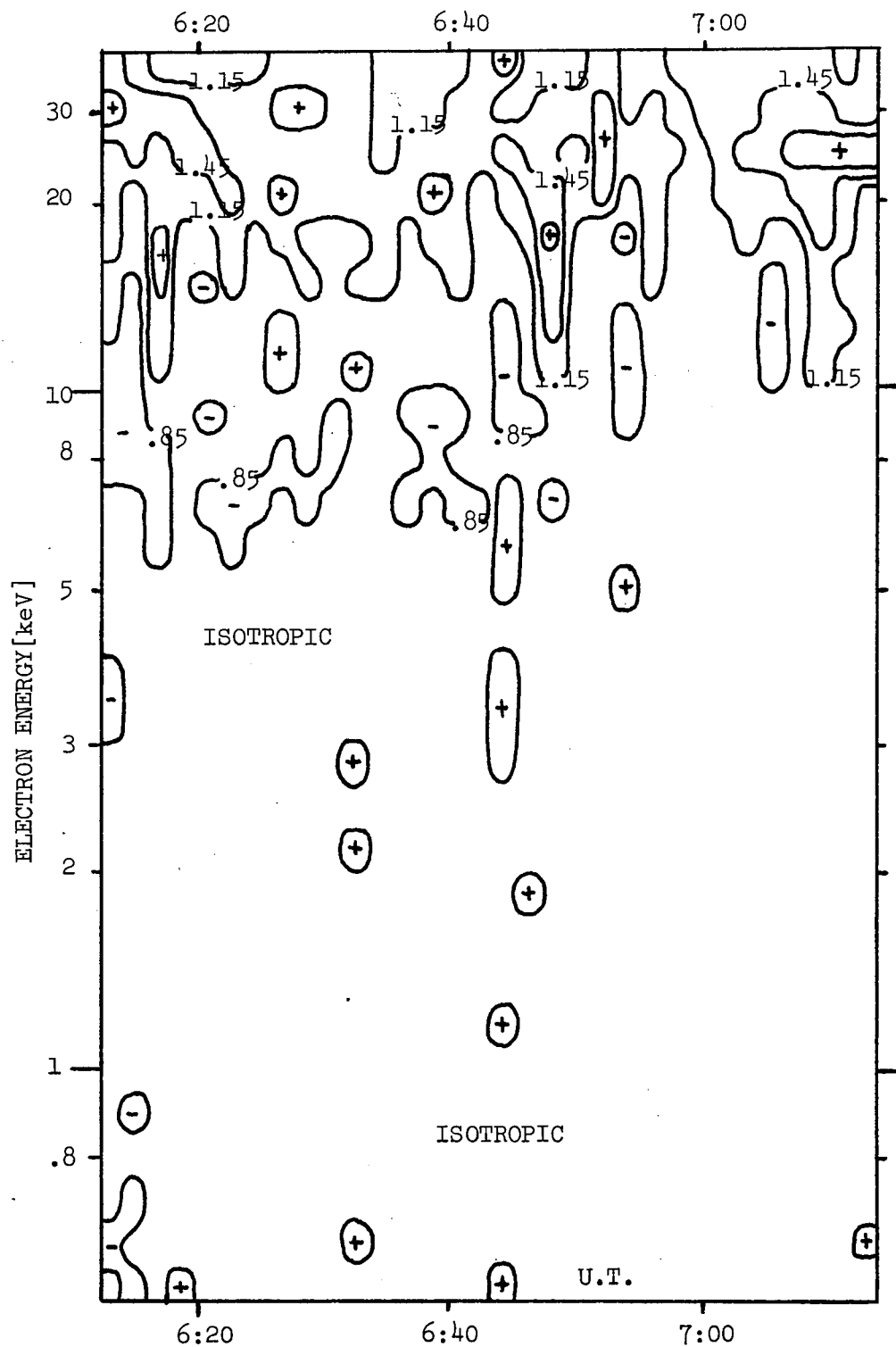


Figure 5.12. Contours of constant values of anisotropy parameter $A(E,t)$ (+ or - indicate small local deviations)

1.15, 1.45, 1.75. The interval corresponding to an isotropic pitch angle distribution would be from $A(E, t) = 0.85$ to $A(E, t) = 1.15$.

Figure 5.11 shows that pitch angle isotropy prevails from 4:20 UT through the rapid rise of the flux at the beginning of the burst until 4:38. The pitch angle distribution then becomes anisotropic with the mirroring flux being greater than the dumped flux over the entire PESPEC energy range. This anisotropy persists until $\sim 5:00$. The anisotropy is greater at the higher energies. The development of an anisotropic pitch angle distribution with an increase in the electron flux is contrary to what one would expect if the increase in flux were due to a shift from weak pitch angle diffusion to strong pitch angle diffusion.

With weak pitch angle diffusion the pitch angle is not altered much per bounce, and electrons scattered into the loss cone are lost. This gives distributions near the atmosphere which are peaked near 90° pitch angle. With strong pitch angle diffusion the electron experiences many, large changes in pitch angle per bounce and the diffusion mechanism not the atmospheric loss governs the pitch angle distribution. All pitch angles are equally likely and isotropy results.

An examination of figure 5.12 shows the unique character of the anisotropic burst in figure 5.11. For energies less than ~ 15 keV in the time interval of figure 5.12 the pitch angle distribution rarely was anisotropic, and instances of anisotropy with the field-aligned (dumped) flux exceeding the mirroring flux are more numerous than vice-versa. The higher energy channels do exhibit anisotropies where the

4-5

mirroring flux exceeds the dumped flux. In the next section using the 18:63 UE P.H.A. data which has much greater angular resolution we will examine more closely the nature of the pitch angle distribution for the whole flight. We hope to show that the higher energy anisotropies in figure 5.12 are consistent with previous observations of McDiarmid, et al [1967] and the theory of pitch angle diffusion, but that the anisotropy in the burst time interval requires a different explanation.

D. Temporal Features of the Pitch Angle Distribution from Pulse Height Analyzer (P.H.A.) Data.

The P.H.A. data were corrected for overranging for channels A and C at pitch angles 40° , 70° and 100° for the entire flight. These special cases were chosen because: (i) we were not totally confident in the overranging corrections for channel B, (ii) the energy channels above channel C had fewer counts per frame and consequently the statistics would have suffered, (iii) pitch angles of 40° and 100° were the minimum pitch angle and the maximum pitch angle respectively which were observed throughout the flight, and (iv) a pitch angle of 70° gave equal intervals to the maximum and minimum pitch angles as well as being the pitch angle of the peak of the pitch angle distribution during the burst from 0604:30 to 0605:00 UT.

Figure 5.13 shows the differential flux (plotted logarithmically) versus time for channel A(22 keV) at pitch angles of 40° and 70° . There are two large intensity peaks at 3:00 and 4:50 UT. The initial peak was measured while the sounding rocket was passing from 103 km to 155 km. Two interesting features of this initial peak are that the flux at both 40° pitch angle and 70° pitch angle are increasing in the time period 0602:39 - 0602:50 UT while the intensity of 5577 A° (see figure 5.2) was essentially decreasing from 0602:20 - 0603:00 UT and the second feature is that the flux at 40° pitch angle exceeds the flux at 70° pitch angle until $\sim 3:05$ UT (140 km). We have attempted to determine whether atmospheric scattering and mirroring in the earth's field would account for both of these features. We have examined the results of Wedde [1970], a Monte-Carlo technique which analyzes the behavior of electrons in a realistic magnetic field

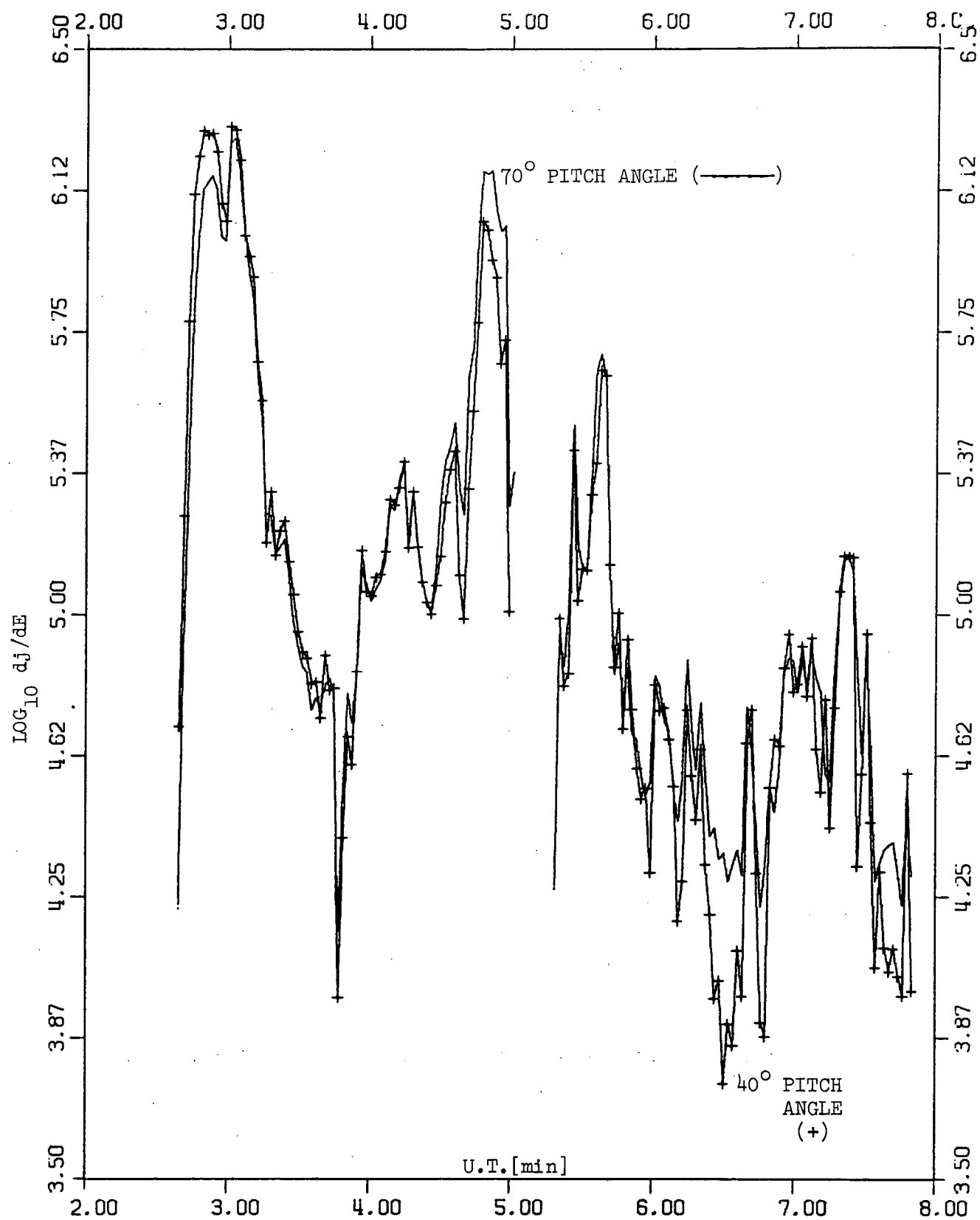


Figure 5.13. P.H.A. channel A (22 keV) at $\alpha=40^\circ$ and $\alpha=70^\circ$

striking the earth's atmosphere. At 0602:45 UT 18:63 UE was at 110 km, and the power law spectral index was ~ 4.7 . Wedde [1970] shows the angular distribution of electrons in the (30-35) keV energy range at various altitudes for a power law differential energy spectrum $E^{-5.7}$ and isotropy ($0^\circ - 90^\circ$) at 1000 km. Under these conditions the flux measured at 70° pitch angle at 110 km would be ~ 0.51 of the value measured at 1000 km, and the flux at 40° would be ~ 0.85 the undistorted value. This would indicate that the ratio between the flux at 40° and at 70° would be ~ 1.67 . The actual ratio at 110 km was 2.24. The actual flux at 40° pitch angle at 22 keV at 110 km was 1.3×10^6 electrons-cm⁻²-sec⁻¹-sr⁻¹-keV⁻¹. Dividing by 0.85 would indicate a value of 1.53×10^6 above the atmosphere. This is still significantly less than the value of 1.9×10^6 measured at 2:49 UT (117 km). This analysis indicates that there may have been a real temporal increase in flux during the time interval over which atmospheric absorption and scattering were important, and that there may also have been a real anisotropic pitch angle distribution with isotropy from 0° to $\sim 60^\circ$ (determined separately) and a reduction of the flux larger than could be accounted for by scattering and absorption for pitch angles greater than 60° . These conclusions are supported by figure 5.14 which shows the differential flux versus time for channel C (90 keV) at pitch angles of 40° and 70° . The early discrepancy between the flux at 40° and at 70° is also apparent at the higher energy, and atmospheric scattering and absorption would be much less important for 90 keV electrons than for 22 keV electrons at 110 km.

During the intensity peak at 4:50 UT the flux at 70° exceeds the flux at 40° . At 4:48 the ratio between the flux at 70° and the flux

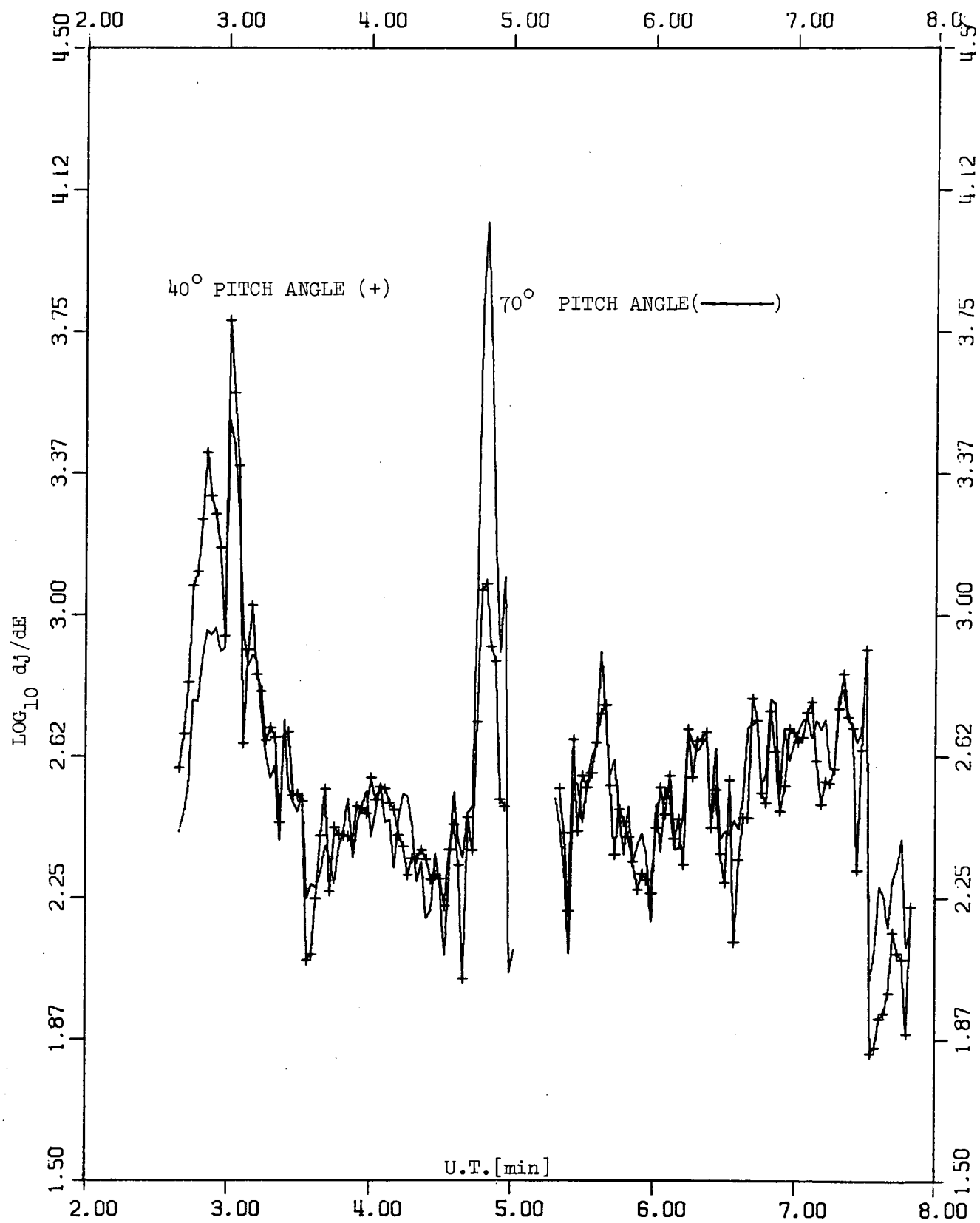


Figure 5.14. P.H.A. channel C (90keV) at $\alpha = 40^\circ$ and $\alpha = 70^\circ$

at 40° for 22 keV electrons was ~ 1.35 . The anisotropy was larger at 90 keV where this ratio was ~ 5.5 . At the lower energy (22 keV) the anisotropy persisted for ~ 30 sec. This anisotropy lasted for about 20 sec at 90 keV, but it is interesting to note that the burst lasted only about 20 sec at 90 keV. In both cases the anisotropy persisted throughout the temporal duration of the enhanced flux levels.

The observation that the anisotropy was larger at the higher energy raises the question of pulse pile-up and non-linear photomultiplier operation at high count rates. Pulse pile-up would tend to cause too many pulses in the voltage interval corresponding to channel C and would falsely indicate a hardening of the spectrum (for a power law spectrum, E^{-n} , this would be a lower value of n). The maximum count rates in the peaks at 0603:00 UT and 0604:50 UT were ~ 800 kHz. As mentioned in Chapter II the linear amplifier could distinguish between pulses at over a 10 MHz rate so it seems unlikely that pulse pile-up was a factor. Land [1971] has studied the problem of non-linear photomultiplier output at high anode currents. Our maximum anode currents were $\sim 2\mu\text{A}$ or $\sim 10\%$ of the current in the resistor voltage divider chain. Land [1971] indicates that for an anode current of 10% of the voltage divider current one can expect the output to deviate less than 3% from the linear operation. We therefore conclude that at the peak flux levels our results are not affected by either pulse pile-up or non-linear photomultiplier operation.

From 3:05 UT to 4:30 UT the pitch angle distribution is remarkably isotropic. The flux changes by a factor of ~ 100 in this time interval. Following the anisotropic burst from 4:30 - 5:00 UT there

was a 20 second telemetry dropout on the 18:63 UE P.H.A. For the rest of the flight the flux at 40° pitch angle is generally equal to the flux at 70° pitch angle. The major exception is in the time interval 6:10 - 6:50 UT when the flux at 70° exceeds the flux at 40° for the 22 keV electrons (the higher energy electrons show no significant differences during this time interval - see figure 5.14). A similar exception wherein the 90 keV electrons are also anisotropic begins at 7:32 UT. We observe a qualitative and a quantitative difference between the examples of anisotropy after 5:20 UT and the anisotropy during the burst from 4:30 - 5:00 UT. The quantitative difference is that the level of precipitation is about a factor of ten less after 5:20 (in the burst the flux in channel A @ 70° is $\sim 2 \times 10^5$ electrons $\text{-cm}^{-2}\text{-sec}^{-1}\text{-sr}^{-1}\text{-keV}^{-1}$ whereas at 6:30 UT it is $\sim 2 \times 10^4$ electrons $\text{-cm}^{-2}\text{-sec}^{-1}\text{-sr}^{-1}\text{-keV}^{-1}$). The qualitative difference is that after 5:20 UT an increase in the flux or burst on a smaller ~ 5 second time scale is accompanied by a more isotropic pitch angle distribution whereas in the longer ~ 30 second burst from 4:30 - 5:00 UT the pitch angle distribution becomes more anisotropic. Examples of the short time scale bursts which are isotropic are at 6:41 UT and 7:48 UT. We suggest that the quantitative and qualitative characteristics of the short term (~ 5 sec) bursts occurring after 5:20 UT are consistent with pitch angle diffusion theory where weak pitch-angle diffusion operates most of the time, but the short bursts represent instances of strong pitch angle diffusion.

CHAPTER VI

DETAILED EXAMINATION OF BURST

[0604:30-0605:00 UT]

In Chapter V we indicated that the burst occurring from 0604:30-0605:00 UT was exceptional because of its anisotropic pitch angle distribution. This burst is also interesting because the rate at which electrons in the 0.5 - 30 KeV range deposited energy during the burst was about four times higher than what might be called a "background" rate (see figure 5.5 at 4:50 UT and at 6:30 UT). In analyzing auroral electron precipitation processes and break-up events in particular one is led to consider in more detail the characteristics of enhancements of the level of precipitation. Therefore we chose to examine this burst in detail in Chapter VI because it does signify an enhancement of the precipitation and because it was characterized by an anisotropic pitch angle distribution. A small note regarding our good fortune is that this burst happened ~12 seconds after the interference from the SESPEC ceased, the payload attitude was such that we had the least problem with telemetry dropout during this time period and the payload was at a high enough altitude (~230 km) during the burst that atmospheric collisions had a negligible effect upon electrons with pitch angles less than 65° .

Our primary concern in studying the burst was to find a way to parameterize the auroral electron differential energy spectrum. We have developed a set of parameters which accurately describe the energy spectrum. These parameters offer a bonus in that three of them can be associated with customary physical meanings. We begin this chapter by

describing our method of parameterizing, and then study the temporal development of these parameters and their interaction during the burst. The unusual pitch angle anisotropy of the burst will be examined next. Finally we will examine the theoretical implications of the data.

A. Parameterizing the Auroral Electron Differential Energy Spectrum.

In figure 6.1 we show the mirroring (M) electron differential energy spectra obtained from the PESPEC at 4:34.6 UT and 4:44.4 UT. The general features these two spectra have in common are: (i) a nearly power-law dependence of flux on energy from a maximum value at the lowest energy (~ 0.5 keV) to ~ 3 keV, (ii) a peaked region of the spectrum with the peak at ~ 10 keV, and (iii) a very steep drop for energies beyond the peak. An examination of figures 5.7 - 5.9 reveals that these features were present in the energy spectrum throughout the flight.

The shape of the energy spectrum at low energies suggests that we can fit the low energy portion by a power law spectrum,

$$\frac{dj}{dE} = J_0 E^{-n} \quad (6.1)$$

Equation (6.1) gives a straight line with slope $-n$ on a log-log plot. J_0 is the differential flux at 1 keV. Westerlund [1969] fitted his auroral electron "continuum" spectrum with the form of equation (6.1) with $n = 1.3 \pm 1.0$. Frank and Ackerson [1971] used a power law dependence with $n \sim 1.5-2.5$ to describe the low energy portion of the auroral electron spectrum measured by Injun -5.

Frank and Ackerson [1971] with auroral electrons, DeForest and McIlwain [1971] with equatorial measurements of electrons by ATS 5 (synchronous orbit at $6.6 R_E$) and Hones, et al [1971] with plasma sheet electrons have fitted the peaked portions of the energy spectrum to a Maxwellian energy dependence

$$\frac{dj}{dE} \propto E e^{-E/kT} \quad (6.2)$$

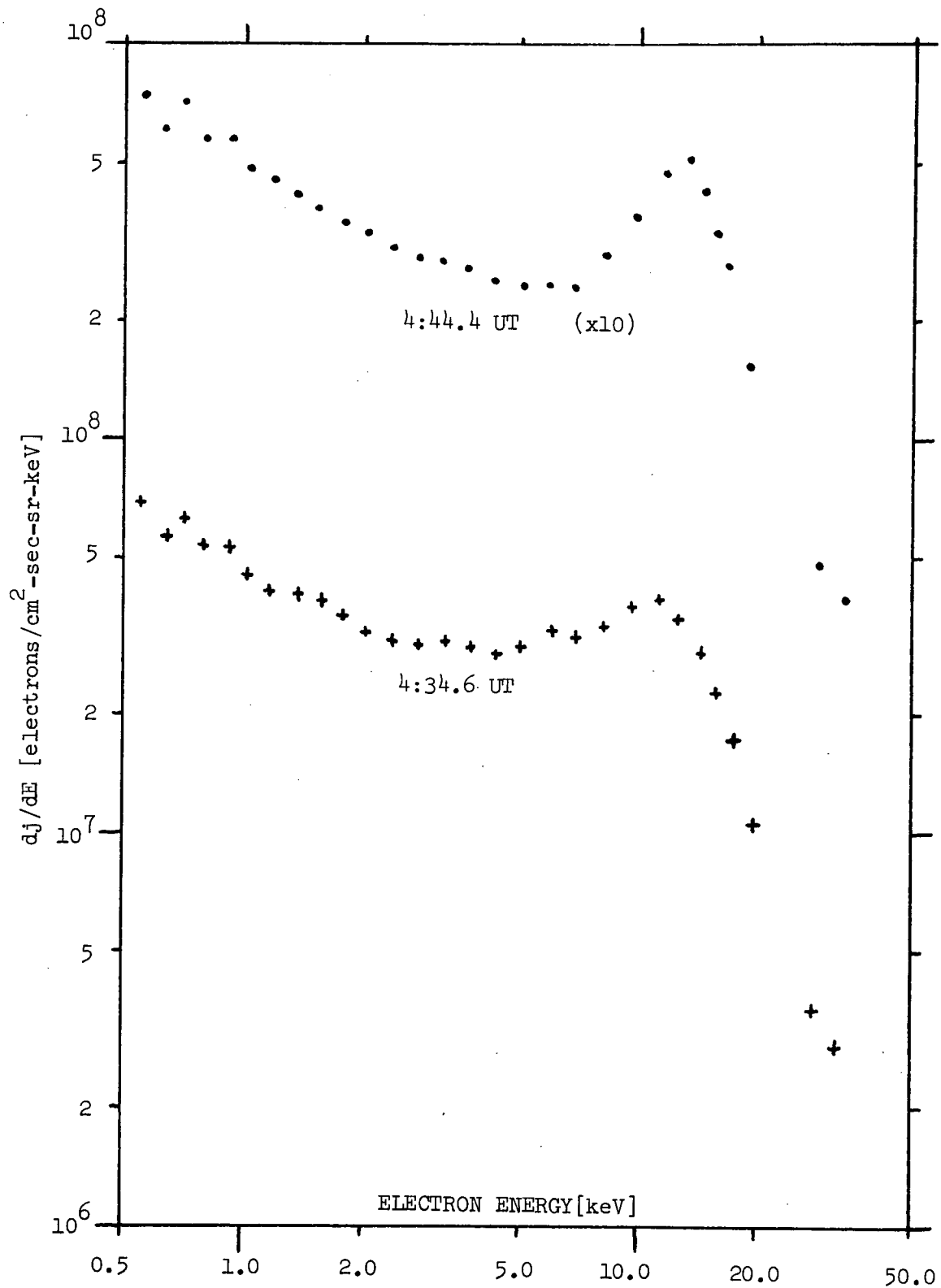


Figure 6.1. Mirroring (M) electron differential energy spectra
(Note shift of origin for upper spectrum)

where the temperature T is determined by the energy and width of the peak (the peak is at $E = kT$). They report values of kT/e from ~ 100 eV to ~ 6 keV.

The peaks in figure 6.1 cannot be fitted by equation (6.2) because to have a peak value at ~ 10 keV one needs a wider peak than is observed. For example if $kT = 10$ keV in equation (6.2) the flux at $E = 30$ keV would be $\sim 40\%$ of the peak flux - obviously it is much less than 40% . One therefore needs to introduce another parameter which will allow independent determination of the peak position and temperature (peak width). We elected to fit the peaked portion of the energy spectrum with the energy dependence of a Maxwellian electron gas with directional density, n_e [electrons $\cdot \text{cm}^{-3} \cdot \text{sr}^{-1}$], and temperature, T_e [keV], moving relative to the observer with a velocity corresponding to an electron kinetic energy, E_o (the directional density is customarily used when the detector is unidirectional rather than omnidirectional). Equation (6.3) gives the functional dependence of these parameters,

$$\frac{dj}{dE} \propto \frac{n_e}{(T_e)^{3/2}} E e^{-(E + E_o - 2\sqrt{E E_o})/T_e} \quad (6.3)$$

As was described in Chapter II it is a non-trivial task to determine $\frac{dj}{dE}$ from the counts N_i . Before we began trying to fit the energy spectrum we had to determine the best combination of order of fit and number of points to use. In general with the piecewise polynomial unfolding technique described in Chapter II one wants to use the lowest order polynomial because cubic and higher order polynomials may

introduce spurious maxima and minima between the fitted points. Yet by using a quadratic form one can still be assured of proper response to any "monoenergetic" components in the spectrum. Figure 6.2 shows the distribution of counts N_i which would result from a monoenergetic energy distribution centered at 10.9 keV. The five data words which have flat spectrum energies E_i nearest 10.9 keV account for over 90% of the counts. The solid line in figure 6.2 shows the result of applying the unfolding technique described in chapter II to the counts. We used a quadratic ($j_{\max} = 3$) form for equation (2.24) and a fit over five N_i at a time. This procedure was then used to unfold the energy spectra of all the data for the four averages (D, M, P and U) described in Chapter IV.

The technique used to fit equations (6.1) and (6.3) to the $\frac{dj}{dE}$ was to first fit the low energy region ($E < 3$ keV) to equation (6.1) to determine J_0 and n . Then starting at the maximum energy the quantity

$$\frac{dj'}{dE}(E_i) \equiv \frac{dj}{dE}(E_i) - J_0 E_i^{-n} \quad (6.4)$$

was computed. Figure 6.1 shows that this quantity which represents the difference between the actual spectrum and an extrapolated value of the low energy spectrum will be negative for the first few, highest energies. We computed $\frac{dj'}{dE}(E_i)$ for successive E_i until we had at least two positive values. Then beginning with the second positive value $\frac{dj'}{dE}(E_i)$ was computed for all the lesser E_i . These $\frac{dj'}{dE}(E_i)$ were then fitted by equation (6.3).

Equation (6.3) is linear only in the electron density, n_e , and

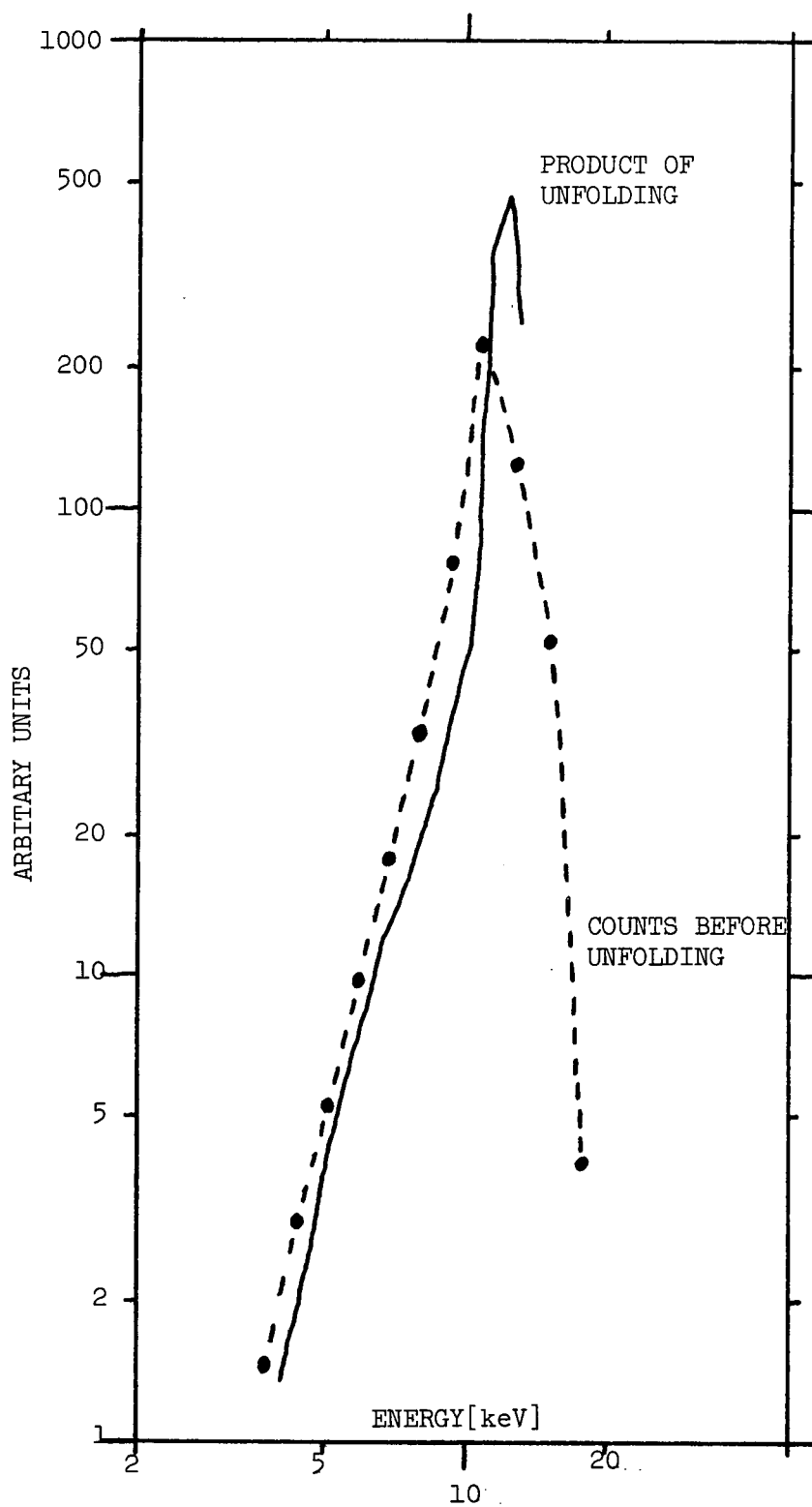


Figure 6.2. Counts which would be measured from a monoenergetic spectrum and results of applying unfolding technique to the counts.

therefore we were unable to analytically fit for E_o and T_e . The technique used to simultaneously determine E_o and T_e involved an iterative direct search over E_o and T_e space to minimize the sum of the squares. The resolution in T_e was 30 eV, and the resolution in E_o was 200 eV. When the fitting procedure was applied to the unfolded monoenergetic spectrum of figure 6.2 the best fit had the smallest available temperature, 30 eV.

After E_o , T_e and n_e were determined the fitted $\frac{dj'}{dE}$ was subtracted from the initial, high energy $\frac{dj}{dE}$ values, and the residuals were fitted with the form of equation (6.1).

Figure 6.3 shows the results of fitting the two energy spectra in figure 6.1. The parameters for $t = 4:34.6$ and $t = 4:44.4$ are given in Table 6.1.

TABLE 6.1

<u>time</u>	<u>J_o</u>	<u>n</u>	<u>n_e</u>	<u>T_e [eV]</u>	<u>E_o [keV]</u>
4:34.6	4.83×10^7	0.491	9.50×10^{-4}	900	8.8
4:44.4	5.08×10^7	0.577	4.47×10^{-4}	450	11.6

The average error in these fits was less than 6%. Throughout the whole flight the typical error was ~8% with ~95% of the spectra having an average error less than 10%. The higher the value of T_e the better we were able to fit the spectra with these functions. Using the University of Maryland Univac 1108 computer we were able to fit more than three spectra per second of execution time.

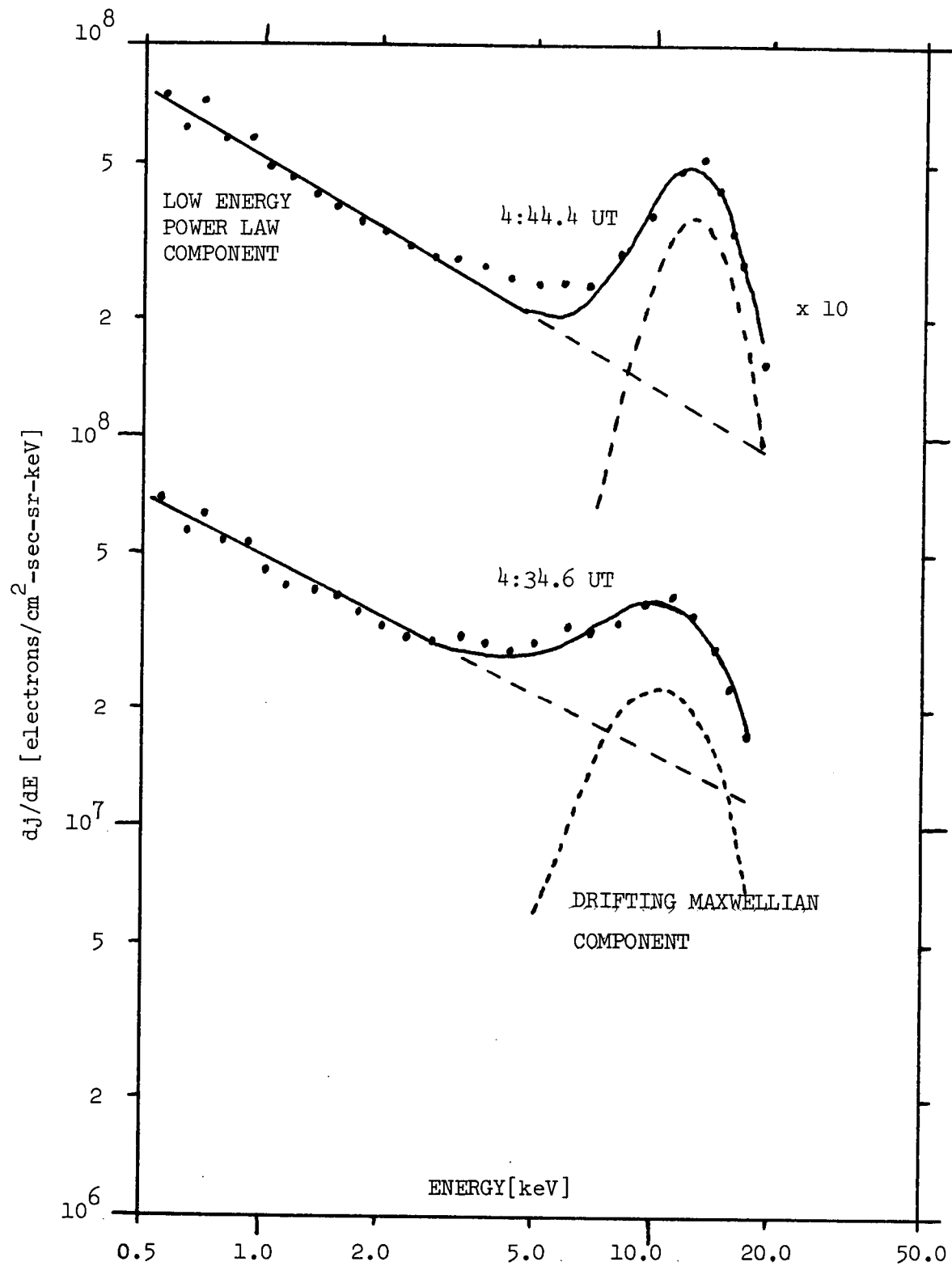


Figure 6.3. Results of fitting differential energy spectra,

B. Observations of Interchange between Acceleration and Thermalization Processes during the Burst

We have determined the values of the parameters describing the auroral electron differential energy spectra which were themselves unfolded from the count data for the three averages (D, M, and P) for the time from 0604:20 UT to the end of the flight. Figure 6.4 shows the values of J_0 , the parameter specifying the magnitude of the low energy flux, for the D, M and P averages. This figure shows the remarkable isotropy of the low energy electrons for all times except the burst period. Figure 6.5 shows the values of the exponent, n , which describes the slope of the spectrum. Interestingly all the values of n are such that $0.40 < n < 0.65$. Recall that Westerlund [1969] and Frank and Ackerson [1971] also observed very consistent though different values of the exponent, n , in a similar energy interval.

In figure 6.6 we show the values of the parameters describing the peaked portion of the energy spectrum, E_0 , T_e and n_e for the precipitating (P) electrons for the complete time period. The value of E_0 ranges between 6 and 13 keV. This parameter is by no means constant or monotonic (see Albert [1967] who reports observing a monotonically increasing energy corresponding to the position of the peak) the maximum rate of change being from $E_0 = 6.6$ keV @ 6:10.9 UT to $E_0 = 10.4$ keV @ 6:14.7 UT. The variation of E_0 during the burst time period is also complex - it has two local minima and two local maxima during the burst. By comparing figure 6.6 and figure 5.5 which shows the total energy deposited by the precipitating, P, electrons we observe that, excluding the burst time period, from ~ 5:25 UT to the end of the flight fluctuations in E_0 agree in time and direction

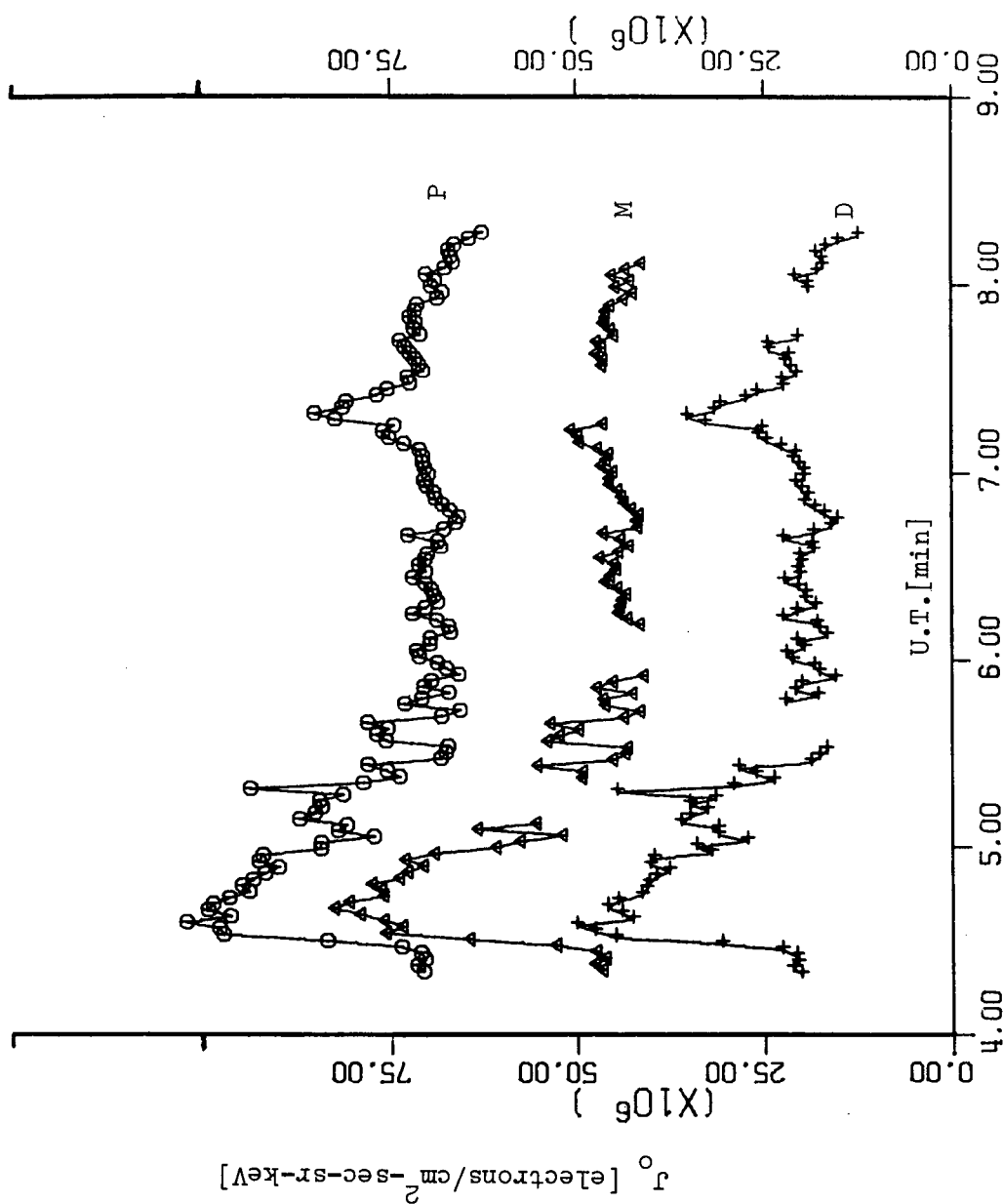


Figure 6.4. Values of J_0 , the low energy power law parameter, for D, M, and P averages (note each succeeding curve has origin displaced by 25×10^6)

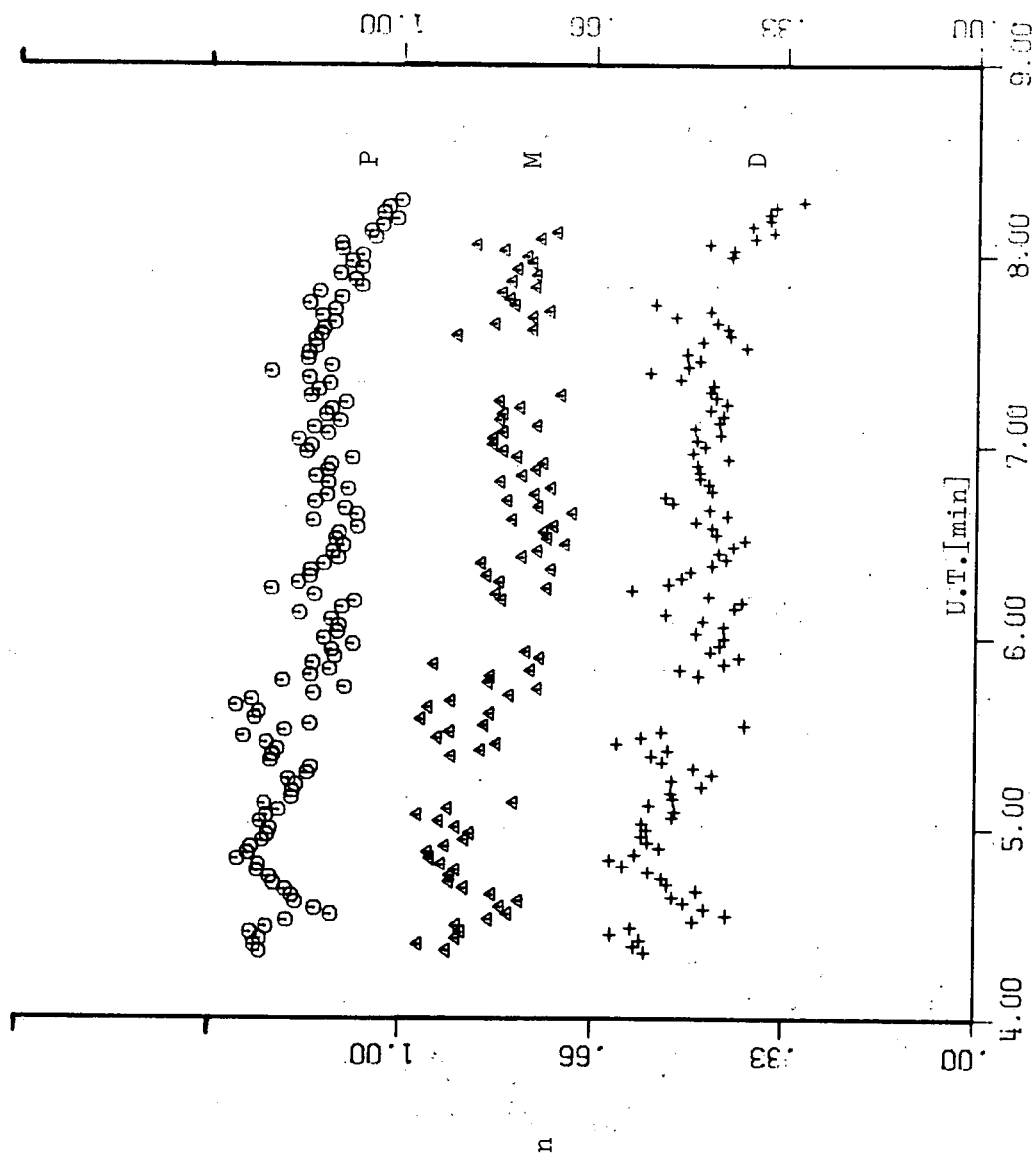


Figure 6.5. Values of low energy power law exponent, n , for D, M, and P averages (note each succeeding curve has origin displaced by 0.33)

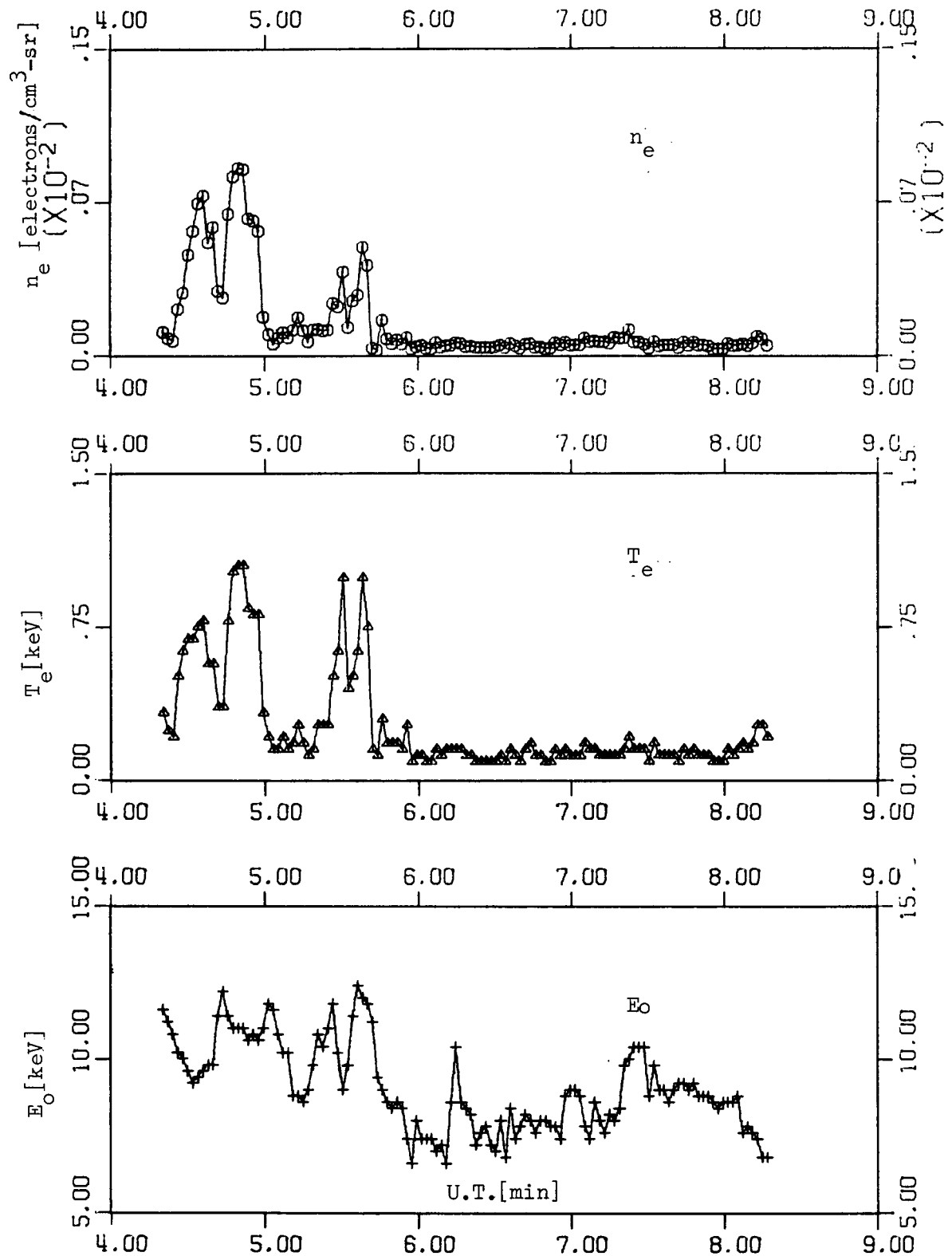


Figure 6.6. Drifting Maxwellian parameters E_0 , T_e , and n_e for complete time period for P average electrons.

if not in magnitude with fluctuations in the energy deposited. This does not seem to be true during the burst. For example both the precursor and afterpulse in the energy deposited (@4:36.4 UT and 4:55.8 UT) occur at local minima of E_o .

The electron temperature, T_e , which is a measure of the width of the peak varies between 90 and 1050 eV. The directional electron density varies between 2.4×10^{-5} and 9×10^{-4} electrons - cm^{-3} - sr^{-1} . From figure 6.6 we observe a correlation between T_e and n_e . For example at 4:36.1 UT both n_e and T_e have local maxima, and then at 4:43.9 UT they both have local minima. We have examined this interdependence in more detail. Figure 6.7 shows the values of T_e as a function of n_e for the burst time period (actually 4:20 - 5:05 UT) for all three averages - dumped, mirroring and precipitating electrons. We have fitted these values with a function of the form

$$T_e = k n_e^{\gamma - 1} \quad (6.5)$$

The values of γ were:

$$\gamma_D = 1.65 \quad \gamma_M = 1.51 \quad \gamma_P = 1.60$$

For $t > 0605:40$ UT both T_e and n_e are approximately constant and at their lowest values indicating that the peaked portion of the spectrum was less significant after 5:40 UT. To some extent it is possible to find correlations between fluctuations of the parameter J_o and either E_o , T_e or n_e , but for the sharp (~2 sec) burst in low energy electrons at 5:19 UT in figure 6.4 there is no significant change in either E_o , T_e or n_e .

Frequently one can observe a relationship between E_o and T_e .

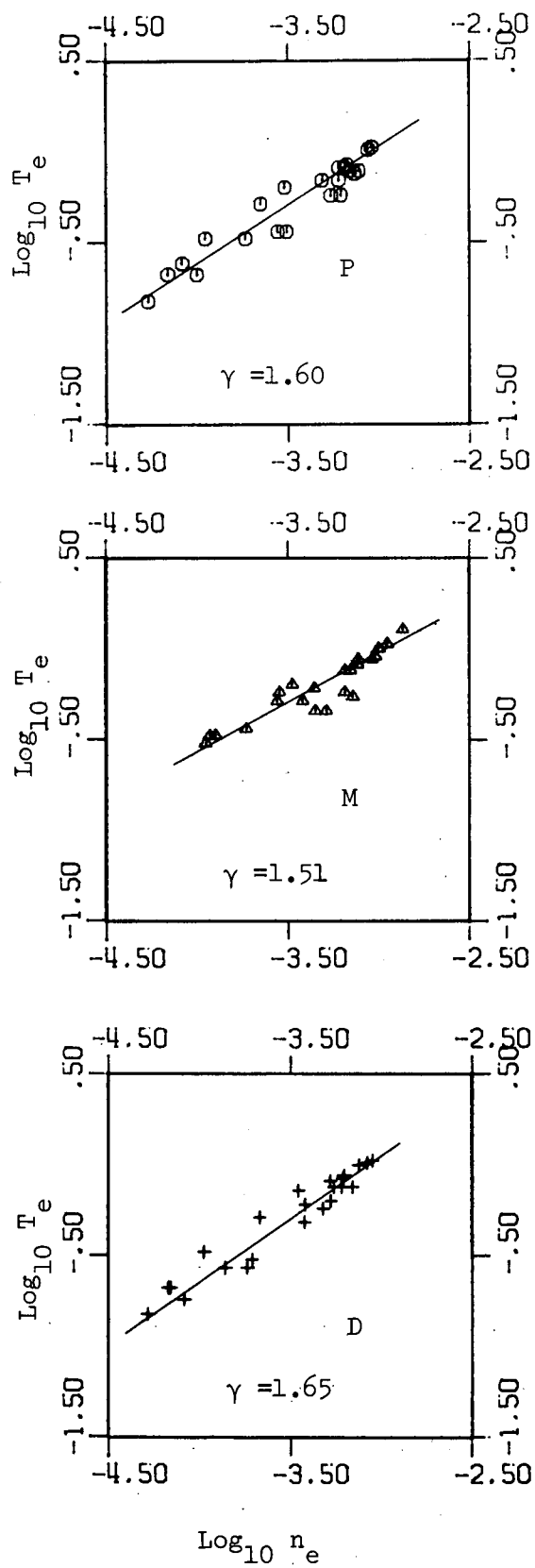


Figure 6.7. Relationship between T_e and n_e for burst time period indicating adiabatic compression

Figures 6.8 and 6.9 show the parameters E_o , T_e and n_e for the dumped (D) and mirroring (M) electrons during the burst. For all the D, M and P averages the time profiles of the parameters E_o , T_e and n_e are essentially the same throughout the burst. From 4:20 UT to ~4:34 UT we observe a decrease in E_o from ~11.5 keV to ~9 keV. Beginning at ~4:24 UT this decrease in E_o was accompanied by an increase in T_e and n_e . T_e and n_e attain local maxima at essentially the time E_o reaches a local minimum. Because it represents a conversion from a higher relative velocity, colder energy distribution to a slower, hotter distribution we call this process a thermalization of the peaked portion of the energy spectrum. We do want to emphasize that we are not moving with and constantly observing the same electron population. Properly one should say that the electrons arriving at 4:34 UT were hotter and moving at a slower apparent relative velocity than the electrons arriving at 4:24 UT.

In the next 10 seconds we observe the opposite of the thermalization process. From 4:34 UT to 4:44 UT the parameter E_o increases while T_e and n_e decrease. While qualitatively the situation at 4:44 UT appears to be the same as 20 sec earlier at 4:24 UT a subtle quantitative difference remains. This difference appears mainly in n_e which for the mirroring electrons for example have increased fourfold from 1.1×10^{-4} electrons $\text{cm}^{-3} \text{sr}^{-1}$ at 4:24.8 UT to 4.5×10^{-4} electrons $\text{cm}^{-3} \text{sr}^{-1}$ at 4:44.4 UT (one can call a fourfold increase subtle when it follows the order of magnitude increase from 4:24 UT to 4:34 UT). From figure 6.10 we can observe the resultant effect of these variations of E_o , T_e and n_e upon the total energy in the Maxwellian, peaked portion of the spectrum for the dumped, mirroring and precipitated

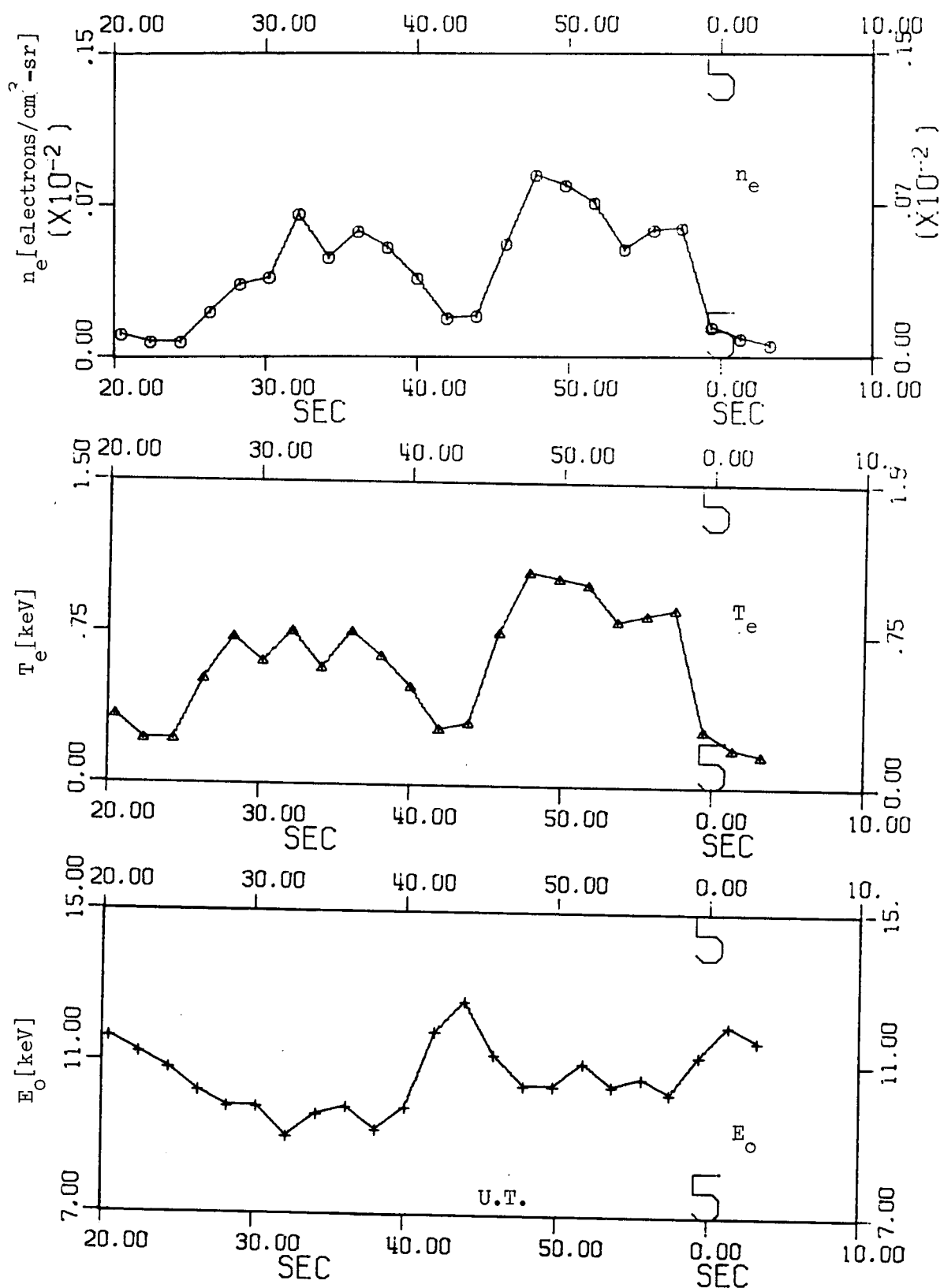


Figure 6.8. Dumped (D) electron parameters E_o , T_e , and n_e during burst.

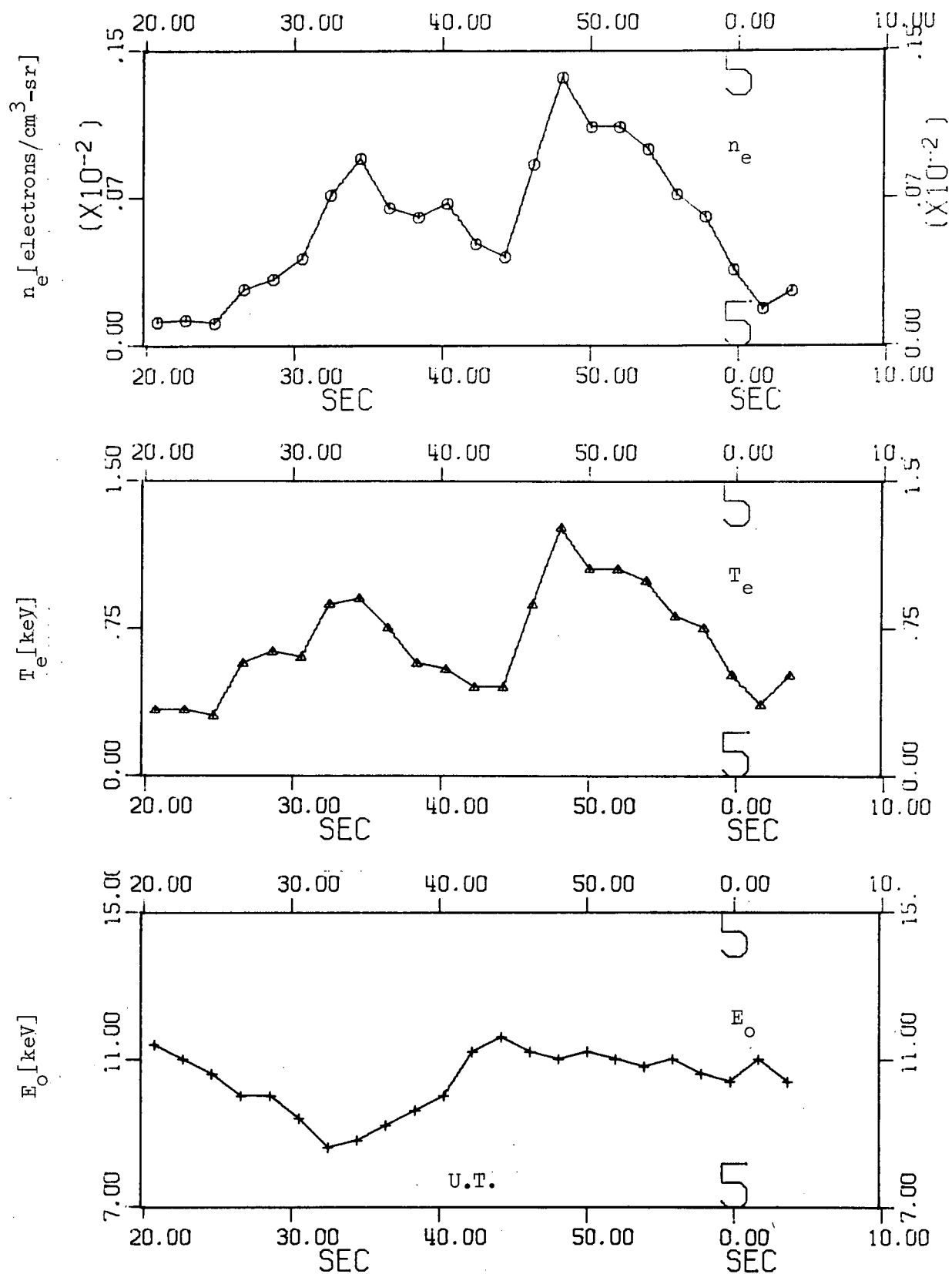


Figure 6.9. Mirroring (M) electron parameters E_o , T_e , and n_e during burst.

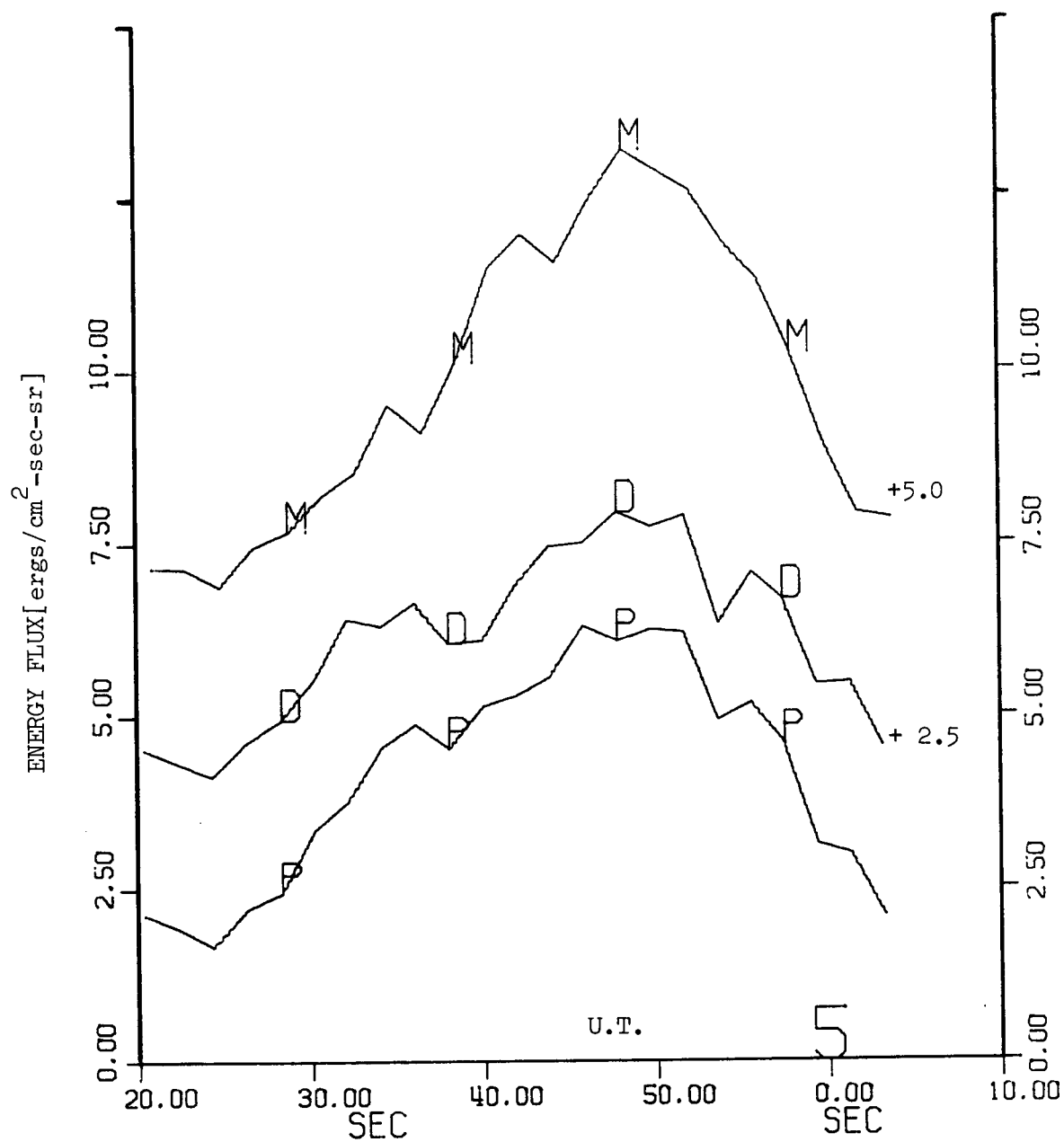


Figure 6.10. Energy flux in Maxwellian portion of spectrum for D, M, and P averages (note each succeed-curve displaced by 2.5 ergs/cm²-sec-sr)

electrons. We see that despite the variations of E_o and T_e the general pattern from 4:24 UT to ~4:50 UT is one of an increasing amount of energy in the Maxwellian portion (all three averages do show a small dip around ~4:36 UT when each T_e begins to fall, but apparently subsequent increases in E_o and the "subtle" fact that the densities do not recede all the way to their pre-burst values overtakes the effect of the falling temperature).

In figure 6.11 we have plotted the times of peak flux for the precipitating (P) electrons at a given energy in the time interval 4:34 UT - 4:44 UT. The energy range from 5.05 keV (word 13 during the voltage sweep) to 15.0 keV (word 6) was used because it represents the energy interval of the peaked portion. We computed the three highest flux levels for each word in the time interval, and each point gives the energy and time of one of the three. The pattern in energy-time space is suggestive of an acceleration process. The lower energy (5 keV) electrons have their peak flux at ~4:34 UT. And each higher energy has its peak flux at a later time until finally the 15 keV electrons have their peak at ~4:44 UT. Figure 6.12 shows the time profiles for the precipitating electron flux for words 6-10 (8 - 15 keV) during the burst. One can observe a peak moving from ~4:40 UT for word 10 to ~4:44 UT for word 6. Because of the energy-time dependence of this peak and the increasing relative velocity (E_o increases) of the Maxwellian peak we ascribe an acceleration process to this time period.

From figures 6.6, 6.8, and 6.9 we see that after E_o reached the local maximum at ~4:44 UT the thermalization process began anew with E_o decreasing and T_e and n_e increasing. The maximum temperatures

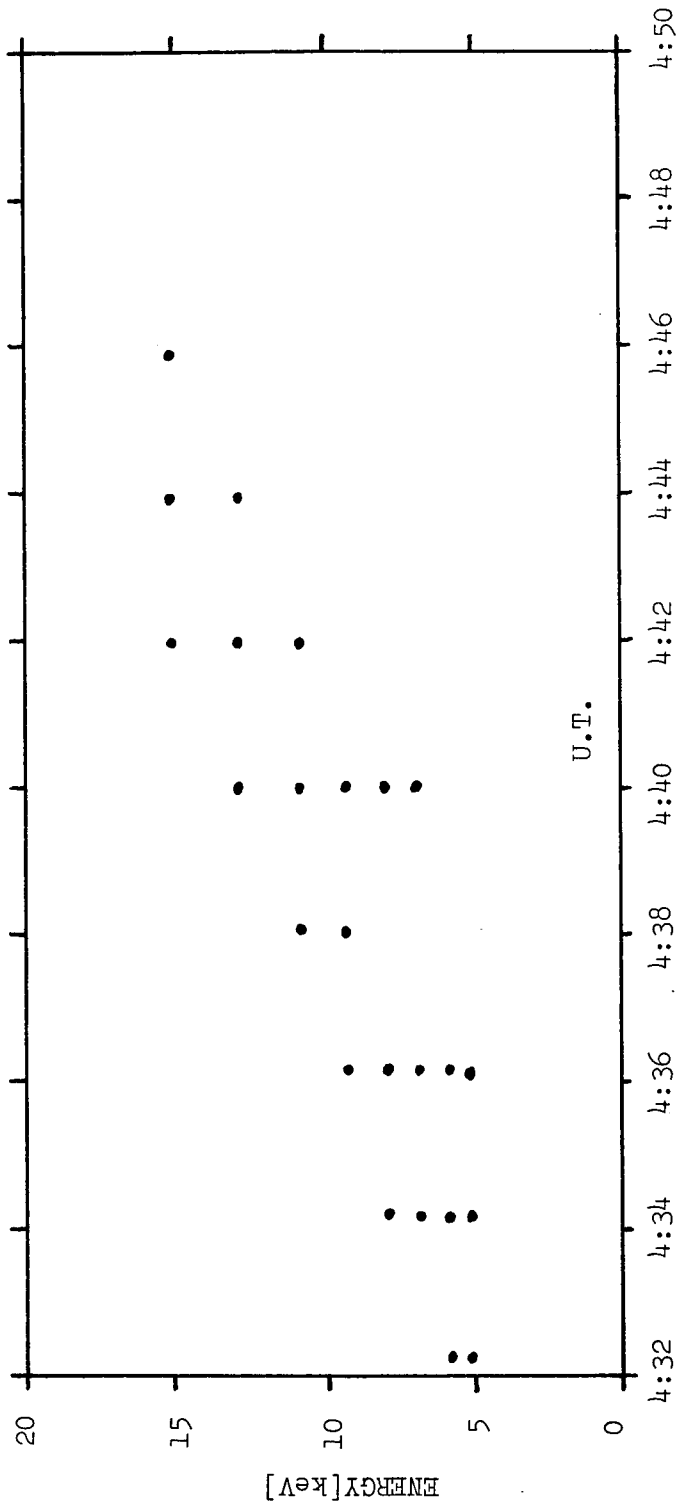


Figure 6.11. Time of occurrence of three highest levels of intensity at energy, E, during acceleration process (P average electrons)

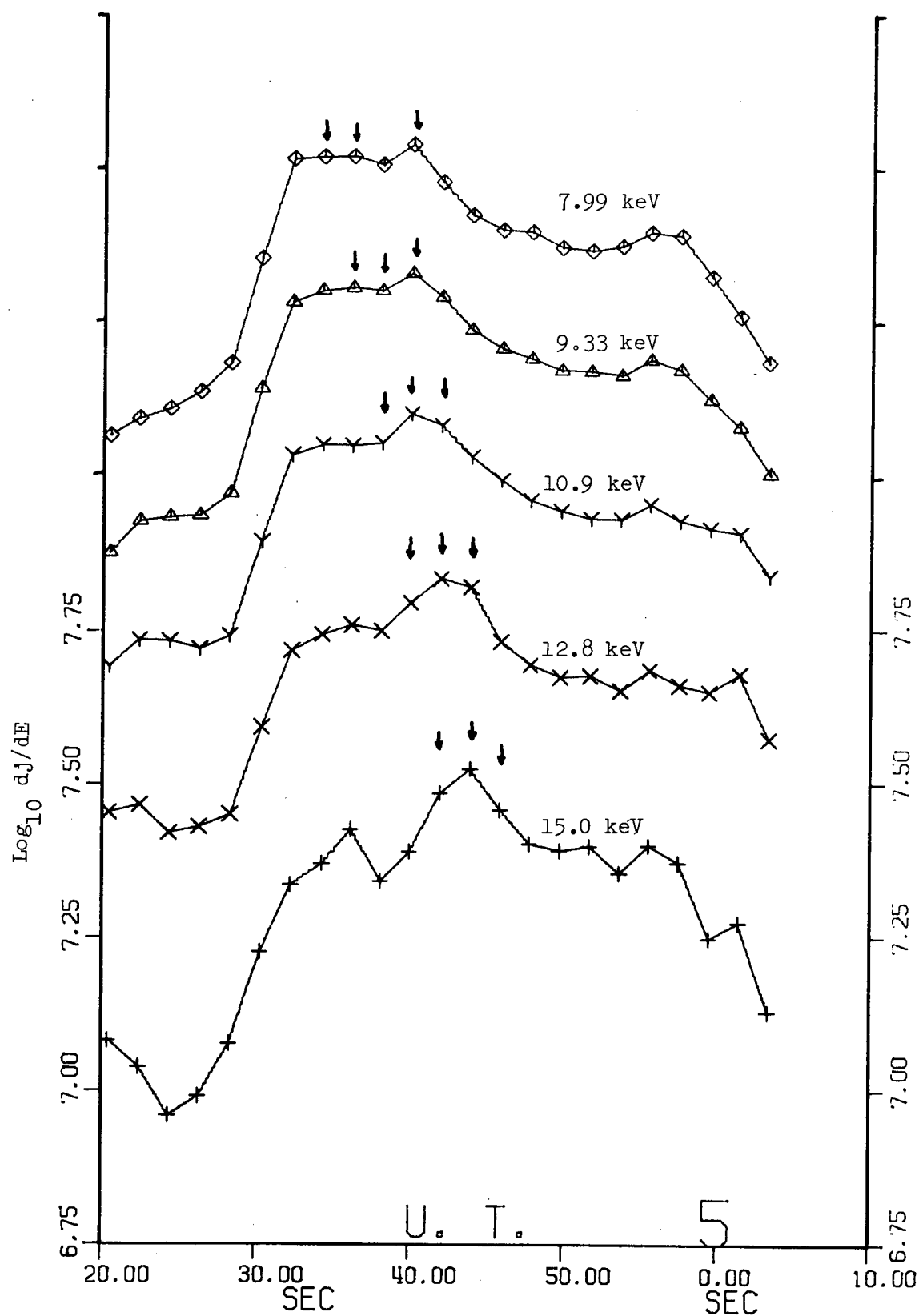


Figure 6.12. Acceleration process showing earlier arrival of peak at lower energies-P average electrons
(note each succeeding curve displaced by 0.25)

were attained around 4:50 UT, however the temperatures remained above ~ 800 eV until $\sim 4:59$ UT when the dumped and precipitating E_o parameters increased and the temperatures fell. The mirroring electrons did not share the time profile of the dumped and precipitating electrons in this time interval (4:55 - 5:05 UT). From figure 6.9 we observe that for the mirroring electrons E_{oM} (the 'P', 'D' and 'M' subscripts identify the average from which they were computed) remained between 10.4 - 11.0 keV (nearly constant) while E_o for the dumped electrons (see figure 6.8) went from $E_{oD} = 10.2$ keV @ 4:57.4 UT to $E_o = 12.0$ keV @ 5:01.4 UT. It is unfortunate that a least squares determination of nonlinear parameters (E_o and T_e in our case) cannot provide estimates of the uncertainties in the parameters.

Throughout most of the flight E_{oD} , E_{oM} and E_{oP} (determined from the dumped, mirroring and precipitated electron energy spectra) are in agreement to ± 0.50 keV. However there are several occasions similar to that at $\sim 5:00$ UT where kilovolt or larger differences occur between E_{oM} and E_{oD} or E_{oP} . From figures 6.8 and 6.9 one can observe that the T_e and n_e profiles are different for the dumped and mirroring electrons in the time 4:55 - 5:05 UT. T_{eM} and n_{eM} are linearly decreasing whereas T_{eD} and n_{eD} have a precipice type profile with a steep decline coinciding with the upswing of E_{oD} at 4:59.4 UT. We also note that in the region where E_{oD} is ~ 1 keV larger than E_{oM} the mirroring electron temperature is ~ 400 eV whereas $T_{eD} \sim 200$ eV.

Figure 6.10 shows that all three averages reach their maximum levels of energy deposited at 4:48.5 UT which corresponds to the maximum values of electron temperature. In figure 6.13 we show the fraction of the total energy deposited for each average which was due to

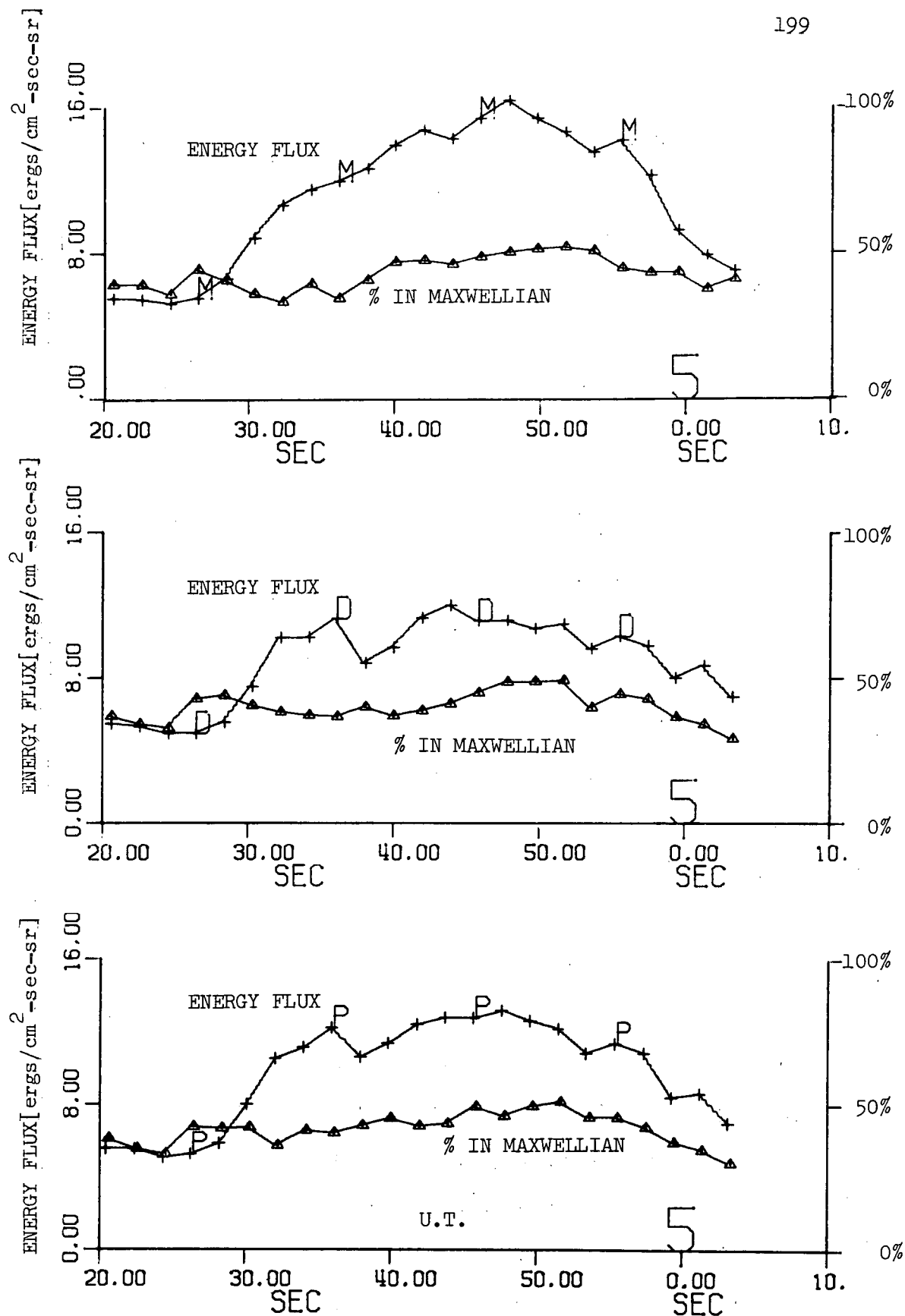


Figure 6.13. Total electron energy flux and percentage in drifting Maxwellian component

the Maxwellian or peaked portion of the energy spectrum. Throughout the burst for all three averages the Maxwellian component accounts for from 25% to 55% of the total energy in the entire spectrum, the largest fraction of the total energy occurring at ~4:50 UT. The peaks in figure 6.13 occur at nearly the same time as the peaks in figure 6.10 which shows the total energy in the Maxwellian component.

Figure 6.13 shows that for the mirroring electrons initially the Maxwellian component accounts for ~40% of the total energy. At ~4:27 UT there is a small peak in the fraction due to the Maxwellian component indicating (see figures 6.4 and 6.9) that the thermalization of the Maxwellian began slightly (~5 seconds) before the steep rise in the low energy component. The sharp increase in the low energy electrons beginning about 4:30 UT causes the fraction due to the Maxwellian to fall below 40% from ~4:30 - 4:38 UT. From 4:40 UT to the end of the burst the Maxwellian contribution to the energy deposited increases and remains above the pre-burst 40% level.

The P.H.A. measured electrons with energies much higher than the energies of the peaked portion of the spectrum. The agreement between the P.H.A. and PESPEC in the overlap region around 22 keV was not good (see figure 6.14 for a comparison at the peak of the burst). As were partially discussed in Chapter II reasons for disparity were; (i) large uncertainty in low energy response of aluminum foil-plastic scintillator, (ii) very soft (steep) energy spectrum (power law exponent of 4-5), (iii) uncertainty in efficiency of aluminum electron multiplier, $\eta(E)$, at high energies, (iv) unusual angular resolution quality of PESPEC, (v) the spectrum unfolding technique must give exceptional

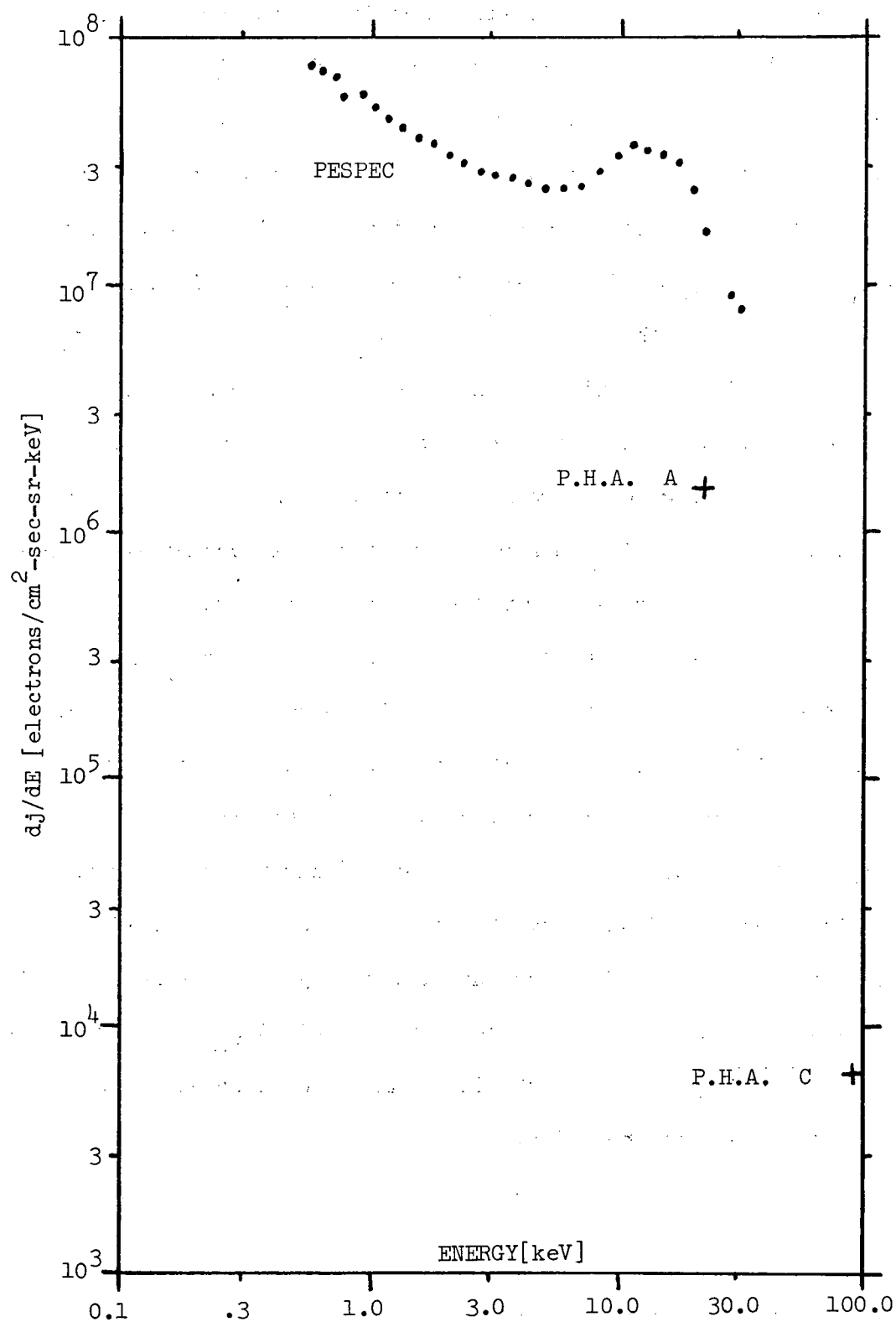


Figure 6.14. Comparison of PESPEC and P.H.A. fluxes at peak of burst.

treatment to the initial and final few data words and (vi) a possible background of ~50 counts per word would tend to raise the PESPEC flux determination for the first few words but would have very little influence on the rest of the words where the counts are over 1000. We emphasize that values of $\frac{dj}{dE}$ computed from the first few words were not used to compute T_e , n_e and E_o (see section A this chapter). Figure 6.15 shows the values of the power law exponents used to describe the 40° and 70° pitch angle high energy ($E > 20$ keV) electrons during the burst. The 40° pitch angle electrons have $4 < n < 5$ during the burst with a gradual progression towards the softer (n larger) spectrum. The 70° pitch angle electrons have a much more variable spectrum with n ranging from less than 3.5 to more than 5. The onset of the burst at 4:30 UT is marked by a softening of the spectrum, and this is consistent with the steep increase in the low energy electrons in figure 6.4. During the peak of the burst the spectrum at both pitch angles hardens but the change at 70° pitch angle is much larger. The value of $n \sim 3.3$ for the 70° pitch angle electrons indicates a very hard spectrum, but it is by no means exceptional because from ~0605:40 UT to the end of the flight n is less than 3.3. The significance is of course that at 4:49 UT J_{OPHA} (the one kilovolt extrapolated value of the PHA flux) is much larger than it is in the latter part of the flight.

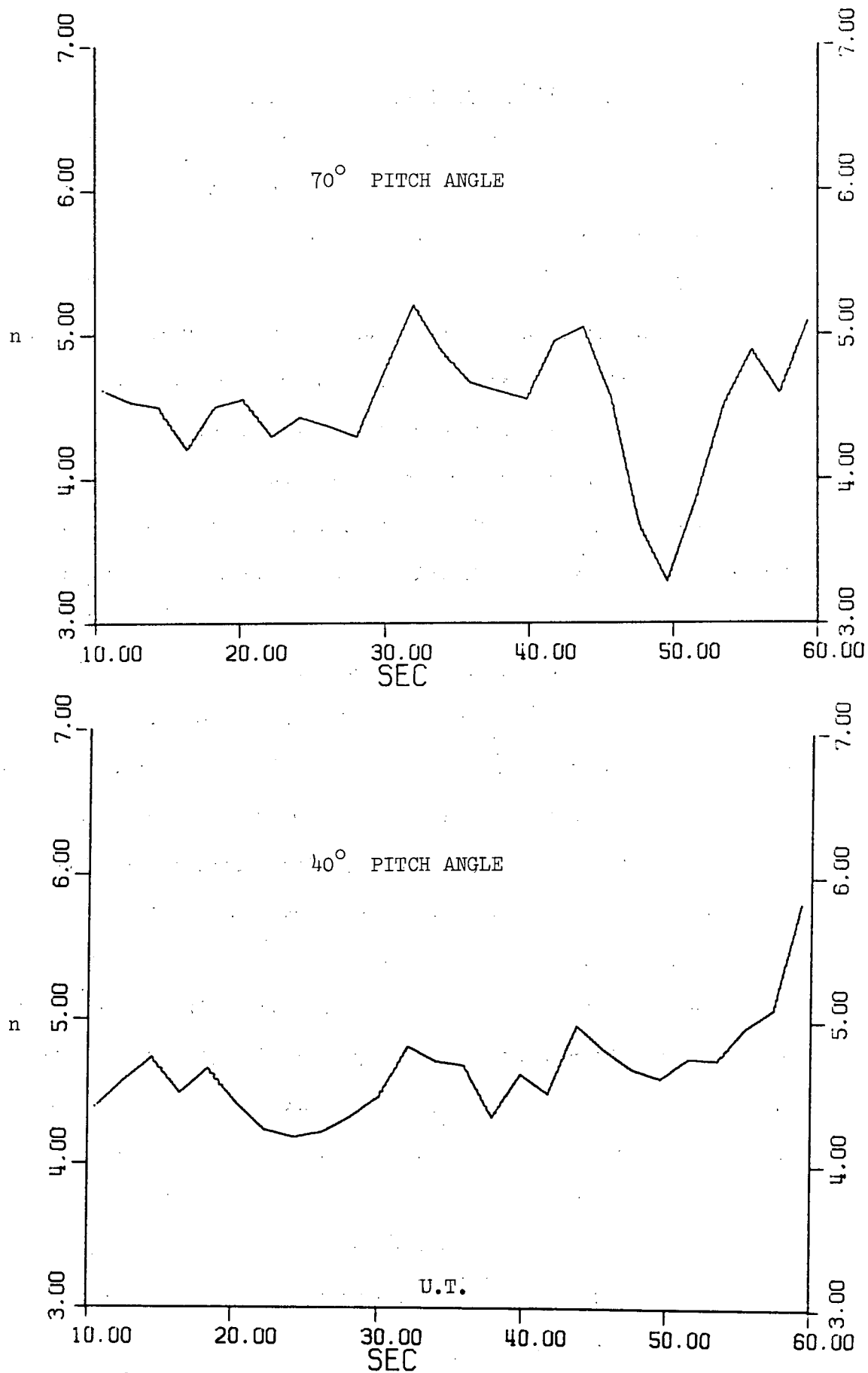


Figure 6.15. Variation of high energy power law exponents during burst

C. Pitch Angle Distributions During the Burst

The burst of an enhanced level of electron precipitation from 0604:30 - 0605:00 UT was characterized by an anisotropic pitch angle distribution wherein the flux at pitch angles less than 45° was smaller than the flux of mirroring electrons. The 18:63 UE P.H.A. provided better pitch angle information than the PESPEC. The P.H.A. angular resolution was defined by the rather large 11° half-angle acceptance cone. The large acceptance angle necessitated the use of the pitch angle unfolding technique described in equations 2.57 - 2.63. The ability of the PESPEC to provide detailed pitch angle information was severely curtailed because it accepted electrons from both slots.

Figures 6.16 and 6.17 show the counts per word in channel A of the 18:63 UE P.H.A. from 4:20 - 5:00 UT. Also shown is the pitch angle of the detector. The detector pitch angle response has been unfolded, and the dead time and overranging corrections have been made. The flat peaks of the count profiles indicate pitch angle isotropy over the downward hemisphere for electron energies from 20 - 40 keV (the nominal channel A energy interval) until 4:28.5 UT. At that time a structure with two peaks per roll begins to form. The peaks are at $\sim 70^\circ$ pitch angle. The profile is not symmetric over one half roll because the counts at $\alpha \sim 100^\circ$ are less than those for $\alpha \sim 10^\circ$. In figure 6.18 we present a contour display of the counts as a function of time and pitch angle α from 4:00 - 5:00 UT. The development of the anisotropy is seen as a relative peak near $\alpha = 70^\circ$ beginning $\sim 4:29$ UT. The count rate is a maximum for $50^\circ < \alpha < 90^\circ$ and $4:47 < t < 4:52$ UT. One can observe that the anisotropy is not

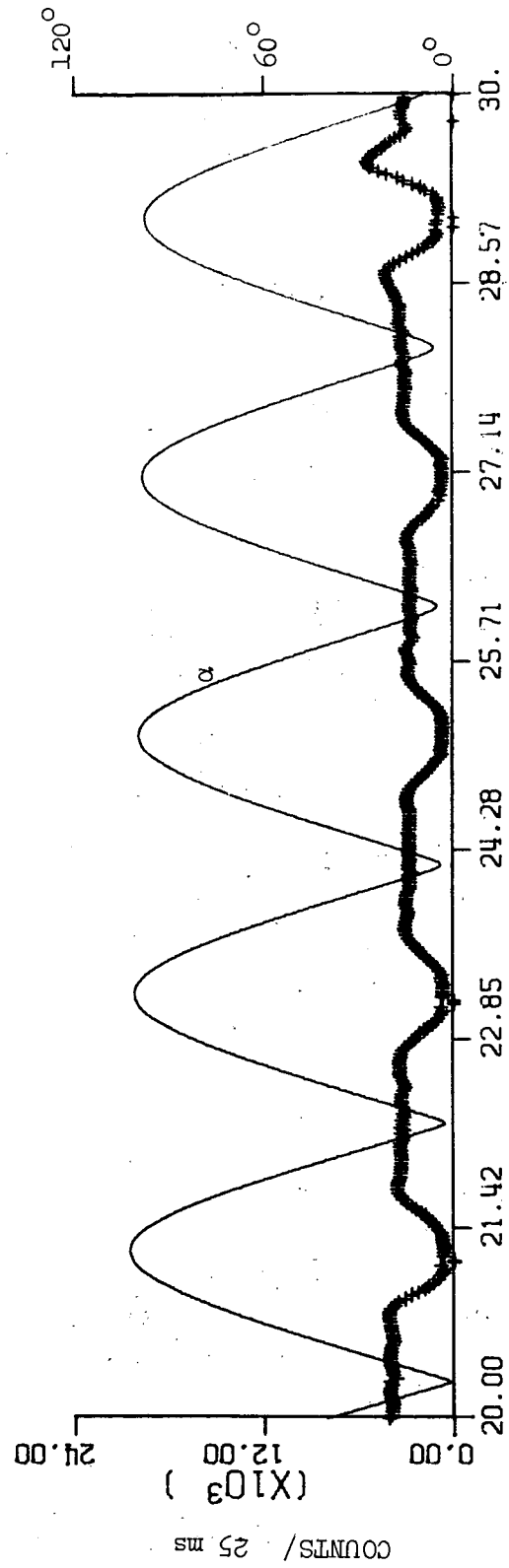
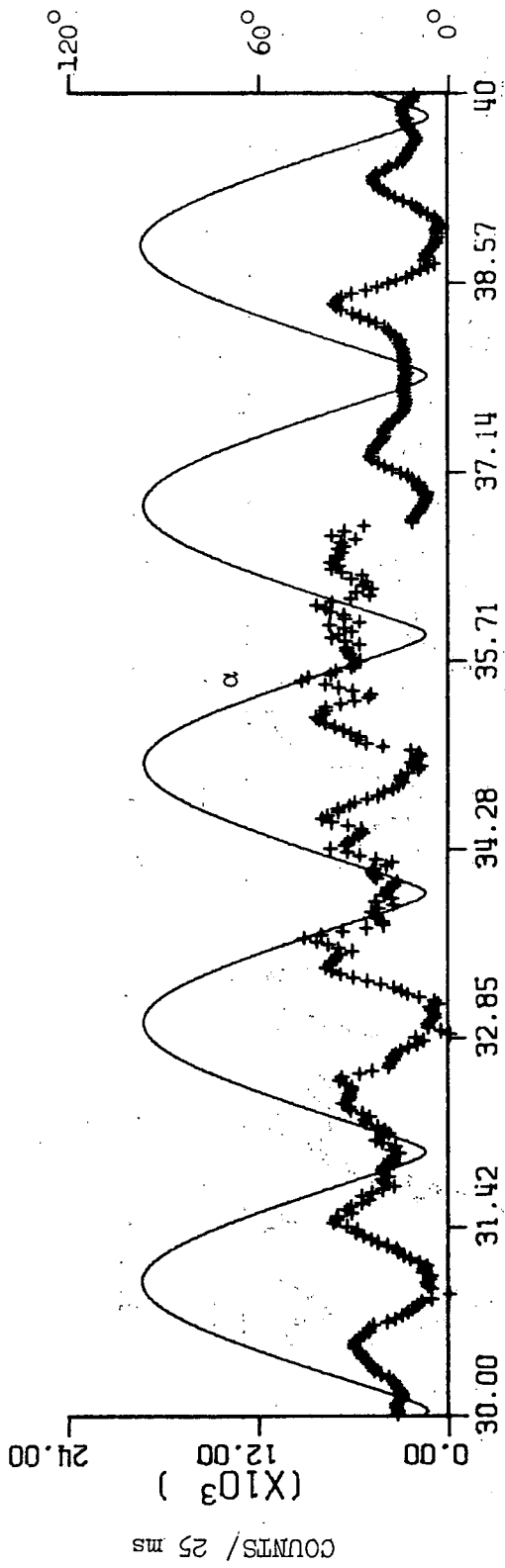


Figure 6.16. Channel A counts and P.H.A. pitch angle versus time

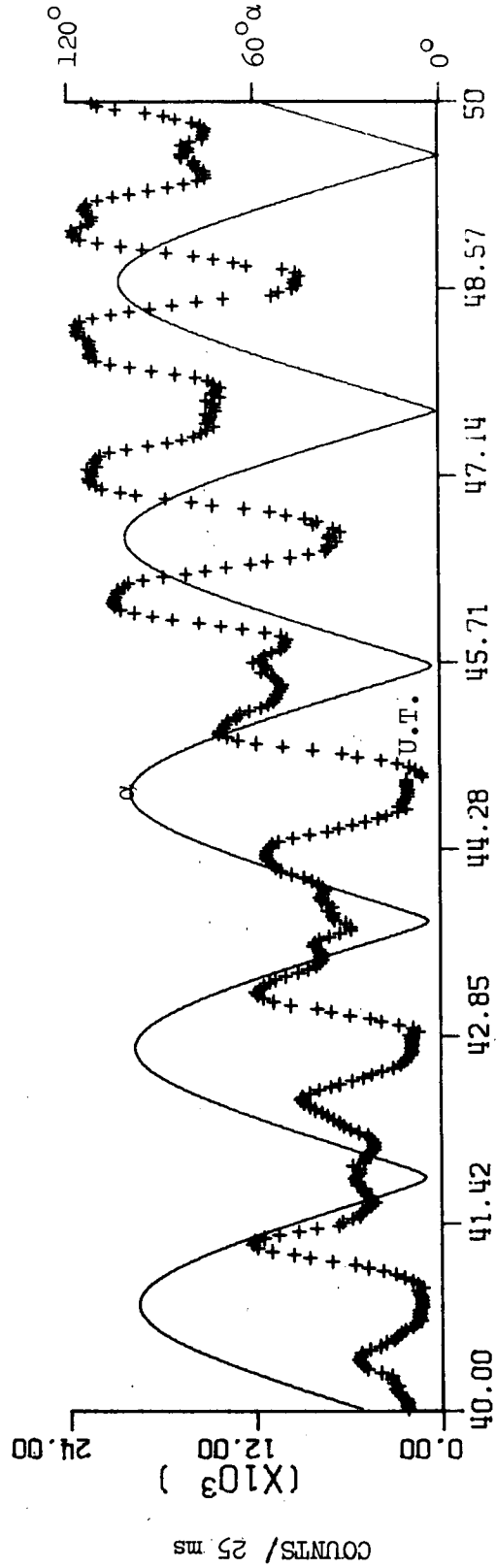
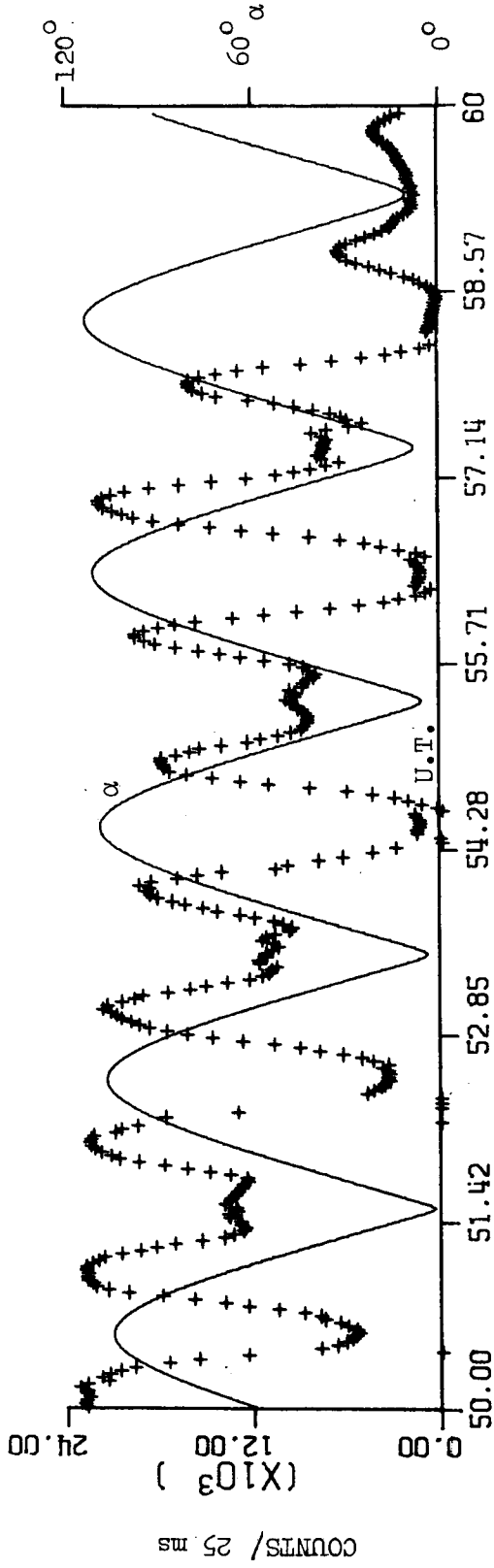


Figure 6.17. Channel A counts and P.H.A. pitch angle versus time

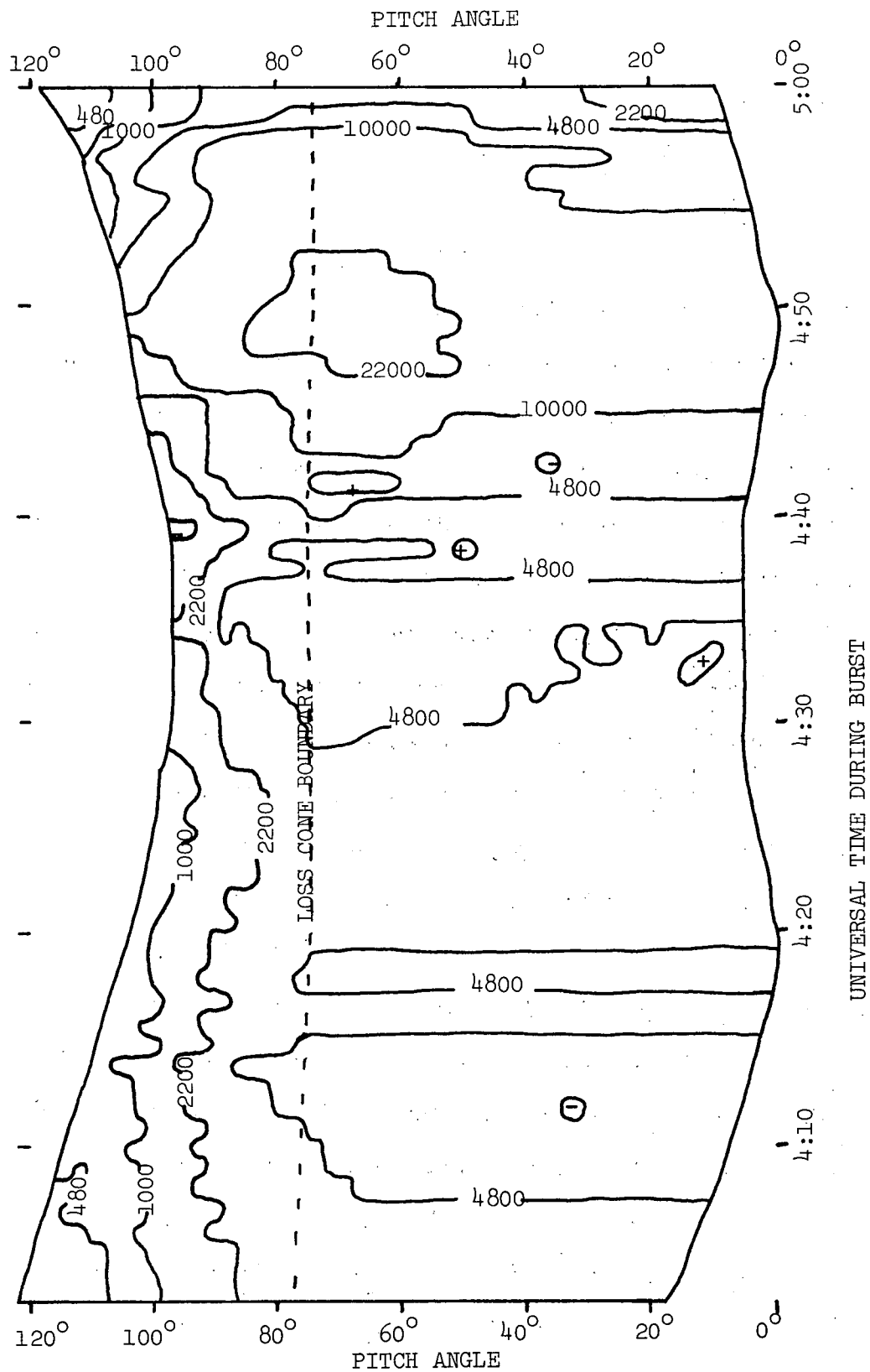


Figure 6.18. Contours of constant channel A counts in time-pitch angle space

due solely to an increase in the flux centered at $\alpha = 70^\circ$ because the smaller pitch angle flux increases also thereby limiting the degree of anisotropy.

A close examination of figure 6.18 for $t < 4:28$ reveals that although the pitch angle distribution is very flat it does begin to decrease for pitch angles greater than $\sim 75^\circ$. At these higher pitch angles electrons coming from above the atmosphere to the ~ 220 km altitude of the payload have had a longer path length in the denser layers of the atmosphere than the minimum path length for zero pitch angle electrons. The longer path length produces more atmospheric scattering and an attenuation of the higher pitch angle flux. Wedde [1970] has shown that the pitch angle at which the attenuation becomes observable is a function of altitude and electron energy. In Chapter V we discussed the attenuation at 70° pitch angle for altitudes less than 130 km and electron energy of 22 keV. Chase [1970] determined that at 1 keV an initially isotropic distribution with a flat energy spectrum will have the $\alpha = 90^\circ$ flux attenuated by a factor of 3 more than the $\alpha = 0^\circ$ flux at ~ 230 km. Wedde [1970] has computed the expected angular distributions of 30-35 keV electrons at 300 km assuming an isotropic pitch angle distribution and a power law $E^{-5.7}$ differential energy spectrum at 1000 km. The computed fractions at 300 km of the 1000 km flux at various pitch angles are: (i) 0.79 @ $\alpha = 75^\circ$, (ii) 0.68 @ $\alpha = 85^\circ$ and (iii) 0.61 @ $\alpha = 90^\circ$. At 155 km Wedde's results are in good agreement with data obtained by McDiarmid et al [1967]. Using the channel A data from 4:20 - 4:26 UT and assuming an isotropic from $0^\circ - 90^\circ$ pitch angle distribution above the atmosphere we have calculated the attenuation as a function of pitch angle for the channel A (20-40 keV)

electrons. The energy spectrum was $\sim E^{-4.3}$. Our results are shown in figure 6.19. Also shown are Wedde's and Chase's results. We fitted the $75^\circ - 90^\circ$ pitch angle interval with a linear function

$$\text{Counts } (\alpha)_o = \frac{\text{Counts } (\alpha)}{1 - 0.03*(\alpha - 75^\circ)} \quad (6.6)$$

$$(75^\circ < \alpha < 90^\circ) \quad .$$

where $\text{Counts } (\alpha)_o$ is the unattenuated level.

The correction factor from equation (6.6) was applied to the data of figure 6.18, and the results are shown in figure 6.20. In general the resulting pitch angle distributions no longer had a peak near $\alpha = 70^\circ$. Figure 6.20 shows that the pitch angle distributions were generally flat from $\alpha = 60^\circ$ to $\alpha = 90^\circ$ after the correction for atmospheric attenuation was made. However there are notable exceptions to this rule including examples where the intensity decreases beyond 70° ($t = 4:14.9, 4:39.4$ and $4:41.3$ UT) and examples where the general increase in counts from $\alpha = 40^\circ$ to $\alpha = 60^\circ$ continues to $\alpha = 90^\circ$ ($t = 4:35.5, 4:46.2, 4:53.0, 4:55.0$ and $4:56.9$ UT). Our linear attenuation model deviates from Wedde's model significantly for $\alpha < 80^\circ$. Wedde has a small but finite attenuation from $\alpha = 65^\circ$ to $\alpha = 75^\circ$ which increases in a non-linear manner. At $t = 4:56.9$ UT we see in figure 6.20 the consequences of using the simpler linear form. There appears to be a peak for $\alpha = 65^\circ$ and then a decrease at $\alpha = 75^\circ$ with a subsequent increase towards $\alpha = 90^\circ$. However the general distribution during the burst from $\alpha \approx 60^\circ$ to $\alpha = 90^\circ$ is flat within $\pm 30\%$ of the peak value. From figure 6.17 we can observe that the lower pitch angle

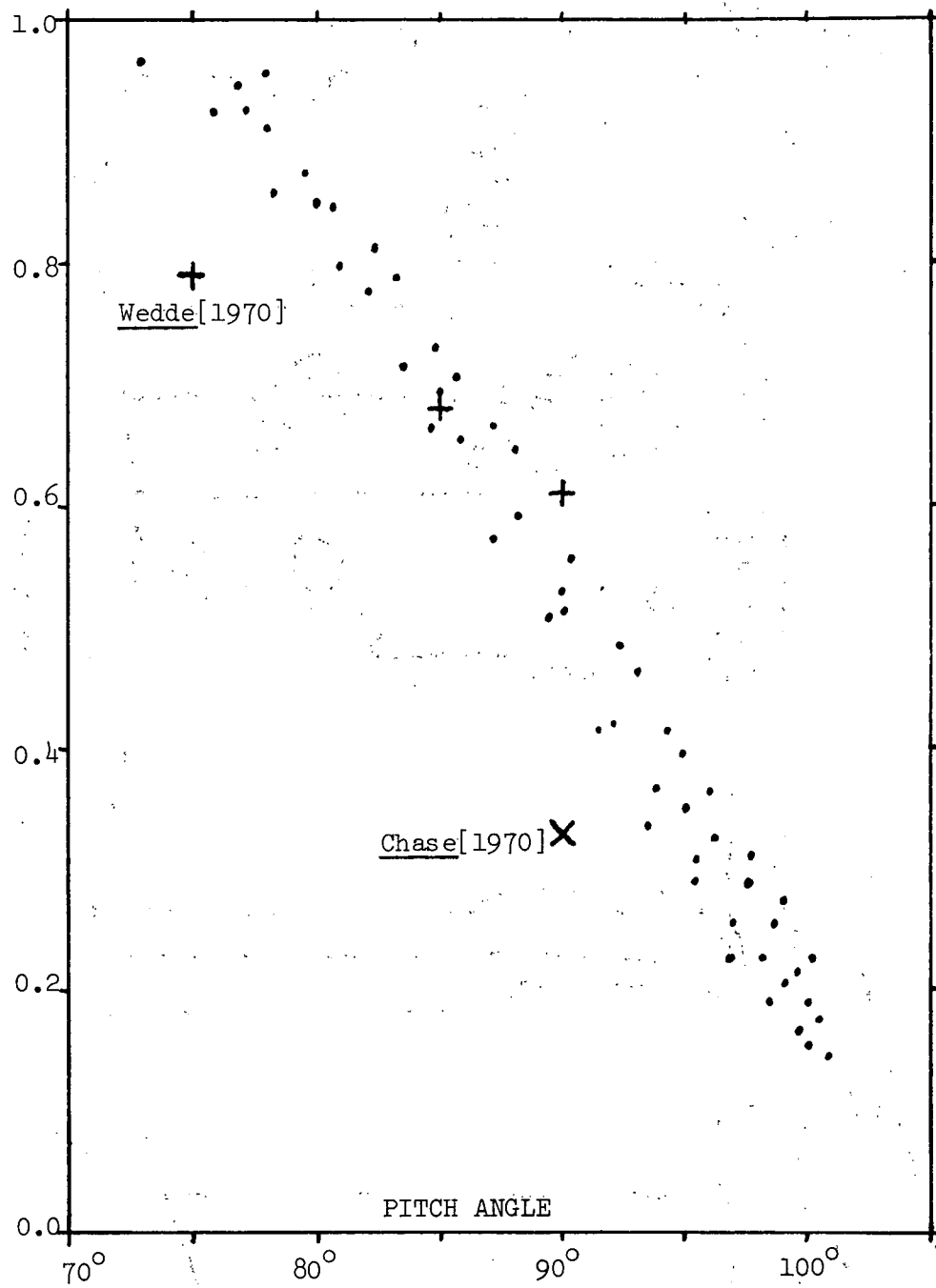


Figure 6.19. Ratio of counts for pitch angles beyond 70° to unattenuated level

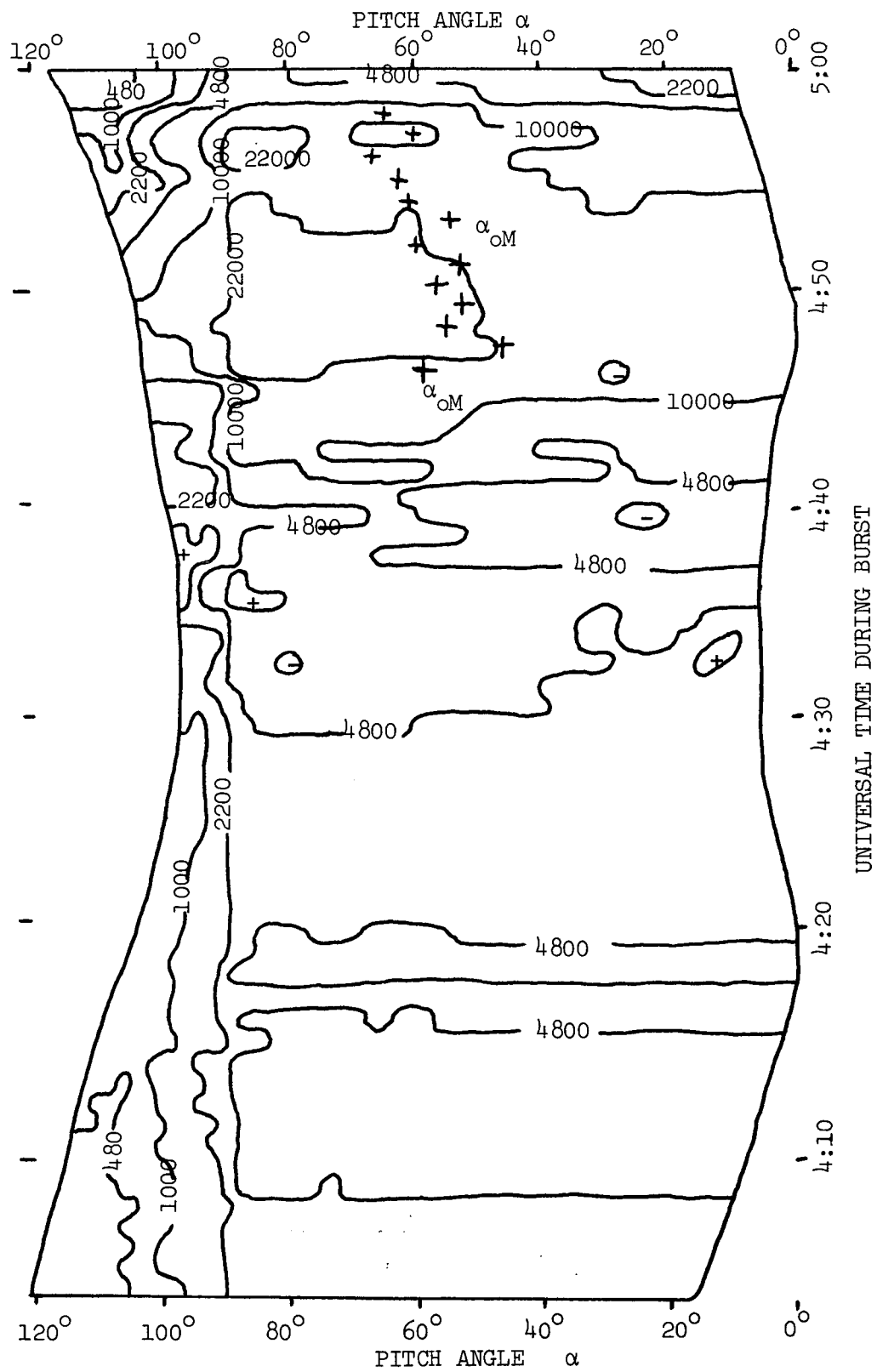


Figure 6.20. Contours of constant channel A counts after correcting for atmospheric attenuation

limit of the flat top, α_{OM} , varies from $\alpha_{OM} \sim 46^\circ$ @ 4:47.2 UT to $\alpha_{OM} \sim 67^\circ$ @ 4:55.9. On figure 6.20 we have indicated the location of this lower limit, α_{OM} , during the peak of the burst. The burst is most intense in channel A near 4:48.5 UT, and at that time the lower limit to the flat top of the distribution was at its minimum value. As the intensity of the burst decreased the lower limiting pitch angle increased. From figure 6.17 one can also observe that the pitch angle distribution is flat for pitch angles less than a critical pitch angle, α_{OD} . The value of α_{OD} ranges from $30^\circ - 40^\circ$ during the peak of the burst. During the burst the interval between the flat distribution for $\alpha < \alpha_{OD}$ and the flat top for $\alpha > \alpha_{OM}$ has a nearly constant value with $\alpha_{OM} - \alpha_{OD} \sim 20^\circ$. There is no uncertainty about the flatness of the pitch angle distribution for $\alpha < \alpha_{OD}$ because we were able to observe all pitch angles $< \alpha_{OD}$ to $\alpha = 0^\circ$ and no significant increase or decrease from the flat value was observed. Thus in the energy range 20-40 keV no field aligned fluxes were observed during the burst. The transition from the flat distribution for $\alpha < \alpha_{OD}$ to the flat top for $\alpha > \alpha_{OM}$ exhibited a linear pitch angle dependence (see for example figure 6.17 @ 4:55.8 UT).

As we previously stated we were unable to unambiguously correct for overranging in channel B during the burst. Figure 6.21 shows the contours of constant values of the counts in channel C from 0604:00 UT to 0604:56 UT. The detector angular response has been unfolded using equations 2.57 - 2.63. From figures 5.14 and 6.21 we see that the burst was of shorter duration (~ 10 sec) at the energies (~ 90 keV) corresponding to channel C. The maximum anisotropy determined from the

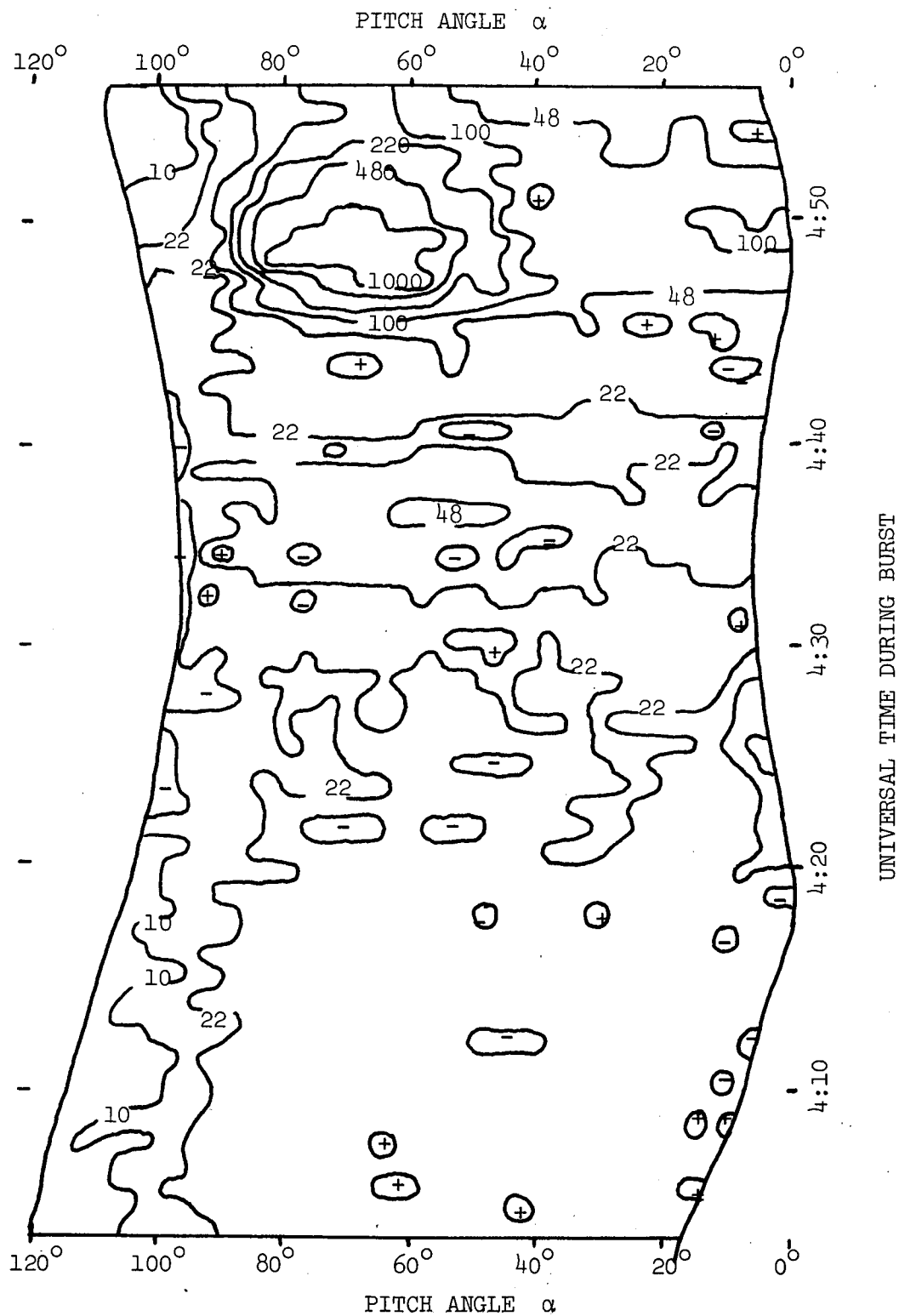


Figure 6.21. Contours of constant channel C counts
in time-pitch angle space during burst

ratio of the counts at $\alpha \sim 70^\circ$ to the counts for $\alpha < 20^\circ$ is about 10 for channel C whereas it was ~ 2 for channel A. From figure 6.21 we observe an essentially isotropic pitch angle distribution for $\alpha \lesssim 80^\circ$ from 4:00 - 4:44 UT. Unfortunately the counts are too few (~ 10 per word) in the $80^\circ < \alpha < 100^\circ$ interval during the period of isotropy to accurately determine the attenuating effect of the longer path length for the $\alpha \sim 90^\circ$ channel C electrons. Also any result may not be applicable during the short burst because of the hardening of the spectrum (see figure 6.15). This hardening was of very short duration so that it affected the channel A results only near $t \sim 4:50$ UT, but the duration was on the order of the burst time for channel C, and all burst data were affected for channel C. Figure 6.21 does show a peak in the time interval $4:47 < t < 4:51$ UT for pitch angles $60^\circ < \alpha < 80^\circ$ with approximately an order of magnitude decrease from $\alpha = 80^\circ$ to $\alpha = 90^\circ$. This decrease is larger than the attenuation correction of equation (6.6) for channel A. Unless the atmospheric attenuation is actually larger at the higher energies we are led to conclude that for the P.H.A. channel C electrons the pitch angle distribution for $\alpha \gtrsim 40^\circ$ is peaked near $\alpha \sim 70^\circ$ during the burst. We note that the discrepancy between the Monte Carlo calculations Wedde [1970] and the observations of the pitch angle dependence of integral (not differential) electron flux McDiarmid, et al [1967] becomes larger as the energy increases. For $E > 25$ keV the agreement is excellent over the downward hemisphere, yet for $E > 75$ keV where McDiarmid, et al [1967] also observed a peak in the pitch angle distribution near $\alpha = 70^\circ$ there is poor agreement.

From figure 6.21 one can observe the "plateau" or flat distribution

for pitch angles less than $\alpha \sim 40^\circ$. The critical angle α_{oD} which represents the maximum pitch angle for which the distribution is flat is $\sim 10^\circ$ larger for channel C than the corresponding angle for the channel A electrons. For example at 4:49 $\alpha_{oD} \sim 33^\circ$ for channel A whereas $\alpha_{oD} \sim 41^\circ$ for channel C. Whereas channel A became anisotropic during the enhancement at $\sim 4:34$ UT the increase in channel C at $\sim 4:34$ UT appears to be nearly isotropic.

The pitch angle information from the PESPEC is essentially limited to an average over pitch angles less than 45° (defined as the D or dumped electrons in Chapter IV) and an average over pitch angles, α , such that $60^\circ < \alpha < 93^\circ$ (defined as the M or mirroring electrons in Chapter IV). Because the PESPEC accepted electrons from two separate directions we were unable to analytically unfold an angular response. We were also unable to unambiguously correct for the atmospheric attenuation for the flatter ($\alpha \sim 90^\circ$) pitch angle electrons. Because of these limitations in the pitch angle information we sacrifice very little detail in using the D and M averages to describe the pitch angle distributions. An illustration of the clarity and simplicity resulting from using the averages is given in figures 6.22 and 6.23. In figure 6.22 we plot versus pitch angle the flux at 10.9 key from word #8. Profiles from succeeding rotations of the payload are vertically displaced to facilitate the determination of the temporal behavior of the pitch angle distribution. Only points for which the acceptance orientations of the two slots are separated by less than 40° are shown. The abscissa for each point was determined from the average of the pitch angles for each slot. The ordinate for each point represents the differential flux for an assumed flat spectrum

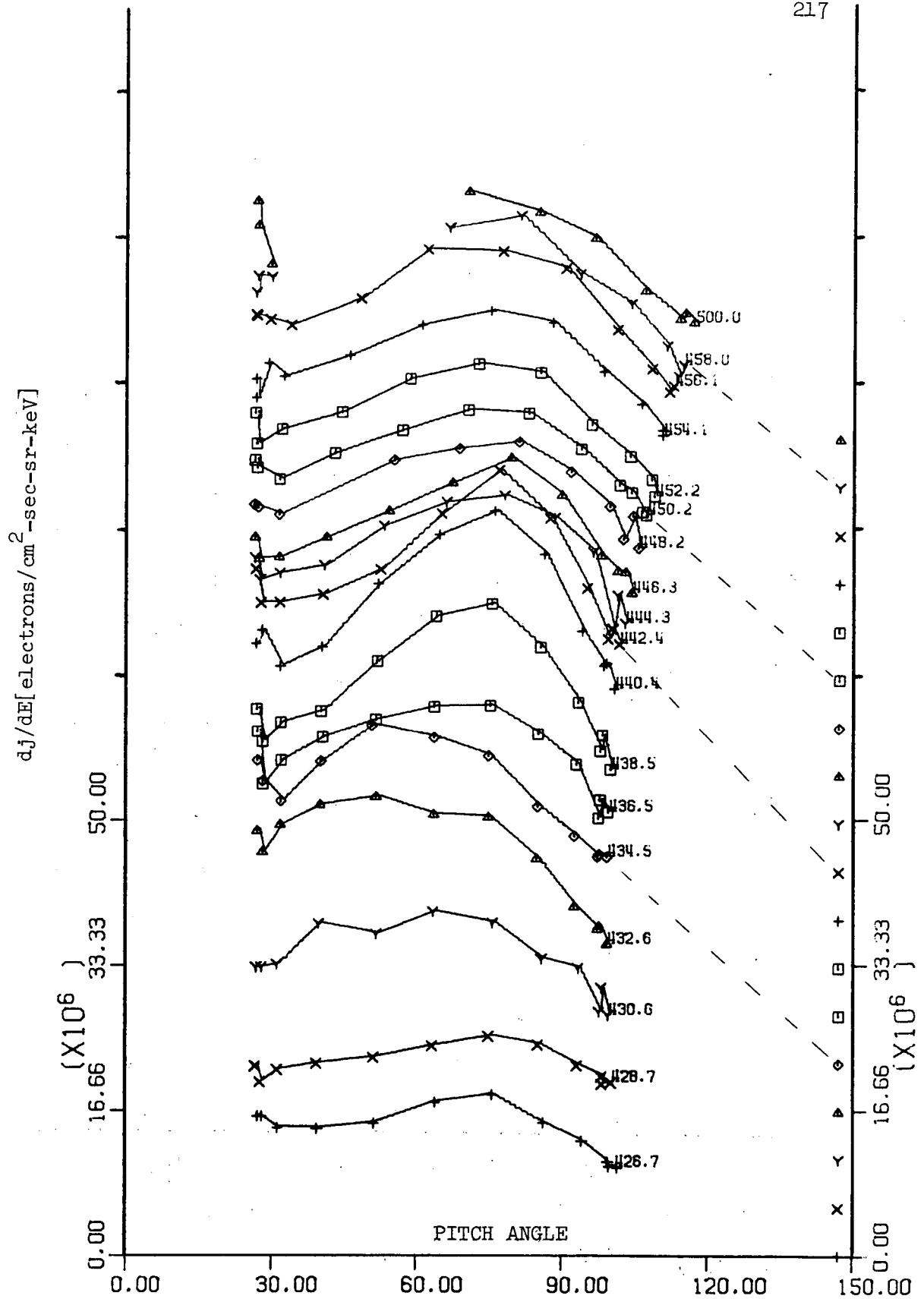


Figure 6.22. Pitch angle distributions of 10.9 keV electrons during burst (time of measurement is next to largest pitch angle /roll)

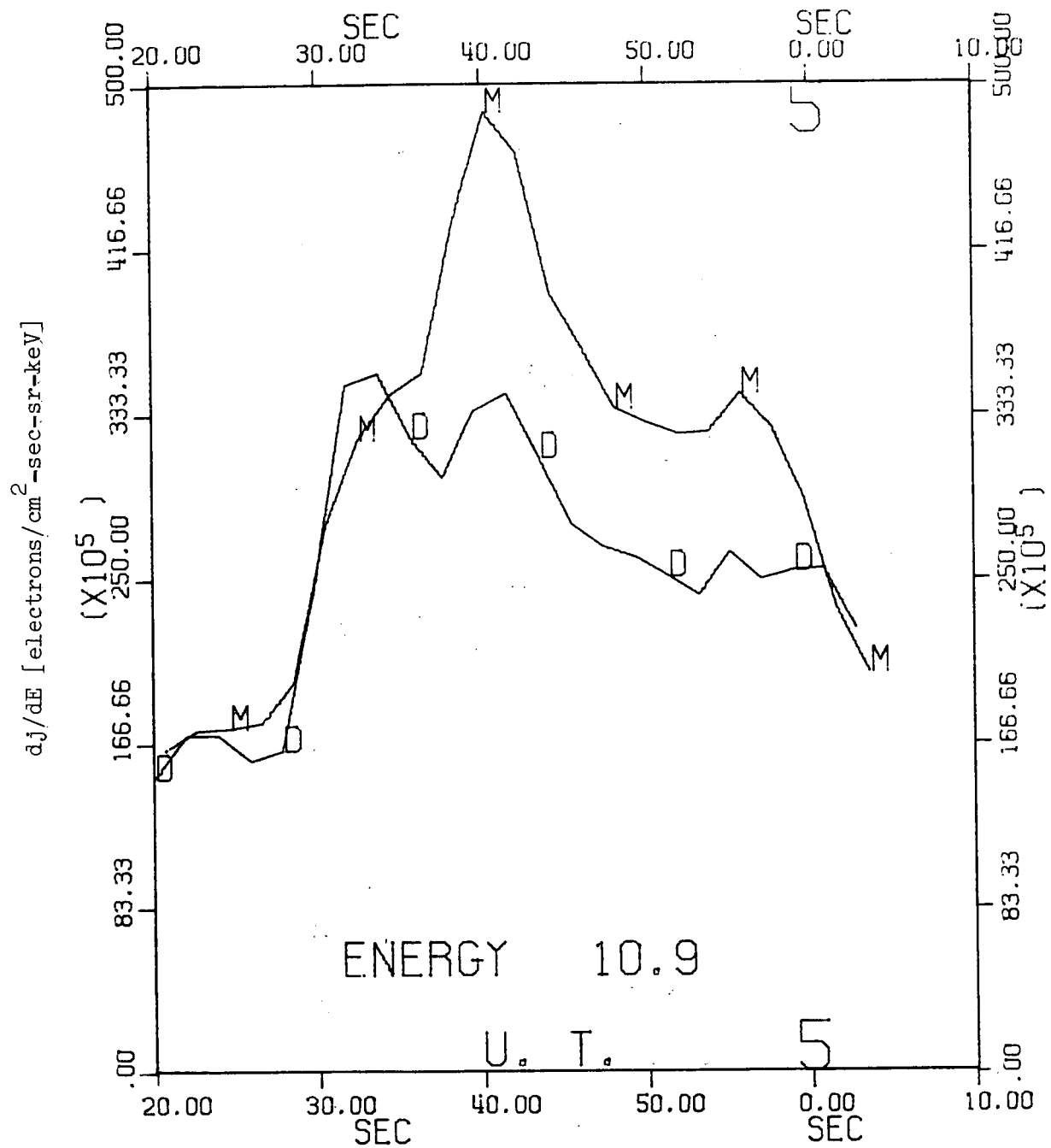


Figure 6.23. Illustration of pitch angle distribution of 10.9 keV electrons during burst using D and M averages

as determined from the individual, unaveraged counts. The dashed lines indicate the zero reference level for each profile. With the roll numbers as defined in Chapter IV rotations 4 - 21 are shown.

Rolls 4 and 5 are essentially isotropic for $PA \lesssim 75^\circ$. Rolls 6 and 7 show some evidence of a higher flux for lower pitch angles. Beginning with roll 6 ($t \sim 4:36.5$ UT) and continuing to roll 20 ($t \sim 5:00$ UT) there is a peak with varying intensity at $PA \sim 75^\circ$. For these 10.9 keV electrons the maximum anisotropy occurs during roll #10 ($t \sim 4:40$ UT). Figure 6.22 emphasizes the pitch angle distribution over the temporal dependence even though the pitch angle look of the PESPEC is somewhat uncertain. To better emphasize the more accurately determined quantity (the time), and yet still indicate the pitch angle distribution with all the precision which is justified we use the D and M averages versus time as in figure 6.23 which shows the D and M fluxes @ 10.9 keV during the burst. Figure 6.23 shows that the pitch angle distribution was anisotropic with the mirror-~~ing~~ electrons exceeding the dumped electrons from $\sim 4:35 - 5:00$ UT. Because no precise information is sacrificed and much clarity and simplicity results we will discuss the PESPEC anisotropies in terms of the behavior of the D and M averages.

We will examine the low energy anisotropy first. In figure 6.24 we show the D and M fluxes at 1.19 keV during the burst. The maximum values of the anisotropy parameter $A(E = 1.19 \text{ keV}, t)$ defined in Chapter IV are at 4:38.3 UT where $A = 1.28 \pm 0.05$ and at 4:49.9 UT where $A = 1.29 \pm 0.07$. The uncertainties were calculated by a propagation of errors technique based on the standard deviations of the D and M averages. The anisotropy peak at 4:38.3 UT demonstrates a

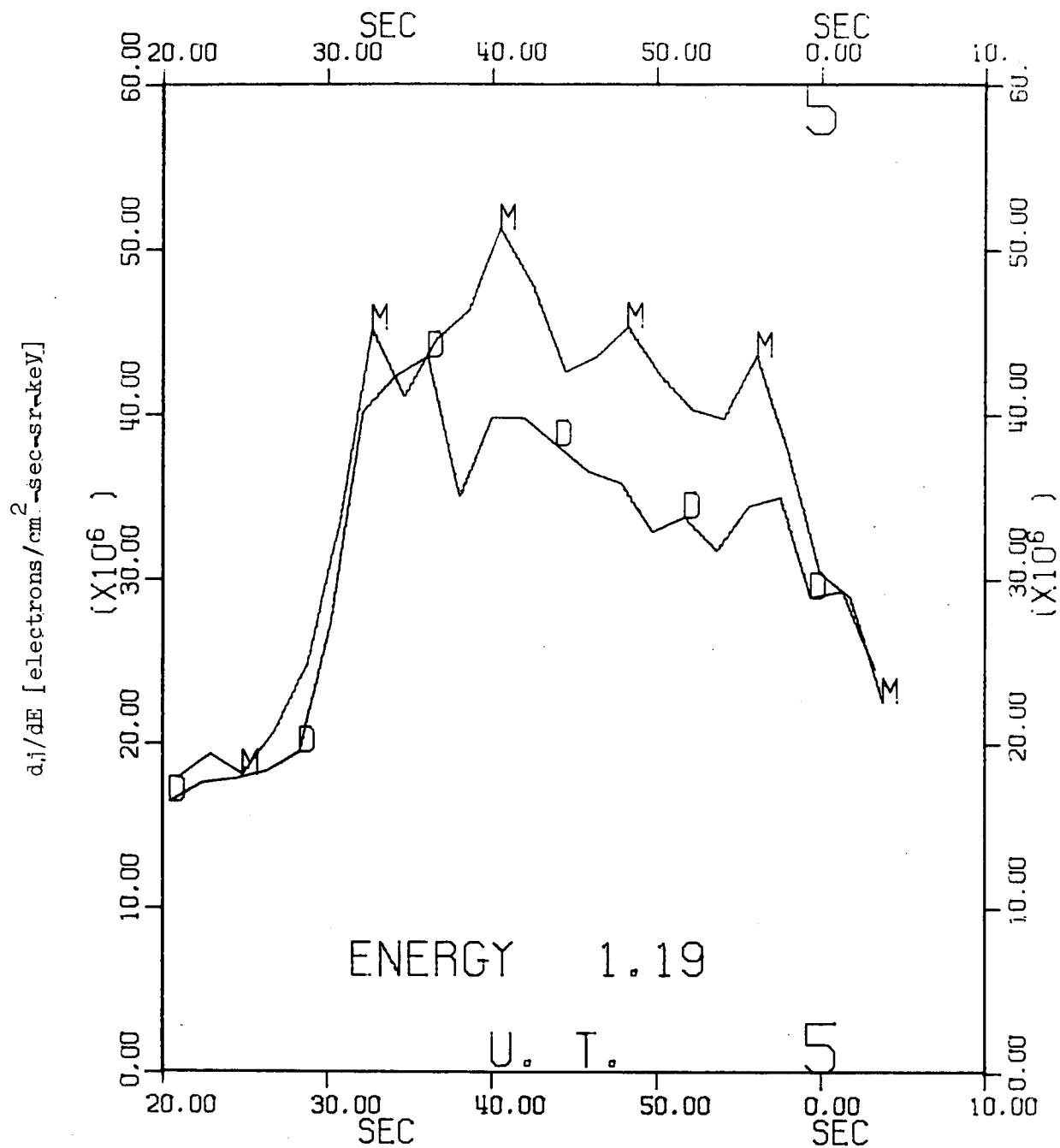


Figure 6.24. Development of anisotropy at low energy during burst by comparison of mirroring and dumped fluxes

degree of independence between fluxes of mirroring electrons and fluxes of dumped electrons at a common energy because the anisotropy is the result of a decrease in the dumped electrons during an increase in the mirroring flux. A comparison of figures 6.4 which shows the temporal dependence of the J_o parameter of the low energy electrons described in the first section of Chapter VI and figure 6.24 shows a remarkable similarity between the dumped and mirroring fluxes at 1.19 keV and the J_o parameter for the dumped and mirroring energy distributions respectively. In figure 6.25 we have compared the anisotropy parameter $A(E, t)$ for the word #23 (1.19 keV) fluxes with the ratio, R_{J_o} , of J_{oM} , the low energy spectral parameter for the mirroring electrons, to J_{oD} , the same parameter for the dumped electrons. The qualitative and quantitative correlation is good. The correlation is not limited to the 1.19 keV electrons but as figure 6.26 (which shows the ratio of the power law spectral parameters, $R_n = n_M/n_D$, versus time) indicates the low energy spectral shape parameter, n , is essentially independent of pitch angle. Figure 6.26 shows that the ratio R_n averaged ~ 1 during the burst and the fluctuations were $\lesssim 10\%$. During the burst the low energy (E^{-n}) portion of the spectrum dominated the drifting Maxwellian portion for energies less than ~ 7 keV therefore figure 6.25 shows the degree of anisotropy for all electrons less than 7 keV during the burst. The small peak in R_{J_o} at 4:30 UT was computed during the very rapid increase of greater than a factor of two of both J_{oM} and J_{oD} . Figures 6.4 and 6.24 show that relative to the temporal change the differences between J_{oD} and J_{oM} during the increase are small. Figure 6.25 shows that the low energy electrons were anisotropic for $4:36 < t < 5:00$ UT. By comparing figures 6.20

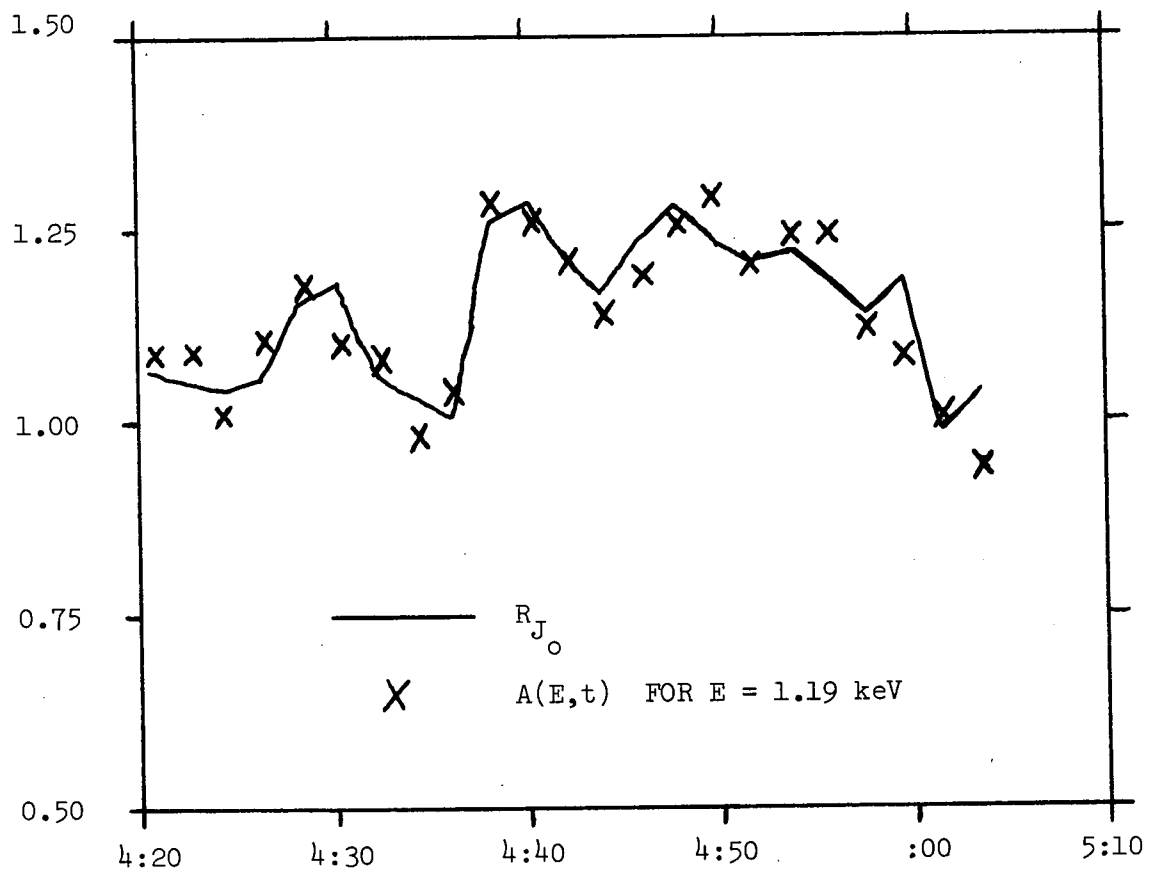


Figure 6.25. Anisotropy parameter $A(E,t)$ for $E=1.19$ keV and R_{J_o} during burst.

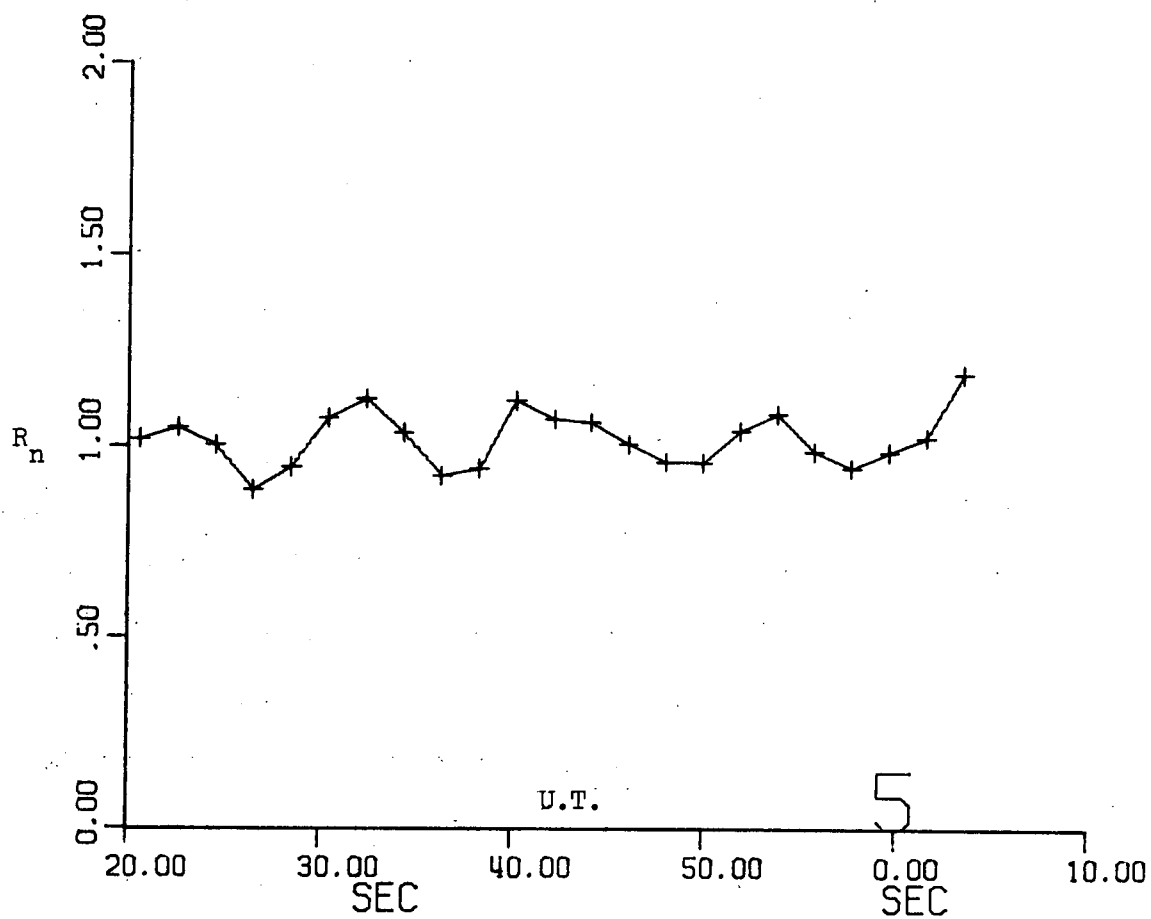


Figure 6.26. Ratio of power law parameter for mirroring electrons
to power law parameter for dumped electrons

and 6.25 we note the contrast between anisotropy for the higher energy electrons and isotropy for the lower energy electrons in the time interval $4:30 \lesssim t \lesssim 4:36$ UT. This feature is also evident in figure 5.11. During the burst the degree of anisotropy, R_{J_O} , averages about 1.2. The degree of anisotropy remains essentially constant during the burst although from figure 6.4 we observe ~25% decreases from their peak values for both J_{OD} and J_{OM} . The dumped and mirroring electron time profiles of figure 6.27 give a good example for summarizing the anisotropy of the low energy electrons. From 4:20 UT to 4:34.5 UT, the mirroring and dumped fluxes are nearly equal indicating isotropy to within the angular resolution of the PESPEC. The critical time period in the development of the anisotropy was from 4:35 - 4:38.3 UT. In this time period (see figures 6.4 and 6.27) the low energy flux of mirroring electrons was increasing while the flux of dumped electrons was decreasing thereby establishing the anisotropy. From ~ 4:39 UT to the end of the burst both the dumped and mirroring fluxes had essentially a "sawtooth" decay temporal dependence while maintaining the previously established level separation.

If a particle source some distance from the point of observation were producing isotropic low energy electrons with a "sawtooth" time dependence beginning at some time t_0 one would first observe the higher energy, smaller pitch angle electrons. The delay, $t - t_0$, between observation of dumped electrons would be shorter than the delay for observation of mirroring electrons at the same energy. We do not believe that such a phenomenon was responsible for the observed pitch angle anisotropy because: (i) such a pitch angle dispersion is not apparent during the steep increase for $t \sim 4:30$ UT, (ii) the $J_O E^{-n}$

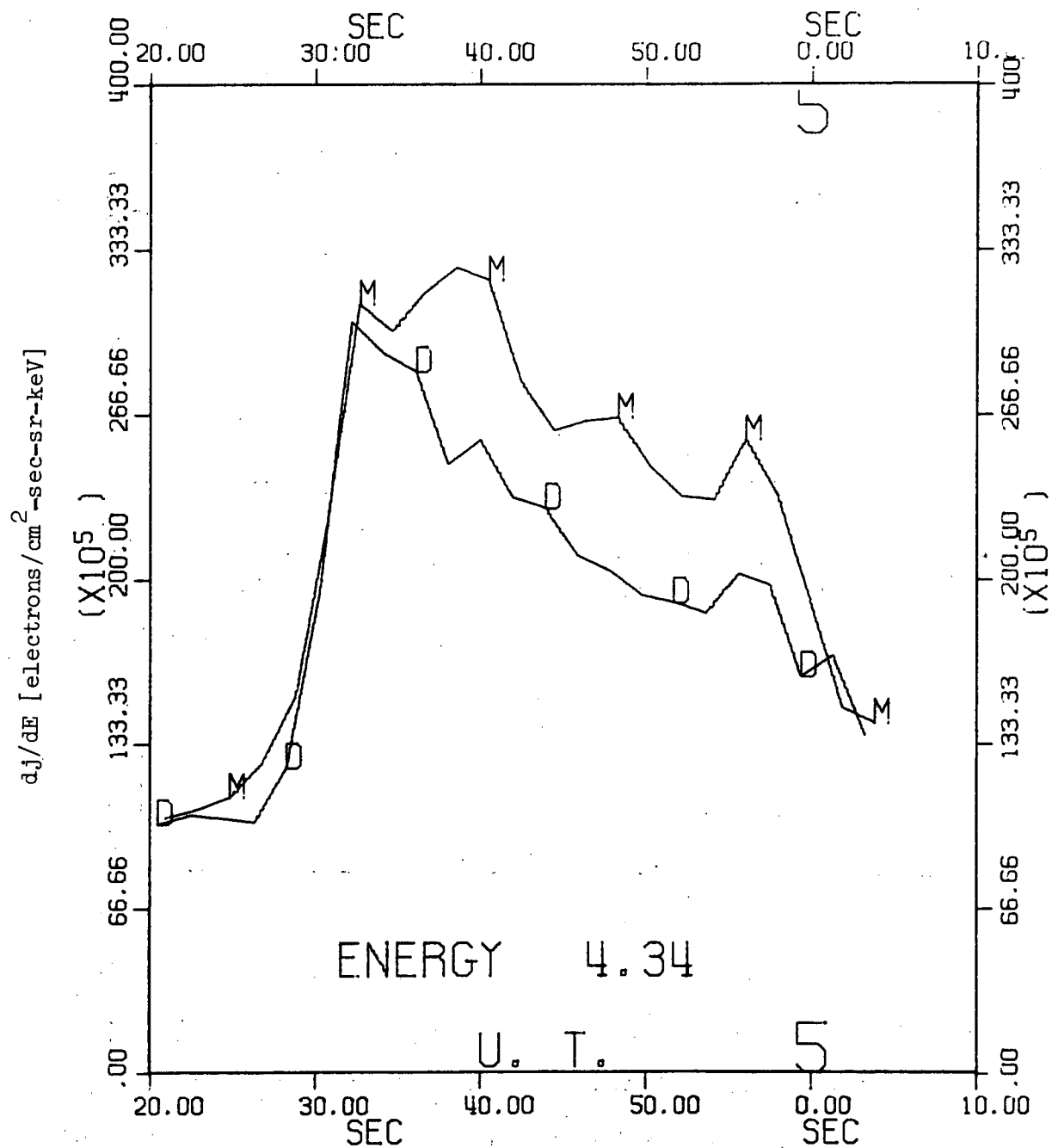


Figure 6.27. Temporal development of low energy flux and anisotropy as summarized by dumped and mirroring profiles at 4.34 keV

low energy spectral dependence gives an excellent fit over an order of magnitude energy range yet figures 6.4, 6.24 and 6.27 show essentially no dispersion of arrival time at various energies (because we are using the averaged data our minimum temporal resolution is ~ 2 sec yet this is obviously less than the ~ 10 sec typical delay between the mirroring and dumped electrons) and (iii) figures 6.4, 6.24 and 6.27 indicate essentially simultaneous observation of the "after-pulse" peak at $\sim 4:56$ UT.

The pitch angle distributions for electrons in the $8 \text{ keV} < E < 20 \text{ keV}$ range which is the energy interval characterized by the drifting Maxwellian energy distribution have a very complicated energy-pitch angle structure. At the low energies essentially all the pitch angle information was contained in the energy independent J_0 parameter. The corresponding situation in the case of the drifting Maxwellian would arise if only the density, n_e , were pitch angle dependent. We define R_{n_e} to be the ratio of the mirroring density, n_{eM} , to the dumped density, n_{eD} . This ratio is computed from n_{eM} and n_{eD} values interpolated to a common time to avoid effects due to temporal variations. The corresponding temperature ratios, R_{T_e} , and E_0 ratios, R_{E_0} , are similarly defined. Figure 6.28 shows the temporal variation of the mirroring to dumped ratios of the three parameters describing the drifting Maxwellian. The density ratio R_{n_e} exhibits the most variability and largest values. E_0 , the parameter related to the drift speed has the smallest range of $0.90 < R_{E_0} < 1.08$. Figure 6.29 shows how each parameter may cause an anisotropy for fixed values of the other two. Only the density anisotropy ($R_{n_e} > 1$) produces an energy independent anisotropy. An example of such an

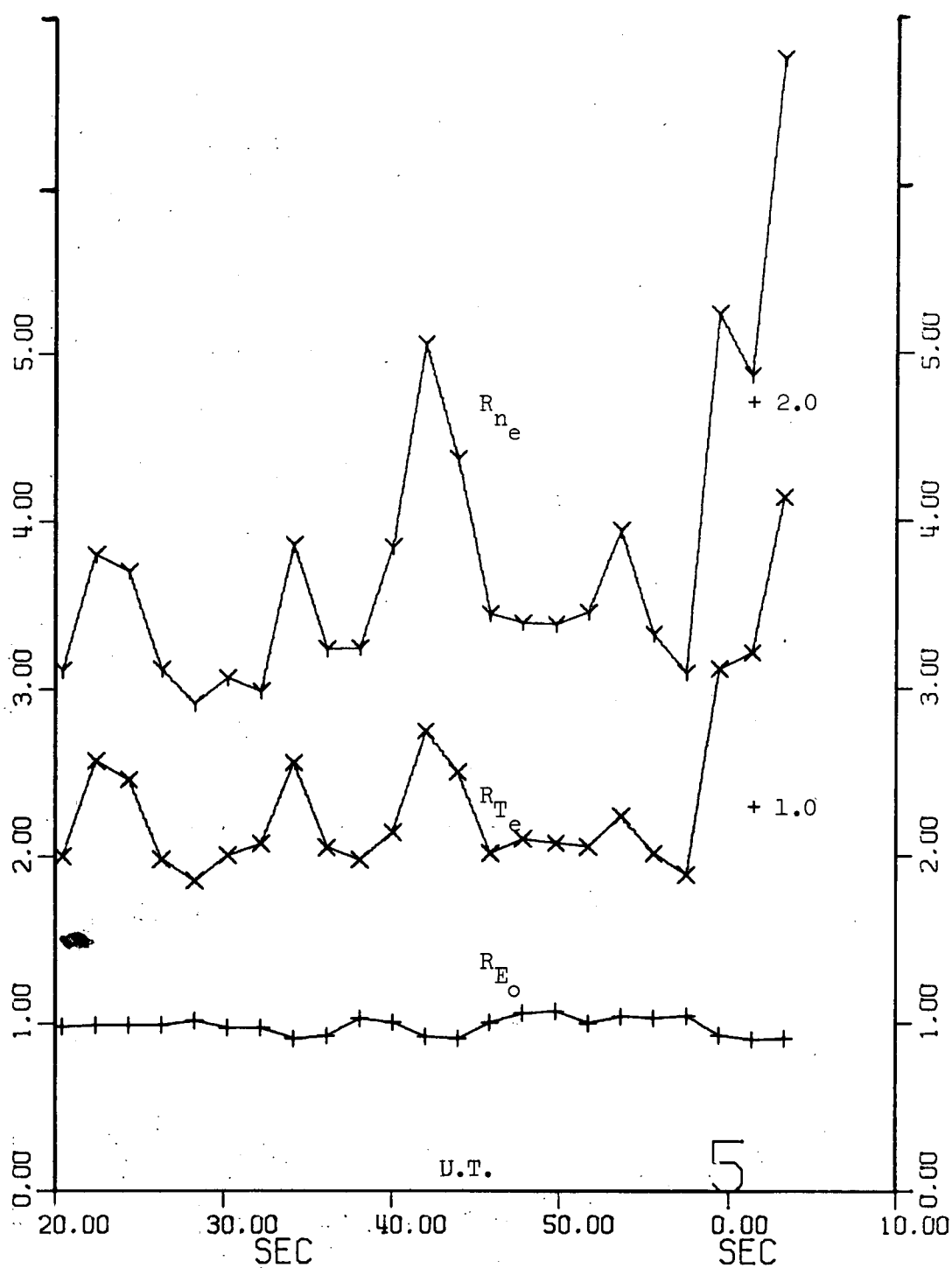


Figure 6.28. Temporal development of mirroring to dumped ratios for the drifting Maxwellian parameters (note each succeeding origin displaced by 1.0).

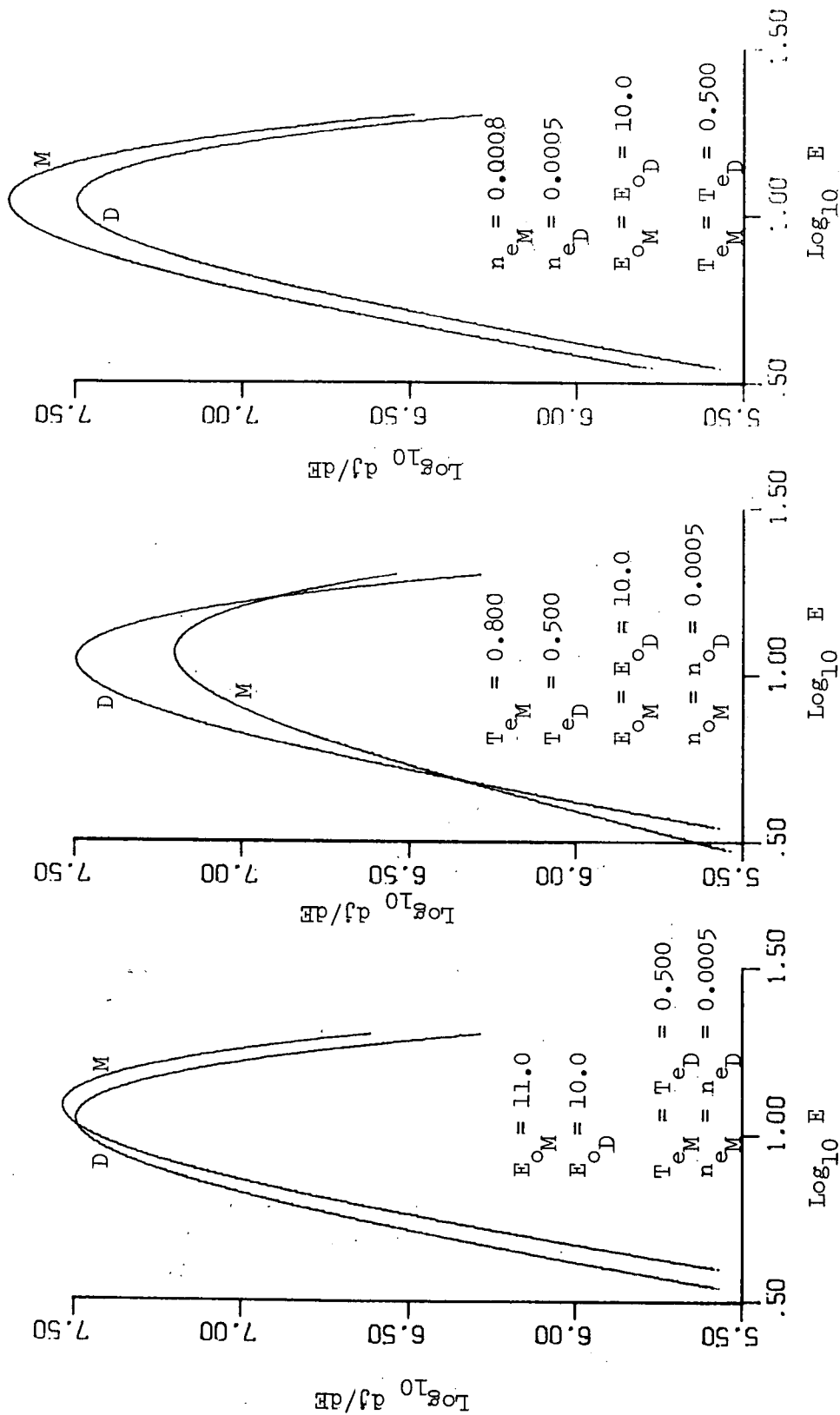


Figure 6.29. Illustration of manner in which drifting Maxwellian parameters produce energy dependent pitch angle distributions

anisotropy occurred at 4:52.0 UT. However as figure 6.28 shows one rarely finds examples where two of the ratios are unity and the anisotropy is due to a difference between the dumped and mirroring value of the remaining parameter. Because the ratio E_o/T_e is large small variations in R_{E_o} can produce significant anisotropies.

Figure 6.30 shows the mirroring and dumped fluxes at 15 keV during the burst. The anisotropy initially develops as the low energy anisotropy with a growth of the mirror flux and a decay of the dumped flux between 4:36 and 4:40 UT. However coinciding precisely with the acceleration process described previously in Chapter VI (see figure 6.8) a rapid factor of two increase in the dumped flux momentarily restores the 15 keV flux to isotropy. Then an equally rapid development of the thermalization process described previously produces the subsequent anisotropy.

The electrons with energies in the range of the drifting Maxwellian are anisotropic during the thermalization process from 4:46 UT $< t < 5:00$ UT, but they remained essentially isotropic during the previous thermalization centered at $t \sim 4:34$ UT. Examination of figure 6.28 indicates that although the temperature and density ratios were larger during the first process the fact that R_{E_o} was less than unity during the first thermalization and greater than unity during the second was responsible for the anisotropy during the latter. The peak anisotropy in the energy range of the drifting Maxwellian occurred at 4:38.3 UT when $R_{T_e} \sim R_{E_o} \sim 1$, and the anisotropy resulted because the directional density at the mirroring pitch angles was larger than at the dumped pitch angles, $R_{n_e} \sim 1.25$.

The directional density for mirroring pitch angles was larger

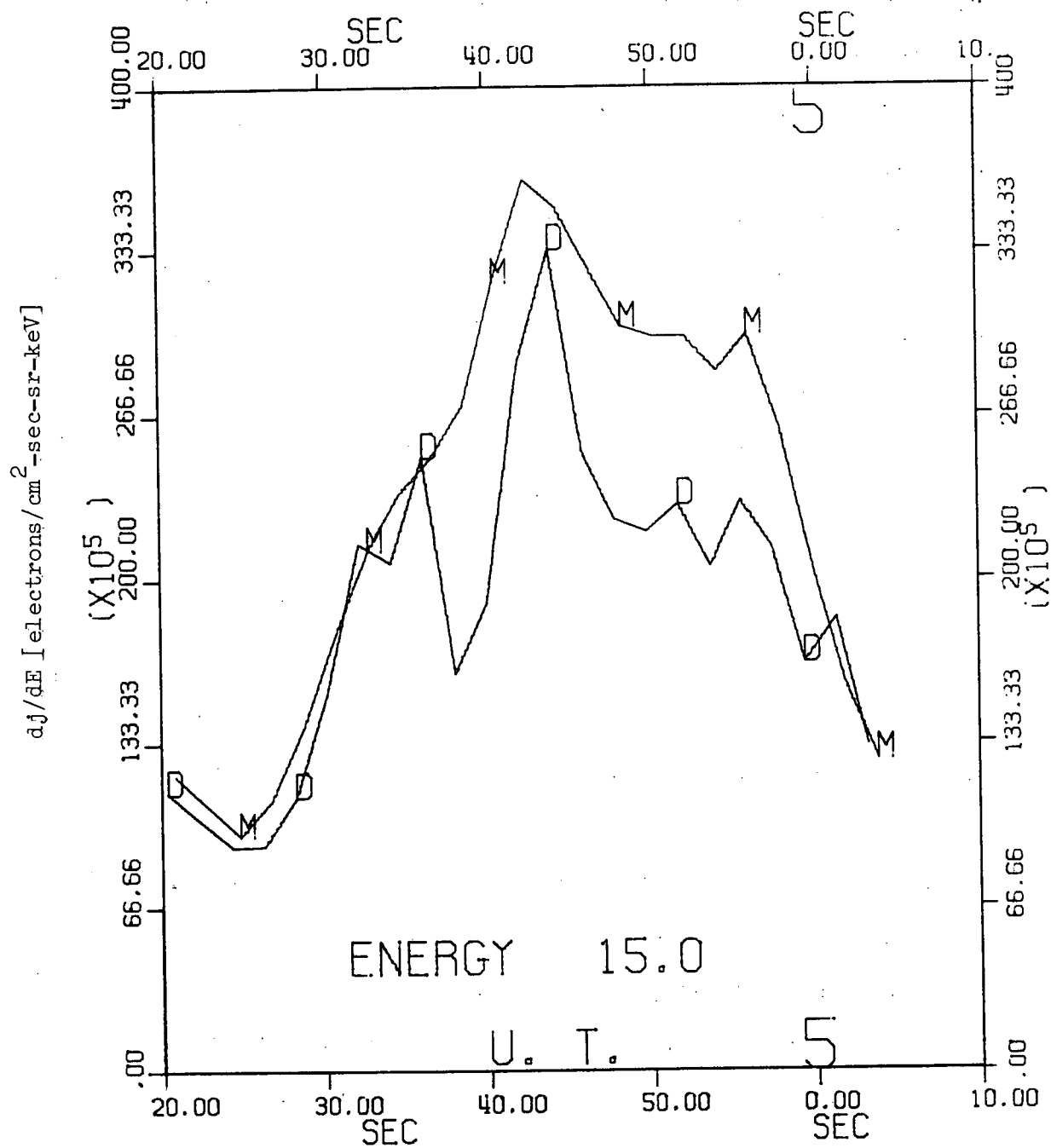


Figure 6.30. Development of flux and anisotropy in energy domain of drifting Maxwellian at 15.0 keV

than the directional density for the dumped pitch angles during the enhanced anisotropy (especially at higher energies) centered at 4:50 UT. However one cannot assume $R_{n_e} > 1$ indicates an anisotropy unless the temperature ratio, $R_{T_e} \sim 1$. Equation (6.5) shows that in general $T_e \propto n_e$ and because equation (6.3) has $T_e^{3/2}$ in the denominator an increase in n_e is accompanied by a compensating increase in T_e . The anisotropy peak at $\sim 4:40$ UT occurs when T_e and n_e for the mirroring electrons deviate the most from equation (6.5). However at 4:50 UT the values of T_e and n_e were in good agreement with equation (6.5).

While the pitch angle distribution can be a very complicated function of the parameters n_{e_D} , n_{e_M} , T_{e_D} , T_{e_M} , E_{o_D} and E_{o_M} figure 6.28 shows that these parameters and especially their ratios R_{n_e} , R_{T_e} and R_{E_o} display a rather consistent pitch angle dependence. We observe that the ratios R_{n_e} and R_{T_e} are consistently greater than unity and can attain values of ~ 3 . Values of R_{n_e} and R_{T_e} less than unity are quite rare. We therefore conclude that $T_{e_M} \geq T_{e_D}$ and $n_{e_M} \geq n_{e_D}$. The mirroring electrons can be hotter and more dense than the dumped electrons, but the reverse case does not occur. The ratio R_{E_o} has values less than unity as well as values greater than unity. There appears to be a preference for the mirror electron parameter, E_{o_M} , to be less than the dumped electron parameter, E_{o_D} . For cases where the payload pitch angle α is less than 70° thus insuring a random averaging over the mirroring pitch angles (see section C of Chapter IV) E_{o_M} is less than E_{o_D} twice as frequently as $E_{o_D} < E_{o_M}$. An anisotropic pitch angle distribution is observed in the energy interval of the drifting Maxwellian electron flux for each instance of $E_{o_D} < E_{o_M}$.

D. Discussion

In this section we compare our results to previous measurements in the auroral ionosphere and elsewhere in the magnetosphere, and we examine the possible contributions of our results to theoretical explanations of magnetospheric phenomena. We preface these remarks by recalling that 18:63 UE was launched near local magnetic midnight into a break-up or post-break-up IBC II-III aurora. Our detailed results correspond to a burst (believed to be temporal in nature) during which the electron pitch angle distributions at essentially all energies were characterized by higher fluxes near pitch angles of 70° than at pitch angles less than 40° . Certainly the universal extrapolation of our results must bear in mind that the pitch angle distribution during most of the flight was isotropic and that previous measurements of auroral electrons have indicated that the pitch angle distribution becomes isotropic with increased levels of precipitation.

Figure 6.5 which shows the low energy power law spectrum exponent, n , for the three pitch angle averages and figure 6.26 which shows the ratio of n for the mirroring electrons to n for the dumped electrons indicate that the shape of the low energy spectrum is nearly constant and pitch angle independent over the 0.5 - 6.0 keV energy range. We found $0.40 < n < 0.65$. Westerlund [1969] reported a value of $n = 1.3 \pm 1.0$ was able to fit every continuum spectrum during his flight. Frank and Ackerson [1971] report fits to the low energy power law portion of the spectrum for $1.5 < n < 2.5$. We note that our measurements were at altitudes $150 \text{ km} < h < 250 \text{ km}$, Westerlund's [1969] results were for $400 \text{ km} < h < 800 \text{ km}$ and Frank and Ackerson [1971] measured auroral particles with Injun 5 for altitudes $677 \text{ km} < h < 2528 \text{ km}$.

The largest variability in n and ambient topside electron densities occurs for Westerlund's [1969] data, but the events are too different to prove that n is height dependent.

The source of the low energy power law spectrum electrons has been considered by Frank and Ackerson [1971] (It should be noted that Westerlund [1969] and Frank and Ackerson [1971] measured the energy spectrum to lower energies than our 0.5 keV lower limit.). Frank and Ackerson [1971] considered (i) atmospheric photoelectrons, (ii) high energy portion of the spectrum of low energy ambient electrons and (iii) secondary electrons from the satellite surface. They rejected the latter possibility. Heikkila [1970] shows that the photoelectron spectrum does not extend beyond 100 eV. In a more general sense we consider the possibility that the low energy component represents secondary electrons resulting from ionizing collisions of higher energy electrons striking the atmosphere. The energy spectrum of secondary electrons in a realistic atmosphere has been calculated by Stolarski and Green [1967]. Above 20 eV the spectrum falls off very steeply as $E^{-2.5}$ essentially independent of primary spectrum. Our low energy spectrum of $\sim E^{-0.5}$ is too hard to be due to atmospheric secondaries. We emphasize that electrons in the 2-6 keV range have essentially the same time dependence as the 0.5 keV electrons (the J_0 parameter describes the flux over an order of magnitude energy interval). The magnitude parameter for the low energy mirroring electrons, J_{OM} , has a peak value at 4:40 UT (see figure 6.4) whereas the maximum energy deposited due to mirroring electrons was at 0604:48.5 UT (see figure 5.8). M. H. Rees [1969] places a 100 eV upper limit to the portion of Westerlund's continuum spectrum which includes appreciable

secondary electrons.

Only the low energy electrons exhibit any periodic behavior during the burst. Figure 6.4 shows small peaks in J_{OM} at 4:32.7, 40.5, 48.3 and 56.3. These peaks are statistically significant, and the ~ 8 sec period corresponds to the bounce period of a ~ 3 keV electron. We would not attribute the peaks to multiple bounces of a cluster of 3 keV electrons because the periodicity appears throughout the 0.5-6 keV energy interval. Figure 6.31 shows the fluxes of dumped and mirroring electrons at 0.636 keV during the burst. The dumped electrons show some indication of a slightly higher frequency periodicity out of phase with the mirroring electron oscillations (until 4:56.3 UT).

The decision to use the drifting Maxwellian energy dependence (equation 6.3) to describe the peaked portion of the spectrum was originally based upon a desire to divorce the position of the peak of the energy spectrum from the width of the peak (for a Maxwellian, $E_{peak} = kT_e$). The Maxwellian portions of the electron energy spectra observed by satellite over the auroral zone Frank and Ackerson [1971], at $6.6 R_e$ by ATS-5 DeForest and McIlwain [1971] and in the distant ($18 R_e$) plasma sheet Hones et al [1971] do not have peaks near 10 keV as we observed on 18:63 UE. Albert [1967] also observed peaks in the electron energy spectrum at energies greater than 10 keV. Because the plasma is collisionless there is no a priori reason for attempting a Maxwellian fit. However the peaked nature of the spectrum suggests that the velocity spread can be determined from the temperature associated with a Maxwellian fit.

At first glance the fact that the spectrum is peaked regardless of the direction of observation obviates the concept of a thermal

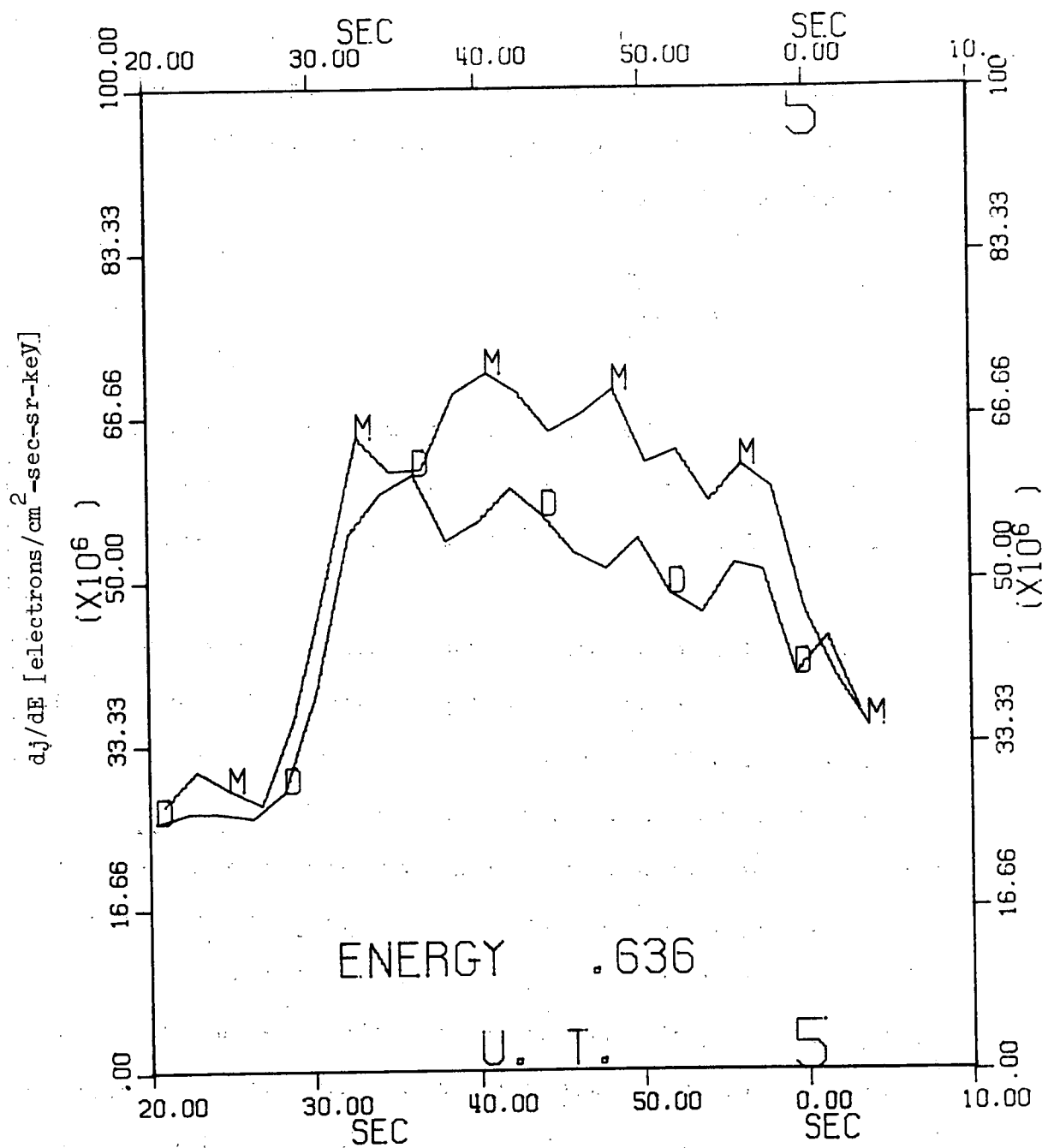


Figure 6.31. D and M fluxes at 0.636 keV indicating small scale periodic behavior

plasma drifting towards the payload. Consideration of the pitch angle flattening effect of the geomagnetic field mirror geometry shows that the component of the drift parallel to the magnetic field in a region of weaker field will be manifested at all pitch angles in the mirror region. The drift velocity, v_D , associated with the peaked portion of the spectrum is given by

$$v_D = \sqrt{\frac{2E_o}{m_e}} \quad (6.7)$$

typically $v_D \sim 6 \times 10^4$ km/sec. This is much, much larger than the solar wind speed, 5.5×10^2 km/sec. v_D is also larger than the maximum Alfvén velocity ($\sim 4 \times 10^3$ km/sec) in the magnetosphere [Dungey, 1968].

For energies beyond the peak the spectrum is very soft. The P.H.A. power law exponent n has typical values of $\sim 4-5$. The absolute flux for $E \sim 30$ keV was difficult to determine, however, the PHA channel C data (see figure 6.14) indicates that an extrapolation of the drifting Maxwellian portion to higher energies would not account for the electrons seen in channel C. Westerlund [1969] reported power law exponent values of $n \sim 10$ for $E > 25$ keV. For $E_o = 11$ keV and $T_e = 1.0$ keV (4:48 UT) this is about the slope in the 30-40 keV region from a drifting Maxwellian distribution. Based on Westerlund's [1969] observations of a separable continuum and peaked spectrum in the absence of a peak near 10 keV we would assume that the low-energy power law spectrum ($n \sim 0.5$) would join the high-energy power law spectrum ($n \sim 5$) near 10 keV. Such spectra have also been reported by Remé and Bosqued [1971].

The origin of the acceleration mechanism for the peaked and monoenergetic auroral electron spectra is unknown. Evans's [1967] original suggestion of an electric field parallel to the magnetic field has many appealing features. Two attractive characteristics of providing a local acceleration and a non-dispersive (energy gain is not proportional to initial energy) acceleration can be illustrated by comparing our precipitated electron data at 4:48 UT with the energy spectrum obtained by Frank and Ackerson [1971] on Injun-5 at 22h55m 00s UT December 30, 1968. The Maxwellian portion of their energy spectrum had a temperature of 1000 eV and a density of 0.6 electrons $(\text{cm}^3\text{-sr})^{-1}$. At 4:48 UT we have a temperature of 1020 eV, a density of 8.7×10^{-4} electrons $(\text{cm}^3\text{-sr})^{-1}$ and a drift energy, E_o , of 11.0 keV. A parallel electric field, $\epsilon_{||}$, over a distance, ℓ , such that, $\epsilon_{||} \ell \sim E_o = 11.0 \text{ keV}$ would be required to precipitate and accelerate \sim one of 500 of the Maxwellian electrons observed by Frank and Ackerson [1971] to produce the peaked portion of our spectrum with the correct temperature, 1000 eV. Assuming $\ell \sim 2 \times 10^3 \text{ km}$, we find $\epsilon_{||} \sim 5 \text{ mV/meter}$. Parallel electric fields of $\sim 20 \text{ mV/m}$ have been reported [Kelley, et al, 1971] but there are strong arguments indicating that they do not accelerate auroral electrons, eg. see O'Brien [1970]. In our example we have picked representative temperatures, densities and drift velocity and no precise temporal correlation is intended.

Sharp, et al [1971] report that in a coordinated study between ATS5 at $6.6 R_e$ on the equator and the low altitude polar orbiting OY1-18 at $\sim 500 \text{ km}$ altitude on nearly conjugate auroral zone field lines that the electron energy spectra at low altitude exhibited a peaked spectrum not present at ATS5. The most significant objection to a

parallel electric field is that only the peaked portion of the Injun-5 spectrum is supposed to be accelerated and the low energy power law portion is somehow overlooked. We also have other evidence that the peaked spectrum is not simply due to parallel electric fields.

Chamberlain [1969] has examined the effects of a parallel electric field and finds a peak in the energy spectrum characteristic of the potential drop, $\epsilon_{||} l$. He predicts a peak at this energy regardless of the pitch angle. From figures 6.8, 6.9 or 6.28 we see that at 5:00 - 5:05 UT the ratio R_{E_O} is less than unity. In particular at 5:01.6 we have:

$$\begin{array}{ll} E_{O_D} = 12.0 \text{ keV} & E_{O_M} = 11.0 \text{ keV} \\ T_{E_D} = 180 \text{ eV} & T_{E_M} = 360 \text{ eV.} \end{array}$$

The fitting technique returns the values of the parameters which give the best fit. We have attempted to determine whether the 1 keV difference between E_{O_D} and E_{O_M} is significant. In figure 6.32 we have plotted the averaged counts $D_i(n = 22)$ and $M_i(n = 22)$ for roll number 22 ($t \sim 5:01.6$ UT) (see Chapter IV for definitions of $D_i(n)$ and $M_i(n)$) versus the flat spectrum energy corresponding to word i on linear-logarithmic scales. The error bars are the standard deviations of the averages. We note that the count peak for the dumped average, D_i , is higher and narrower than the peak for the mirroring average, M_i . The width at half maximum for the M_i average is ~ 1.5 wider than the corresponding width for the D_i average, and the center of the peak at half maximum is ~ 1 keV less for the mirror average, M_i . Therefore apparently the unfolding technique which converts the

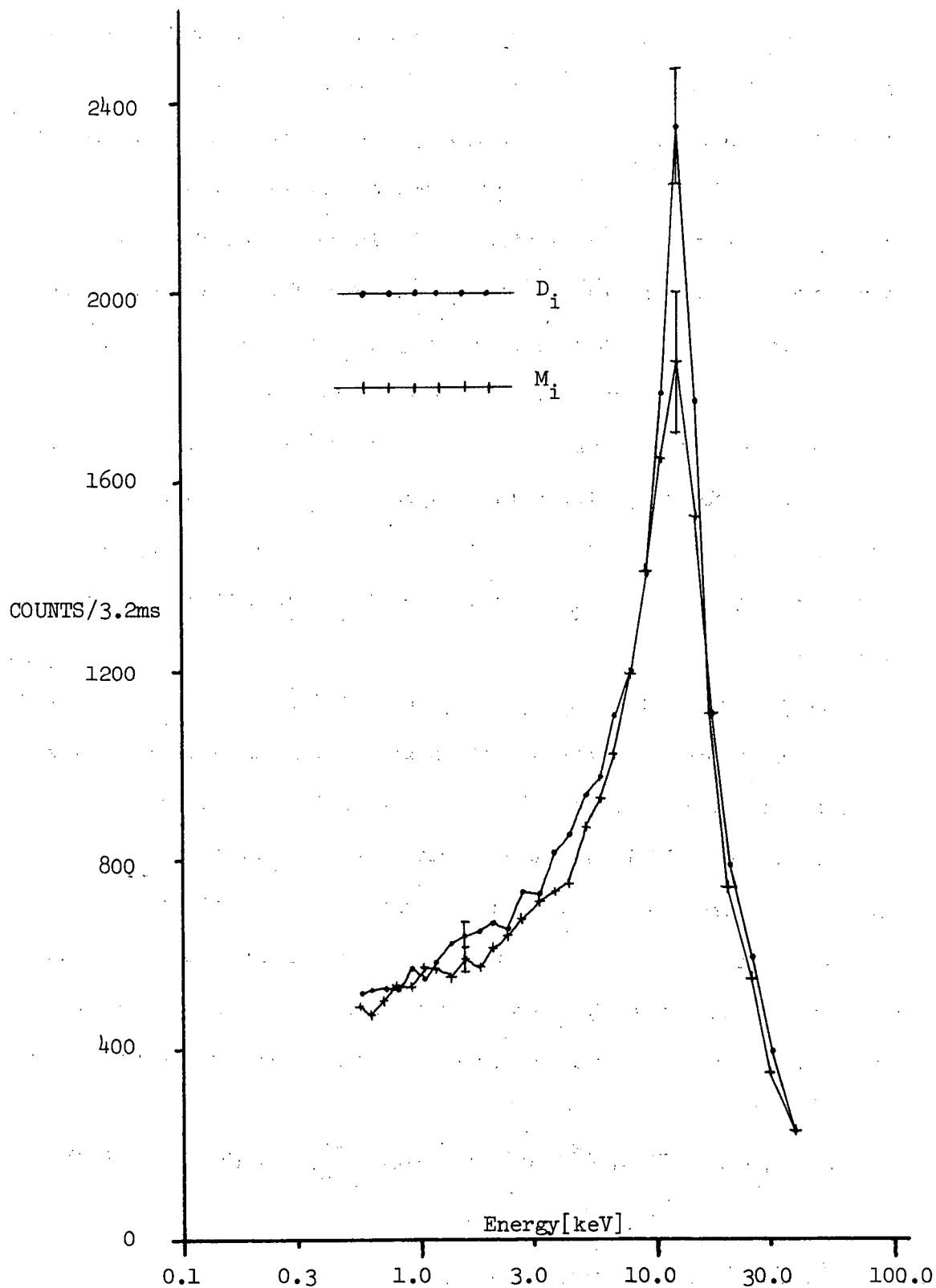


Figure 6.32. Averaged counts for D and M electrons versus energy (note the peak is more distinctive for the count distribution than for the energy spectrum)

count profile into an energy spectrum and the fitting routine which determines E_o and T_e have correctly preserved this essential qualitative difference between the energy spectra of the dumped and mirroring electrons. From figure 6.28 we see that in general the mechanism responsible for the peak energizes both classes of pitch angles an equal amount. Because the ratio R_{E_o} is more frequently less than unity (twice as often) the mechanism may be slightly more efficient at energizing the electrons initially more parallel to \vec{B} . An alternate assumption would be an initial ~ 1 keV separation of the peaks. Mechanisms which act preferentially upon the mirroring pitch angle particles to convert some of the more directed ($\sim E_o$) motion into thermal energy (recall R_{T_e} has a lower limit of unity) will be discussed later.

Swift [1965] and Kindel and Kennel [1971] have proposed plasma instabilities which would produce a high, anomalous resistivity parallel to the magnetic field. These instabilities are linked to field aligned currents which give the electrons a drift motion relative to the ions. These instabilities can be developed when the field aligned current exceeds a threshold value. The field aligned current is proportional to the total downward flux determined by integrating the differential energy spectrum over energy over the downward hemisphere,

$$J(\text{electrons-cm}^{-2}\text{-sec}^{-1}) = \int_0^\infty dE \int \cos\alpha \frac{dj}{dE}(E,\alpha) d\Omega. \quad (6.8)$$

We cannot compute the integral in equation (6.8) over the energy range 0 - 500 eV. From figures 4.2 and 4.3 one can observe that we would have been able to detect in our D_i or P_i averages any

extraordinarily large field-aligned fluxes at energies over 500 eV. The integral over $d\Omega$ in equation (6.8) contributes a factor $\sim \pi$. In figure 6.33 we show results of integrating equation (6.8) over our energy range from 0.5 keV to 30 keV for the drifting Maxwellian component of the precipitating electrons. Assuming the upward flux to be less than 1/5 the downward flux (this is consistent with results of the $U_i(n)$ average when a reasonable fraction of the upward hemisphere was observed) we find that the drifting Maxwellian contributes a net downward flux of $\sim 0.5 \times 10^9$ electrons-(cm²-sec)⁻¹. In figure 6.33 we have also shown the drift energy E_{op} versus time during the burst. We note that there is no correlation between E_{op} and the integral flux. Therefore if an anomalous parallel resistivity is present preventing the ~ 5 mv/m parallel electric field from being shorted out the resistivity is not related to the integral flux of the drifting Maxwellian. The integral flux of the low energy power law spectrum electrons has time dependence as shown by J_o in figure 6.4. It also appears to be uncorrelated with E_o . However we cannot rule out the possible existence of a flux ($E < 500$ eV) with a temporal variation related to that of the parameter E_o . Alternatively as we shall demonstrate later the large ratio of drift velocity to thermal velocity may indicate that an instability capable of giving the anomalous resistivity has developed independent of the integral flux.

Parker [1968] and Sharber and Heikkila [1971] have suggested an enhanced Fermi acceleration process as the energizing mechanism for auroral electrons. The Fermi mechanism is the type B described by Northrup [1963] wherein the mirror points are fixed but a convection of the flux tube from deep in the plasma sheet toward the

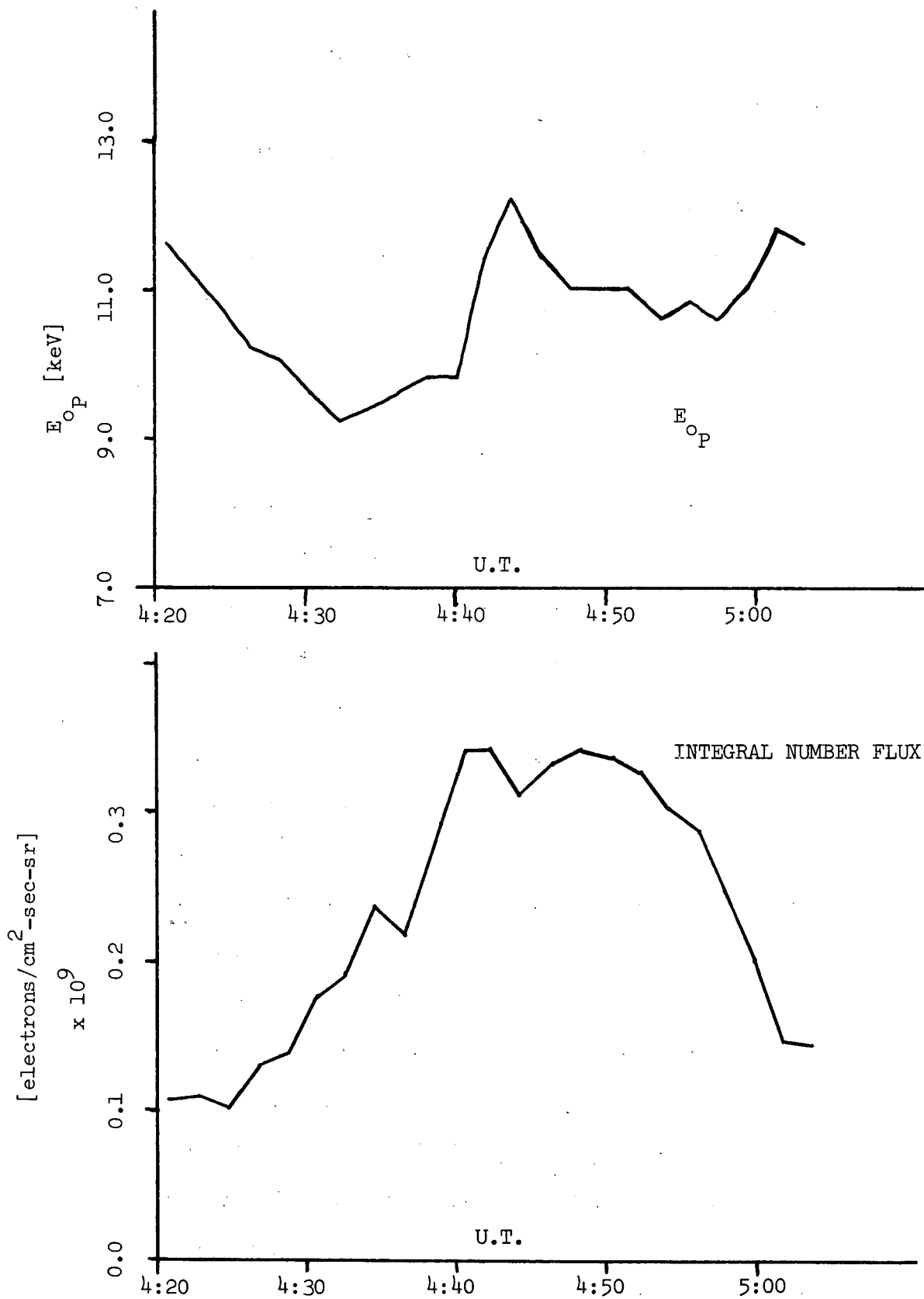


Figure 6.33. Comparison of time profiles of E_{op} and integral number flux in drifting Maxwellian

earth produces an ever decreasing length between mirror points.

Equation (6.9)

$$\langle v_{g||} \rangle \ell = \text{const} \quad (6.9)$$

describes the constancy of the second adiabatic invariant where

$\langle v_{g||} \rangle$ is the average over the bounce time of the parallel velocity of the guiding center and ℓ is the field line length between mirror points. If ℓ_1 is the initial field line length, ℓ_2 is the final length and E_1 is the initial energy Sharber and Heikkila [1971] determine the final energy E_2 to be

$$E_2 = E_1 (\ell_1 / \ell_2)^2 \quad (6.10)$$

Thus the adiabatic compression of the flux tube accelerates the electrons to higher energies. By using the expression "heat the particles" [Parker, 1968] one can understand more clearly that this mechanism increases the electron energy to an amount proportional to the initial electron energy. This raises a very serious objection to such a mechanism. As we have previously stated one cannot fit the peaked spectra of Westerlund [1969] or our own peaked spectra by a simple Maxwellian which has the peak flux at the energy corresponding to the electron temperature. Such a mechanism would indeed require a "monoenergetic" initial energy spectrum to produce the 200 eV wide spectrum at $E_0 = 11$ keV we observe at ~ 4:23 UT (assuming a factor of 20 increase in energy this would imply an initial peak at 550 eV with a 10 eV width). Obviously not all rocket measurements of auroral electron differential energy spectra exhibit

narrow peaks at energies greater than 3 keV, but an examination of the excellent collection of 24 sounding rocket energy spectra of Hones, et al [1971] shows that $\sim 1/3$ of them exhibit such peaks. Although no claim is made that the collection of energy spectra represents a statistically good survey it is obvious that any theory of an auroral precipitation mechanism must be able to produce the narrow, peaked spectra. Our results as well as those of Westerlund [1969] and Albert [1967] show peaks at energies of 10 keV and greater, and we emphasize that the use of phrase "a few keV" to describe the energy of the peak may be confusing and misleading.

Although we would favor acceleration mechanisms for which the final energy is independent of the initial energy our study of the density-temperature relationship (equation (6.5)) does indicate that the drifting Maxwellian portion of the spectrum may have experienced adiabatic compression. Spitzer [1967] shows that equation (6.5) would describe an adiabatic compression where γ , the ratio of specific heats, is related to the degrees of freedom, m , by

$$\gamma = \frac{m + 2}{m} \quad . \quad (6.11)$$

Our determination of the values of γ_D , γ_M and γ_P was over an order of magnitude variation of the parameters. Our results ($\gamma \sim 1.6$) would clearly indicate a compression corresponding to 3 degrees of freedom. As we mentioned previously the mirroring electrons exhibited the most non-adiabatic behavior. Because γ is neither 2 nor 3 one could argue that neither the first nor the second adiabatic invariant is conserved [Axford, 1967]. Throughout the flight such compression leads to order of magnitude fluctuations in the electron temperature,

but we must note that such changes occur in a much shorter time scale (~ 10 sec) than could be associated with a compression of the entire magnetotail.

From a plasma physics point of view the peaked electron energy spectrum can be unstable. We must emphasize that the payload is essentially fixed and is observing the electrons passing by; therefore the distribution may well have had different properties before arriving at our observation point. From the 18:63 UE R.P.A. data we know the properties of the ambient thermal plasma electrons. The density of $\sim 1 \times 10^5$ electrons- cm^{-3} and temperature of $\sim 2300^\circ\text{K}$ correspond to a plasma frequency, $\omega_{pe} \sim 2 \times 10^7$ radians/sec and a Debye length, $\lambda_D \sim 1$ cm. The electron cyclotron frequency, Ω_e , is $\sim 9 \times 10^6$ radians/sec. The magnetic pressure is much, much larger than the plasma pressure. Davidson [1969] shows that for a one dimensional bump-in-tail distribution the electron-plasma wave growth rate is positive for wavelengths given by

$$k \sim \omega_{pe} / v \quad (6.12)$$

where v is a typical velocity in the region where the number of electrons is increasing as a function of energy (or velocity). For our case these would be 10-20 meter waves at frequencies near the plasma frequency. The temporal development is that the waves grow, and they reduce the peaked region to a region with a flat variation with increasing velocity. As the peak is flattened the main body of the distribution over which $\frac{\partial f}{\partial v} < 0$ (where f is the electron velocity distribution function) is slightly heated by $\sim 1/2$ the energy removed from the peaked configuration. The remaining energy taken from the

peaked portion sustains field fluctuations.

In higher dimensions the mere presence of a positive slope ($\frac{\partial f}{\partial v} > 0$) in the velocity distribution does not assure unstable wave growth. However if the positive slope is sufficiently steep, unstable wave modes will also be excited. The non-linear development is not the same as for the one dimensional case. Initially while the growth rate, γ , is positive the wave spectrum grows, but when the peaked portion becomes so broad that the slope is not sufficiently steep the growth rate γ passes through zero and asymptotically the wave spectrum itself reaches zero. A stable peaked distribution remains because infinite wave energy is required to remove it.

For our method of parameterizing the electron differential energy spectrum the ratio of the drift velocity to the thermal velocity is a measure of the slope of the corresponding velocity distribution function in the region of the peak where $\frac{\partial f}{\partial v} > 0$. Because the thermal velocity is related to the temperature we can write

$$v_D/v_{th} = \sqrt{E_o/T_e} \quad . \quad (6.13)$$

We emphasize that not all the electrons are described by the drifting Maxwellian and therefore the drift velocity, v_D , does not apply to the entire electron population. Figure 6.34 shows the ratio v_D/v_{th} for the dumped, mirroring and precipitated electrons during the burst. Throughout the flight we measured $3.0 < v_D/v_{th} < 10$. Initially at $t \sim 4:20$ UT $v_D/v_{th} \sim 6$. Then corresponding to what we have labeled as a thermalization process the ratio decreases to ~ 3 . No experiment was flown on 18:63 UE to measure plasma waves, but

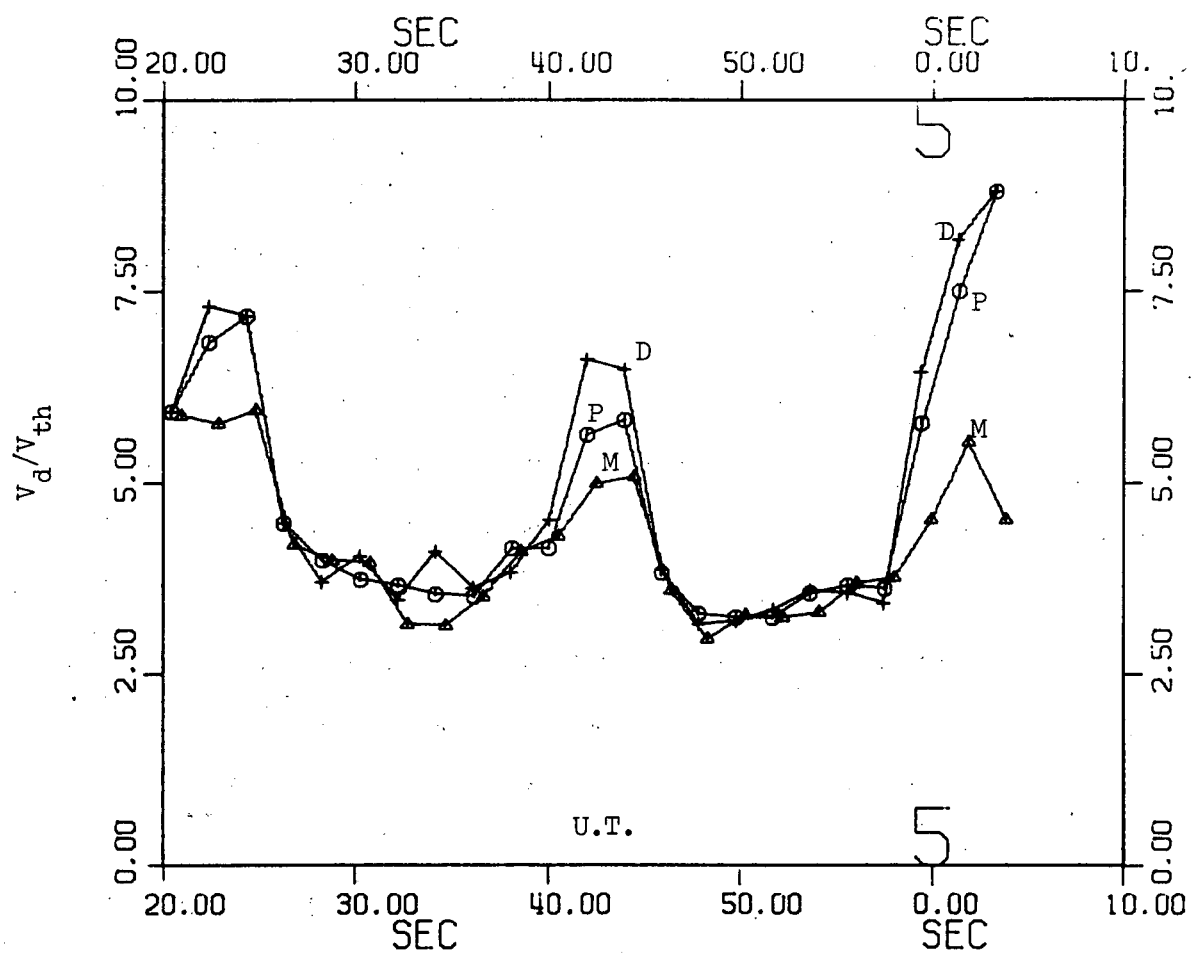


Figure 6.34. Ratio of drift velocity to thermal velocity for D, M, and P electrons during burst

we can interpret the thermalization process by assuming waves were generated by the initially large v_D/v_{th} ($\frac{\partial f}{\partial v}$ was sufficiently large). As the wave spectrum grew it thermalized the peaked portion of the spectrum and even heated the low energy electrons to some extent (see figure 6.5 which shows n decreasing indicating a harder spectrum). The thermal electrons were also heated during this first thermalization process, but we must recall that the energy flux of the electrons was increasing and the heating need not be due to waves. The thermalization process stopped at $v_D/v_{th} \sim 3$. This could be interpreted as being the slope at which the growth rate was no longer positive.

The subsequent temporal behavior from 4:34 - 4:44 UT which we called an acceleration process is somewhat unclear. Perhaps electrons with energies ~ 8 keV were trapped in waves produced during the thermalization process and became energized. Landau damping of the waves may also have energized the electrons. Or perhaps the mechanism responsible for the peaked spectrum initially may have operated to increase E_0 which characterizes the acceleration process.

From figure 6.30 we note two features of the acceleration process (i) initially the pitch angle distribution was highly anisotropic peaked perpendicular to the field lines, and (ii) the recovery to near isotropy at $\sim 4:44$ UT is very indicative of a rather local origin for the acceleration because at large magnetospheric distances the pitch angle separation between the mirroring and dumped electrons would be quite small and differences such as those shown in figure 6.30 would be unlikely.

From 4:44 UT to 5:03 UT the thermalization - acceleration cycle repeats itself. The temperatures of the drifting Maxwellian are

higher during the second cycle, but again the apparent lower limit to $v_D/v_{th} \sim 3$ was reached before the acceleration process began anew.

The burst was studied because of the anisotropic pitch angle distributions during the burst. Because the pitch angle distributions were isotropic before the initial thermalization process began we assume that an anisotropic pitch angle distribution is not a necessary condition for triggering the thermalization process. Wave electric field vectors perpendicular to \vec{B} (whistler waves for example) would tend to produce anisotropic pitch angle distributions peaked perpendicular to \vec{B} . Such an electric field orientation would also account for the observation that $T_{eM} > T_{eD}$ (see figure 6.28). The observations (anisotropy and greater heating) that the mirroring electrons were influenced more than the dumped electrons also indicate a near earth location for the source because if the electrons were not already on trajectories which would bring them to low altitudes these interactions would serve to raise their mirror heights.

A comparison of figure 6.20 which shows the channel A time-pitch angle development of the burst and figure 6.34 which shows the v_D/v_{th} ratio during the burst indicates that the thermalization processes resulted in larger and more anisotropic fluxes at energies above the domain of the drifting Maxwellian. We cannot suggest a mechanism capable of producing the peak in the pitch angle distribution near the loss cone pitch angle for the 90 keV electrons. One could interpret figures 6.20 and 6.21 as indicating that these higher energy electrons had the "wrong" loss cone pitch angle. The loss cone boundary should be at a pitch angle $\alpha \sim 76^\circ$. The 22 keV (channel A) electrons have an apparent loss cone boundary at $\alpha_{22} \sim 40^\circ$. The

90 keV, channel C, electrons exhibit a loss cone type distribution with a boundary at $\alpha_{90} \sim 50^\circ$. For a constant value of the magnetic moment we have

$$\frac{E' \sin^2 \alpha'}{B'} = E_o / B_o \quad (6.14)$$

where the "o" subscript refers to an original mirror point and the " ' " superscript refers to the observed values of the "new" values. If the electrons have not changed energy ($E' = E_o$) the apparent lower loss cone pitch angles ($\alpha' < 76^\circ$) would imply $B_o > B'$ which may indicate convection of the field lines from higher latitudes to lower latitudes during the burst. If the field lines were undisturbed ($B_o = B'$) the lowering of the loss cone boundary could be due to an energization, $E' > E_o$. Equation (6.14) shows that the 22 keV electrons would have been accelerated from 9 keV electrons, and the 90 keV electrons would have been accelerated from 52 keV electrons.

Cummings, et al [1966], Maehlum and O'Brien [1968] and Wedde [1970] have shown that electrojet currents are capable of disturbing the apparent loss cone boundary also, but one must pass close (~ 1 km) to a field line through the region of the current. The magnetic bay at the ground was not exceptionally large ($< 200\gamma$), and our attitude was determined from the locally measured magnetic field.

A study of auroral processes must include an analysis of the energy budget. Was the energy deposited by the precipitated electrons sufficient to account for the known energy sinks in an aurora? An inadequately balanced energy budget led Matthews and Clark [1968] to the first search for low altitude acceleration mechanisms. In

this thesis we have presented several phenomena which require near earth mechanisms, and we will now examine the energy budget to see if more local mechanisms are needed. During the burst the energy flux measured by the PESPEC was $\sim 40 \text{ ergs-cm}^{-2}\text{-sec}^{-1}$. The 5577 \AA peak intensity was $\sim 20 \text{ KR}$ measured $\sim 10\text{-}15 \text{ km}$ from the payload field line. Because [D. Matthews, 1972b] one needs $\sim 1 \text{ erg - cm}^{-2} - \text{sec}^{-1}$ per kilorayleigh the measured energy was certainly adequate assuming no severe variations of spatial structure. On re-entry the E-region electron density was $\sim 2 \times 10^5 \text{ electrons-cm}^{-3}$. The 5577 \AA intensity was $\sim 4 \text{ KR}$. The energy flux measured by the PESPEC had decreased to $\sim 9 \text{ ergs-cm}^{-2}\text{-sec}^{-1}$. The 5577 \AA was measured very near the correct re-entry point, and we observe that the energy budget is very well balanced.

In conclusion we note that although we have obtained more detailed information restricting the mechanism responsible for the sharply peaked auroral electron energy spectra the actual mechanism is still unknown. We have presented evidence which suggests near earth influences upon auroral electrons. A new method of parameterizing the auroral electron energy spectrum has revealed indications of non-linear wave-particle interactions possibly originating in the topside ionosphere.

APPENDIX I

PROCEDURE FOR ACTIVATING BERYLLIUM-COPPER

DYNODES FOR ELECTRON MULTIPLIER.

The dynodes were made from 0.005" thick 2% Be -98% Cu sheet. The activation procedure was necessary to produce a surface coating of BeO rather than CuO because BeO has a larger secondary emission coefficient γ . Therefore once the dynodes have been shaped one must first remove all oxides from the surface. The first (essentially degreasing) step in the cleansing process was a five minute bath in trichloroethylene in an ultrasonic cleaner. This was followed by an ultrasonic rinse in methanol. When the dynodes were removed from the methanol we used a lint-free wiper to quickly dry up any droplets of methanol.

Following the degreasing process two acid pickles were used to remove the oxides. The first solution was 25% by volume nitric acid and 75% by volume orthophosphoric acid at room temperature. The dynodes were left in this solution for 1 minute. This process removed oxides and provided some polishing action. It was followed by a thorough rinsing. The second acid solution was 60-70% by volume sulfuric acid with the remainder water. The temperature of the solution was $\sim 120^{\circ}\text{f}$, and the dynodes were in this solution for 5 minutes. This process completed the oxide removal. Following rinsing in water the dynodes were rinsed in methanol to remove any remaining water. Once again the dynodes were individually dried with a lint-free wiper to remove any droplets. The dynodes were then prepared for the activation

process.

The dynodes were placed in a stainless steel r.f. induction oven inside a vacuum chamber. The temperature inside the oven was monitored with a chromel-alumel thermocouple. Water vapor was used for the oxidization of the beryllium. A flask filled with ice was connected through a valve to the vacuum chamber. To keep the water vapor pressure low we cooled the flask with dry ice.

With the valve closed the vacuum chamber was pumped down to a pressure of $\sim 2 \times 10^{-5}$ mmHg. Then the oven was heated with the r.f. coil. The oxidation procedure began after the temperature had been at 625°C for 15 minutes (this temperature was then maintained throughout the process). Opening the valve allowed water vapor to enter the vacuum chamber. When the pressure reached $\sim 15\mu$ (as measured by a thermocouple gauge) the valve was closed. After ~ 10 minutes the chamber was pumped down to less than 0.1μ . Again the valve was reopened allowing water vapor to enter the chamber. The valve was closed when the pressure reached $\sim 25\mu$. This ~ 10 minute cycle was repeated until ~ 50 minutes of oxidation had elapsed. During each succeeding cycle the water vapor pressure was allowed to rise above the preceding valve until during the final cycle the pressure was $\sim 50\mu$. When the chamber was pumped down the final time the heating was discontinued.

After activation the dynodes were assembled to form the electron multiplier. Gloves were worn to avoid getting fingerprints on the surfaces. No loss of gain was observed over a period of months. About 10% of this time the multipliers were in an oil-pumped, untrapped vacuum system. During the remainder of the time they were in storage where no special clean-box techniques were used.

APPENDIX II

DETERMINATION OF $\Delta\alpha_{ij}$ - THE RANGE OF ALLOWED ENTRANCE ANGLES IN THE PLANE OF THE TRAJECTORY

We assume that the electrostatic force is central and neglect fringing fields. We define symbols used to determine the trajectories. These symbols follow those of [Paolini and Theodoridis, 1967] (see also figures 2.7, 2.8 and 2.9).

R_o - outer plate radius of curvature

R_i - inner plate radius of curvature

ΔR - plate separation

r, ϕ - polar coordinates of electron between plates

r_{oi} - entrance radius

ϕ_{oj} - central angle subtended by trajectory

V_o - outer plate voltage (<0)

V_i - inner plate voltage (>0)

$V \equiv V_o - V_i$ - potential difference between the plates (<0)

$\Phi(r)$ - electrostatic potential energy of electron between plates
at radius r

$T(r)$ - kinetic energy of electron at (r, ϕ)

T_∞ - kinetic energy of electron before entering plates.

Solving Laplace's equation for the scalar potential, ψ , in spherical coordinates for two concentric spheres with voltages V_o and V_i one obtains

$$\psi = k_1 r^{-1} + k_2 \quad (\text{AII.1})$$

The electrostatic potential energy is

$$\Phi(r) = -Kr^{-1} + \Phi_{\infty} \quad (\text{AII.2})$$

where

$$K = \frac{-e(R_o)(R_i)V}{\Delta R}, \quad \Phi_{\infty} = \frac{-e(V_o R_o - V_i R_i)}{\Delta R}.$$

Conservation of energy as the electron enters the plates gives

$$T_{\infty} = T(r) + \Phi(r) = T(r) - Kr^{-1} + \Phi_{\infty} = \text{constant} \quad (\text{AII.3})$$

We now have the additive constant needed to determine the total energy, E , of the electron

$$E = T_{\infty} - \Phi_{\infty} = T(r) - Kr^{-1} = \text{constant} \quad (\text{AII.4})$$

Because an elliptical trajectory is needed to pass between the plates we need $E < 0$. One can differentiate equation (AII.2) to get the electrostatic field, $\vec{\epsilon}(r)$

$$\vec{\epsilon}(r) = \nabla \left[\frac{\Phi(r)}{e} \right] = \frac{K}{er^2} \hat{r} \quad (\text{AII.5})$$

The electrostatic force is then an attractive, inverse square, radial force.

$$\vec{F} = -e\vec{\epsilon}(r) = -\frac{K}{r^2} \hat{r} \quad (\text{AII.6})$$

Because the force is radial the trajectory will lie in a plane and the angular momentum, ℓ , will be constant [Goldstein, H., 1950].

$$\ell = mr^2\dot{\phi} = \text{constant} \quad (\text{AII.7})$$

The eccentricity, ϵ , of the conical motion is given by

$$\epsilon = \sqrt{1 + \frac{2E\ell^2}{mK^2}} \quad (\text{AII.8})$$

To determine ϵ we must evaluate ℓ . As the electron enters the plates with some angle α at a radius r_{oi} (see figure 2.7) it has kinetic energy $T(r_{oi})$

$$T(r_{oi}) = 1/2 mv^2 = 1/2 m(\dot{r}^2 + r_{oi}^2 \dot{\phi}^2) \quad (\text{AII.9})$$

One can determine v , \dot{r} and $\dot{\phi}$ from α and $T(r_{oi})$.

$$v = \sqrt{\frac{T(r_{oi})}{2m}}$$

$$\dot{r} = v \sin \alpha \quad (\text{AII.10})$$

$$\dot{\phi} = (v/r_{oi}) \cos \alpha$$

Using equations (AII.10) and (AII.7) we can determine ℓ ,

$$\ell^2 = \text{constant} = m^2 r^4 \dot{\phi}^2 = 2mT(r_{oi}) r_{oi}^2 \cos^2 \alpha. \quad (\text{AII.11})$$

$T(r_{oi})$ is determined from equation (AII.3)

$$T(r_{oi}) = T_{\infty} - \Phi_{\infty} + K r_{oi}^{-1} \quad (\text{AII.12})$$

We then introduce U defined by

$$U \equiv \frac{mK}{\ell^2} = \frac{K}{2T(r_{oi}) r_{oi}^2 \cos^2 \alpha} \quad (\text{AII.13})$$

and the eccentricity can be determined from

$$\epsilon^2 = 1 + \frac{2E}{KU} \quad (\text{AII.14})$$

The equation of the trajectory [Goldstein, H., 1950] is

$$r^{-1} = U(1 + \epsilon \cos (\phi - \phi')) \quad (\text{AII.15})$$

The angle of apsides, ϕ' , can be determined from the slope of the trajectory at r_{oi} and the derivative of equation (AII.15) with respect to time.

$$\begin{aligned} -r^{-2}\dot{r} &= -U\epsilon \sin (\phi - \phi')\dot{\phi} \\ \sin (\phi - \phi') &= \frac{\tan \alpha}{U\epsilon r} \end{aligned} \quad (\text{AII.16})$$

At the entrance ($r = r_{oi}$) we have $\phi = 0$, therefore

$$\sin \phi' = \frac{-\tan \alpha}{U\epsilon r_{oi}} \quad (\text{AII.17})$$

These conditions in equation (AII.15) gives

$$\begin{aligned} r_{oi}^{-1} &= U(1 + \epsilon \cos (-\phi')) = U + U\epsilon \cos \phi' \\ \cos \phi' &= \frac{1 - Ur_{oi}}{U\epsilon r_{oi}} \end{aligned} \quad (\text{AII.18})$$

Equations (AII.17) and (AII.18) uniquely determine ϕ' ,

$$\phi' = \tan^{-1} \left[\frac{-\tan \alpha}{(1 - Ur_{oi})} \right]. \quad (\text{AII.19})$$

Using the parameters determined in equations (AII.2), (AII.4), (AII.12), (AII.13), (AII.14) and (AII.19) one can use equation (AII.15)

to determine the trajectory of the electron as it passes through the plates for a given T_∞ , r_{O_i} and α .

However an electron may have a trajectory which does not strike the plates but is intercepted by the exit collimator. After the electron exits the plates at $\phi = \phi_{O_j}$ we assume it follows a straight ray trajectory. We define α_{exit} to be the value of the angle α defined in figure 2.7 when $\phi = \phi_{O_j}$. If r_{exit} is the radius at $\phi = \phi_{O_j}$ we can use equation (AII.16) to determine α_{exit} ,

$$\tan \alpha_{\text{exit}} = U \epsilon r_{\text{exit}} \sin (\phi_{O_j} - \phi') \quad (\text{AII.20})$$

For an exit slot thickness, W , we can use the sine of the angle A defined in figure 2.10 to compute the distance, d , in the plane of the trajectory which the electron must drift to pass through the exit collimator,

$$d = W / \sin A \quad (\text{AII.21})$$

The radial distance the electron will drift (for $W \ll R_i$) is given by

$$\Delta r = d \tan \alpha_{\text{exit}} = \frac{\epsilon W U r_{\text{exit}}}{\sin A} \sin (\phi_{O_j} - \phi') \quad (\text{AII.22})$$

Therefore the radial position of the electron as it exits the collimator, r_c , is given by

$$r_c = r_{\text{exit}} + \Delta r \quad (\text{AII.23})$$

A necessary condition for an allowed trajectory is that $R_i < r_c < R_o$.

For a given value of the entrance radius, r_{oi} , equations (2.19) and (2.20) give the maximum and minimum possible values of α , $\alpha_{\max_{ij}}$ and $\alpha_{\min_{ij}}$, depending upon the entrance collimator width. The value of $\Delta\alpha_{ij}$ is determined from the maximum and minimum values of α within the interval $\alpha_{\min_{ij}} < \alpha < \alpha_{\max_{ij}}$ which have trajectories which are always between the plates.

The computer program which determines $\Delta\alpha_{ij}$ for given T_∞ , r_{oi} , ϕ_{oj} , etc. first determines $\alpha_{\max_{ij}}$ and $\alpha_{\min_{ij}}$. Beginning at $\alpha_{\min_{ij}}$ test values of α within this interval are used to compute the parameters in equations (AII.15) and (AII.23). Calculating time is minimized by checking first for exit clearance and then by varying ϕ in equation (AII.15) from ϕ_{oj} back to $\phi = 0^\circ$ in 1° steps. At each step r is calculated to determine whether the electron is still between the plates. The first value of α which has an allowed trajectory is defined as α_1 . One then continues increasing α until the trajectory hits the plates. Defining the last allowed trajectory as α_2 we can calculate $\Delta\alpha_{ij}$,

$$\Delta\alpha_{ij} = \alpha_2 - \alpha_1 \quad . \quad (\text{AII.24})$$

The use of elliptical rather than circular trajectories frees this method from the [Paolini and Theodoridis, 1967] assumption that $\Delta R/R_i$ is small. Furthermore, by subdividing the entrance slot one can compute the geometric factor without requiring the [Paolini and Theodoridis, 1967] assumption that $\Delta\alpha$ and $\Delta\beta$ are small. By including collimation effects this method represents an improvement upon [Smith and Day, 1971] wherein the limiting angles α_1 and α_2 are calculated. The

limitations imposed upon the range of α by the collimators can be very important. Neglect of the collimation in computing the upper slot geometric factor produces a factor of 2 error. The Univac 1108 computer time needed to compute the geometric factors for both entrance slots was less than two minutes.

REFERENCES

- Akasofu, S. -I., The Development of the Auroral Substorm, Planet. Space Sci., 12, 273-282, 1964.
- Akasofu, S. -I. and Chapman, S., Geomagnetic Storms and Auroras, p. 1143, Physics of Geomagnetic Phenomena, Matsushita and Campbell, Vol. II, Academic Press, New York and London 1967.
- Albert, R. D., Energy and Flux Variations of Nearly Monoenergetic Auroral Electrons, J. Geophys. Res., 72, 5811, 1967.
- Albert, R. D. and Lindstrom, P. J., Auroral-Particle Precipitation and Trapping Caused by Electrostatic Double Layers in the Ionosphere, Science, 170, 1398-1401, 1970.
- Alfvén, H., Theory of Magnetic Storms, I. Kgl., Svenska Vetenskapsakad. Handl., [3], 18, No. 3, 1939.
- Alfvén, H. and Fälthammer, C. -G., Cosmical Electrodynamics, 2nd ed., Oxford Univ. Press (Clarendon), London and New York, 1963.
- Allen, J. S., An Improved Electron Multiplier Particle Counter, Review of Scientific Instruments, 18, 739, 1947.
- Barcus, J. R., R. R. Brown, R. H. Karas, T. J. Rosenberg, H. Trefall, and K. Bronstad, Auroral X-Ray Pulsations in the 1.2 - to 4 - second Period Range, J. Geophys. Res., 76, 1971, p. 3811-3815.
- Bingham, R. A., A Stable Aluminum Electron Multiplier, J. Sci. Instrum., 43, 74, 1966.
- Birkeland, K., The Norwegian Aurora Polaris Expedition, 1902-1903, H. Aschehoug and Co., Christiania, Norway, Pt. 1, pp. 39-315, 1908; Pt. 2, pp. 319-551, 1913.
- Chamberlain, J. W., Electric Acceleration of Auroral Particles, Rev. Geophys. Space Phys., 7, 461-482, 1969.
- Chase, L. M., Energy Spectra of Auroral Zone Particles, J. Geophys. Res., 75, 7128, 1970.
- Choy, L. W., Arnoldy, R. L., Potter, W., Kintner, P., and Cahill, L. J., Field-Aligned Particle Currents Near an Auroral Arc, J. Geophys. Res., 76, 8279-8298, 1971.
- Cloutier, P. A., H. R. Anderson, R. J. Park, R. R. Vondrak, R. J. Spiger, and B. R. Sandel, Detection of Geomagnetically Aligned Currents Associated with an Auroral Arc, J. Geophys. Res., 75, 2595, 1970.

- Courtier, G. M., Bennett G., and Bryant, D. A., Pitch-angle Diffusion of Electrons in a Glow Aurora, J. of Atmospheric and Terrestrial Physics, 33, 847-858, 1971.
- Cummings, W. D., R. E. La Quey, B. J. O'Brien, and M. Walt, Rocket-borne measurements of particle fluxes and auroral light, J. Geophys. Res., 71, 1399, 1966.
- Davidson, R. C., Non-Linear Plasma Theory, class notes, 1969.
- Davis, L. R., Berg, O. E., and Meredith, L. H., Direct Measurements of Particle Fluxes in and Near Auroras, Space Research, [Proc. Intern. Space Sci. Symp.] North-Holland Publishing Company, Amsterdam, 721-735, 1960.
- Davis, T. N., The Aurora, p. 227, Introduction to Space Science, Edited by W. Hess & G. Mead, 2nd Ed., Gordon and Breach, Science Publishers, New York/London/Paris, 1968.
- DeForest, S. E. and McIlwain, C. E., Plasma Clouds in the Magnetosphere, J. Geophys. Res., 76, 3587, 1971
- Dungey, J. W., Interplanetary Magnetic Field and the Auroral Zones, Phys. Rev. Letters, 6, 47-48, 1961.
- Dungey, J. W., Waves and Particles in the Magnetosphere, in Physics of the Magnetosphere, Ed. by R. L. Carovillano, J. F. McClay, and H. R. Radoski (Springer-Verlag New York Inc., New York, 1968), p. 220.
- Eather, R. H., Auroral Proton Precipitation and Hydrogen Emissions, Reviews of Geophysics, 5, 207-285, 1967.
- Evans, D. S., A 10-cps Periodicity in the Precipitation of Auroral-Zone Electrons, J. Geophys. Res., 72, 4281, 1967.
- Evans, D. S., The Observation of a Near Monoenergetic Flux of Auroral Electrons, G.S.F.C. Tech Note X-611-67-487, 1967.
- Frank, L. A., and Ackerson, K. L., Observations of Charged Particle Precipitation into the Auroral Zone, J. Geophys. Res., 76, 1971, p. 3612-3643.
- Foster, J. C., Fairfield, D. H., Ogilvie, K. W., and Rosenberg, T. J., Relationship of Interplanetary Parameters and Occurrence of Magnetospheric Substorms, J. Geophys. Res., 76, 6971, 1971.
- Goldstein, H., Classical Mechanics, Addison-Wesley Press, Inc., Cambridge, Mass., 1950.
- Heikkila, W. J., Smith, J. B., Tarstrup, J., and Winningham, J. D., The Soft Particle Spectrometer in the ISIS-I Satellite, 1970, Rev. Sci. Instruments, 41, 1393.
- Heikkila, W. J., Photoelectron Escape Flux Observations at Midlatitudes, J. Geophys. Res., 75, 4877-4879, 1970.

- Hoffman, R. A., and Evans, D. S., Field-Aligned Electron Bursts at High Latitudes Observed by OG04, 1968, J. Geophys. Res., 73, 6201-6214.
- Hones, E. W., Asbridge, J. R., Bame, S. J., and Singer, S., Energy Spectra and Angular Distributions of Particles in the Plasma Sheet and Their Comparison with Rocket Measurements Over the Auroral Zone, J. Geophys. Res., 76, 1971, p. 63-87.
- Hultquist, B., Borg, H., Riedler, W., and Christophersen, P., Observations of Magnetic Field Aligned Anisotropy For 1 and 6 keV Positive Ions In the Upper Ionosphere, Planet. Space Sci., 19, 279-295, 1971
- Johnstone, A., Wertz, R. P., and Davis, T. N., Low Altitude Auroral Particle Acceleration, EoS Abstracts, 52, Nov. 1971, p. 896.
- Kanter, H., Electron Scattering by Thin Solids for Energies Below 10 keV, Phys. Rev., 121, 461, 1961.
- Kanter, H. and Sternglass, E. J., Interpretation of Range Measurements for Kilovolt Electrons in Solids, Phys. Rev., 126, 620, 1962.
- Kelley, M. C., Mozer, F. S., and Fahleson, U. V., Electric Fields in the Nighttime and Daytime Auroral Zone, J. Geophys. Res., 76, 6054-6066, 1971.
- Kennel, C. F., and Petschek, Limit on Stably Trapped Particles, J. Geophys. Res., 71, 1-28, 1966.
- Kindel, J. M. and Kennel, C. F., Topside Current Instabilities, J. Geophys. Res., 76, 3055-3078, 1971.
- Land, P. L., A Discussion of the Region of Linear Operation of Photomultipliers, Rev. Sci. Instrum., 42, 420, 1971.
- Langel, R., private communication, 1971.
- Lincoln, J. V., Editor, Geomagnetic and Solar Data, J. Geophys. Res., 73, 5019, 1968.
- Maehlum, B. and B. J. O'Brien, The mutual effect of precipitated auroral electrons and the auroral electrojet, J. Geophys. Res., 73, 1679, 1968.
- Matthews, D. L. and Clark, T. A., Simultaneous Observation of Electron Fluxes, Ionization, and Luminosity in an Aurora, Canadian Journal of Physics, 46, 201 (1968).
- Matthews, D. L., to be published, 1972a.
- Matthews, D. L., private communication, 1972b.

- McDiarmid, I. B., Rose, D. C., and Budzinski, E., Direct Measurement of Charged Particles Associated with Auroral Zone Radio Absorption, Canad. J. Phys. 39, 1888, 1961.
- McDiarmid, I. B. and Budzinski, E. E., Angular Distribution and Energy Spectra of Electrons Associated with Auroral Events, Canad. J. Phys., 42, 2048 (1964).
- McDiarmid, I. B., Budzinski, E. E., Whalen, B. A., and Schopke, N., Rocket Observations of Electron Pitch Angle Distributions During Auroral Substorms, Canad. J. Phys., 45, 1755 (1967).
- McIlwain, C. E., Direct Measurement of Particles Producing Visible Auroras, J. Geophys. Res., 65, 2727-2747, 1960.
- Northrup, T. G., The Adiabatic Motion of Charged Particles, Interscience Publishers - John Wiley and Sons, New York, London, Sydney, 1963.
- O'Brien, B. J., Lifetimes of Outer-Zone Electrons and Their Precipitation into the Atmosphere, J. Geophys. Res., 67, 3687-3706, 1962.
- O'Brien, B. J., Considerations That the Source of Auroral Energetic Particles is not a Parallel Electrostatic Field, Planet. Space Sci., 18, 1821-1827, 1970.
- Ogilvie, K. W., Auroral Electron Energy Spectra, J. Geophys. Res., 73, 2325, 1968.
- Park, R. J., and Cloutier, P. A., Rocket-Based Measurement of Birkeland Currents Related to an Auroral Arc and Electrojet, J. Geophys. Res., 76, 7714-7733 (1971).
- Parker, E. N., Dynamical Properties of the Magnetosphere, in Physics of the Magnetosphere, Ed. by R. L. Carovillano, J. F. McClay, and H. R. Radowski (Springer-Verlag New York, Inc., New York, 1968), p. 55.
- Paolini, F. R. and Theodoridis, G. C., Charged Particle Transmission Through Spherical Plate Electrostatic Analyzers, Rev. Sci. Instrum., 38, 579, 1967.
- R.C.A., Phototubes and Photocells, Technical Manual PT-60, Radio Corporation of America, Lancaster, Pa., 1963.
- Reagan, J. B., Carr, D. L., McDaniel, J. D. and Sanders, T. C., Low Energy Electron and Proton Satellite Instrumentation for Auroral Studies, IEEE Trans., NS-14, 49, 1967.
- Rees, M. H., Auroral Electrons, Space Science Reviews, 10, 413-441, 1969.

- Rème, H. and Bosqued, J. M., Evidence Near the Auroral Ionosphere of a Parallel Electric Field Deduced from Energy and Angular Distributions of Low-Energy Particles, J. Geophys. Res., 76, 7683-7693, 1971.
- STP Notes, Inter-Union Commission on Solar-Terrestrial Physics, No. 9, 1971.
- Sharber, J. R. and Heikkila, W. J., Enhanced Fermi Acceleration During Magnetospheric Substorms, Submitted to J. Geophys. Res., Sept., 1971.
- Sharp, R. D., Carr, D. L., Johnson, R. G., and Shelley, E. G., Coordinated Auroral-Electron Observations from a Synchronous and a Polar Satellite, J. Geophys. Res., 76, 7669-7682, 1971.
- Sherman, I. S., Freedman, M. S., Porter, F. T., and Wagner, F., Electron Response of NaI (Tl) and a Comparison With Anthracene and Pilot-B. IEEE, Trans., NS-11, 20, 1964.
- Smith, Z. K. and Day, J. R., A Mathematical Model of the Arc Pioneer 6/7 Plasma Probe, Rev. Sci. Instrum., 42, 968, 1971.
- Spitzer, L., Physics of Fully Ionized Gases, Interscience Publishers - John Wiley & Sons, New York, London, Sydney, 1967.
- Stolarski, R. S. and Green, A. E. S., Calculations of Auroral Intensities from Electron Impact, J. Geophys. Res., 72, 3967, 1967.
- Störmer, C., The Polar Aurora, Oxford Univ. Press, London and New York, 1955.
- Swift, D. W., A Mechanism for Energizing Electrons in the Magnetosphere, J. Geophys. Res., 70, 3061, 1965.
- Theodoridis, G. C. and Paolini, F. R., The Angular Response of Spherical Plate Electrostatic Analyzers, Rev. Sci. Instrum., 40, 621, 1969.
- Vegard, L., Emission Spectra of Night Sky and Aurora, Reports of the Gassiot Committee, p. 82, The Physical Society London, 1948.
- Wedde, T., On The Influence of Inhomogeneous Magnetic Fields Upon the Scattering and Absorption of Auroral Electrons, Intern Rapport E-162, Norwegian Defence Research Establishment, 1970.
- Westerlund, L. H., The Auroral Electron Energy Spectrum Extended to 45 eV, J. Geophys. Res., 74, 351, 1969.
- Winckler, J. R., Peterson, L., Arnoldy, R., and Hoffman, R., X-Rays From Visible Aurorae at Minneapolis, Phys. Rev., 110, 1221-1231, 1958.